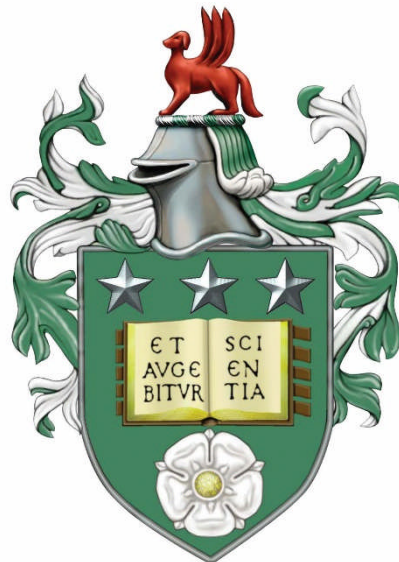


# Computational modelling of coalescence filtration process

Kirijen Vengadasalam

Submitted in accordance with the requirements for the degree of  
Doctor of Philosophy

The University of Leeds  
School of Mechanical Engineering



October, 2016

The candidate confirms that the work submitted is his/her own and that appropriate credit has been given where reference has been made to the work of others.

This copy has been supplied on the understanding that it is copyright material and that no quotation from the thesis may be published without proper acknowledgement.

The right of Kirijen Vengadasalam to be identified as Author of this work has been asserted by him in accordance with the Copyright, Designs and Patents Act 1988.

© 2016 The University of Leeds and Kirijen Vengadasalam

## **Acknowledgements**

*First of all, I would like to express my sincere gratitude and special appreciation to my supervisors Dr Mark Wilson and Professor Nikil Kapur for their help, guidance and also being supportive and encouraging through my PhD. They have been tremendous mentors and this work would not have been possible without their support.*

*I would like to thank Professor Stephen Russell, Dr Parikshit Goswami and Dr Umer Farooq for their time for sharing their knowledge. I would like to thank Dr Nicolas Delbosc for helping me in the CUDA programming.*

*I especially thank my mom (Manjula Vengadasalam), brother (Lavanan Vengadasalam) and uncles (Shivakumar and Udayakumar) for their continuous support, encouragement and love.*

*This thesis is dedicated to my late father (Vengadasalam Perumal), who unfortunately didn't stay in this world long enough to see me become a doctor.*

*Finally would like to thank all my friends and colleagues.*

## **Abstract**

The low water-diesel interfacial tensions arising in biodiesels pose a problem for fuel filters designed to separate water contamination from diesel fuel. Such filters operate by passing the fuel through a fibrous non-woven material with the aim of capturing small water droplets on the fibres and holding them while further droplets coalesce with the captured droplets until the droplets are large enough to be carried away from the fibres and subsequently settle out of the fuel by gravity. The coalescence process is however less effective at lower interfacial tensions.

The main purpose of this research is to explore the mechanisms at work in a coalescence filter by developing and applying computer simulations of the process, and to understand the effects of fibre properties such as wettability, size and separation on the filtration performance. Following a detailed review of the relevant literature, a macroscopic simulation of the flow within a filter housing is first presented, using finite element analysis via COMSOL Multiphysics to establish the main flow patterns through the filter system. The filter medium itself in this model is treated as a continuous porous medium.

The flow at the pore/fibre scale is then analysed by means of a multiphase lattice Boltzmann method based on the multicomponent Shan-Chen model. The wettability of the fibres is incorporated through specification of a fluid density at the solid surfaces, allowing easy control of the local contact angle. The code developed is tested against previously published and validated finite volume/volume-of-fluid simulations of free droplet coalescence, with good agreement seen in the predicted dynamics.

The interactions between individual water droplets and fibres is explored, in particular to establish critical conditions (flow speed, fibre contact angle, droplet/fibre size, droplet-fibre separation, fuel viscosity etc.) under which droplets carried by the flow can be captured by fibres, and the conditions under which droplets are released from fibres. The results confirm the difficulties in achieving rapid and effective coalescence when the interfacial

tension is low, and reveal the sensitivity of the droplet-fibre dynamics to the contact angle on the fibres and the relative size of the droplets and fibres. In particular larger fibres are not effective for small droplets, so small fibres are essential in the filtration process.

Also investigated are the dynamics of multiple droplets with arrays of fibres representing the filtration media. It is found that higher contact angles ( $\theta > 120^\circ$ ) lead to lower capture efficiency compared to lower contact angle, while contact angles less than  $106^\circ$  tend to produce a small variation in capture efficiency and capture most of the droplets at a filter porosity of 0.87. It is concluded that the inlet layer of the filter should have fibres with  $78^\circ$  contact angle and the exit layer fibres with contact angle  $106^\circ$ .

## Table of Contents

<b>Acknowledgements</b> .....	<b>iii</b>
<b>Abstract</b> .....	<b>iv</b>
<b>Table of Contents</b> .....	<b>vi</b>
<b>List of Tables</b> .....	<b>xi</b>
<b>List of Figures</b> .....	<b>xiv</b>
<b>List of Abbreviations</b> .....	<b>xx</b>
<b>Chapter 1 Introduction</b> .....	<b>1</b>
1.1 Motivation for Research .....	1
1.2 Aims and Objectives.....	3
1.3 Structure of Thesis .....	3
<b>Chapter 2 Literature review</b> .....	<b>5</b>
2. Introduction .....	5
2.1 Types of Diesel fuel.....	5
2.1.1 Fuel Ultra-low sulphur Diesel or EN590 Diesel .....	5
2.1.2 Biodiesel.....	6
2.2 Contaminants in Diesel .....	7
2.2.1 Particles in Diesel.....	7
2.2.2 Water in Diesel.....	9
2.2.3 Organic contaminants of Diesel .....	11
2.3 Fuel properties .....	11
2.3.1 Density .....	11
2.3.2 Viscosity .....	12
2.3.3 Interfacial tension .....	12
2.3.4 Summary.....	13
2.4 Emulsion of Water in Diesel fuel .....	14
2.4.1 Three-Phase Emulsion.....	17
2.4.2 Two-Phase Emulsion .....	17
2.5 Filtration methods.....	18
2.5.1 Solid from fluid separation process .....	19
2.5.2 Liquid from liquid filtration process in a fibre bed .....	20
2.6 Capture mechanism .....	21
2.7 Types of filter.....	23

2.7.1	Cake filtration .....	24
2.7.2	Deep-bed filtration.....	25
2.7.3	Membrane filtration.....	25
2.8	Porous media flow.....	28
2.8.1	Darcy's law .....	28
2.8.2	Permeability .....	29
2.8.3	Porosity .....	30
2.8.4	Effect of particle shapes.....	31
2.8.5	Effect of particle size and distribution.....	32
2.9	Fibre Media .....	33
2.9.1	Woven media .....	33
2.9.2	Non-Woven media.....	35
2.9.3	Advantages and disadvantages of woven and non-woven methods.....	38
2.10	Wettability.....	38
2.11	Liquid-liquid filtration.....	41
2.11.1	Oil in water and water in oil separation methods.....	41
2.12	Coalescence filtration.....	42
2.12.1	Effect of wettability .....	47
2.12.2	Effect of velocity on filtration.....	49
2.12.3	Effect of fibre bed .....	52
2.12.4	Summary of filtration & coalescence literature review .....	52
2.13	Fluid simulation methods.....	53
2.13.1	Finite difference method (FDM).....	54
2.13.2	Finite volume method (FVM) .....	54
2.13.3	Finite element method (FEM).....	54
2.13.4	Lattice Boltzmann method (LBM) .....	55
2.13.5	Difference between Traditional CFD and LBM .....	56
2.13.6	Summary of flow modelling methods.....	58
2.14	Chapter Summary .....	58
<b>Chapter 3 Filter cartridge optimisation .....</b>		<b>59</b>
3.1	Introduction of filter cartridge optimisation.....	59
3.2	Comsol methodology (governing equations) .....	59
3.2.1	Boundary condition.....	60
3.3	Problem setup .....	62
3.4	Analysis method.....	66

3.4.1 The flow field .....	66
3.4.1 particle tracking .....	67
3.5 Comsol results .....	68
3.5.1 Effect on water droplet diameter in original filter cartridge geometry .....	68
3.5.2 Changing the inlet annulus.....	69
3.5.3 Effect of L2 change in the filter cartridge .....	70
3.5.4 Effect of L3 change in the filter cartridge .....	71
3.6 Discussion .....	72
3.6 Summary .....	72
<b>Chapter 4 Lattice Boltzmann Method .....</b>	<b>74</b>
4. Introduction .....	74
4.1 Lattice Boltzmann Method (LBM) .....	75
4.1.1 Discretization of the Boltzmann Equation.....	75
4.1.2 Hydrodynamic Moments.....	76
4.1.3 Equilibrium Distribution Function $f^{eq}$ .....	77
4.1.4 Temporal Discretization.....	79
4.1.5 kinematic viscosity ( $\nu$ ) .....	80
4.2 From the Lattice Boltzmann equation (LBE) to Navier Stokes equations (N-S).....	81
4.2.1 Chapman-Enskog expansion .....	81
4.2.2 Lattice Boltzmann equation (LBE) to Navier-Stokes equations (N-S) .....	81
4.3 LBM computer implementation process .....	83
4.3.1 Streaming step .....	83
4.3.2 Collision step .....	84
4.4 Boundary condition.....	84
4.4.1 Periodic boundary conditions .....	84
4.4.2 Bounce back Boundary conditions .....	85
4.4.3 Zou-He (pressure boundary) .....	86
4.4.4 Force Equilibrium .....	88
4.4.5 Zero gradient boundary (Neumann boundary condition) ....	88
4.5 Summary of procedure.....	88
4.6 Multiphase flow modelling. ....	89
4.7 Shan-Chen Multiphase Model .....	91
4.7.1 Phase separation .....	91

4.7.2	Wetting boundary condition.....	92
4.7.3	Force inclusion.....	92
4.7.4	Equation of state (EOS).....	93
4.8	Shan-Chen Multicomponent Multiphase model.....	93
4.8.1	Phase separation.....	93
4.8.2	Wetting boundary condition.....	94
4.8.3	Force inclusion.....	95
4.8.4	Equation of state (EOS).....	95
4.9	Parallel computing.....	96
4.10	LB Unit conversion.....	96
4.11	Fluid flow parameters.....	97
4.12	LBM algorithm flow chart.....	99
4.13	Summary.....	100
	<b>Chapter 5 Sensitivity &amp; Validation studies.....</b>	<b>101</b>
5.1	Introduction.....	101
5.2	Sensitivity studies.....	101
5.2.1	Domain Size.....	102
5.2.2	Influence of outlet Boundary condition.....	108
5.2.3	Laplace Law for Interfacial tension.....	110
5.2.4	Contact Angle behaviour.....	112
5.2.5	Summary.....	116
5.3	Validation against FVM/VOF simulations of free droplet coalescence.....	117
5.3.1	Analysis method for stage 1 & 2 Coalescence time.....	118
5.3.2	Results for speed.....	121
5.3.3	Results for Dynamic viscosity.....	129
5.3.4	Results for Interfacial tension.....	137
5.3.5	Discussion.....	150
5.3.6	Effect of Lattice Resolution.....	152
5.4	Sensitivity study for critical droplet detachment velocity.....	154
5.4.1	Simulation setup.....	154
5.4.2	Results of Contact angle.....	156
5.4.3	Results for different Boundary condition & interfacial tension.....	156
5.4.4	Results for Different droplet diameter.....	157
5.4.5	Results for Dynamic viscosity.....	158

5.4.6 Discussion.....	158
5.5 Summary and Conclusion .....	160
<b>Chapter 6 Interaction of water droplets with filter fibres .....</b>	<b>162</b>
6.1 Introduction .....	162
6.2 Droplet attachment on a single fibre.....	162
6.2.1 Simulation setup.....	163
6.2.2 Effect of flow speed and contact angle.....	165
6.2.3 Effect of droplet size.....	167
6.2.4 Effects of fibre size .....	168
6.2.5 Discussion.....	169
6.3 Two droplets coalescing on a single fibre.....	169
6.3.1 Simulation setup.....	170
6.3.3 Effect of contact angle.....	172
6.3.4 Effect of dynamic viscosity ratio .....	175
6.3.5 Effect of second droplet size .....	177
6.3.6 Effect of the held droplet size .....	177
6.3.7 Effect of fibre size.....	179
6.3.8 Discussion.....	181
6.4 Continuous droplets on fibres.....	183
6.4.1 Simulation setup.....	183
6.4.2 Effect of contact angle and interfacial tension .....	187
6.4.3 Effect of dynamic viscosity ratio .....	189
6.4.4 Discussion.....	191
6.5 Summary and conclusion .....	195
<b>Chapter 7 Conclusion and future work .....</b>	<b>197</b>
7.1 Conclusions.....	197
7.1.1 Conclusions from changes to filter housing.....	197
7.1.2 Conclusions from validation of the model.....	197
7.1.3 Conclusions of droplet coalescence studies.....	198
7.2 Future work .....	200
<b>List of References .....</b>	<b>202</b>

## List of Tables

<b>Table 2.1 Comparison of Fuel Properties between Diesel and Biodiesel[37-40].</b>	<b>13</b>
<b>Table 2.2 Fuel blend Properties[17, 38].</b>	<b>14</b>
<b>Table 2.3 Separation process for different phases [4].</b>	<b>19</b>
<b>Table 2.4 Advantage and disadvantage of woven and non-woven fabrics[93]</b>	<b>38</b>
<b>Table 2.5 difference in Traditional CFD vs LBM.</b>	<b>56</b>
<b>Table 3.1 the parameters and their values used in the Comsol simulation.</b>	<b>64</b>
<b>Table 3.2 L1, L2 and L3 parameter variation for Comsol simulations.</b>	<b>65</b>
<b>Table 4.1 D2Q9 and D3Q19 models discrete velocity, weighting factor and point in Figure 2.9.2 are labelled.</b>	<b>79</b>
<b>Table 4.2 LB unit conversion.</b>	<b>97</b>
<b>Table 5.1 The operating conditions and two phase properties for different velocity. (l.b.u= lattice Boltzmann units).</b>	<b>122</b>
<b>Table 5.2 shows the snapshots of the coalescence progress for each simulation 1 ( 0.75 m/s collision velocity) in LBM validation with Mohammadi et al[179] model. First and second column of time represents respectively the Mohammadi et al time and LBM simulation time.</b>	<b>123</b>
<b>Table 5.3 shows the snapshots of the coalescence progress for simulation 2 ( 1.00 m/s collision velocity) in LBM validation with Mohammadi. et al (2012)[179] model. First and second column of time represents respectively the Mohammadi et al time and LBM simulation time.</b>	<b>125</b>
<b>Table 5.4 shows the snapshots of the coalescence progress for simulation 3 ( 1.25 m/s collision velocity) in LBM validation with Mohammadi et al model. First and second column of time represents respectively the Mohammadi et al time and LBM simulation time.</b>	<b>127</b>
<b>Table 5.5 The operating conditions and two phase properties for different dynamic viscosities of diesel. (l.b.u= lattice Boltzmann units)</b>	<b>130</b>
<b>Table 5.6 shows the snapshots of the coalescence progress for simulation 4 ( 1.97 Dynamic viscosity ratio) in LBM validation with Mohammadi et al[179] model. First and second column of time represents respectively the Mohammadi et al time and LBM simulation time.</b>	<b>131</b>

<b>Table 5.7</b> shows the snapshots of the coalescence progress for simulation 6 ( 3.97 Dynamic viscosity ratio) in LBM validation with Mohammadi et al[179] model. First and second column of time represents respectively the Mohammadi et al time and LBM simulation time. ....	<b>133</b>
<b>Table 5.8</b> shows the snapshots of the coalescence progress for simulation 5 and 7, respectively with a 2.99 and 5.07 Dynamic viscosity ratio in LBM .First and second column of time represents respectively the Mohammadi et al[179] time and LBM simulation time.....	<b>135</b>
<b>Table 5.9</b> The operating conditions and two phase properties for different Interfacial tension. (l.b.u= lattice Boltzmann units) .....	<b>138</b>
<b>Table 5.10</b> shows the snapshots of the coalescence progress for simulation 8 ( 0.01 N/m interfacial tension) in LBM validation with Mohammadi et al model. First and second column of time represents respectively the Mohammadi et al time and LBM simulation time. ....	<b>139</b>
<b>Table 5.11</b> shows the snapshots of the coalescence progress for simulation 10 ( 0.02 N/m interfacial tension) in LBM validation with Mohammadi et al model. First and second column of time represents respectively the Mohammadi et al time and LBM simulation time. ....	<b>141</b>
<b>Table 5.12</b> shows the snapshots of the coalescence progress for simulation 12 ( 0.028 N/m interfacial tension) in LBM validation with Mohammadi et al model. First and second column of time represents respectively the Mohammadi et al time and LBM simulation time. ....	<b>143</b>
<b>Table 5.13</b> shows the snapshots of the coalescence progress for simulation 13 ( 0.03 N/m interfacial tension) in LBM validation with Mohammadi et al model. First and second column of time represents respectively the Mohammadi et al time and LBM simulation time. ....	<b>145</b>
<b>Table 5.14</b> shows the snapshots of the coalescence progress for simulation 9 and 11, respectively with a 0.015 and 0.025 (N/m) Interfacial tension in LBM .First and second column of time represents respectively the Mohammadi et al time and LBM simulation time.....	<b>147</b>
<b>Table 5.15</b> shows the snapshots of the lattice resolution for a Reynolds number of 65.6 and d is the distance of separation for the two droplets.....	<b>153</b>
<b>Table 5.16</b> parametric studies for the droplet detachment velocity...	<b>155</b>
<b>Table 6.1</b> Parameters for the studies exploring the maximum offset h resulting in attachment of a droplet on a fibre. ....	<b>165</b>
<b>Table 6.2</b> Parameter studies for maximum h distance.....	<b>171</b>

<b>Table 6.3 shows the snapshots of a droplet coalescing with a different droplet on a fibre (for different contact angle) at h distance (offset-parameter) of 16<math>\mu</math>m. ....</b>	<b>172</b>
<b>Table 6.4 shows the snapshots of a droplet coalescing with a different droplet on a fibre for contact angles of 120°, 106°, 90°, 78° and 64° at h distance (offset-parameter) of 25.....</b>	<b>174</b>
<b>Table 6.5 shows the snapshots of a droplet coalescing with a different droplet on a fibre for different dynamic viscosity ratio. ....</b>	<b>176</b>
<b>Table 6.6 shows the snapshots of a droplet coalescing with a different droplet on a fibre (for 90° contact angle) at h distance (offset-parameter) of 25.....</b>	<b>178</b>
<b>Table 6.7 shows the snapshots of a droplet coalescing with a different droplet on a different fibre radius (for 90° contact angle).....</b>	<b>180</b>
<b>Table 6.8 Parameter studies for the effect of L value (A).....</b>	<b>187</b>
<b>Table 6.8 Equivalent porosity value for L (B).....</b>	<b>187</b>

## List of Figures

Figure 1.1 process of removing water in diesel fuel. Taken from [10].	2
Figure 2.1 Diesel fuel filters: (A) is the unused clean diesel filter, (B) is the used diesel filter: Brown and black on the filter media are the particles captured during filtration [22].	8
Figure 2.2 Diesel fuel filter, (A) the water droplet separation from diesel fuel on filter media is shown and water droplets are transparent circles and diesel fuel is the yellow liquid [16].	10
Figure 2.3 Organic contaminant diesel fuel filter [34].	11
Figure 2.4 (A) – creaming process and (B) – coalescence process[45].	15
Figure 2.5 Three-phase emulsion concepts [51].	17
Figure 2.6 Two-phase emulsion concepts [51].	18
Figure 2.7 Coalescing process and droplet adhesion on coalescer fibre surface [59]	21
Figure 2.8 (A) Single fibre capture mechanisms efficiency versus particle diameter, (B) : Filter mechanisms [60].	22
Figure 2.9 (a) Cake filtration, (b) deep-bed filtration and (c) membrane filtration [55].	24
Figure 2.10 Clogging layer effects in dead-end-filtration and cross flow-filtration [73].	26
Figure 2.11 Process selections according to different particle sizes [56].	27
Figure 2.12 Cad model of representing the fluid flow through the void of particle bed [84]. Flow of fluid is shown in green, pores in black and particles in brown.	31
Figure 2.13 3Dimesional images of particle size and distribution in a filter cake [83].	33
Figure 2.14 (A) Warp and weft yarns position in plain woven fabric[90]. (B) Woven fabric methods [a] spun staple, [b] monofilament and [c] multifilament[56].	34
Figure 2.15 types of weaves. Plain weave [a], twilled weave [b], Dutch weave [c], Twilled Dutch weave [d], Reverse Dutch weave [e], Duplex Dutch weave [f], Betamesh Dutch weave [g] and Basket weave [h] [56].	35
Figure 2.16 (A) represents the meltblown non-woven material at 51x magnification and (B) represents the 500x magnification for fibre diameter.	36

Figure 2.17 Nonwoven manufacturing process (A) is Dry laid, (B) is Air laid, (C) is wet laid and (D) is spunlaid[92].	37
Figure 2.18 (A) is contact angle of wetting droplet on a solid surface[97]. And (B) droplets advancing contact angle ( $\theta_A$ ) and receding contact angle ( $\theta_R$ ).	39
Figure 2.19 water droplet on fiber surface with different wetting properties: contact angle for hydrophilic(A) and hydrophobic(B).	40
Figure 2.20 Coalescing filters process with three main step. And shown the gravitational effect on water droplet.	42
Figure 2.21 Photomicrographs of drop coalescence of single fibres. Flow direction from page bottom to top [118]. Teflon fibre with a diameter of 16-17 $\mu$ m.	46
Figure 2.22 Water droplets in air sitting on a tubular mat[121].	47
Figure 2.23 shows the critical velocity ( $V^*$ ) for nylon fibre radius on water droplet radius (R)[129].	50
Figure 2.24 shows the effect of different velocity on drop size separation efficiency in polypropylene to solvent concentration[101].	51
Figure 2.25 Two different methods used to solve fluid dynamic problems (left hand side ) Top-Down approach and (right hand side ) Bottom- Up approach [131, 133].	53
Figure 2.26 Models used to solve fluid dynamic problems and their advantages in computation efficiency per volume, system complexity per volume, system size range and Knudsen number range[140].	57
Figure 3.1 Filter geometry with inlet, outlet and boundary condition. Also the equations solved in the free space (open flow) and porous media are shown.	60
Figure 3.2 (A) shows the two dimensional axisymmetric fuel filters inlet, outlet and material properties, (B) represents the 2D axisymmetric fuel filter dimension from Dmax filter and (C) Particle tracking inlet and outlet with gravitational force.	63
Figure 3.2 (A) represents the variation of droplet size and (B) represents the inlet thickness (L1), free space thickness (L2) and free space height (L3) were varied.	65
Figure 3.3 velocity field in 2D axisymmetric fuel filter.	66
Figure 3.4 represents shows the results of a comsol simulation, (A) shows the flow of the diesel (red arrows). (B) Is the analysing method for these simulations and (C) shows the water droplet settling below the plastic material.	67
Figure 3.5 (A 1-6) represents the Comsol simulation results and (B) analysed results for the water particle sizes variation.	68

Figure 3.6 (A 1-6) represents the Comsol simulation results and (B) analysed results for L1 or inlet thickness variation.....	69
Figure 3.7 (A1-5) represents the Comsol simulation results and (B) analysed results for L2 or free space thickness variation.....	70
Figure 3.8 (A 1-4) represents the Comsol simulation results and (B) analysed results for L3 or free space height variation. ....	71
Figure 4.1 Discrete velocity models used currently for 2 Dimensional and 3 Dimensional. D2Q7 model is rarely used.[131] .....	78
Figure 4.2 Shows the initial step (a) of lattice node a (modelled as a fluid node), (b) is streaming step and (c) is collision step[150]. ....	83
Figure 4.3 shows the periodic boundary condition from Right to Left .....	85
Figure 4.4 Half-way and Full-way boundary conditions are shown. The $t_1$ -denotes a time step after streaming step and $t'_1$ -denotes the time step after boundary condition[154]......	86
Figure 4.5 Missing distribution function at the inlet boundary node (A) and unknown distribution function modelled with Zou & He method. ....	87
Figure 4.6 LBM programming flow chart.....	99
Figure 5.1 represents the inlet, outlet region with a droplet in centre of NY and equivalent radius away from inlet boundary for NX centre. This system was studied for square domain size. ....	101
Figure 5.2 Node deviation from initial vertical position versus x position in the domain for droplet sizes of 20,30 and 40 (respectively 13, 20 and 26 $\mu\text{m}$ ). (A) of 400x400, (B) OF 600x600, (C) of 800x800 and (D) of 1000x1000 domain size.....	104
Figure 5.3 Node deviation from initial vertical position versus x position in the domain for droplet sizes of 20,30 and 40 (respectively 13, 20 and 26 $\mu\text{m}$ ). NX=1000 and NY Domain size of (A) 600, (B) 700, (C) 800, (D) 900 and (E) 1000 were simulated for same conditions & parameters as Square Domain (NX=NY).....	107
Figure 5.4 Comparison of change in droplet radius in LB units near inlet and outlet for different droplet sizes. ....	108
Figure 5.5 Figure 5.5 (A), (B) and (C) shows the nodes, which has been effected for a droplet size of 20 LB units/ 13 $\mu\text{m}$ , 30 LB units/ 20 $\mu\text{m}$ and 40 LB units/ 26 $\mu\text{m}$ in a velocity profile. ....	110
Figure 5.6 Droplets of 20, 40 and 60 radii were simulated for (A) Gww- interaction potential of 0.68, 0.71, 0.75, 0.78, 0.80 and 0.81, (B) different diesel tau values and respectively are 1.00 , 1.26, 1.51 and 1.76 ( fixed water tau value is 0.71 ). ....	112

Figure 5.7 Demonstration of the $\theta/2$ method according to Equation 5.2.....	113
Figure 5.8 (A) shows the initialisation time step and (B) is the different contact angle of 40 LBM unit radius droplet with a dynamic viscosity ratio of diesel to water is 2. ....	114
Figure 5.9 Calibration of wettability coefficient with contact angle for different droplet radii and diesel: water dynamic viscosity ratio 2. ....	115
Figure 5.10 Calibration of wettability coefficient with contact angle for different G <sub>ww</sub> -interaction potential values are 0.68, 0.71, 0.75, 0.78, 0.80 and 0.81 and diesel: water dynamic viscosity ratio 2. ....	115
Figure 5.11 Calibration of wettability coefficient with contact angle for different relaxation values for diesel are 1, 1.26, 1.51 and 1.76. Respective diesel: water dynamic viscosity ratio are 2, 3, 4 and 5. ....	116
Figure 5.12 Domain size and droplet separation for simulation cases. Water droplets are in blue and diesel the continuous phase in red. ....	117
Figure 5.13 Visual representation of stage 1 coalescence time at time=0 to time=t1.....	118
Figure 5.14 (A):the initial time step,(B)during the coalescence stage. Where the blue dotted line represents the horizontal centreline of the domain ( $y = 1/2NY$ ). And (C) is the density profile plotted at $y = 1/2NY$ . Also the red and yellow lines in (B) are respectively the vertical distance and horizontal distance during the coalescence time stage. ....	119
Figure 5.15 (A):is during coalescence time stage, shows the density profile along the horizontal centreline of the domain ( $y = 1/2NY$ ). (B):is the density profile along the vertical axes at coalescence time stage (Figure 5.14 (B) red line position for x). ....	120
Figure 5.16 Stage 2 coalescence time is shown in these images. Coalescence time is the difference of t2&t1 . ....	121
Figure 5.17 the stage 1 coalescence time versus the collision velocity.....	129
Figure 5.18 the stage 1 coalescence time versus the dynamic viscosity ratio of Diesel/water.....	137
Figure 5.19 the stage 1 coalescence time versus the water-diesel interfacial tension (N/m). ....	149
Figure 5.20 the stage 2 coalescence time versus the water-diesel interfacial tension (N/m). ....	150

Figure 5.21 represents the inlet, outlet region with a droplet and a fibre. This system was studied for rectangular domain size.....	155
Figure 5.22 (A),(B) and (C) shows the droplets detachment at fibre contact angle of $78^\circ$ , $90^\circ$ and $120^\circ$ . .....	156
Figure 5.23 the detachment velocity versus contact angle, bounce back and periodic boundary condition to different interfacial tension. ....	157
Figure 5.24 the detachment velocity versus contact angle for different diameter of droplet. ....	157
Figure 5.25 the detachment velocity versus contact angle for different dynamic viscosity ratios. ....	158
Figure 5.26 Droplets of equal volumes sitting on a fibre in quiescent conditions with different contact angles between 12 and 180 degrees. ....	159
Figure 6.1 Represents the inlet, outlet region with a droplet and a fibre. This system was studied for rectangular domain size.....	164
Figure 6.2 Visual representation of droplet adhering to fibre surface.(A) shows the initialisation step, (B) is during the position of $x=1/2 N_x$ , at 15000 time step and (C) is at 35000 time step (final position).....	164
Figure 6.3 The critical $h^*$ (offset-position) versus velocity for (A) shows contact angle range of $0^\circ$ to $180^\circ$ and (B) for intermediate contact angle range of $78^\circ$ - $120^\circ$ .....	167
Figure 6.4 The critical $h^*$ (offset-position) versus droplet radius. ....	168
Figure 6.5 The critical $h^*$ (offset-position) versus fibre radius.....	168
Figure 6.6 Represents the inlet, outlet region with two droplets and a fibre. This system was studied for rectangular domain size. ....	170
Figure 6.7 Visual representation of droplet coalescing a different droplet on a fibre surface.(A) shows the initialisation step, (B) is before two droplets coalescence and (c) is coalesced droplet on a fibre.....	171
Figure 6.8 The critical $h^*$ (offset-position) versus contact angle. ....	175
Figure 6.9 The critical $h^*$ (offset-position) versus dynamic viscosity ratio. ....	176
Figure 6.10 The critical $h^*$ (offset-position) versus away droplet radius. ....	177
Figure 6.11 The critical $h^*$ (offset-position) versus top droplet radius. ....	179
Figure 6.12 shows the critical $h^*$ (offset-position) versus fibre radius. ....	181

<b>Figure 6.13 (A) shows a sketch of 3D fibres top view, (B) is the boundary condition in 2D view and (C) is the effective parameter change for porosity. ....</b>	<b>186</b>
<b>Figure 6.14 show the capture efficiency versus porosity for different contact angles and (A), (B) and (C) represents the interfacial tension of 10mN/m, 20mN/m and 28.5mN/m respectively. ....</b>	<b>189</b>
<b>Figure 6.15 show the capture efficiency versus porosity for different contact angles and dynamic viscosity ratio are 2, 3, 4 and 5 are respectively (A), (B) (C) and (D).....</b>	<b>191</b>
<b>Figure 6.16 show the capture efficiency versus porosity for different contact angles.(A) is 120, (B) is 106, (C) is 90 and (D) is 78° .....</b>	<b>193</b>
<b>Figure 6.17 show the capture efficiency versus porosity for different contact angles of 120°(A), 106°(B), 90°(C) and 78° (D). ....</b>	<b>195</b>

## **List of Abbreviations**

FAME - Fatty acid methyl esters

KOH - Potassium hydroxide

NaOH - Sodium hydroxide

ppm - Parts Per Million

Surfactant - Surface Active Agent

ULSD - Ultra-low sulphur diesel or EN590 diesel

W/D - Water in Diesel

D/ W - Diesel in Water

PP - Polypropylene

PVDF-HFP – Poly(vinylidene fluoride-co-hexafluoropropylene)

PTFE - Polytetrafluoroe

## Chapter 1 Introduction

### 1.1 Motivation for Research

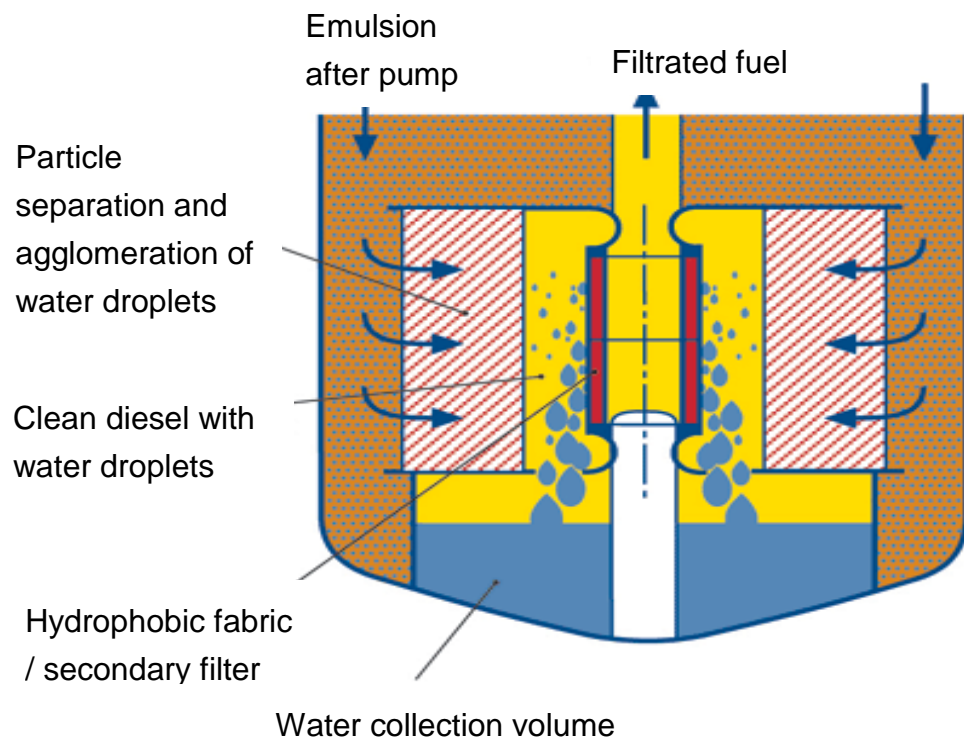
Diesel vehicles are widely used for rail and sea transport with the majority of vehicles used for heavy goods transport are diesel engines. The fuel efficiency of diesel engines on large vehicles is higher (20%) than petrol engine (12%) [1, 2]. Consequently a diesel engine requires less fuel compared to petrol engines [3]. Diesel engines have high thermal efficiency, high power/weight ratio, high fuel economy and strong structural design [2]. The quality of the diesel fuel is important to the performance of the engine. Diesel fuel typically contains impurities including water either from storage (eg: condensation with in the fuel tank of the vehicle) or from contaminants present at the pump. These impurities clog the fuel line and injector [4], while water condensation in the fuel tank causes rust, corrosion and can deposit in injector parts and the fuel pump [4-6]. Excessive water causes steam expansion and/or lubricity effects (resistance between or/and damage to surface) and is a primary source of catastrophic injector nozzle failure [7]. A high concentration of water vapour in the engine cylinder leads to corrosion. During cold weather, diesel fuel becomes more viscous and flows slowly into the fuel system and the presence of water in the fuel line can lead to freeze-up and reduction in power [4, 6, 8, 9]. To achieve maximum efficiency, the fuel should be clean [5, 10].

Figure 1 [10] shows a typical filter used to clean the diesel. The fuel and water mixtures separation path is indicated. Water is present in fuels as free water, emulsified water and dissolved water. The free water is generally separated by gravity settling. The emulsified water droplet often has a drop sizes less than 100µm and is commonly separated using a depth filtration process (this is described in more detail in Chapter 2). Note the presence of a hydrophobic fabric material where the surface of the fabrics is water hating

[11, 12]. This allows filtrated diesel to enter the injection nozzle and produce maximum power.

The specification of efficient separation media is:

- Material that can coalesce water particles.
- The coalesced water droplets are large enough to prevent passing the secondary filter.
- The diameter of water particles are large enough to free fall for specific inlet velocity.
- Material should perform in different temperatures.
- Material should be non-toxic with minimal weight and cost.



**Figure 1.1** process of removing water in diesel fuel. Taken from [10].

## **1.2 Aims and Objectives**

This thesis aims to provide an understanding of the fundamental concepts of fluid passing through a fibre structure in relation to a water in diesel. Specifically the focus is on how the fibres of the filter (size, spacing and contact angle) influence the behaviour of droplets. The effect of the fluid properties on wettability of fibres will also be investigated. The combination will allow the optimisation of the coalescence filtration process.

The objectives of this thesis are:

- To examine the potential for performance gains through altering the current filter housing using computational fluid dynamic (CFD).
- To develop an understanding of Lattice Boltzmann Method for two phase simulations.
- To investigate the coalescence behaviour of droplets for different fluid properties using LBM.
- To investigate the contact angles influence of droplet on a fibre structure using LBM.

## **1.3 Structure of Thesis**

The chapter which follows will detail an extensive literature review (Chapter 2) covering the topics of different types of contaminants in diesel, filtration methods, porous media flow, fibre media, wettability and coalescence filtration.

Chapter 3 will detail the study of the filter housing geometry using a conventional CFD methodology (within the commercially available software Comsol) through changing the dimensions within the filter housing.

Chapter 4 will detail the Lattice Boltzmann (LB) method (LBM) for Shan-Chen multicomponent multiphase model which has been utilised throughout this thesis. This includes the derivation of Lattice Boltzmann method equation to Navier-Stokes equation, computational implementation process, boundary conditions and conversion of LB parameter to fluid flow parameter.

Chapter 5 will display the sensitivity studies and the validation studies for droplet behaviour using the Lattice Boltzmann method. Validation studies will be examined using the fluid properties and coalescence behaviour of two droplets. The sensitivity studies will focus on the domain size, the minimum droplet radius, wettability and the effect of different boundary condition for fluid flow.

Subsequently, Chapter 6 details the effect of single fibre study of a droplet and coalescence of two droplets on a various contact angle fibre for different fluid properties. Finally the continuous droplets on fibres for different fluids properties will be considered.

Finally, Chapter 7 will conclude this thesis with recommendations for future work.

## **Chapter 2**

### **Literature review**

#### **2. Introduction**

The literature review in this chapter aims to explore key work that help explain the water in diesel filtration, particularly during the coalescence process. Section 2.1 - 2.10 provides the fundamental understanding of the filtration process. These sections are divided into fuel study, cause of diesel filtration, fuel properties, emulsion types, filtration methods, capture mechanism, types of filter, porous media flow, fibre study and wettability. Sections 2.11-2.12 focuses on liquid-liquid filtration and coalescence filtration. These sections helps to identify the key parameters for the water in diesel filtration. Finally the fluid simulation methods are introduced in section 2.13.

#### **2.1 Types of Diesel fuel**

##### ***Fuel literature review***

This section reviews the different types of diesel fuel (2.1.1), the main reasons to filter diesel fuel (2.1.2), the properties of diesel fuel (2.1.3) and finally the emulsion of Water in Diesel such as three-phase emulsions and two-phase emulsion. Currently there are three different kinds of diesel fuel generally used across the world and they are Ultra-low sulphur diesel (ULSD) or EN590, Biodiesel and EN590 +Biodiesel blends.

##### **2.1.1 Fuel Ultra-low sulphur Diesel or EN590 Diesel**

Ultra-low sulphur diesel (ULSD) is considered a cleaner burning fuel by environmental regulatory bodies in the US, Japan and European Union (EU) [13]. ULSD is diesel fuel with substantially lowered sulphur content than other diesels. Since 2007, diesel that conforms to standard EN590 has been referred to as ULSD in the European union. ULSD, diesel fuel with a maximum sulphur content of 15 ppm (parts per million) [14]. The refinery typically applies a hydrotreating process to remove sulphur from crude oil to make ULSD. This process also removes non-wax type species from the

diesel fraction. This leads to an ultra-clean fuel which has lost naturally-occurring lubricants, where fuel lubricity protects the injectors systems from catastrophic wear[15]. Also wear could lead to engine failure. Industry overcame this issue by adding fuel additives(discussed the effects in section 2.3.3) like lubricity enhancers, rust inhibitors and anti-wear agents to ULSD [16]. In addition, distillation temperature, fuel oxidation stability, conductivity, and aromatics content are lowered, while cetane number (is the measure of a fuel's ignition quality and higher cetane number has a shorter the delay between injection and ignition), cloud point (is the temperature at which a cloud of wax crystals first appear in a liquid fuel) and wax content are increased . These changes are dependent on specific operating conditions like temperature, pressure and catalysts [14]. Some of these changes in the fuel make the filtration process difficult.

### **2.1.2 Biodiesel**

Biodiesel is a fuel produced from renewable resources such as soybean or rapeseed oils, and the biodiesel industry is expanding as a result of renewable energy development. Biodiesel is an alternative to ULSD or can be used as a blend with ULSD. Large scale biodiesel production uses soybean oils and animal fats. Biodiesel is a blend of fatty acid methyl esters (FAME) derived from a caustic catalysed reaction between methanol and plant/animal fats, for example soybean oil is converted to a methyl ester by reacting with methanol using NaOH or KOH as the catalyst. Biodiesel improved ULSD lubricity, as a result it is blended with fossil fuel to improve its engine, provide higher cetane number and reduce emissions relative to ULSD. Also other advantages are it is non-toxic, degrades four times faster than diesel and produces 80% less carbon dioxide and 100% less sulphur dioxide emissions, it provides a 90% reduction in cancer risks [17]. Biodiesel is also known to have a higher cloud point and more unsaturated hydrocarbon content than ULSD diesel [14].

## **2.2 Contaminants in Diesel**

There are many opportunities for contaminant entry in fuels from production to point of use. 90% of diesel problems are due to dirt or water in the fuel [18]. Sulphur has been removed due to the emission standards from the diesel fuel, however dirt, water and soft organic contaminants still remain. Filtration determines the efficiency of the engine performance. Therefore filtration industries are developing diesel fuel filters to remove particles, water and soft organics [19].

### **2.2.1 Particles in Diesel**

Road dusts, engine rust or wear particles and any other hard particles (grit) that could cause engine damage are considered to be particles contaminants. Modern newer engines also have smaller tolerances. Therefore it is more common for particles to get jammed in fuel injectors. These particles are typically rigid in nature and can cause wear to a fuel injection system. The damage depends on particle size, shape, rigidity, concentration and sometimes on chemical composition [14]. Particle contamination makes its way into vehicle fuel systems through multiple ways. The primary cause is through the diesel fuel itself, since diesel fuel cleanliness varies from one gas station to another. A secondary reason is through the tank vent. As the air is drawn into the fuel tank. Finally, wear debris from fuel system components provides particles. Figure 2.1 (B) shows the captured particles as brown and black on the filter media compared to a clean filter (Figure 2.1 (A)). Clean fuel minimizes fuel system wear and engine exhaust emissions[20, 21].

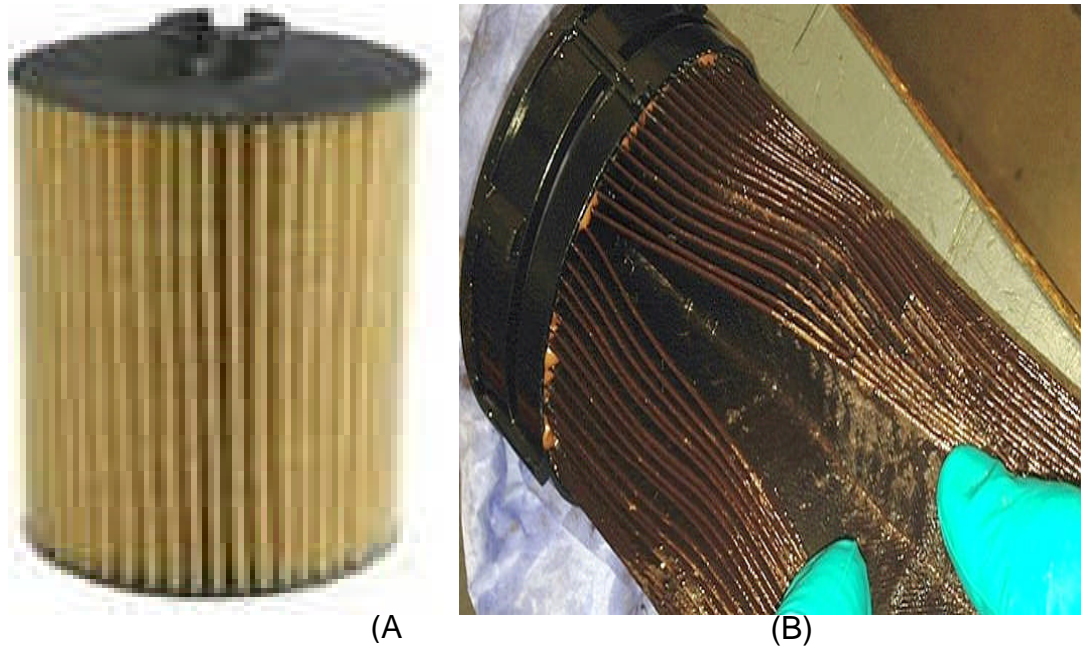


**Figure 2.1** Diesel fuel filters: (A) is the unused clean diesel filter, (B) is the used diesel filter: Brown and black on the filter media are the particles captured during filtration [22].

Particulate contamination can be measured according to the ISO cleanliness code as defined by ISO 4406:1999[23]. Particle filtration efficiency is measured through a beta ratio and it defines the filter medium effectiveness of capturing wear particles in diesel fuel. Beta ratios [24], defined as the ratio of the number of particles upstream to the number of particles downstream at a specific particle size. Beta ratios are derived from standardised multi-pass fuel filter tests but on-vehicle fuel filtration generally occurs in a single pass. Particle filtration media are generally manufactured from cellulose, glass, blends of cellulose and glass, melt blown/cellulose composites and spunbond polyester[14].

### **2.2.2 Water in Diesel**

The presence of a very small amount of water in fuels can cause numerous problems. Water contamination issues lead to fuel thermal oxidation stability, fuel filterability, fuel lubricity, promotion of an environment where bacteria can grow at the fuel/water interface, development of particulate matter, fuel injector deposit build-up, fuel filter plugging, corrosion and erosion of engine parts and fuel combustion efficiency degradation [25-27]. Fuel quality standard ASTM D975[28] recommends a maximum water contamination level in diesel fuel to be less than 500 ppm and the European standard EN590 recommends for less than 200 ppm.

Water appears in three forms: free state, emulsified and dissolved [29]. Water is unavoidably introduced into the fuel during fuel storage, shipping, pumping and through condensation. Free water can usually be separated by gravity settling or other mechanical operations. The emulsified water often has drop sizes less than 100  $\mu\text{m}$  and is commonly separated using a coalescing filter [30, 31]. Free and emulsified water must be effectively removed from fuel and a significant amount of dissolved water can be a threat to the engine. A hydrophobic barrier media is the most typical filtration media that can be found in this kind of separator, for example silicone-treated cellulose [32]. Other effective materials are hydrophobic depth-coalescing media such as glass microfibers.

Water contamination is introduced to the fuel system through the same paths as particle contamination. Fluctuations in environmental conditions like changes in temperature and relative humidity increases the water contamination in diesel fuel . Figure 2.2 (A) shows the emulsified water droplets on the filter media during the filtration process. Water droplets are transparent circles and diesel fuel is the yellow liquid.

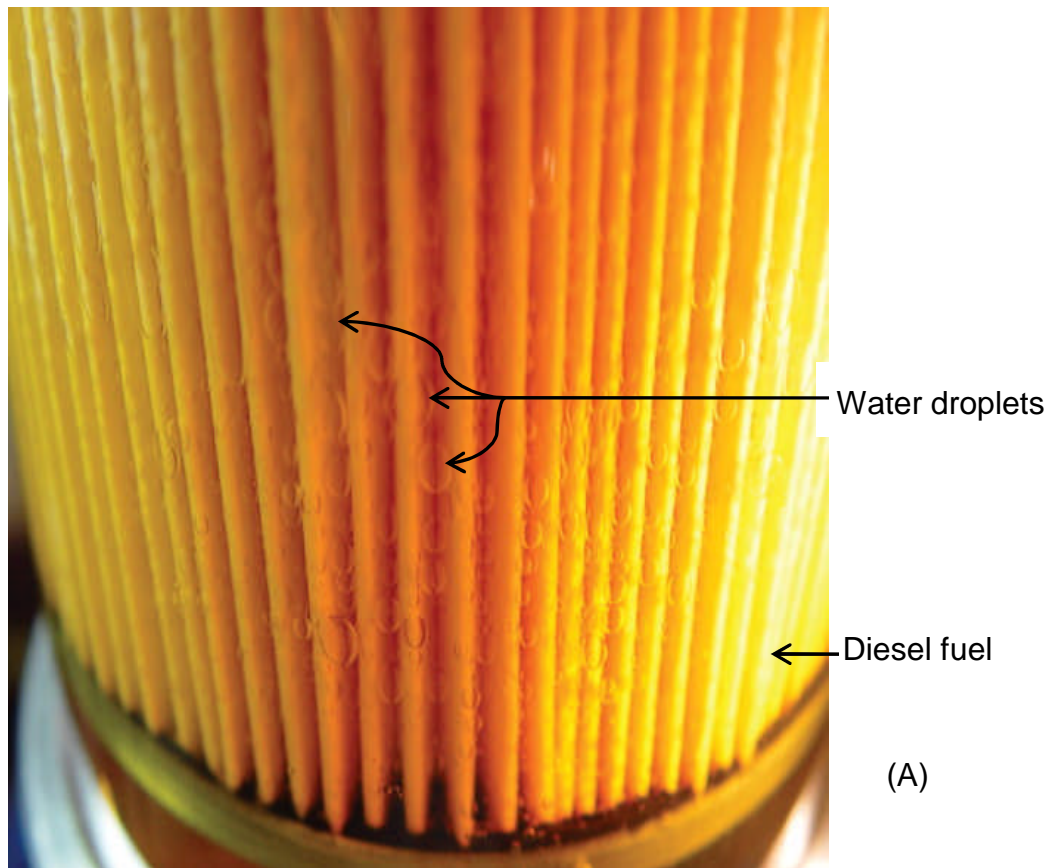


**Figure 2.2** Diesel fuel filter, (A) the water droplet separation from diesel fuel on filter media is shown and water droplets are transparent circles and diesel fuel is the yellow liquid [16].

In ULSD, lubricity additives are added to the fuel. Therefore fuel also performs as a lubricant and protects the moving engine components. Fuel surfactancy increases due to the lubricity additives, and unintentionally increases the stability of water droplets in the fuel. For water in fuel, interfacial tension (IFT) is a measure of the affinity between water and fuel. A lower value of IFT represents a higher affinity where water is more difficult to separate from fuel. An emulsion is stable enough to prevent further coalescence of water droplets at IFTs below 10 mN/m [14]. Water-repellent cellulose and melt blown/cellulose composites are used in high IFT fuel and coarse water filtration[33].

Biodiesel fuel contains glycerine, which stabilises the emulsified water. Also due to the surfactant nature emulsified water will contain a finer droplet distribution. Consequently, after biodiesel is blended with ULSD, emulsified

water removal becomes even more challenging. ULSD and its biodiesel blends can exhibit a range of interfacial tension from about 3 to 30 mN/m.

### **2.2.3 Organic contaminants of Diesel**

Organic contaminants are soft and sticky. They occur due to fuel degradation or naturally. Fuel oxidation is the result of thermal stressing, after the effect of fuel additives interacting with fuel elements, 'apple jelly' types of materials, or a mix of all of these phenomena occur in the organic contaminants. Also when the temperature is lowered, ULSD lowers the wax solubility and promotes wax precipitation. This can lead to premature plugging of fuel filters and corrosion in tank. Gelling is a natural phenomena based on the cloud point of the fuel blend in use. Figure 2.3 shows the effect of soft contaminants[33].



**Figure 2.3** Organic contaminant diesel fuel filter [34].

## **2.3 Fuel properties**

### **2.3.1 Density**

Density is temperature dependent and for diesel fuel it is normally determined at 15 °C. The overall diesel density depends on the composition of the fuel. Density is strongly correlated with other fuel parameters such as cetane number, experiment viscosity and distillation (boiling range or

volatility) and typical values are respectively 100, 2.93 ( $\text{mm}^2/\text{s}$ ) and  $287^\circ\text{C}$ . Also fuel density has an effect on engine power, emission and fuel consumption [35].

### **2.3.2 Viscosity**

Viscosity is a measure of a fuel's resistance to flow. It affects the performance of diesel fuel pumps and injection systems. Viscosity is dependent on fuel composition and so is reflected in the distillation (boiling range or volatility), density and cold flow properties. Current test methods measure the kinematic viscosity ( $\text{mm}^2/\text{s}$ ) at  $40^\circ\text{C}$ . Liquid viscosity has a significant impact on the droplet coalescence process. Two droplets must first travel through the liquid and collide. Then fusion of the two droplets happens when the liquid/liquid interface between the droplets breaks down. The droplets must overcome a higher drag force to reach one another. The breakdown of the liquid/liquid interfaces to create larger droplets is made more difficult by a higher viscosity fluid. Therefore more time is required to accomplish the same coalescence level compared to a lower viscosity fluid [25, 36].

### **2.3.3 Interfacial tension**

The ability of a filter to remove water improves as the IFT between the two phases increases. The IFT between two liquids is a measure of the different attraction force experienced by molecules at the interface, for example water is attracted to itself more strongly than it is to diesel. The Ring-pull method (Du Noüy ring method) or Wilhelmy plate method are commonly used to measure IFT. The typical units of IFT are  $\text{mN/m}$ . The IFT is a critical factor when considering liquid/liquid coalescence because the largest possible stable droplet size that will form by the coalescence process will be dictated by the IFT. A system with a high IFT (i.e.,  $> 10 \text{ mN/m}$ ) gives a larger stable coalesced droplet size, which can be easily separated. Systems with a low IFT (i.e., water in fuels with additives:  $< 10 \text{ mN/m}$ ) form smaller stable coalesced droplets require high efficiency separators. The relative droplet velocity, density and viscosity will influence the coalesced droplet size. The fuel/water mixture's temperature can also affect separation efficiency. As temperature increases the IFT decreases and lowers the water droplets size.

Also fuels saturated with water at high temperatures can contain a high concentration of dissolved water that cannot be removed by the liquid/liquid coalescer. Once the temperature decreases the dissolved water changes into emulsified or free water in fuel, and therefore can be removed by a liquid/liquid coalescer[25, 36].

### 2.3.4 Summary

Table 2.1 summarises the diesel and biodiesel fuel properties. Interfacial tension and surface tension are measured against water and air respectively for Table 2.1 and 2.2 . And Table 2.2 summarises the diesel + biodiesel fuel blend properties since these fuels are currently sold.

**Table 2.1** Comparison of Fuel Properties between Diesel and Biodiesel[37-40].

Fuel Property	Unit	Diesel/ EN590	Biodiesel	Water
Density at 15°C	kg/m <sup>3</sup>	820-845	840-910	1000-1012
Water content		200 (ppm)	0.05 max (vol.%)	-
Kinematic viscosity, 40°C	mm <sup>2</sup> /s	1.20-4.50	1.90-6.00	1.30
Interfacial tension with water (IFT)	mN/m	3.00 to 38.0	3.00 to 38.0	-
Surface tension	mN/m	28.0	25.0-30.0	69.3-72.0

**Table 2.2** Fuel blend Properties[17, 38].

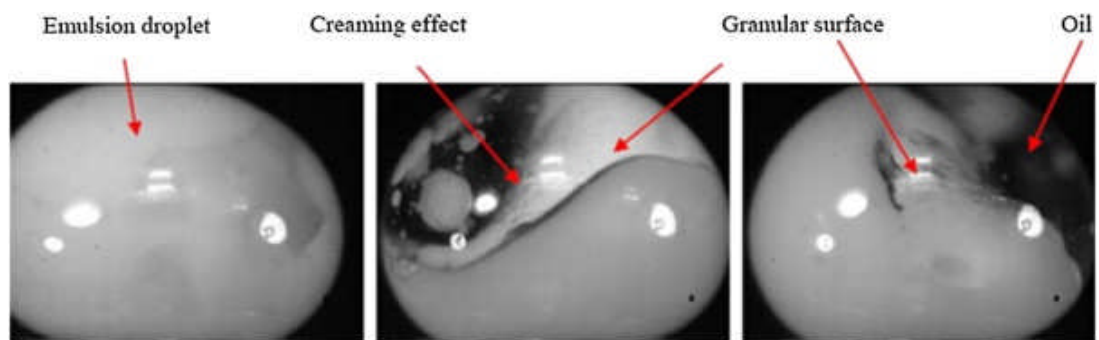
Fuel Blend		Density (kg/m <sup>3</sup> )	Kinematic viscosity (mm <sup>2</sup> /s)	Interfacial tension with water (mN/m)	Surface tension (mN/m)
Diesel	Biodiesel				
100%	-	846	2.60	7.40	28.0
80%	20%	848	3.39	8.30-15.4	28.5
60%	40%	856	4.63	9.00-16.8	28.6
40%	60%	864	5.42	10.0-18.2	29.2
20%	80%	869	6.56	12.0-19.0	30.2
-	100%	876	9.60	12.0-19.5	30.7

## 2.4 Emulsion of Water in Diesel fuel

It is important to have stable emulsions in alternative fuels, in order to run the engine effectively. Unstable water emulsion is the main reason for a high engine failure. This causes damage to the engine parts. The stability of water-in-diesel emulsion fuel can be maintained for to 3 months [41]. depending upon the type and percentage of surfactant, the temperature, viscosity, specific gravity and water content [42].

An emulsion is a mixture of two or more immiscible liquids, one present as a droplet (0.2-50µm is macro-emulsion and 0.01-0.2µm micro-emulsion) or dispersed phase and spread throughout the continuous phase [43].The destabilisation process of water in diesel (W/D) emulsion fuel will occur after creaming, aggregation, and coalescence. The creaming process [44] is due to the density difference between the two phases, and water will sink to the bottom of the fuel. This is shown in Figure 2.4 (A) [45]. The aggregation process is due to the polarity difference of the two phases. This helps to attract the droplets in the internal phase (water) together. The final stage of the aggregation process is the coalescence process [44, 46]. The W/D

emulsion fuel starts to destabilize when the repulsive force of the dispersed droplets become weaker; the dispersed droplets tend to gather towards each other. Thus, they will form bigger droplets. Then newly formed droplets are separated by a thin film and this process is called the flocculation process [44, 45]. The attraction of the van der Waals forces will reduce the thin film thickness and when it reaches the critical value, it will lead to newly formed droplets that merge into larger droplets (i.e., coalescence process). The coalescence process sequence is presented in Figure. 2.4 (B) [45]. Finally those droplets (water droplets) will settle at the bottom due to density difference. This process is called the sedimentation process. All of these processes will decrease the emulsion until the water and the diesel fuel are fully separated. In addition to these processes, the W/D emulsion fuel separation can be improved by a low speed environment (gravity effect), increase in temperature (lower viscosity), external electric field, high shear stress in the emulsion, the addition of a chemical that influences the emulsifier or liquids and the addition of a diluting liquid [46].



(A) – Creaming process



(B) – Coalescence process

**Figure 2.4** (A) – creaming process and (B) – coalescence process[45].

An emulsion is generated by the presence of surfactants or emulsifiers and crucial in forming stable emulsion. The surfactants possess an equal ratio of polar or hydrophilic heads and nonpolar or hydrophobic tails[47]. As the surfactant blends into the mixture of water and diesel, the surfactants polar group orients toward the water and the non-polar group towards the diesel, therefore lowering the interfacial tension between the two liquids [47]. Hence, the surfactant functions by adsorbing at the liquid–gas interface, reducing the surface tension of the water, and also by adsorbing at the liquid–liquid interface, reducing the interfacial tension between diesel and water [48]. The surfactants have four types of polar group; they are cationic, anionic, amphoteric, and non-ionic. Surfactants in the market are categorised based on their Hydrophilic-Lipophilic Balance (HLB). Low-HLB is generally suitable for forming water in diesel emulsion and high-HLB (hydrophilic) for diesel in water emulsion [42, 49]. The value of HLB ranges from 1 to 20.

Surfactants should easily burn with no soot and free of sulphur and nitrogen [50]. Also they should have no impact on the physiochemical properties of the fuel. The most common surfactants used in the water-in-diesel emulsion are sorbitan monooleate and polyethylene glycol sorbitan monooleate mixture, polyethylene glycol sorbitan monooleate and sorbitol sesquioleate (SSO) mixture[45, 49, 51] and t-octylphenoxy polyethoxy ethanol (cka Triton X-100). Usually the amount of surfactant added to the fuel mixture is generally between 0.5–5% by volume ratio, and as the surfactant concentration is decreased, leads to rapid coalescence [42] and reduces the emulsion stability.

There are two types of emulsification techniques, namely, two-phase (primary) and three-phase emulsion (multiphase or secondary emulsions with more than three liquid components). The two-phase emulsion constitutes one continuous phase and one-dispersed phase liquids while the three-phase emulsion constitutes one continuous phase and two or more dispersed phase liquids.

### 2.4.1 Three-Phase Emulsion

There are two types of three-phase emulsions depending on the inner and outer phases. Two types of emulsion are oil-in-water-in-oil and water-in-oil-in-water are shown in Figure 2.5 Oil-in-water-in-oil emulsions are applicable for fuelling purposes. Water-in-oil-in-water emulsion is applied in cosmetics, food, or pharmaceutical manufacturing [52]. Three-phase emulsion can be prepared by three techniques; phase inversion, mechanical agitation, and two-stage emulsion [52]. Three-phase emulsion do not feature in fuel filtration.

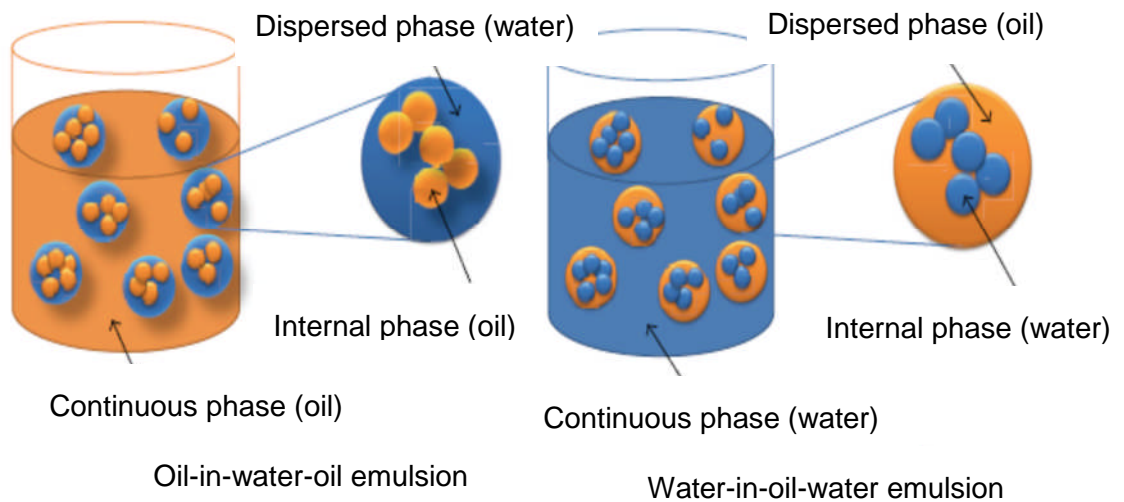


**Figure 2.5** Three-phase emulsion concepts [51].

### 2.4.2 Two-Phase Emulsion

There are two basic forms of two-phase emulsion. The first is the oil-in-water (O/W) emulsion in which oil droplets are dispersed within the water continuous phase. The second is the water-in-oil (W/O) emulsion in which water droplets are within the oil continuous phase. Figure 2.6 shows the two phase emulsion concepts. Conditions for stable emulsion to form are the two liquids must be immiscible, sufficient agitation must be applied to disperse one liquid into the other and surfactant must be present[53].

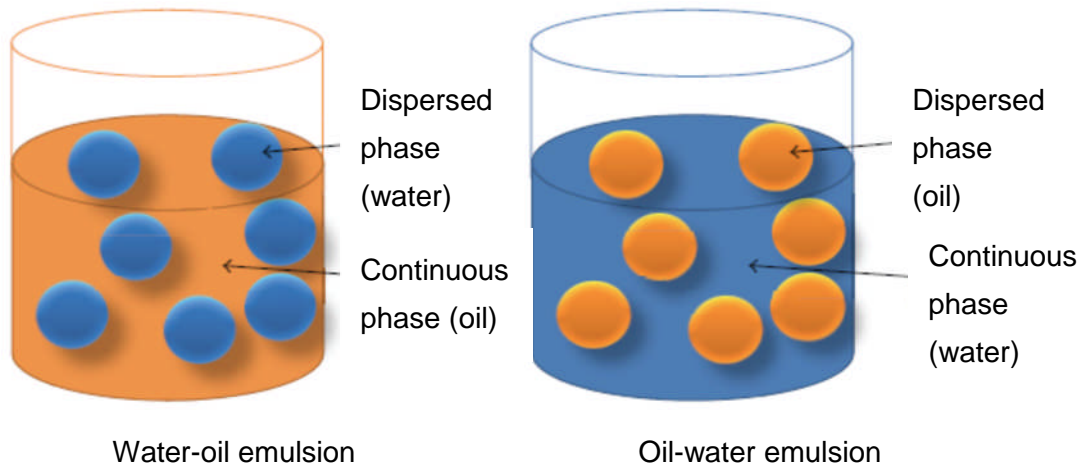


**Figure 2.6** Two-phase emulsion concepts [51].

## 2.5 Filtration methods

The flow of liquid or gas through a porous material that performs the operation of removal, separation and collecting small particles or droplets from suspension in a carrier in fluid is called filtration [54, 55]. Table 2.3 [4] shows a range of separation processes for different material types. Diesel fuel contains solid impurities and water, the separation process would therefore require separating solid from fluid & liquid from liquid phases; this could be achieved through any combination of filtration, sedimentation, flotation, scrubbing, electrostatic precipitation or coalescing. In practice filtration & sedimentation are used due to unit cost, simplicity and safety[4].

**Table 2.3** Separation process for different phases [4].

Separation process	
Distinct phase	
Phase	Process
Solid from solid	Screening and Elutriation
	Classification
Solid from fluid	Filtration
	Sedimentation
	Flotation
	Scrubbing
	Electrostatic precipitation
Liquid from liquid	Sedimentation
	coalescing
Liquid from gas	Demisting
	Sedimentation
Gas from liquid	Defoaming
	Sedimentation

### 2.5.1 Solid from fluid separation process

1. **Filtration** functions by particle or droplet size [4]. Particles less than a certain size would pass through the filter media. Large particles are blocked by the filter media and removed later. The separation size depends on filter fiber thickness and porosity. This process depends on pressure difference across the filter media [4].
2. **Sedimentation** functions on density difference between the particle and fluid. For a given density difference a large particle would settle faster compared to small particles. Settlement area is important in sedimentation [4].
3. **Flotation** is gravity driven separator using air or gas bubbles to carry solid or liquid to the upper surface of a liquid, where they float and are

removed later. Therefore the correct size of bubbles and attachment to solid or liquid are required. Flotation is categorised as dispersed air and dissolved air. The particles need to be hydrophobic in order to float [56].

4. **Scrubbing** uses liquid to remove particulate matter or gases from gas stream. This process is capable of handling explosive and flammable gas, but frequently has a high corrosion and slurry waste. Scrubbers are categorised as dry scrubbers and wet scrubbers [57].
5. **Electrostatic precipitation** removes dust, particle and powder from (typically) a gas stream. The process involves a rectangular sectioned duct with corona electrodes in the centre and at regular intervals. Electrodes charges dust or particles and make them attract to the duct. The charging rate depends on electric and current density field [58].

### **2.5.2 Liquid from liquid filtration process in a fibre bed**

**Coalescing process**, droplets smaller than 100 $\mu$ m (droplets that are too small for gravitational separation) are separated using coalescer fibers. When a liquid mixture (droplet in fluid) is passed through a fibres, the droplets are captured on the surface of fibre bed. Then droplets coalesce into a large size on surface of fibre, eventually detach and then separate using gravity. After that naturally sedimentation happens to separates droplets and liquid. This process is shown in Figure 2.7 below and is called a depth filtration process (discussed later in this chapter). Pressure drop and separation efficiency are important parameters for the design of coalescing filters. Separation efficiency depends on composition, density, viscosity of and droplet diameter of fluid & material, diameter, surface structure and porosity of coalescing filter media [59]. There is a secondary filter which contains hydrophobic material to further coalesce water droplets. This makes 99% efficient for the filtration process.

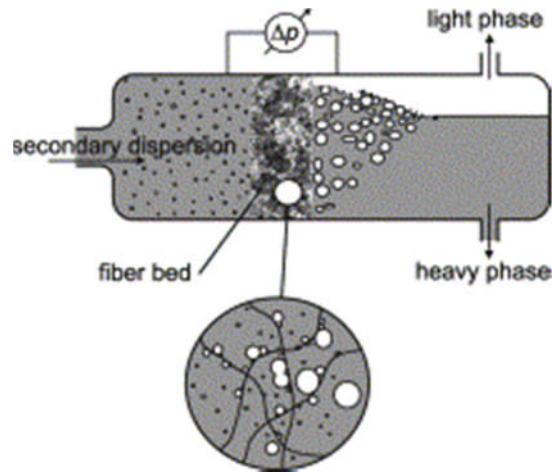


**Figure 2.7** Coalescing process and droplet adhesion on coalescer fibre surface [59]

The porous material used in this process is called a filter. Factors to be considered while selecting filter equipment include the fluid properties like viscosity, density and corrosiveness, as well as solid particle properties like size, shape, size distribution and packing characteristics [54]. The rate of filtration depends on the pressure drop from feed to filter end, the surface area of the filter, the viscosity of fluid and the filter cake resistance [54].

## 2.6 Capture mechanism

Fibre diameter, porosity and filter thickness are important parameters in defining the materials to capture particles (or droplets). A fibrous filter works either through a mechanical collection mechanism or via charged fibres mechanism. Mechanical collection mechanisms are inertial impaction, interception and diffusion. Inertial impaction and interception collects large size particles, whilst diffusion collects small particles. The charged fibres mechanism is electrostatic attraction, is capable of collecting small and large particles [60].

Particles are removed and held by molecular attractive forces onto fibres. In Figure 2.8 (A) shows the single fibre capture mechanisms, where particles are less than  $0.1\mu\text{m}$  diameter show high efficiency with diffusion mechanism. For particle between  $0.1$  and  $0.4\mu\text{m}$  the diffusion and interception mechanisms are relevant, but at lower efficiency, as particles are large for

diffusion mechanism yet small for interception mechanism. For particles greater than  $0.4\mu\text{m}$ , the interception and inertial impaction mechanisms are useful with high efficiency. The best test for filter performance is to measure particle collection at its most penetrating particle size [60, 61]. These mechanisms are shown in Figure 2.8 (B).

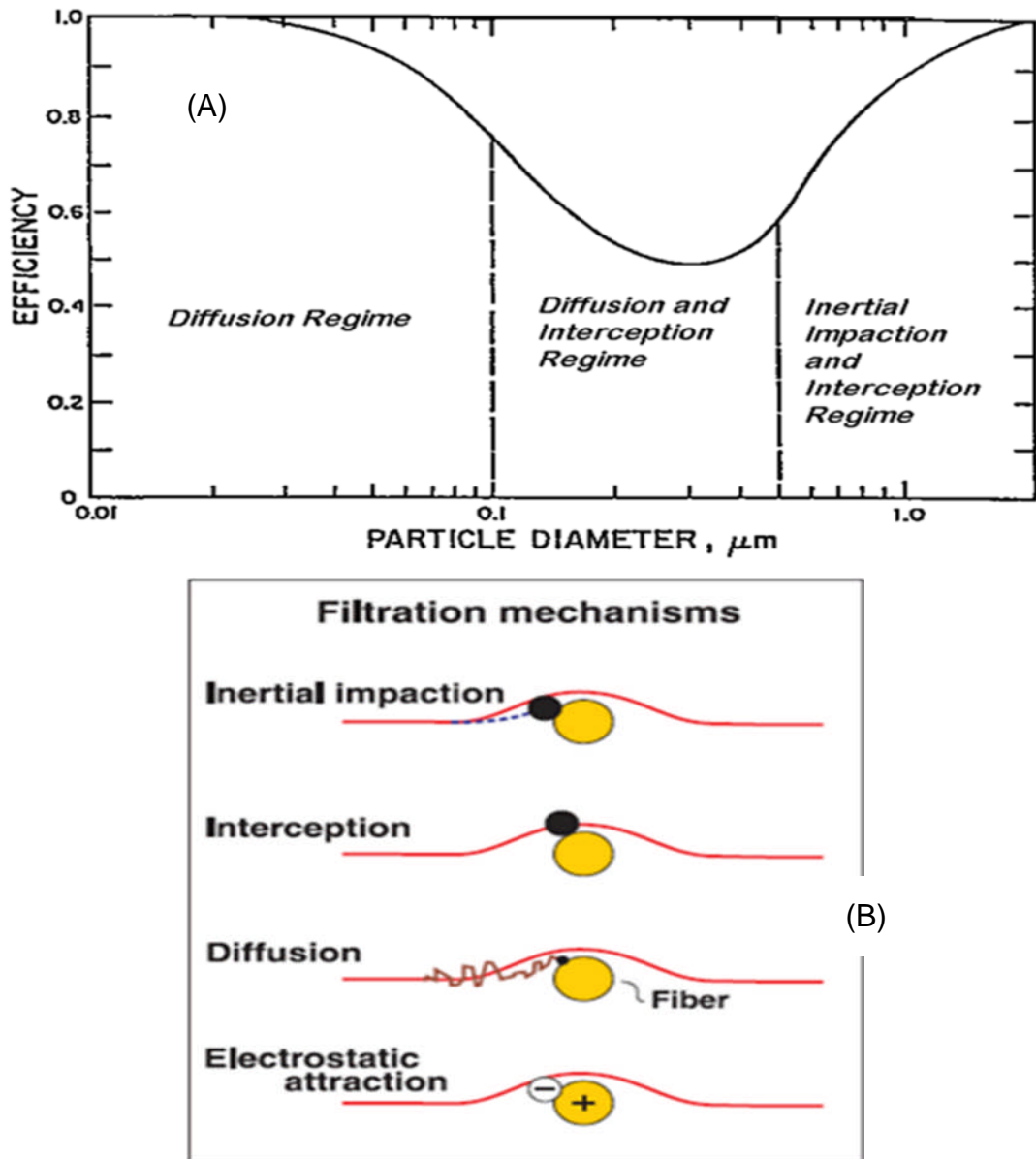


**Figure 2.8** (A) Single fibre capture mechanisms efficiency versus particle diameter, (B) : Filter mechanisms [60].

### **1. Inertial impaction**

Particles with large sizes are unable to adjust to a sharp change in flow direction near the fibre. Because of the inertia of the particle, it will follow the original path to collide with the fibres. This mechanism is useful during high gas velocities and dense fibre packing in filter media [61].

### **2. Interception**

A particle (or water droplet) following the streamlines of the laminar flow can be captured by a fiber because both the particle and fibers have finite sizes. If the radius of the particle is greater than the distance between the streamline which contains the particle and the fiber; the particle collides with the fiber and is hence captured. Streamlines further than one particle radius away from a filter fiber will not contribute to the interception mechanism. Particles in the range of 0.3-1.0 $\mu\text{m}$  in diameter usually follow the streamline; they will intercept a fiber if the distance of stream line approaches to less than the particle's radius to the fiber surface [61].

### **3. Diffusion**

This filter mechanism works on gas state and Brownian motion of the molecules leads to diffusion mechanism of particle transport. Small particles tend to have a random motion due to particle interaction with molecules. Diffusion is strongest for small particles and slow flow. This causes the molecules to have more 'erratic' pattern around the particle to hit and stick to the fibre surface [61]. The rate of diffusion increases with temperature [62].

### **4. Electrostatic attraction**

Fibres with large diameter depend on electrostatic charges to remove fine particle to have better efficiency. Large diameter fibres are low in cost and relevant to liquid flow. Filters over time will be neutralised in charge due to particle capturing on the surface of the fibre diameter [62].

## **2.7 Types of filter**

There are three types of filtration and they are cake filtration, deep-bed filtration and membrane filtration[55]. These filtration mechanisms are shown in Figure 2.9 [55].

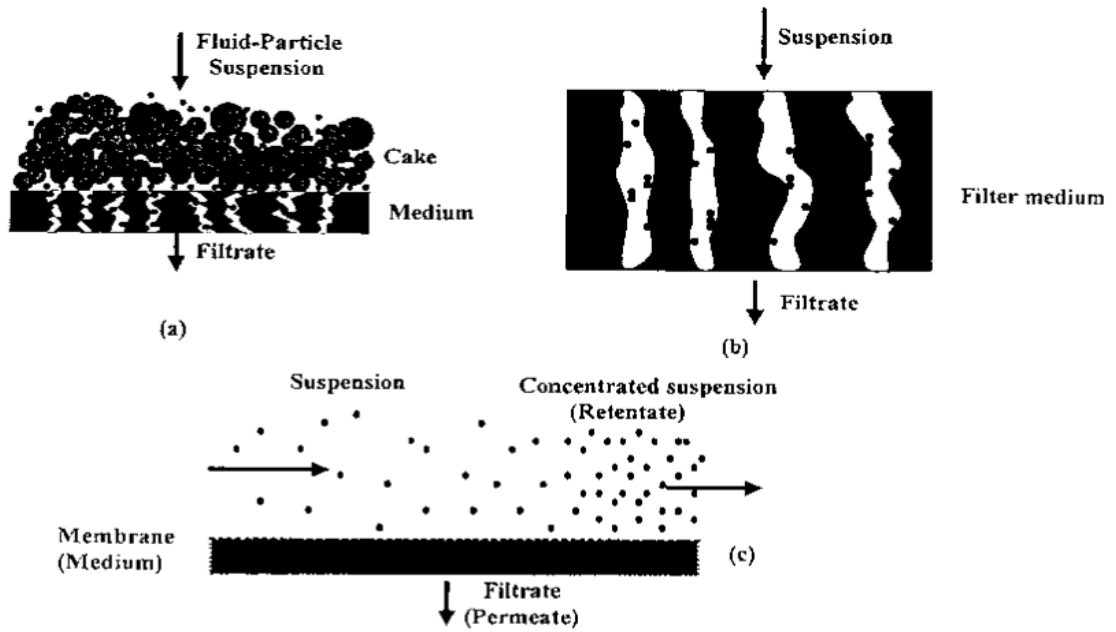


**Figure 2.9** (a) Cake filtration, (b) deep-bed filtration and (c) membrane filtration [55].

### 2.7.1 Cake filtration

Cake filtration (Figure 2.4.1(a)) is the most commonly used liquid filtration mechanism [55, 63]. This filtration mechanism is an unsteady process [63]. Solid/fluid suspension is processed through porous medium under a pressure. In cake filtration, the size of porous medium should be less than the size of particles [64]. The porous medium will allow fluid to flow and stop the particles on top of the porous medium. As particles stop on the filter medium, the thickness of the cake increases with time and would grow with its own porous structure. Once cake thickness increases filtration becomes more efficient, although the pressure drop increases [55, 65, 66]. There are two types of cake, incompressible cake and compressible cake. Incompressible cake, where drag force doesn't deform the particles structure in a given pressure gradient. Compressible cake, is when drag force deforms and compresses particle structures in a given pressure gradient. The reason behind this is the stress formed in the particles structure. Compression in cake would change the porosity and permeability [54, 55, 66].

### **2.7.2 Deep-bed filtration**

Deep-bed filtration (Figure 2.9(b)) is mostly used in water treatment procedures [67], but it is also of particular relevance to this project. Flow of fluid suspension through a deep-bed filtration will cause particles to be removed from fluid and bonded onto the filter media. This bonding of particles will take place in several depths of the filter medium [54, 55, 67]. Deep-bed filtration mechanism is applied in low solid concentration of particle size from 0.1 to 50 $\mu\text{m}$  with large amount of liquids [55, 67, 68]. Therefore deep-bed filtration is used in macroscopic and microscopic level of droplets [69]. Filter media are silica sand, anthracite coal, active carbon and non-woven textiles [55]. As mentioned before, particles will bond to filter media because of the forces and interaction between particles. Typically when the diameter of the particles in fluid is larger than 10 $\mu\text{m}$  the main forces in particles are hydrodynamic and gravitational. If the diameter of particles in fluid is smaller than 10 $\mu\text{m}$  then electrochemical forces such as double-layer forces, van der Waals forces and Brownian diffusion will dominate [70]. Deep-bed filtration is an unsteady process as pore voids are changing due to small particles bonding; this leads to a decrease in porosity. Deep-bed filter efficiency will depend on the size and the distribution of particles [68]. As particles are bonded, the filter efficiency and permeability decreases [71].

### **2.7.3 Membrane filtration**

Membrane filtration is applied to waste treatment, desalting and clarification. Micro filtration, ultrafiltration, nano filtration are all types of membrane filtration [55]. In this filtration mechanism, the membrane acts as a filter medium. The membrane absorption is measured only through the size and shape of particles in the fluid suspension [55, 72]. If the particle size is larger than the pore size of the membrane then particles would be separated easily. When the particle size is smaller than the pore size membrane then particles would be absorbed through the inertial impaction. Diffusion mechanisms for absorption play a major role when particle size decreases [55]. As filtration progresses the absorbed particles in fluid suspension would form a dynamic boundary layer (clogging layer [73]) next to the membrane

structure [55]. Long filtration time will cause the absorbed particles at membrane surfaces to reduce the permeability [55, 74]. The permeate velocity ( $U$ ) is proportional to transmembrane pressure (TMP) ( $\Delta P$ ). The TMP, can be reduced by minimising the hydraulic resistance of the cake [74].

There are two types of membrane filtration and they are dead-end filtration and cross-flow filtration. The differences between both methods are the feed direction. This is shown in Figure 2.10 [73] and the cross-flow filtration clogging layer is less compared to dead-end filtration. This leads to high filtration efficiency in cross-flow filtration compared to dead-end filtration [73].

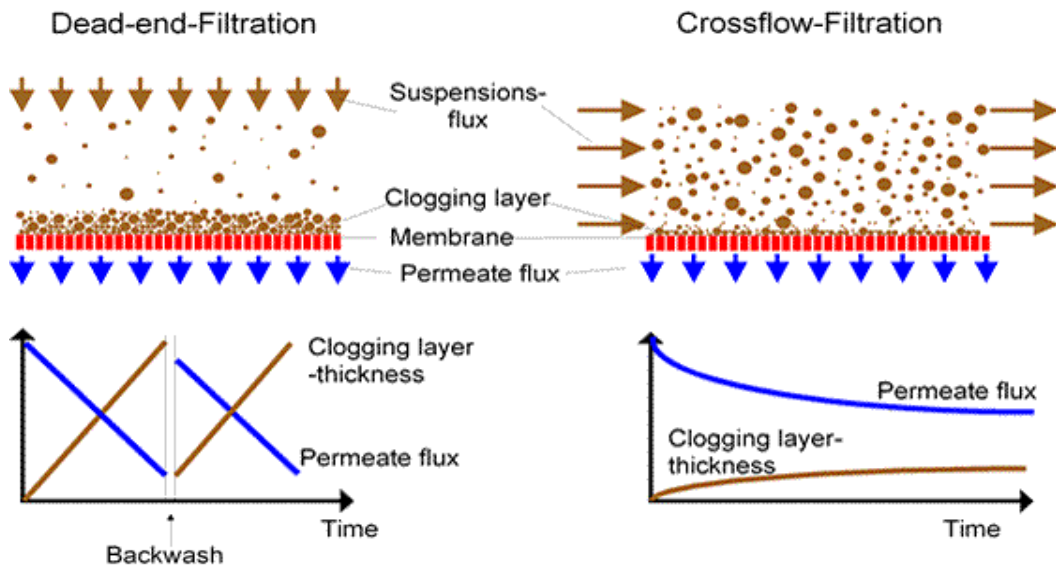


**Figure 2.10** Clogging layer effects in dead-end-filtration and cross flow-filtration [73].

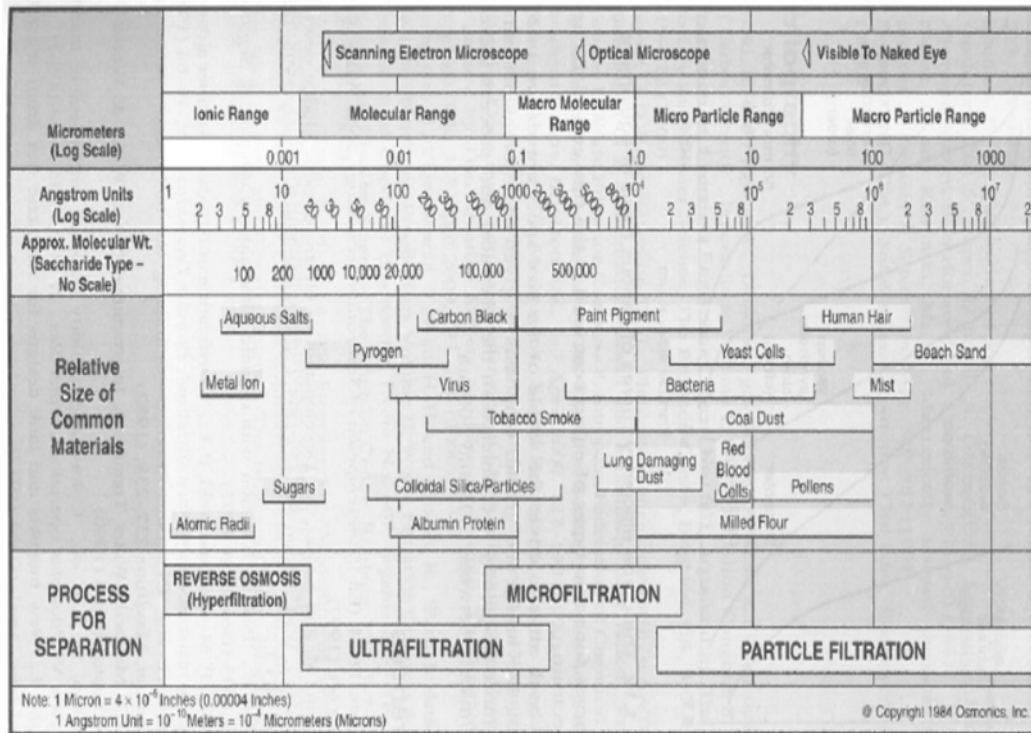


**Figure 2.11** Process selections according to different particle sizes [56].

Macrofiltration separates particles between 5µm to 1mm. Microfiltration separates particle between 0.1µm to 5µm. Below microfiltration is ultrafiltration, nanofiltration and reverse osmosis. Process selections according to different particle sizes are shown in Figure 2.11 [56]. Membrane technology has surface fouling problems and concentration polarization effect [55, 75] due to accumulation of species in the boundary layer next to the surface of the membrane [76], and permeability (k) would be reduced progressively. When the pressure is released the effects disappear [76]. The effects can also be reduced by helical fluid flow through a tubular cross-flow (membrane) filtration [72]. Dynamic filtration results in high shear rates on the membrane and decreases the cake formation [77]. For membrane filtration there is a disadvantage due to cake formation and this problem is minimised through vibratory membranes, charged membrane surfaces, turbulent promoters and air sparging [74]. Membrane filtrations are more expensive in waste water treatment compared to non-membrane filtration [74, 75]. Membrane filtration advantages are energy saving and good quality of product [77, 78].

## 2.8 Porous media flow

Flow inside the filter media is important to understand as it helps to optimise the filter unit. The fluid flow and structural properties are the focus of this section. Fluid flow through a porous medium is well characterized by Darcy's law. The porous media structural properties are particle shape, size, distribution and porosity. A lot of understanding of porosity & permeability, particle shape & size has evolved from work in packed beds of particles (eg found in the chemical industry). For this reason the following sections (2.8.1 - 2.8.5) refer to the geometry so it best illustrates the key concepts of flow through a packed bed geometry.

### 2.8.1 Darcy's law

Darcy's law is perhaps the classical approach of filtration analysis and it has been successfully used to model of laminar flow and uniform incompressible porous media [79-81]. The pore level properties are linked to macroscopic flow properties such as permeability and tortuosity (defined as the measurement of fluid flow length in the bed ( $l'$ ) compared with actual bed length ( $l$ )), and parameters of pore structure, such as porosity and specific surface area [80, 82], but the fundamental relationships are not known a priori for a given design [83]. Darcy's law states that 'the average velocity measured over the complete area of the bed is proportion to pressure and inversely proportion to the thickness of the bed' [54]. Darcy's law equation is written below.

$$\Delta P = \frac{1}{k} \times \frac{QL\mu}{A} \quad \text{Equation 2.1}$$

In Equation 2.1[54, 80, 81],  $\Delta P$  is the pressure drop across the bed (Pa),  $k$  is the permeability ( $m^2$ ),  $Q$  is volumetric flow rate ( $m^3/s$ ),  $A$  is the cross-sectional area of the bed ( $m^2$ ),  $l$  is the thickness of the bed (m),  $\mu$  is the dynamic viscosity of fluid (Pa·s).

Since the velocity of the fluid and the characteristic length of the pore are small then the Reynolds number is generally low, therefore the behaviour is dominated by viscous drag, hence the significance of Darcy's law having a viscosity term in the equation [54]. Generally for a given filter the quantities such as pressure drop, thickness of the filter and the cross section on area

of a filter are determined by the filtration equipment. According to this volumetric flow rate is proportional to the permeability. With most filtration process, as the filter removes particles from the flow effective permeability of the filter decreases [54]. Also when fluid flow rate is maintained constant then the pressure as would increase as time increases, alternatively with a constant pressure drop the flow rate decreases with time.

### 2.8.2 Permeability

Permeability is an important factor in fluid flow as it directly relates to porosity and surface area. It has been proven that micro geometry of the depth media has a strong influence in permeability calculation [84]. The Carmen-Kozeny equation can be used to estimate the permeability based on key characteristics of the filter:

$$k = \frac{\varepsilon^3}{k' s_o^2 (1 - \varepsilon)^2} \quad \text{Equation 2.2}$$

In Equation 2. 2 [54, 81], k is the permeability (m<sup>2</sup>),  $\varepsilon$  is voidage or porosity, k' is the kozeny constant, s<sub>o</sub> is the specific surface area of the particles (m<sup>-1</sup>) .The term k' is described below.

- **The Kozeny constant** (k') is important for permeability because it compares the tortuosity, defined as the measurement of fluid flow length in the bed (l') compared with actual bed length (l).A constant k<sub>o</sub> is dependent on the pore shape factor. k<sub>o</sub> is roughly 2 for circular and 1.78 for square. The Kozeny constant equation is shown below [55, 80].

$$k' = \left( \frac{l'}{l} \right)^2 \times k_o \quad \text{Equation 2.3}$$

The kozeny constant can be chosen to represent particles in different shape and sizes. For non-spherical particles having different shapes and sizes would have Kozeny constant(k') between 3 and 6. For spherical particles Kozeny constant is 4.8 or 5. For fibre filters the Kozeny constant is influenced by porosity and the orientation fibres. Randomly packed fibres with porosity between 0.55-0.86 has a Kozeny constant of 5.5.The Kozeny

constant will also depend on porosity when the porosity is higher than 0.86 [85].

For fibrous beds consisting of randomly packed fibres will have mean diameter of  $d_p$  and shape factor  $\lambda$  (defined as the ratio of surface area of particles random shape compared to surface area of an equivalent sphere). The classical approach assumed particles are sphere and have a shape factor of 1. Therefore permeability (Carmen-Kozeny equation) equation for sphere particles is shown below [79], for a sphere Kozeny constant is 5 [54, 85].

$$k = \frac{\varepsilon^3}{k' s_o^2 (1-\varepsilon)^2} = \frac{\varepsilon^3}{5 \left( \frac{6}{d_p} \right)^2 (1-\varepsilon)^2} = \frac{d_p^2 \times \varepsilon^3}{180(1-\varepsilon)^2} \quad \text{Equation 2.4}$$

According to permeability equations (Equation 2.2 and Equation 2.4), it can be seen that the permeability is depended on porosity, tortuosity or kozeny constant, specific surface area, mean pore diameter and shape factor of the particle. In Equation 2.2, permeability is dependent on the porosity of the fibre bed. All the Kozeny constant values are dependent on tortuosity values and whether fluid flows in between the surface wall and particles (where the porosity value is higher than bed porosity [86]). This causes the tortuosity value to decrease and leads to a decrease in kozeny constant.

### 2.8.3 Porosity

Porosity is also referred to as voidage. Porosity is a measure of the region accessible to fluid flow in porous medium. The porosity is the proportion of the void volumes to the total volume, the equation is for porosity :

$$\varepsilon = \frac{V_v}{V_T} = 1 - \frac{V_s}{V_T} \quad \text{Equation 2.5}$$

In Equation 2.5 [83, 85],  $\varepsilon$  is the porosity,  $V_v$  is the volume of void,  $V_s$  is the volume of solid and  $V_T$  is the total volume. If the porosity is increased then permeability would increase as well. Therefore the flow rate under a given pressure drop would increase if the porosity is high[84].An example of a

simulation of fluid flow through the void of a particle bed (a common application in chemical processing) is shown in Figure 2.12, where flow of fluid is shown in green, pores in black and particle in brown. The porosity is affected by shape of the particles during packing. There are two methods of packing particles and they are random close or dense packing (RCP), random loose packing (RLP). Random close packing is adding small amounts of particle and pushing them to be dense at different stages. Random loose packing is 'by tipping the filled container horizontally, slowly rotating it about its axis and gradually returning it to the vertical position'. Even though same packing method is followed there was a difference in porosity of the beds this mainly because of surface friction of wall [86].

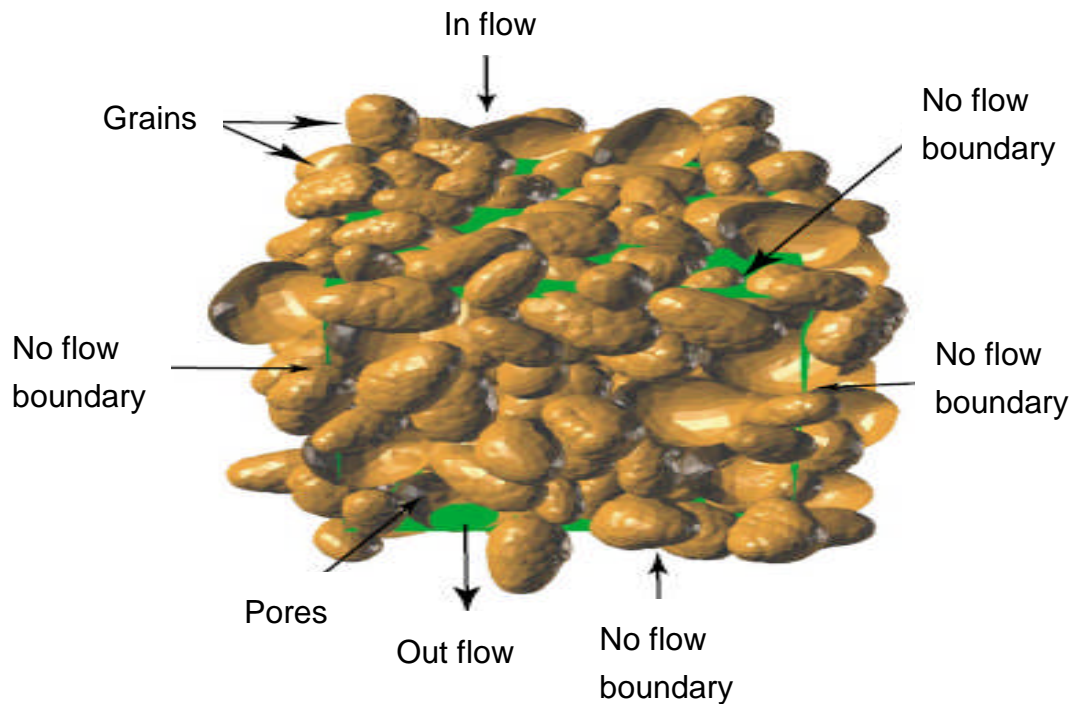


**Figure 2.12** Cad model of representing the fluid flow through the void of particle bed [84]. Flow of fluid is shown in green, pores in black and particles in brown.

#### 2.8.4 Effect of particle shapes

Particle shape is a key factor in a packed bed systems and porous flows. For fibres packing shapes are fundamental. Due to different shapes in particles, there are models for spheres, cylinder, rings (hollow cylinder) and etc. For theoretical calculations the model particles should be multiplied by the shape

factor (defined as the ratio of surface area of particles random shape compared to surface area of an equivalent sphere) as a reasonable approximation[54]. Shape factors defined by Wadell[87] and Heywood[88] are commonly used [89].

Cylinders or fibres do not follow the general trend observed between pressure drop and the cylinder dimensions. As the cylinders are unsymmetrical the orientation of packing is also important. Fluid flow through the cylindrical fibres, such as found in non-woven filters, could have different aspect ratio and tortuosity depending on the orientation [86].

### **2.8.5 Effect of particle size and distribution**

From porosity calculations it is obvious that particle diameter size and particle distribution are important. The particle size could be homogenous or heterogeneous, the same follows for distribution of the particles as well. If the particles have a homogeneous size and homogeneous distribution then porosity of the bed should be constant through the filtration process. Particles with heterogeneous size and heterogeneous distribution would have different porosity throughout the bed. This makes the performance of a filtration system difficult to predict.

In general, particle size and distribution is analysed through sieving analyses, microscopic analyses, sedimentation and elutriation methods, permeability methods, electronic particle counters, laser diffraction analysers, X-ray or photo sedimentometers and sub-micron particle sizing. For example cone beam x-ray microtomography can analyse the internal structure through 3D images, an example of the analysed images are shown in Figure 2.13 [83].

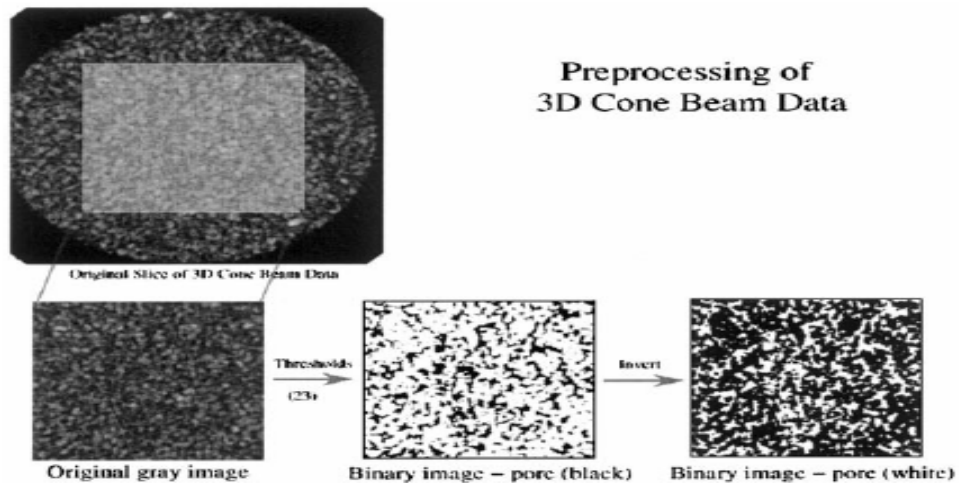


**Figure 2.13** 3Dimesional images of particle size and distribution in a filter cake [83].

## 2.9 Fibre Media

### *Filter media*

Fibrous filter media is in form of fine synthetic, minerals or natural fibers and categorised as woven media or nonwoven media. In the 1960s, asbestos fibres contained  $0.01\mu\text{m}$  in diameter and recognised as best filters. But due to health hazard from asbestos, finer micron glass and synthetic polymer fibres were used.

### 2.9.1 Woven media

Woven fibre is created where two sets of yarns interlace at right angles to each other. Longitudinal or warp yarn are named as end and transverse or weft yarns are named as picks. The warp and weft yarns are shown in Figure 2.14 (a) [90]. Woven materials are flexible so it is difficult to characterise the holes (sizes). Examples of materials are nylon, polyester, polypropylene, polyethylene and Stainless steel. Woven fibres are made by spun staple, monofilament and multifilament, These are shown in Figure 2.14 (b) [56]. Spun staple yarn [a] is made by twisting short length fibres into continuous fibril, this gives the property to contain 'hairy' filaments that can hold particles on the surface. Monofilament yarns [b] are made from single

continuous fibres and produces good cleaning & minimum blinding. Multifilament yarns [c] are made by twisting two or more continuous monofilament yarns together. They have a greater tensile strength, compared to other yarns [56].

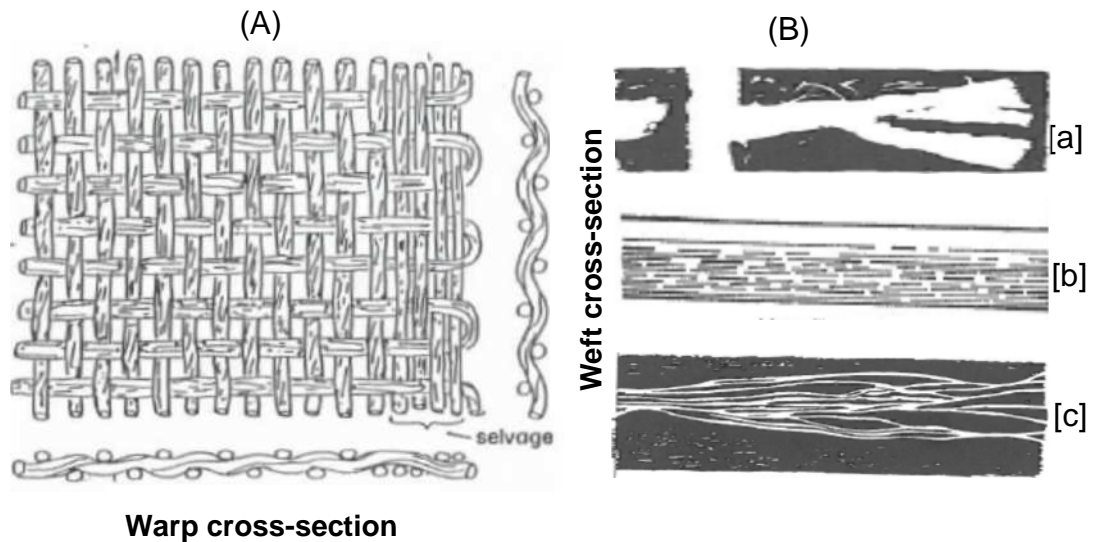


**Figure 2.14** (A) Warp and weft yarns position in plain woven fabric[90]. (B) Woven fabric methods [a] spun staple, [b] monofilament and [c] multifilament[56].

Woven media weaves are plain, twilled, plain Dutch, twilled Dutch, reverse Dutch, duplex Dutch, betamesh Dutch & basket. These are shown in Figure 2.15. Plain weave [a] has wires passing over and under each other, these have square or rectangular opening for flow in the perpendicular direction. The wire diameter and number of wires in a unit square control the width of the opening. Small openings and a finer mesh give a reduced physical strength. Twilled weave [b] has wire alternatively crosses over and under by two wires. It produces a diagonal pattern. Multiple wires in warp and weft in twilled weave would cause dense and strong fabrics known as basket. Multiple weft wires can twist around each other to cause irregular opening mesh [56].

Dutch weave [c] has two different wires and generally one would be larger than the other. The large wire would be called warp and other wire is shute. Shute wire passes alternatively on warp wire such as over and under. This makes small opening with high physical strength. The angle of material

would lead to a twist and causes triangular opening. Reverse Dutch weave [e] has a reverse arrangement of Dutch weave and has a resistance to blinding and good clean ability. Duplex Dutch [f] weave has two small diameters warp compared to one large warp in Dutch weave. This makes Duplex Dutch weave stronger than Dutch weave. Betamesh Dutch weave [g] retains large portion of solid on the surface and lead to back-flushing properties & good contaminant properties [56].

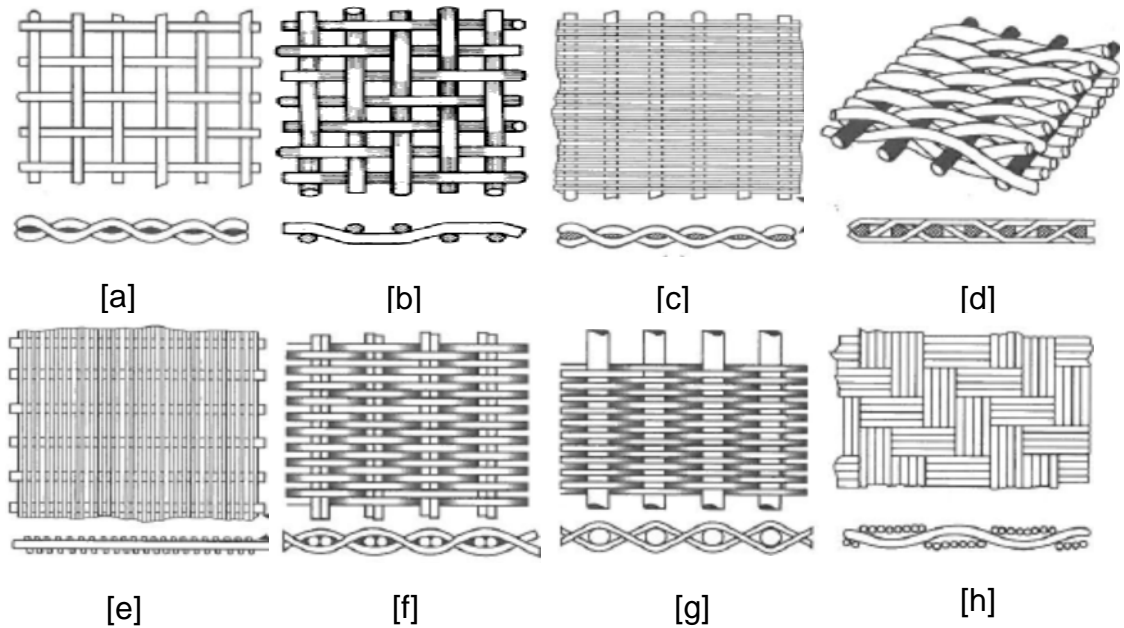


**Figure 2.15** types of weaves. Plain weave [a], twilled weave [b], Dutch weave [c], Twilled Dutch weave [d], Reverse Dutch weave [e], Duplex Dutch weave [f], Betamesh Dutch weave [g] and Basket weave [h] [56].

### 2.9.2 Non-Woven media

Non-woven media is a loose collection of fibres arranged in short form and physically bonded with a bonding system. They are lighter, thinner and with a high permeability than woven media. The porous structure is random. The interlocking layers of fibres determines the physical strength of non-woven fabrics. The non-woven material properties such as fibre thickness, porosity and density of the medium can all be controlled. Non-woven fabrics can exhibit a good particle adhesion onto the fibres and resistance to corrosion for depth filters. Non-woven material handle high pressure filtration and are less sensitive to the process changes such as particle size variability or concentration change[91]. Non-woven materials are made from polyester,

olefin, rayon, nylon, cotton, glass, acrylic, and fluorocarbon fibres[56]. Examples of scanning electron microscope(SEM) images for non-woven materials taken by the author are shown in Figure 2.16, (A) represents the meltblown non-woven material at 51x magnification and (B) represents the 500x magnification. Figure 2.16(B) also highlights the random nature of the fibre orientation.

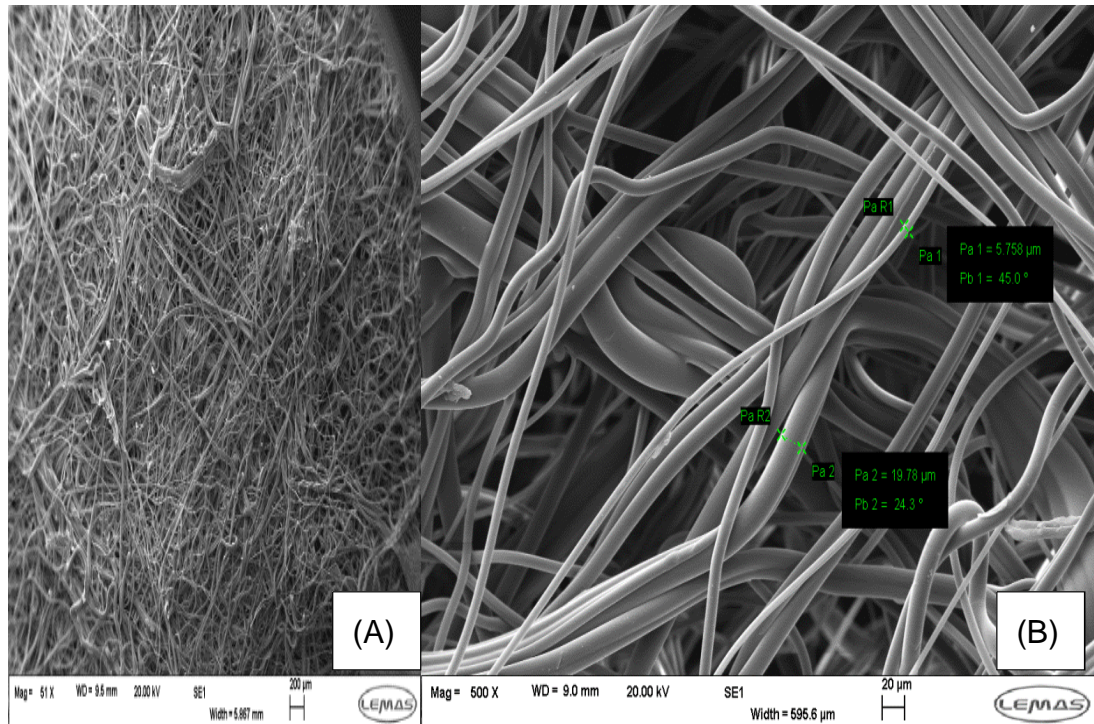


**Figure 2.16** (A) represents the meltblown non-woven material at 51x magnification and (B) represents the 500x magnification for fibre diameter.

Non-woven manufacturing processes consists of four principle elements of manufacturing: fibre selection and preparation, web formation, web consolidation and finishing. The processes of manufacturing non-woven fabrics can be grouped as textile, paper and extrusion.

- Textile technology is known as garneting, carding, and air laid. In this, textile fibres are formed into oriented webs. Textile based non-woven fibres are formed in dry state and uses the dry or air laid technology to build the non-woven fabrics. This method is shown Figure 2.17 (A) & (B).
- Paper technology is known as dry laid pulp, and wet laid. These contain synthetic fibres and wool pulps. Undissolved and short non-woven fibres

mixed with fluid are used to form webs in a wet laid state. This method is shown Figure 2.17 (C).

- Extrusion technology is based on spunbond, meltblown and porous film. Generally known as the polymer laid, where the nonwoven fabrics (polymer) are formed by extrusion. In polymer laid system fibre structures are continuously formed and manipulated. Extrusion based non-woven fabrics have less variability in the product properties, however the spunbound process has fabric structures with good strength to weight ratio (This method is shown Figure 2.17 (D)), fabric structures with high surface area to weight characteristics in meltblown and fabric structure with high property uniformity per unit weight in porous film[90].

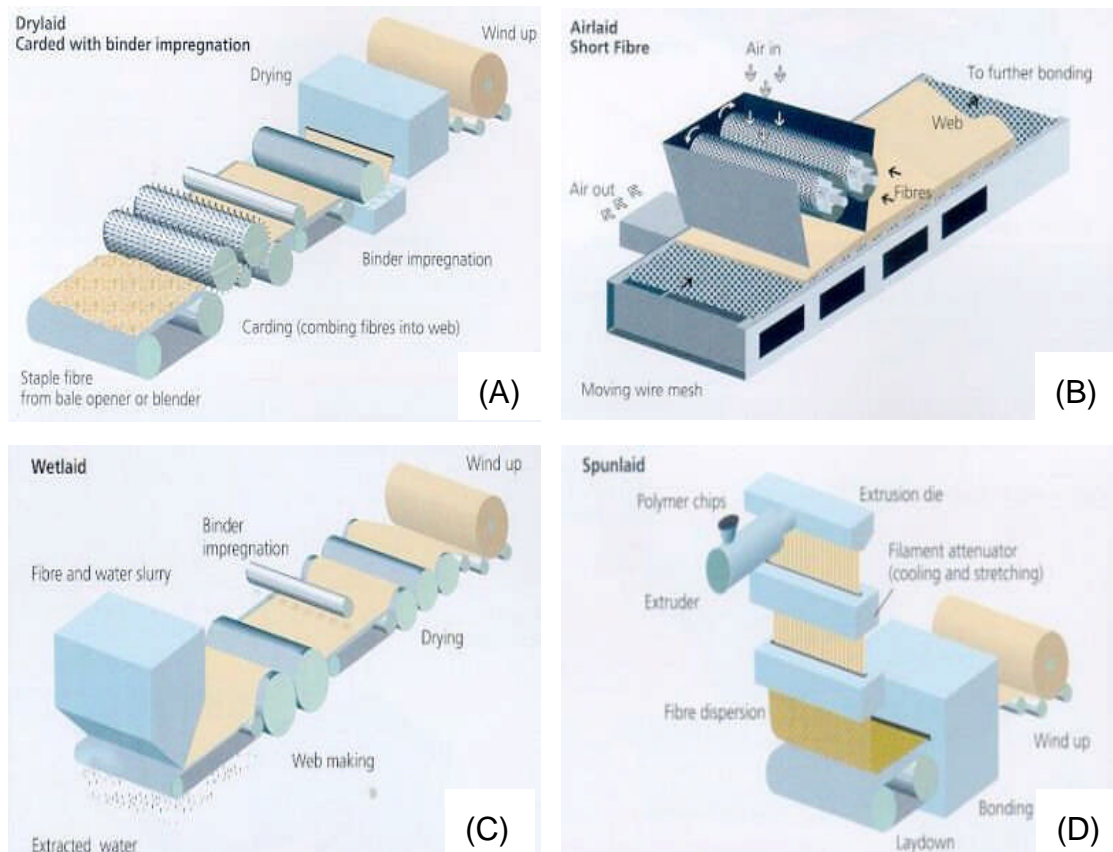


**Figure 2.17** Nonwoven manufacturing process (A) is Dry laid, (B) is Air laid, (C) is wet laid and (D) is spunlaid[92].

### 2.9.3 Advantages and disadvantages of woven and non-woven methods

**Table 2.4** Advantage and disadvantage of woven and non-woven fabrics[93] .

Woven filter fabric	Nonwoven filter Fabric
Expensive in manufacturing	Low-cost in manufacturing
High strength fabric	Low strength fabric
Two dimensional structure	Three dimensional structure
Low permeability	High permeability
Chance of yarn slippage	No chance of yarn slippage
Only surface filtration occurs	In-depth and surface filtration occurs due to its construction and thickness
Separation predominantly by sieve mechanism	Separation by impact, interception, diffusion, electrostatic charge mechanism

### 2.10 Wettability

Fluid behaviour close to a solid interface is complex and involves the wettability of the solid, the shear rate or flow velocity, the bulk pressure, surface roughness and dissolved gas [94]. The surface energy of the solid is defined as “The energy required to create unit area of new surface” [95]. Also wettability or surface energies is a result of molecular interaction between the fluid, solid and gas [96]. The surface energy of the fibres in coalescence filter media controls the performance of coalescing filters. High surface energy fibers capture and hold onto droplets, slowing their movement through the filter and hence increase coalescence between drops. Low surface energy fibers allow drops to slip through the filter with little or no hindrance but do not contribute significantly to the coalescence (Figure 2.19). The contact angle quantifies the wettability. The contact angle ( $\theta_w$ ) is the angle between the liquid-vapour interface and solid surface, and is measured inside the liquid and shown in Figure 2.18 (A).

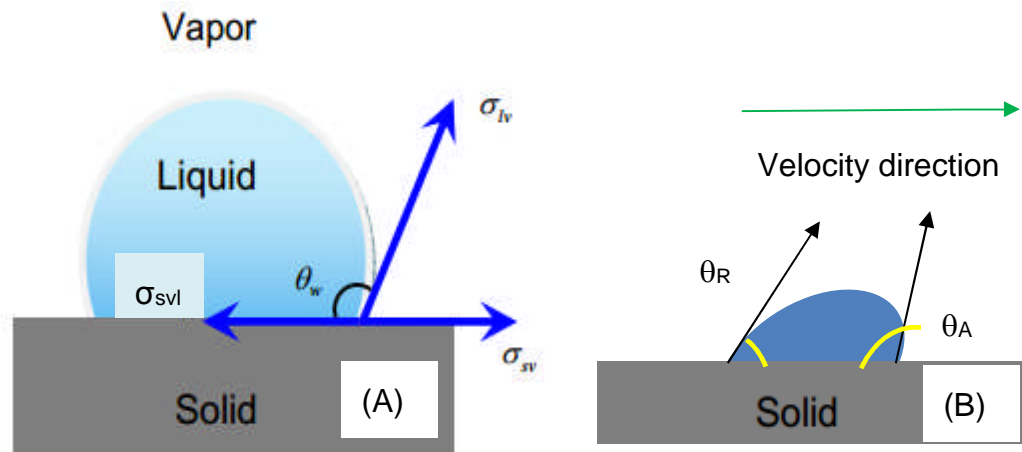


**Figure 2.18** (A) is contact angle of wetting droplet on a solid surface[97]. And (B) droplets advancing contact angle ( $\theta_A$ ) and receding contact angle ( $\theta_R$ ).

Young developed an equation in 1805 for the equilibrium contact angle, this is expressed through the force balance at the contact line[97, 98]. This is shown in Equation 2.6 [94].

$$\cos \theta_w = \left( \frac{\sigma_{sv} - \sigma_{sl}}{\sigma_{lv}} \right) \quad \text{Equation 2.6}$$

Where  $\sigma_{sv}$ ,  $\sigma_{sl}$  &  $\sigma_{lv}$  are respectively surface tension of solid-vapour-liquid, solid-liquid and liquid-vapour. The intermolecular forces between liquid molecules are responsible for the surface tension. Gravitation force deforms the droplet shape [99]. If the contact angle is larger than  $90^\circ$  then the system is described as non-wetting and for an aqueous system (hydrophobic or low surface energy). For contact angles less than  $90^\circ$  then the surface is described as wetting for an aqueous system (hydrophilic or high surface energy). Super hydrophobic surfaces are observed during contact angle more the  $150^\circ$ , with a very small amount of contact between liquid droplet and solid surface. This is often called the “lotus effect” [100]. These contact angles are shown in Figure 2.19 [100].

Two types of contact angle values are used: static and dynamic contact angles. Dynamic contact angles are non-equilibrium contact angles. Static contact angles (Figure 2.18 (A)), where a drop is deposited on the surface and the value is obtained by a goniometer. Dynamic contact angles (Figure 2.18 (B)) are measured during the growth (advancing contact angles) and shrinkage (receding contact angles) of a water droplet. The difference between advancing and receding contact angle is defined as contact angle hysteresis (H).

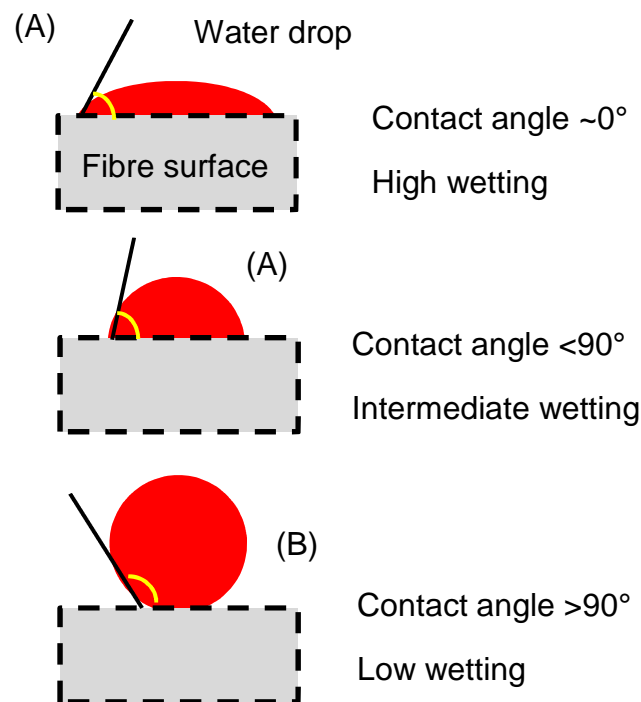


**Figure 2.19** water droplet on fiber surface with different wetting properties: contact angle for hydrophilic(A) and hydrophobic(B).

Patel and Chase [101] suggested typical depth media is made of hydrophilic glass fibres to capture water from diesel. This provides the water droplets to cling on the fibre and displace the diesel. Variation of surface wettability of fibres affects the filter medium performance. Therefore superhydrophobic membranes of electrospun polypropylene (PP) and poly(vinylidene fluoride-co-hexafluoropropylene) (PVDF-HFP) were studied. Fluorinated polymers (PVDF-HFP) are expensive and have compatibility issues with some fuels. Porosities, PP average fibre diameter range and solvent (Cyclohexane-Acetone-DMF: 80/10/10 parts by weight) percentage are respectively 0.94,

876nm, 2%; 0.94, 1082nm, 3%; 0.95,1710nm, 4%. Also beads were found on fibre images and reduces the pore size of the mat which increases the critical pressure to push the droplets through the pore. Generally pressure drop increased with decrease in fibre size. PP media had a lower pressure drop compared to PVDF-HFP media for similar water separation.

## **2.11 Liquid-liquid filtration**

Many industrial application use liquid-liquid filtration for the separation of dispersed immiscible liquids. Within the automotive industry uses for separation of water from diesel fuel is used to increase engine performance and reduces the exhaust pollutants & corrosion potential (exhaust pollutants produces a harmful effect on human health [102]).Filters are used to separate the immiscible liquids and extend the engines life time.

The traditional approach is to use a porous medium such as a fibrous filter for separating dispersed water droplets. Normally glass fibres are hydrophilic media and captures the water droplets in diesel fuel. Water droplets are likely to hang on the fibres and coalesce into larger droplets [103]. Then flow of the fluid (Diesel) will drag the coalesced droplets through the filter medium. The enlarged size and higher density compared to diesel will settle the water droplets in the downstream side [104]. The disadvantage of this approach is number of water droplets holding on will increase in hydrophilic fibres of filter, reduces the permeability of filter and increases the pressure drop for the flow [105]. The second approach is to use hydrophobic (cellulosic material treated with silicone) filter media to reject water droplets in the flow, all the fine droplets coalesce into large droplets and settles by gravity on upstream side of filter [104].

### **2.11.1 Oil in water and water in oil separation methods**

Membrane filtration, ultrafiltration, nanofiltration and reverse osmosis technologies are used in water treatment industry to filter and remove chemical & biological waste from the waste water and improvement of the wastewater treatment plant downstream [101, 106]. These filters are useful to remove dispersed oils from water.

Gravity separation, centrifugal separation, absorbent polymer separation, coalescing-based filtration, and vacuum dehydration are well-known water decontamination techniques in diesel fuel. Among them, the most cost-effective technique for removing free and emulsified water from diesel fuel at constant flow rates is coalescing-based filtration [107].

## 2.12 Coalescence filtration

Coalescing filters are used to separate emulsion of water droplets from diesel. There are three main steps; initially, water droplets are captured on the fibres of filter medium. Next, water droplets in the flow collides and coalesce with the previous water droplets or on the fibres. Causing droplets to merge. Finally, the coalesced droplets increase in size in the filter medium until drag of the diesel flow or gravity force are strong enough to migrate the enlarge water droplets through the filter [108]. Figure 2.20 shows the three main steps.

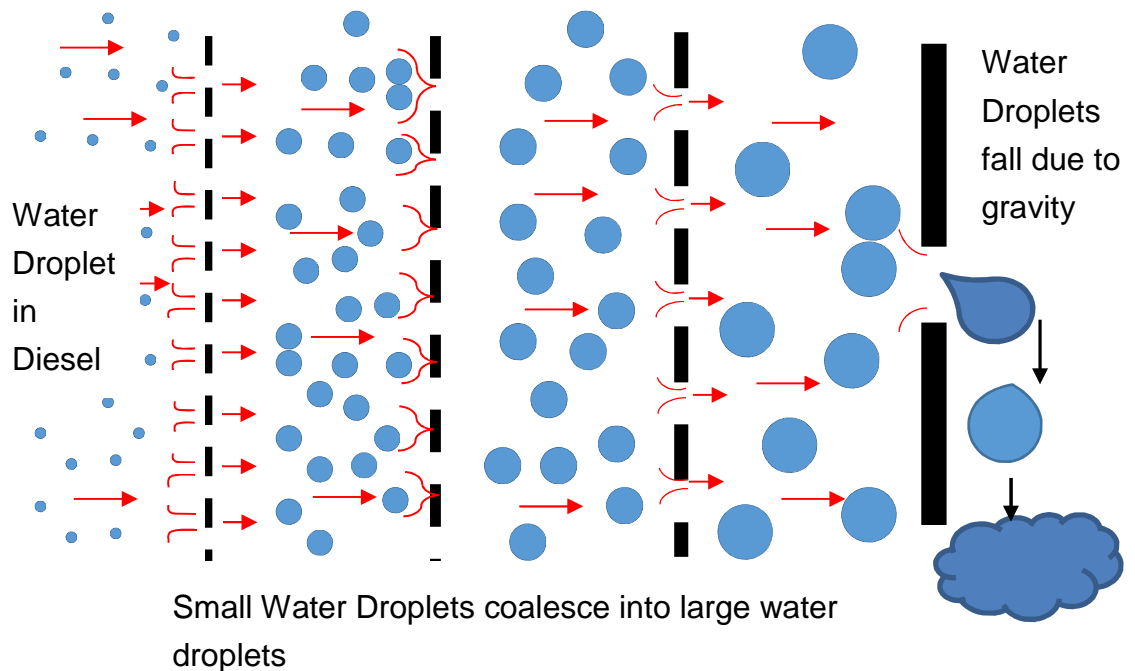


**Figure 2.20** Coalescing filters process with three main step. And shown the gravitational effect on water droplet.

The local velocity, fibre size, interfacial tension and contact angle influences the critical size of the water droplet when it detaches from the fibre. For the

case of a small contact angle of the drop on the fibre the drop is transported along fibre direction of fluid stream and drop doesn't break away [109]. The liquid-liquid separation of filter media is quantified through separation efficiency and depends upon the properties of the dispersion (such as liquid viscosity, liquid density, droplet diameter, liquid velocity, pressure, surfactant content and temperature) and fibre bed properties (fibre sizes, fibre orientation, wetting properties of fibres, filter thickness) [110]. The droplet formation is influenced by the surface tension of the liquid. Also temperature change affects the surface tension and viscosity of the liquid proportionally [111]. Filter media performance is effected by the emulsion flow rate and the surface tension of liquid. The hydrodynamic force acting on a droplet must overcome the adhesion force between the droplet and fibre before detachment occurs [112].

Hazlett et al [108] studied the coalescence process of droplets as approach, attachment, and release on fibre. For approach of a droplet to a fibre the interception mechanisms are important. 2 $\mu\text{m}$  fibre is about 15 times more effective than a 10  $\mu\text{m}$  fibre in removing 1 $\mu\text{m}$  water drop from a jet fuel system. Sherony and Kintner et al [113, 114] define the overall coalescence efficiency,  $\eta_c$ , as a mixture of capture efficiency and the fraction of collisions between drops that result in coalescence. The highest degree of drop hold up happens at or near the inlet edge of the fibrous bed. They also found that degree of coalescence increases with increasing saturation, decreases with increasing fibre sizes, decreases with increasing velocity, increases with increasing inlet droplet size and increases with increasing bed length. Sareen et al [115] studied water in oil and oil in water flow, conclude that interception is the dominant mechanisms in the start-up and steady-state operation of the coalescer. Microscopic observations have shown that small (about 5 $\mu\text{m}$ ) drops do not coalesce while moving together in a moving stream. The size of the capillary opening must be relatively large. Also rough fibre surface increases the ability capture and hold drops of dispersed phase.

Many materials have been used in coalescing filters such as glass fibres, glass spheres, Teflon fibres, and polyethylene fibres. Experiments have been performed to investigate the effects of various factors on the

performance of coalescence process. Hazlett et al [108] studied a number of parameters in the water-in-jet fuel emulsions, including: surfactant concentration, fibre size and material, bed depth, water content and the flow velocity of the continuous phase. Their work also showed fuel containing additives allowed droplets to slide on the fibres and detach more readily than fuel with no additives. Efficiency increases with bed depth up to a certain depth. In beds composed of two different-size fibres, the emulsion should first pass through the smaller fibres for optimal separation. They concluded that the large downstream fibre size has a significant effect on separation efficiency.

Robelein and Blass et al [116] examined the separation of micro-dispersion droplets from liquids using fibre beds. Stainless steel, glass, and PTFE-fibre media were tested in several aqueous-organic systems. The parameters varied were the organic and aqueous phase as dispersed drops, the thickness of the fibre, the depths and porosity of the fibre bed, the drop size, the volume flow and the holdup of the dispersed phase. The higher viscosity of continuous phase causes the small dispersed drops to be carried away from fibre bed due to higher force resistance for dispersed drop to stick on fibre bed. Separation performance decreases with the decreasing drop sizes, increasing superficial velocity and higher continuous viscosity. Also decreasing fibre size increases the separation performance of all fibre materials. The depth of fibre bed influenced the separation performance only a little. They also found little dependence of the separation performance on porosity over the limited range that they tested.

Magiera and Blass et al [100] reported work on a fibre bed consisting of thin and unarranged fibres of various materials for coalescence process. They identified advantages of fibre bed separators of low-cost, ease to set-up and continuous operation, but ideally the dispersion shouldn't contain solid particles. They studied the dispersion of oil in water in porous bed with fibre materials of Teflon, glass and stainless steel. The separation performance decreased for smaller droplets and increasing fibre diameter. At a constant bed porosity with decreasing fibre diameter causes an increase in fibre number per area and decreases the pore size between fibres, therefore probability of interception mechanism and adhering droplets on fibres

becomes higher in a closed network. The decreasing surface energies of materials are respectively; Glass, Stainless steel, Nylon and Teflon. Fahim and Othman et al [117] studied oil in water dispersion using composite beds of different materials. And suggested the best separation efficiency is with high surface energy (glass fibres) in the front part of packing and mixed layers of lower surface energy (stainless steel/ polypropylene) at the fibre bed exit.

Secerov Sokolovic et al [112] suggested that emulsion flow in porous media is affected by the wettability, fluid velocity and the surface chemistry of the drops, and polyurethane foam exhibits high separation efficiency in oily water treatment in a steady-state regime. The velocity of emulsion flow controls the capture mechanism and capture probability. The critical velocity is the maximum value of working velocity to be employed in the bed coalescer. Increasing bulk density decreases the bed porosity, permeability and coalescence efficiency in polyurethane foams media. The separation efficiency decreases with increasing fluid velocity. The effect of concentration and thickness of polyurethane filter bed for fluid velocities below critical value are negligible.

Bitten et al [118] investigated the coalescence of micro size water droplets on single fibres positioned perpendicular to the flow. 91% of the droplet size distribution were below  $6.7\mu\text{m}$  and adding sodium sulfonate decreased further the size of emulsion droplets. Direct collisions of droplets with the fibres were important during start-up and at steady-state operation of the coalescer. A droplet that is held on a fibre for a long period of time will undergo a greater number of collisions with dispersed phase droplets. Teflon fibers would support a droplet of diameter up to  $65\mu\text{m}$ - $75\mu\text{m}$ , treated and untreated fibre glass could support droplet diameters up to  $400\mu\text{m}$ - $500\mu\text{m}$ , Dacron fibre could grow droplet diameter to  $60\mu\text{m}$  but not released from fibre and stop growing and nylon fibre could grow droplets to  $100\mu\text{m}$ . The droplet growth were stopped because of the 5ppm of sodium sulfonate (surfactant) addition. Figure 2.21 shows 1000ppm water emulsion in fuel with a minimum  $0.01\text{m/s}$  velocity on Teflon fibre. Noticeable the water droplets adhesion on to the fibres. Difference in a coalescence on a single fibre and in a fibre bed are important. Also pressure builds up due to water droplets holds on fibre

surfaces. In single fibre, there is not this same potential for pressure build up. The study concluded treated or untreated glass fibres are better than plastic fibres (Teflon and nylon) for fibre bed coalescer. As the fibre diameter reduces, more complete coalescence is obtained.

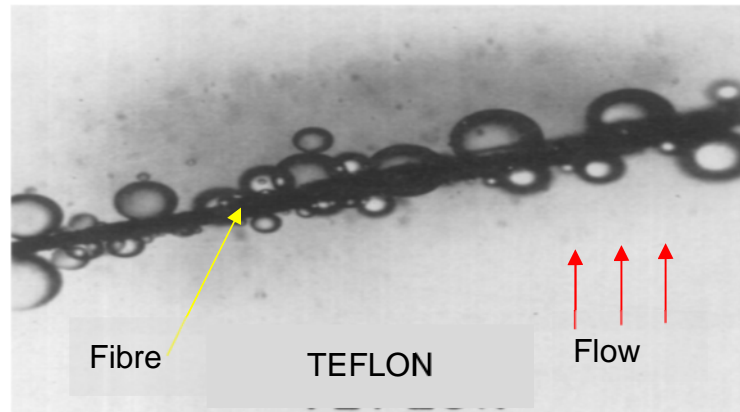


**Figure 2.21** Photomicrographs of drop coalescence of single fibres. Flow direction from page bottom to top [118]. Teflon fibre with a diameter of 16-17 $\mu\text{m}$ .

Rose et al [119] studied the coalescence of water- organic suspensions and varied fibre diameter, fibre material and fluid properties. They found that coalescence improved with higher interfacial tension but suggested that inlet drop size was influenced by the variation in interfacial tension. Vinson et al [120] investigated the coalescence of dispersion of an organic solvent in water. Below interfacial tension 11mN/m the coalescence performance decreased.

Viswanadam and Chase et al [121] studied the separation of water in oil dispersion separation. Separation of dispersed droplets smaller than 100 $\mu\text{m}$  are improved by continuous sub-micron sized fibres produced by electrospinning form thin non-woven fiber mats or membranes. The electrospun fibres contains small pores and large surface area to mass ratio. They are useful to capture micron and submicron size particles in fluid streams but with reduced drag force[122]. The fibre materials have a low surface energy that gives membranes a hydrophobic properties (polypropylene). The overall separation efficiency of tubular filter (Figure 2.22) was 98.9% compared to 91.5% of flat filter. Flat filter separated drops larger than 20 $\mu\text{m}$  but the tubular filter separated drops larger than 7 $\mu\text{m}$ . The

surface tension force resisting the drop from rolling by gravity is proportional to the length of three phase contact-lines. Therefore curvature of tubular filter results with shorter contact lines than similar drop volume and with the same contact angle on a planar surfaces. This provides the smaller drops to roll by gravity on cylindrical surfaces.



**Figure 2.22** Water droplets in air sitting on a tubular mat[121].

### **2.12.1 Effect of wettability**

Wetting is a consequence of the interaction between the solid and liquid phases. Robelein and Blass et al [116] suggested an angle of  $0^\circ$  means the droplets could wet the solid surface completely and  $180^\circ$  non-wetting by the dispersed phase. At a contact angle of  $90^\circ$ , two mixed liquids have the same wettability. Advancing and receding contact angles of aqueous-oil system on materials are respectively,  $112^\circ$  and  $78^\circ$  on stainless steel,  $138^\circ$  and  $107^\circ$  on glass and  $180^\circ$  and  $180^\circ$  on PTFE-fibre. Voyutskii et al [123] explored the water in oil emulsion filtration using fibrous materials. They observed that intermediate wettability gave the most effective separation and concluded that for the best performance the filter should be sufficiently water-wetted to coalesce the water, but not so saturated as to produce an excessive pressure drop by the accumulated water. Akagi et al [124] identified when the dispersed phase wetted the fibres there was an increase in the separation efficiency for oil in water flow in glass fibre bed. Hazlett et al [108] reported that the water droplets in water-in-oil emulsions must displace the oil film from the wet fibre for attachment to be effective. A water droplet easily displaces oil on hydrophilic surfaces. The displacement of the

continuous phase by the discontinuous phase on polyethylene or Teflon (low surface energy) should be considerably less than on a glass (high surface energy). Angelov et al [125] studied oil in water dispersion in multilayer packing. The first hydrophobic (polyester) layer caused a coalescence of oil droplets and the second hydrophilic layer (cotton) supported the detachment of large droplets. The third hydrophobic layer (polyethylene) captured the larger oil droplets and formed as a film.

Magiera and Blass [100] reviewed for droplets larger than 100 $\mu$ m the influence of the wetting properties of the fibres. They showed the contact angle decreases with increasing fibre diameter in a constant liquid system. Therefore contact angle measurements on flat pieces are insufficient to characterise the wetting behaviour of thin fibres. Spielman and Goren [126] obtained approximate mathematical solutions for a model describing coalescence by flow through porous media in oil-in-water systems. In their work, two wettability situations were considered: oil preferentially wetting and oil nonwetting. The wetting behaviour of the water-in-oil or oil-in-water emulsions is considered to be important in determining the performance of the coalescence efficiency. Moses and Ng [127] visually observed a model porous media coalescer and determined that in the case of oil droplets in water the oil droplets adhere more to the oil nonwetting surface than to the oil wetting surface.

Kocherginsky et al [128] demonstrates a hydrophilic polymer membrane for the demulsification of surfactant-stabilized water-in-oil emulsions. The good operability and high efficiency were investigated and it was found that membrane material, pore size and trans-membrane pressure has the strong effect on demulsification. Demulsification is only possible with hydrophilic membrane having pore size smaller than the emulsion droplet diameter. Also, the smaller the pore size, the better the demulsification efficiency as well as leading a high pressure drop. The membrane thickness does not play an essential role and the membrane acts as a coalescer with simultaneous permeation of emulsions through porous.

Viswanadam and Chase [121] reviewed that sub-micron scale roughness can enhance the hydrophobic properties. Also electrospun fibre membranes

are superhydrophobic with contact angles greater than  $150^\circ$  [101]. Kulkarni et al [122] investigated dispersed water in oil with blended microglass and electrospun polypropylene fiber filter media. This work also showed wettability has an effect on separation of two immiscible phases in surface filtration or depth coalescing filtration. Filters fabricated of fibres with high wettability were found to be more efficient in coalescence but also increases the pressure drop. The lipophilic to hydrophilic ratio (L/H) defines the relative wettability of filter medium performs when it is in contact with a non-polar liquid (oil) compared to contact with a polar liquid (water).  $L/H = 1$ , represents a medium with same wettability for water and oil phases. With  $L/H > 1$ , the fibre media is favourably hydrophobic and  $L/H < 1$  the fibre media is favourably hydrophilic. For glass fibres media L/H is 0.89 and favourably water wetted. Therefore media with  $0.9 < L/H < 1.2$  had the highest separation efficiency and least increase in pressure drop during operation. A further study examined smaller fibre diameter PVDF-HFP mats with PP fibre mats had a water contact angle of  $156^\circ$ - $162^\circ$  submerged in diesel. These had a similar water separation efficiency but PVDF-HFP mat required a higher pressure difference compared to PP mat.

### **2.12.2 Effect of velocity on filtration**

Sherony and Kintner, Robelein and Blass, Secerov Sokolovic et al [112-114, 116] found that the degree of bed (fibrous filter) saturation decreases as the velocity is varied from 0.002 m/s to 0.014 m/s. Increasing superficial velocity decreases the amount of coalescence efficiency. Secerov Sokolovic et al [112] investigated the mean critical velocity in oil in water. 'Critical velocity' is defined the maximum value of the working velocity to be employed in the bed coalescer, and it is important for the design of the coalescer. The maximum critical velocity was obtained for the smallest oil content and biggest bed length. Vice versa for minimum critical velocity. Voyutskii et al [123] claims separation occurs only below a certain critical velocity and found that the fibre contact surface area is more important than pore size for coalescence. Sareen et al [115] suggested that surfactants reduces the interfacial tension and delays coalescence. The critical separation velocity decreased with increased oil viscosity, and reaches an upper limit at higher oil viscosities. Figure 2.23 shows the critical velocity ( $V^*$ ) for nylon fibre

radius on water droplet radius (R)[129]. The critical velocity decreases with increasing drop radius. Moreover, for a given drop, the thicker the fiber, the higher the critical velocity, where it was shown that the capillary force increases (linearly) with the fiber radius. Viswanadam and Chase [121] showed the higher face velocity results in higher pressure drop. The pore size, the drop size and the surface tension determines the pressure required to push the drop through pores. As pressure increases the smaller droplets will be pushed through and decrease the filter efficiency. Patel and Chase [101] measured the water–fuel IFT of ultra-low sulphur diesel is 22mN/m. A lower IFT of fluid is more difficult to separate and the separation efficiency becomes much more sensitive to fluid velocity. The distribution of the inlet droplets ranged from 0.5 $\mu$ m to 50 $\mu$ m with a mean drop size of 16 $\mu$ m, Figure 2.24 [101] shows the effect of different velocity on drop size separation efficiency in polypropylene to solvent concentration. Therefore 2% solvent on polypropylene fibre with 0.0003m/s or 2cm/min face velocity had the best performance.

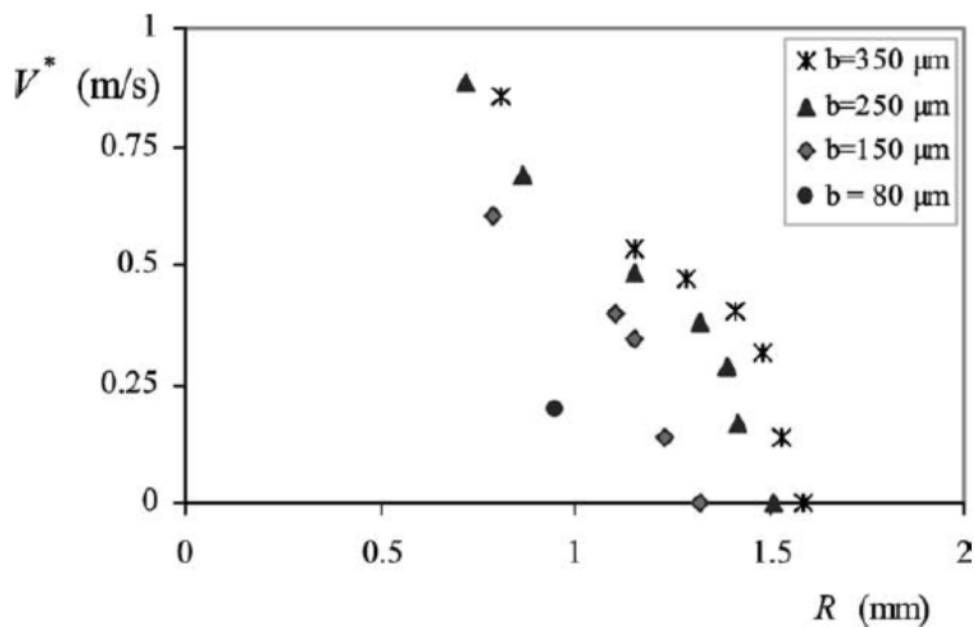


**Figure 2.23** shows the critical velocity ( $V^*$ ) for nylon fibre radius on water droplet radius (R)[129].

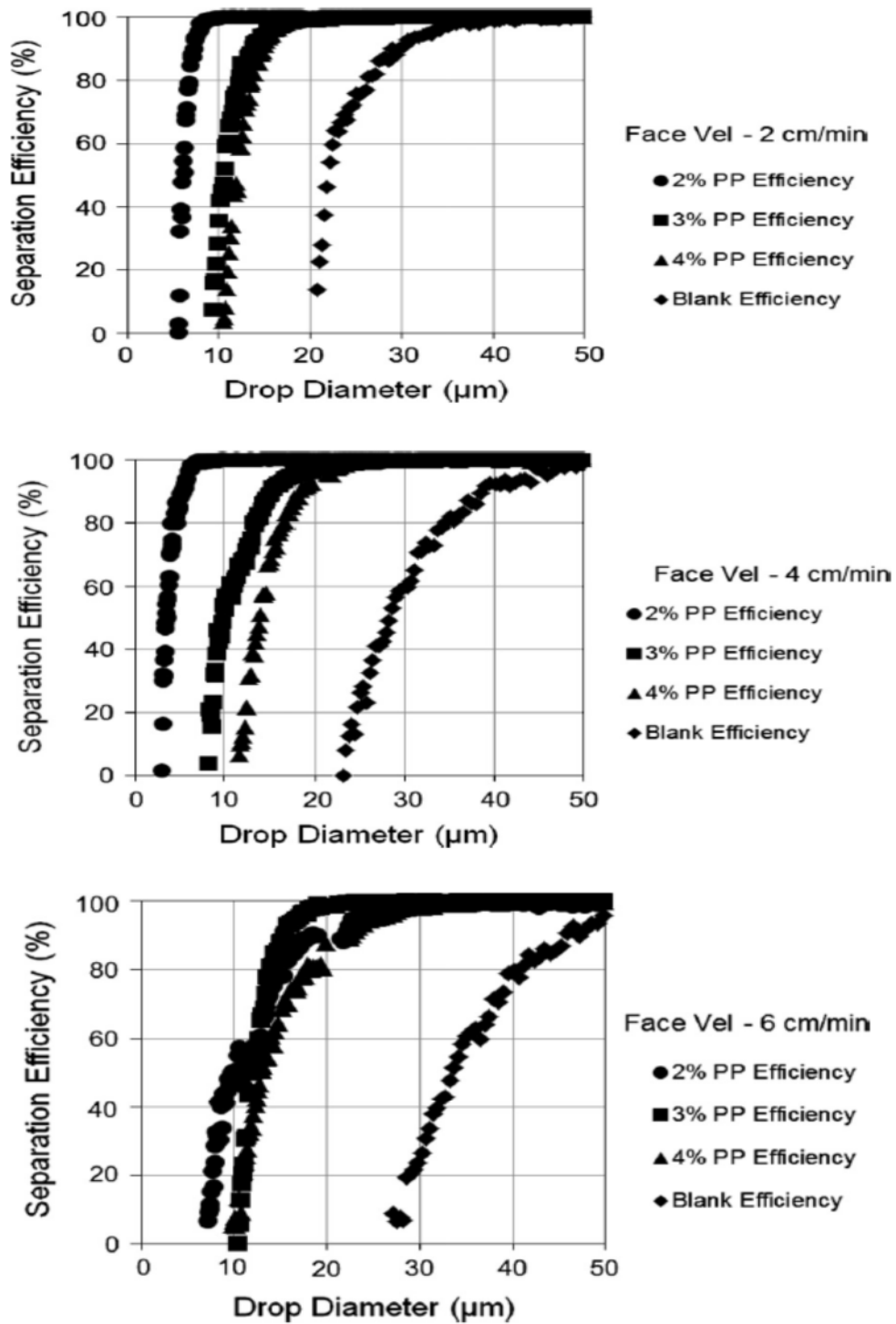


**Figure 2.24** shows the effect of different velocity on drop size separation efficiency in polypropylene to solvent concentration[101].

Separation efficiency is defined by  $E = \frac{C_{in} - C_{out}}{C_{in}}$ , where  $C_{in}$  and  $C_{out}$  are

the mass concentrations of water drops in the inlet and outlet flow streams.

### **2.12.3 Effect of fibre bed**

Sarreen et al [115] suggested that a longer residence time in a deeper bed gives better coalescence, but there is also a high pressure drop across the bed and this results in breakage of coalesced drops. Magiera and Blass [100] studied fibre bed depths of 5mm, 10mm and 30mm with a porosity of 0.95. Fibre bed depth of 10mm combined with 2 $\mu$ m of fibre diameter resulted in good coalescence efficiency. But for a fibre bed of depth of 30mm with a thicker fibre diameter of 12 $\mu$ m was required for better efficiency. High pressure drop across the fibre bed results in the coalesced drops to redisperse. Robelein and Blass [116] studied fibre medias with a porosity range of 0.818-0.984. Unarranged fibres of stainless steel with sizes from 5 $\mu$ m to 50 $\mu$ m were used with a constant value porosity. A fibre bed depth of 5mm is sufficient to coalesce droplets but depth more than 30mm should not be used due to pressure loss and gives no further rise in separation performance. Secerov Sokolovic et al [112] investigated polyurethane foams media, bed porosity in the range of 0.85-0.96 and respectively with a permeability of 4.60-48.3x10<sup>-9</sup> m<sup>2</sup>. Bed lengths of 7cm and 15cm had approximately equal efficiency due to the process of redispersion and repeated coalescence.

### **2.12.4 Summary of filtration & coalescence literature review**

Coalescence by flow through appropriate porous solids can give continuously high effective separation under a range of conditions. Micrometre or even smaller droplets can be coalesced into millimetre and larger droplets. These droplets can then be separated using gravitational force. The controlling parameters that affect the coalescence process are listed below:

- As pore size is decreased the coalescence performance increases, pore size can be decreased by reducing fibre size from micron to submicron or nanofibres. Nanofibres contain large surface area to volume ratios (large contact areas per unit volume) and smaller pores to increase the efficiency.
- Face velocity as it controls the capture mechanism of droplets on fibre. Lower face velocities have higher coalescence performance.

- Droplets size of dispersed phase, it is easier to coalesce larger mean droplet sizes.
- Interfacial tension. Emulsions with higher interfacial tension coalesce better than lower interfacial tension.
- Viscosity of continuous phase. Lower viscosity of continuous phase supports the coalescence process better than higher viscosity.
- Dirt and surfactants reduces the chance of coalescence of dispersed phase.

### 2.13 Fluid simulation methods

Fluid simulation is capable of predicting the dynamics of fluid problems. The computational method approximates the results to physical world[130]. Two numerical methods are ('traditional') computational fluid dynamics (CFD) and lattice Boltzmann methods (LBM). Conventional fluid simulations (CFD) includes finite difference, finite element, finite volume and spectral methods (these are called discrete methods). They normally start with nonlinear partial differential equation (Navier Stokes equation). These equations are discretised and numerically solved. This is called the top-down approach[131]. LBM has bottom-up approach, where it starts with a discrete microscopic model and yields to Navier stokes equations[132] by a multiscale analysis.

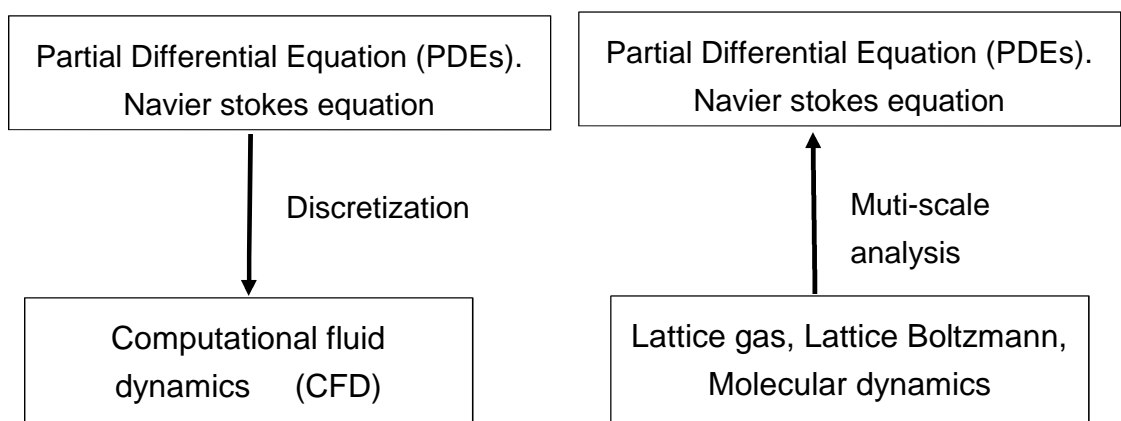


**Figure 2.25** Two different methods used to solve fluid dynamic problems (left hand side ) Top-Down approach and (right hand side ) Bottom- Up approach [131, 133].

### **2.13.1 Finite difference method (FDM)**

This is the oldest method used to acquire numerical solution of differential equation. This method is based on the properties of Taylor's expansion[134]. A Taylor's series expansion allows derivatives of variable to be written as difference between values of variable in different point in space or time[135]. FDM is simplest method to apply on uniform meshes, but the limitation of structured grid makes it hard to apply on complex geometry. The FDM is generally only used for specialist CFD problems and is not frequently used in commercial software[136].

### **2.13.2 Finite volume method (FVM)**

FVM has the most versatile discretization techniques used in CFD. This method is used mostly due to its conceptual simplicity and implementation on structured and unstructured grids[134]. The unstructured grid is useful for complex geometries[131]. The FVM is based on discretization of integral forms of conservation equations. The FVM is used in software applications such as ANSYS Fluent and OpenFOAM and is the most popular discretisation method as it conserves mass, energy and momentum at a cell level, which ensures that these same three quantities are also consistently conserved for any given control volume.

### **2.13.3 Finite element method (FEM)**

FEM was used in structural analysis initially, before finding use in fluid flow problems[134]. In this method, the fluid domain is divided into a finite sub-domain called 'elements'. The whole flow field is described through the summation of the variable in each element[135]. In FEM the partial differential equations are multiplied by a test function and integrated over a domain. This makes the solution weak compared to other methods[134]. Mostly formulations are based on linear variation of the variable in each element. But higher order variation like quadratic or cubic variation needs more points to describe them. This makes the computation more inefficient [135]. A big advantage of this method is the flexible grid implementation compared to other CFD methods. Comsol software uses FEM techniques and is used to analyse filter housing in the next chapter (chapter 3).

#### **2.13.4 Lattice Boltzmann method (LBM)**

Figure 2.25 represents the lattice Boltzmann method as a different approach to the conventional CFD method. LBM was derived from Lattice Gas Automata (LGA). LGA uses Boolean nature[134] and streams individual particles along lattice velocities[137]. LBM considers that the volume of fluid is made of a collection of particles, represented by particle distribution functions for each fluid component at each node of the domain. The macroscopic flow density is obtained by the integration of the distribution functions. LBM is used to simulate fluid flow and other complex systems. It successfully simulates multiphase and multicomponent fluid flow involving complex interfacial dynamics[134]. Magneto hydrodynamics, blood flow, filtration flow, viscoelastic flow, chemical reaction flow, turbulence and large eddy simulation and wave propagation are some applications simulated through Lattice Boltzmann method [131, 138]. This method is described in detail in chapter 4 and used in chapter 5 and 6.

### 2.13.5 Difference between Traditional CFD and LBM

**Table 2.5** difference in Traditional CFD vs LBM.

Comparison of Computational Fluid Dynamic method (CFD) vs Lattice Boltzmann Method (LBM)	
CFD	LBM
Based on the solution of second order differential equations (PDE). Navier-Stokes is a second order PDE	The LB equation is a special discretisation of the first order partial differential equations (PDE). Boltzmann's equation is a first order PDE.
Deals with the nonlinear convective term. $u \cdot \nabla u$	LBM this term become simple advection
Pressure is obtained using Poisson equation	Pressure is calculated from equation of state
Small scale simulations are difficult. check Figure 2.26	It is kinetic based and small scale details can be simulated
hard to apply on complex geometry	Easy to define complicate boundary geometries.
It does not scale so well for parallel execution	Local based method and therefore amenable to parallel execution
Multiphase flows require a complex physical models	Multiphase flows involve simple physical models

Figure 2.26 illustrates in microscopic level how all the fluids are assumed as a cluster of simple particles. The Knudsen number ( $Kn$ ) is the ratio of mean free path of molecules to characteristic length or hydraulic diameter of the duct. Specific case of flow between parallel plate separated by distance  $H$  would have characteristic length equal to twice of plate separation[139, 140].

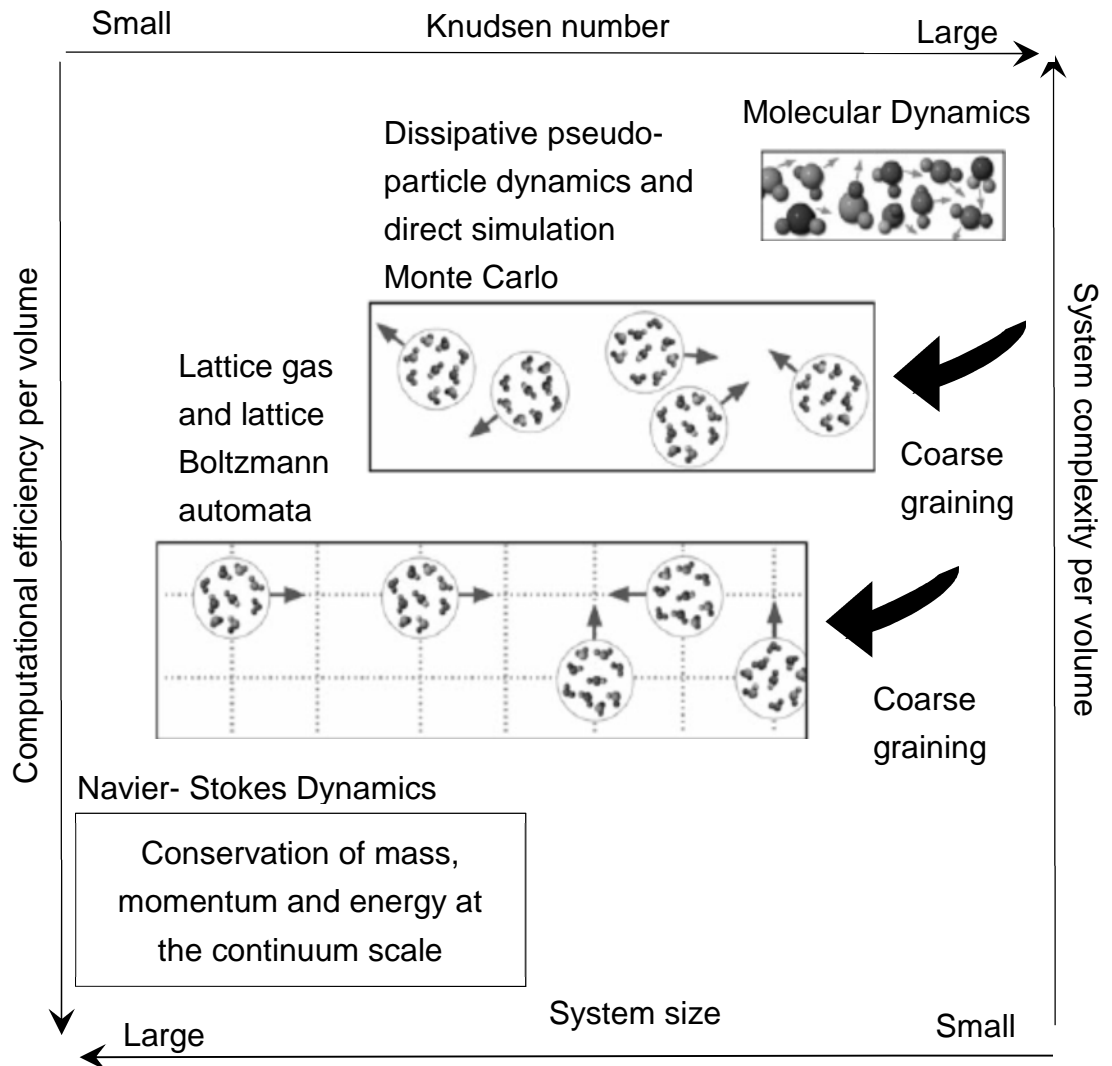


**Figure 2.26** Models used to solve fluid dynamic problems and their advantages in computation efficiency per volume, system complexity per volume, system size range and Knudsen number range[140].

### **2.13.6 Summary of flow modelling methods**

Traditional CFD methods are particularly difficult in simulating complex boundaries. These problems can be overcome by using LBM. A second advantage is the ease at which parallel programming algorithms can be implemented, less time required to simulate results compared to traditional CFD methods. It can successfully simulate multiphase and multicomponent fluid flow involving complex interfacial dynamics.

## **2.14 Chapter Summary**

This chapter has given an overview of filtration in general, and specifically the separation of a dispersed liquid phase with a continuous liquid phase. Some of the additional physics around wetting are reviewed. There is a gap in knowledge around the fundamental dynamics of droplets during filtration. A brief review of numerical methods has been carried out. From this study there is an opportunity to investigate droplet dynamics using a twin approach- (i) the flow within a filter housing using conventional CFD and (ii) the dynamics of coalescence using lattice Boltzmann method. Chapter 3 examines flow within the filter housing using conventional CFD. Chapter 4 introduces the lattice Boltzmann method in detail, chapter 5 and 6 presents a validation and results from the lattice Boltzmann method respectively, and finally chapter 7 concludes and presents the future work.

## Chapter 3 Filter cartridge optimisation

### 3.1 Introduction of filter cartridge optimisation

The commercial diesel filter and housing (Dmax filter, Parker Hannifin ) was modelled through the use of computational fluid mechanics to identify the opportunity for reducing the free space inside the filter and to the side of the filter. A focus of this work is the gravity separation of the droplets. The CFD package used was Comsol and this section consist of comsol methodology (governing equations), analysing method and results. The approach of using CFD to model the flow is to capture the pathways that droplets follow, not the actual process of coalescence itself. The filter itself consists of a depth filtration media and as coalescence occurs droplets leave the downstream face with (ideally) a size greater than entering. To analyse the flow, a coupled simulation is made of the fluid flow in the open areas (using the Navier-Stokes equation) and the porous media zones using Darcy's equation to determine the flow paths, see Figure 3.1. Particle tracking is then used to visualise the motion of particles from the downstream face of the filter.

### 3.2 Comsol methodology (governing equations)

For flow, where  $\rho$  is density of the liquid ( $\text{kg/m}^3$ ),  $\rho$  can be considered constant for liquid under isothermal conditions. For constant  $\rho$ , the mass flow continuity is given by:

$$\nabla \cdot \mathbf{u} = 0 \quad \text{Equation 3.1}$$

For steady flow, the general momentum (or Navier-Stokes) equation is

$$\rho \frac{\partial \mathbf{u}}{\partial t} + \rho(\mathbf{u} \cdot \nabla)\mathbf{u} = \nabla \cdot \left[ -p\mathbf{I} + \mu \left( \nabla \mathbf{u} + (\nabla \mathbf{u})^T \right) \right] + \mathbf{F} \quad \text{Equation 3.2}$$

Where  $\mathbf{u}$  is the velocity vector ( $\text{ms}^{-1}$ ),  $p$  is the pressure (Pa),  $\mathbf{F}$  is the volume force vector (the body force, ie due to gravity) ( $\text{Nm}^{-3}$ ),  $\mathbf{I}$  is the identity tensor and  $\mu$  is dynamic viscosity of fluid (Pa.s)[141].

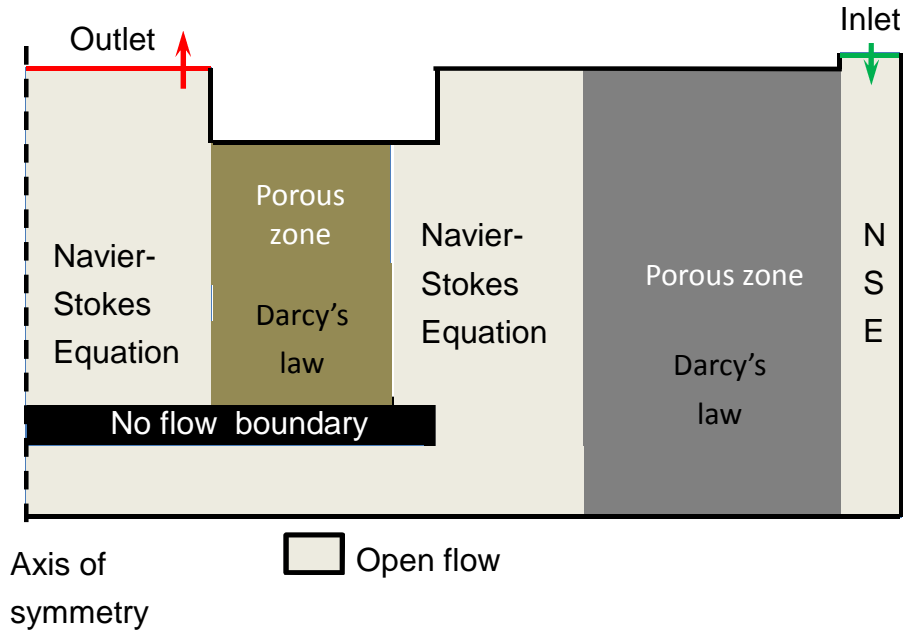


**Figure 3.1** Filter geometry with inlet, outlet and boundary condition. Also the equations solved in the free space (open flow) and porous media are shown.

Flow in the porous media part of the domain is governed by Darcy's law:

$$u = \frac{-k}{\mu L} \nabla p \quad \text{Equation 3.3}$$

Where  $k$  is permeability ( $m^2$ ) and  $L$  is the thickness of filter cake.

### 3.2.1 Boundary condition

Figure 3.1 shows a general schematics of the filter and the boundary condition used to simulate. All the boundary conditions for the Navier-Stokes equations and Darcy's law are by:

$$u = -u_0 \cdot n \quad \text{Inlet} \quad \text{Equation 3.4}$$

Where  $n$  represents the vector normal to boundary and  $u_0$  is the inlet speed.

$$\mu(\nabla u + (\nabla u)^T) \cdot n = 0 \quad p = p_o \quad \text{outlet} \quad \text{Equation 3.5}$$

$p_o$  is the pressure value (Pa) inserted at a reference point or atmospheric pressure.

$$u = 0 \quad \text{no slip/wall} \quad \text{Equation 3.6}$$

The no flow boundary is actually modelled using Darcy's law (Equation 3.3) but with very low permeability of  $1 \times 10^{-19}$  [m<sup>2</sup>].

At the boundaries (denoted by  $\Gamma$ ) between the porous media (Darcy's law) regions and open flow (Navier-Stokes) regions, the following continuity condition applies[142, 143]:

Continuity of the normal velocities:

$$\mathbf{u}_{NS} \cdot \mathbf{n} = \mathbf{u}_{darcy} \cdot \mathbf{n} \text{ on } \Gamma \quad \text{Equation 3.7}$$

And  $\mathbf{u}_{NS}$  is the Navier-Stokes equation velocity and  $\mathbf{u}_{darcy}$  is the Darcy's law velocity.

Continuity of the normal stresses:

$$-\mathbf{n} \cdot \left( \mu (\nabla \mathbf{u}_{NS} + (\nabla \mathbf{u}_{NS})^T) - p_{NS} \mathbf{I} \right) \cdot \mathbf{n} = p_{darcy} \text{ on } \Gamma \quad \text{Equation 3.8}$$

Where  $p_{NS}$  is the Navier-Stokes equation pressure and  $p_{darcy}$  is the Darcy's law pressure.

Condition of Beavers-Joseph-Staffman (BJS):

$$-\frac{\mathbf{n} \cdot \left( \mu (\nabla \mathbf{u}_{NS} + (\nabla \mathbf{u}_{NS})^T) - p_{NS} \mathbf{I} \right) \cdot \boldsymbol{\tau}}{\rho} = \frac{\nu \alpha}{\sqrt{k}} \mathbf{u}_{NS} \cdot \boldsymbol{\tau} \text{ on } \Gamma \quad \text{Equation 3.9}$$

Also  $\nu$  is the kinematic viscosity,  $\alpha$  is a dimensionless experimental parameter and  $\boldsymbol{\tau}$  is the unit vector tangential to  $\Gamma$ .

Particle tracking is time dependent and based on the fluid flow solution. The particle momentum comes from Newton's second law:

$$\frac{d \left( \begin{matrix} m_p \\ \mathbf{p} \end{matrix} \mathbf{v} \right)}{dt} = \mathbf{F}_D + \mathbf{F}_g \quad \text{Equation 3.10}$$

Where  $m_p$  denotes the particle mass (kg),  $\mathbf{v}$  is the velocity of particle (ms<sup>-1</sup>),  $\mathbf{F}_D$  is the drag force (N) and  $\mathbf{F}_g$  is the gravitational body force (N).

Drag force is shown in Equation 3.11. and particle velocity response time is shown in Equation 3.12.

$$F_D = \frac{m_p (u - v)}{\tau_p} \quad \text{Equation 3.11}$$

$$\tau_p = \frac{\rho_p d_p^2}{18\mu} \quad \text{Equation 3.12}$$

Where  $F_D$  is the drag force(N),  $u$  is the local fluid velocity ( $\text{ms}^{-1}$ ) obtained from the steady solution of Equations 3.1 and 3.2,  $\tau_p$  is the particle velocity response time(s),  $d_p$  is the particle diameter (m) and  $\rho_p$  is the particle density ( $\text{kgm}^{-3}$ ).

The gravitational body force is shown in Equation 3.13. where  $F_g$  is the gravitational force(N) and  $g$  is gravitational acceleration ( $\text{ms}^{-2}$ ).

$$F_g = \frac{m_p g (\rho_p - \rho)}{\rho_p} \quad \text{Equation 3.13}$$

### 3.3 Problem setup

In the CFD package, the two dimensional axisymmetric fuel filter was created according to dimensions shown in Figure 3.2 (B). And these dimensions were measured from the commercial Dmax filter from Parker Hannifin. Also Figure 3.2 (A) shows the inlet, outlet, flow direction and material used in the filter. The flow domains were identified as either free (laminar) or porous zones within the simulation, and particle tracking (with gravitational force and drag force) was added in the region between inlet and the blue dotted lines (where non-woven material, inlet free space width(L1) and free fall region(L2) and shown in Figure 3.2 (A). In practice the non-woven material would coalesce the water particles, but coalescence of water particle cannot be modelled in comsol due to complexity of the problem. The coalescence of water droplets are modelled through using the Lattice Boltzmann method in subsequent chapters. Instead hypothetical droplets of a range of sizes are considered, as a result of the coalescence process. The particle tracking for the fluid flow was used to track water droplets in the region shown in Figure 3.2 (C). Inlet and outlet of particle tracking region are shown in Figure 3.2 (C). The parameters used are listed in the Table 3.1.

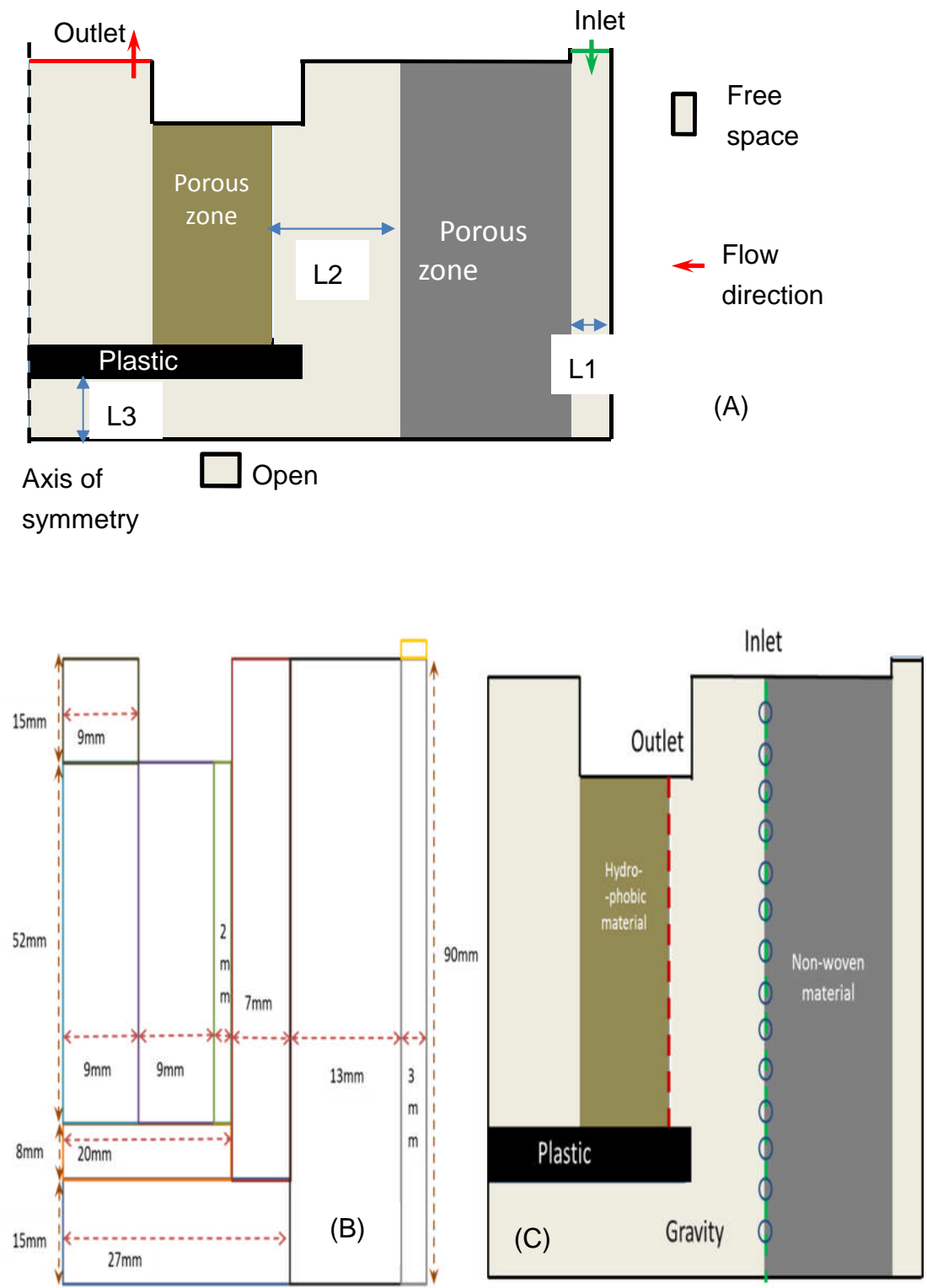


**Figure 3.2** (A) shows the two dimensional axisymmetric fuel filters inlet, outlet and material properties, (B) represents the 2D axisymmetric fuel filter dimension from Dmax filter and (C) Particle tracking inlet and outlet with gravitational force.

**Table 3.1** the parameters and their values used in the Comsol simulation.

<b>Parameters</b>	<b>value</b>
Diesel Density	845 [kg/m <sup>3</sup> ]
Diesel Dynamic viscosity	6×10 <sup>-3</sup> [Pa.s]
Non-Woven porosity	0.85
Non-Woven permeability	1×10 <sup>-9</sup> [m <sup>2</sup> ]
Inlet velocity	2.192 [m/s]
Water Density	1000 [kg/m <sup>3</sup> ]
Plastic porosity & permeability	0.02 , 1×10 <sup>-19</sup> [m <sup>2</sup> ]
Hydrophobic material porosity & permeability	0.7 , 1×10 <sup>-10</sup> [m <sup>2</sup> ]
Gravitational acceleration	9.81 [m/s <sup>2</sup> ]

The free and porous flow is a steady state problem. This flow field is used throughout to allow particle tracking which is time dependent. Initially the water droplet sizes were varied within the particle tracking method (the original filter dimensions were fixed) to check the range of droplet sizes that would free fall in gravity within the geometric region. Geometrical changes like inlet thickness (L1), free space thickness (L2) and free space height (L3) were then varied. Variations in filter geometry are shown in Figure 3.2 (A)& (B) respectively and there parameters varied are shown in Table 3.2.

**Table 3.2** L1, L2 and L3 parameter variation for Comsol simulations.

Variable under study	Other parameters				
	L1	L2	L3	Droplet size	Inlet flow velocity
Droplet size	3mm	7mm	15mm	1 $\mu$ m-1cm	2.192ms <sup>-1</sup>
L1	2mm-30mm	7mm	15mm	1mm	Flow velocity scaled to give a flow rate of 3.7litres/min-equivalent to 2.19ms <sup>-1</sup> for other studies.
L2	3mm	3mm-30mm	15mm	1mm	2.192ms <sup>-1</sup>
L3	3mm	7mm	5mm-30mm	1mm	2.192ms <sup>-1</sup>

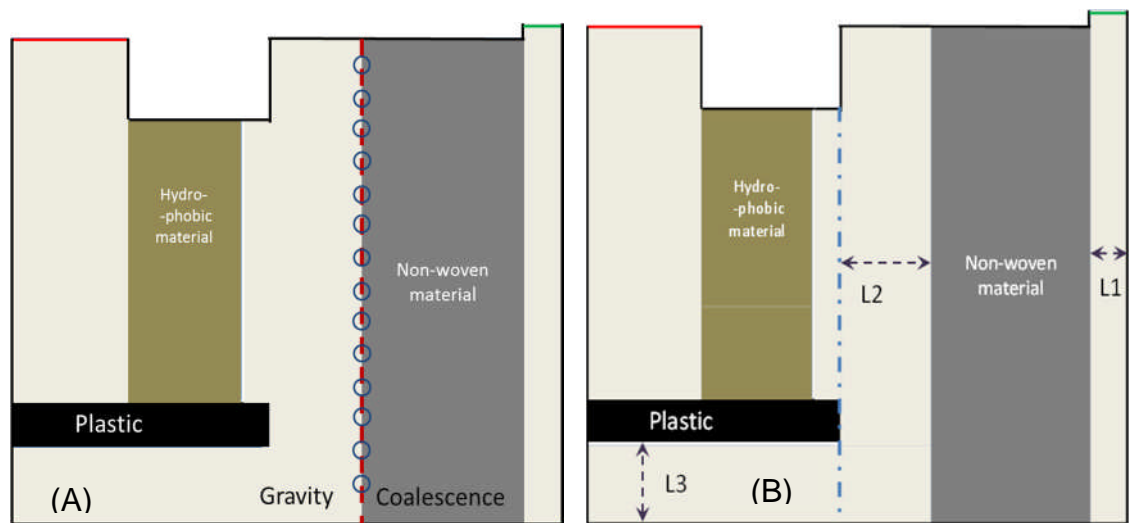


**Figure 3.2** (A) represents the variation of droplet size and (B) represents the inlet thickness (L1), free space thickness (L2) and free space height (L3) were varied.

### 3.4 Analysis method

#### 3.4.1 The flow field

Figure 3.3 shows the velocity magnitude and velocity field in 2D axisymmetric fuel filter. The Inlet velocity is 2.19 m/s, in the L1 region velocity field and decreases towards the bottom of the filter. The velocity field remains the same throughout the non-woven material section but comparatively less than the inlet velocity due to the increase in area. The velocity is largely constant due to the relative high resistance of the material. In the L2 region the velocity is higher near edges of the filter housing, then hydrophobic material had similar velocity field behaviour as non-woven material, finally the velocity field was higher at the outlet boundary region due to conservation of mass .

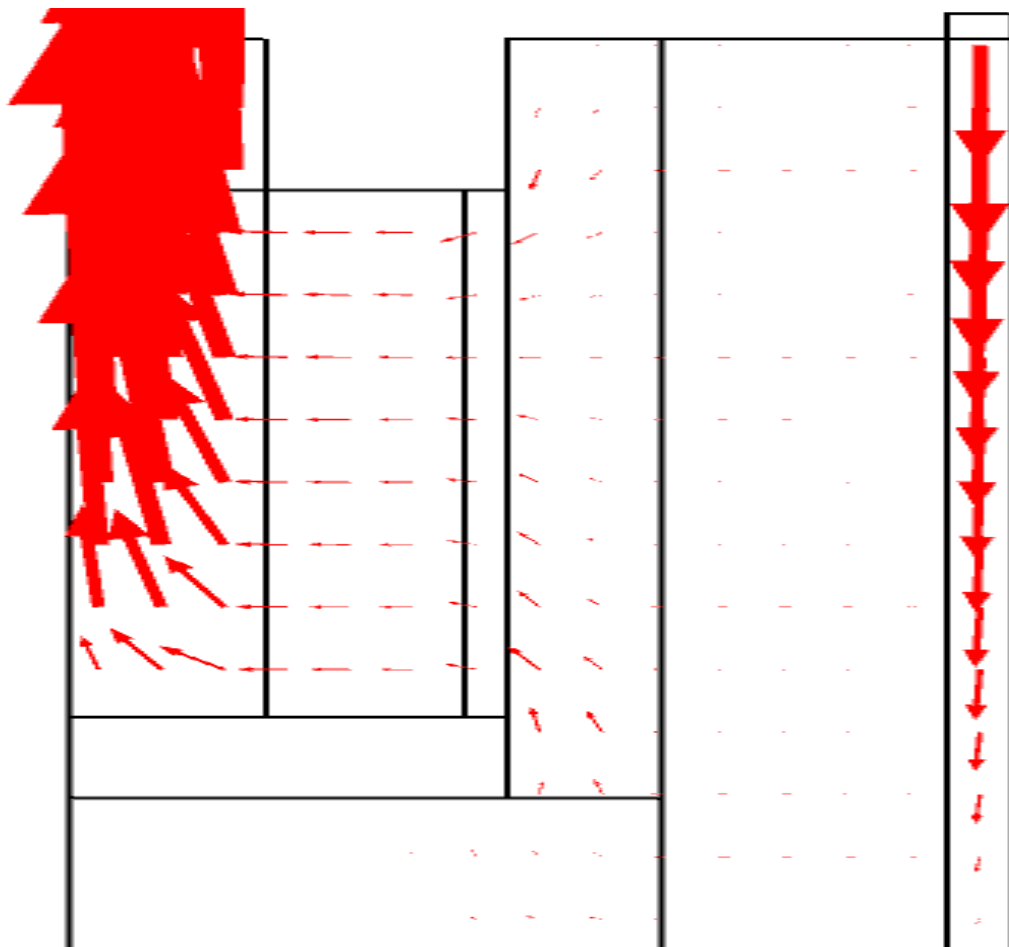


**Figure 3.3** velocity field in 2D axisymmetric fuel filter.

### 3.4.1 particle tracking

Figure 3.4 (A) represents the comsol simulation results with the water particle tracking of the flow and (B) is the analysing method for these simulations. To quantify the performance of the filter media from the comsol results, a parameter defined as the cut-off line was used. The cut-off line (red dotted lines in (B)) defines the height in the filter below which the water particles free fall to the base of the filter and above which follow the flow. Above cut-off line water droplet are swept out with flow which means separation is required at the hydrophobic filter and below this line the water droplets settles under gravity. The latter is preferable. In each of the simulations, droplets are released from the outlet of the coalescing filter, along the line shown in green in Figure 3.4 (A). Droplet settling below the plastic material is shown by a blue line in Figure 3.4 (C).

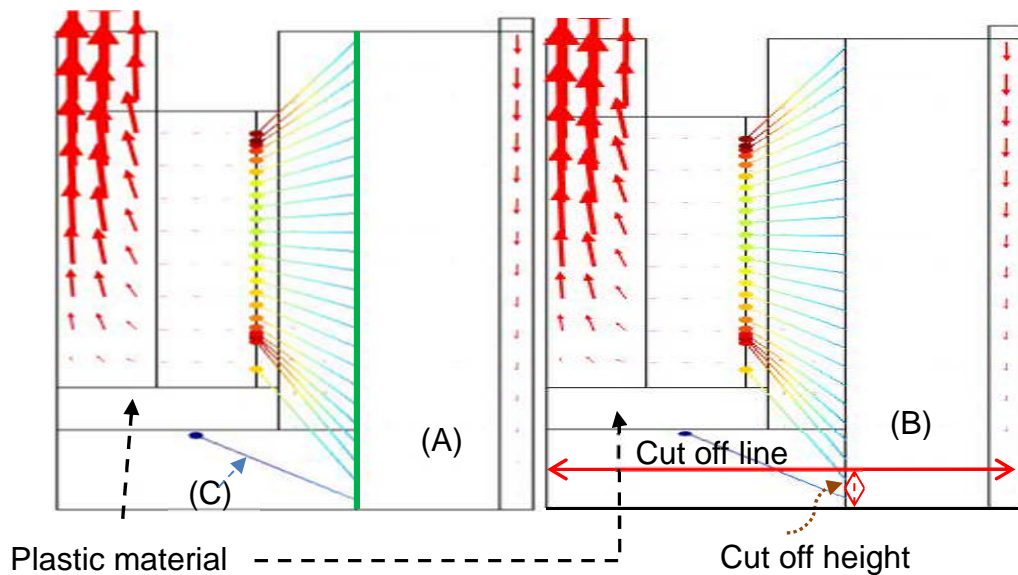


**Figure 3.4** represents shows the results of a comsol simulation, (A) shows the flow of the diesel (red arrows). (B) Is the analysing method for these simulations and (C) shows the water droplet settling below the plastic material.

### 3.5 Comsol results

The parameters are varied according to the titles (Table 3.2) in the following subsections, and a single discussion is included.

#### 3.5.1 Effect on water droplet diameter in original filter cartridge geometry

The effect of the droplet size, with all other parameters kept constant (as shown in Table 3.2) is considered. The cut off height is shown in the graph.

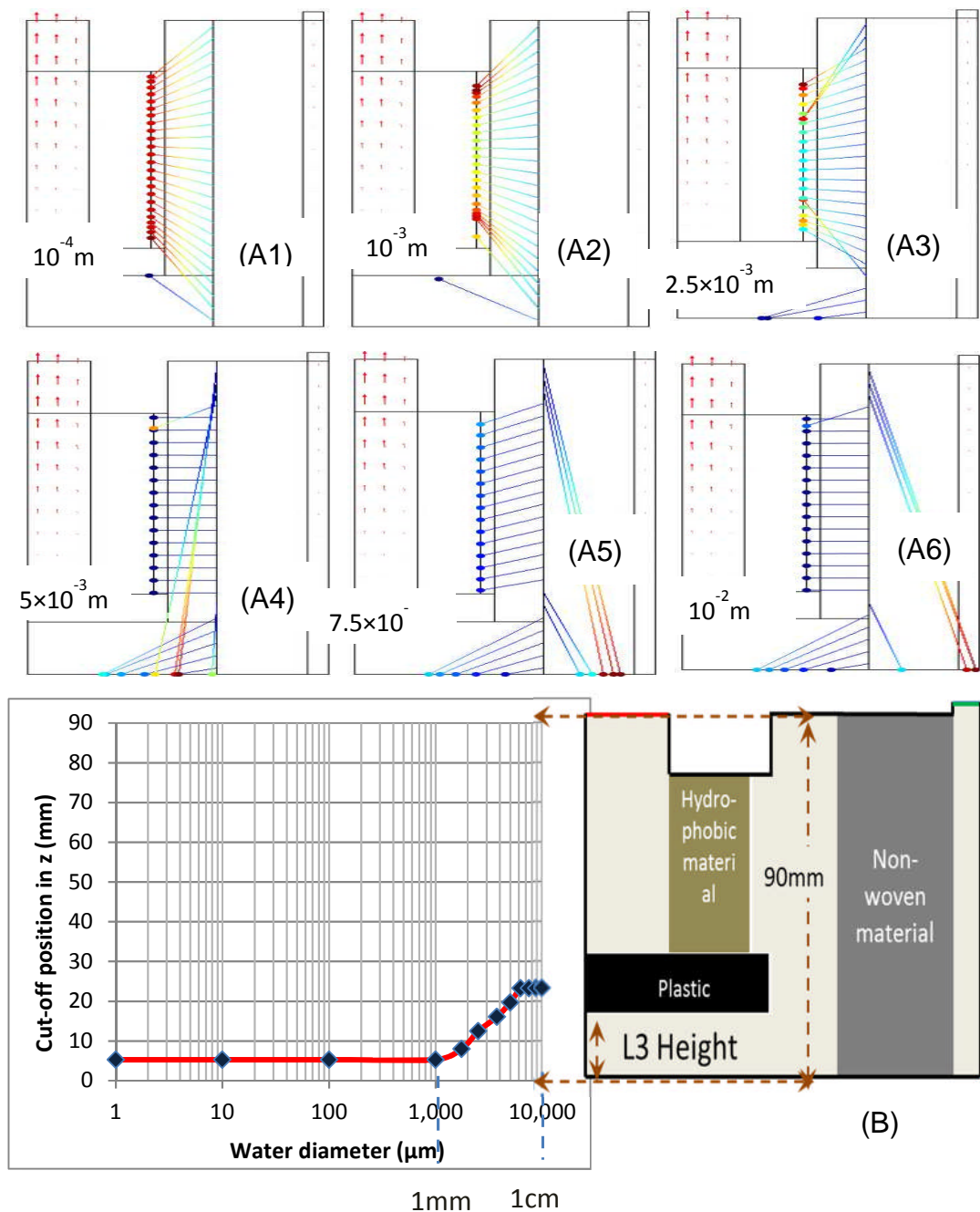


**Figure 3.5** (A 1-6) represents the Comsol simulation results and (B) analysed results for the water particle sizes variation.

### 3.5.2 Changing the inlet annulus

Effect of the width of inlet is varied, with all other parameters kept constant as shown in Table 3.2. This is to analyse whether the inlet can cause mal-distribution of the flow, which in turn affects the droplet movement.

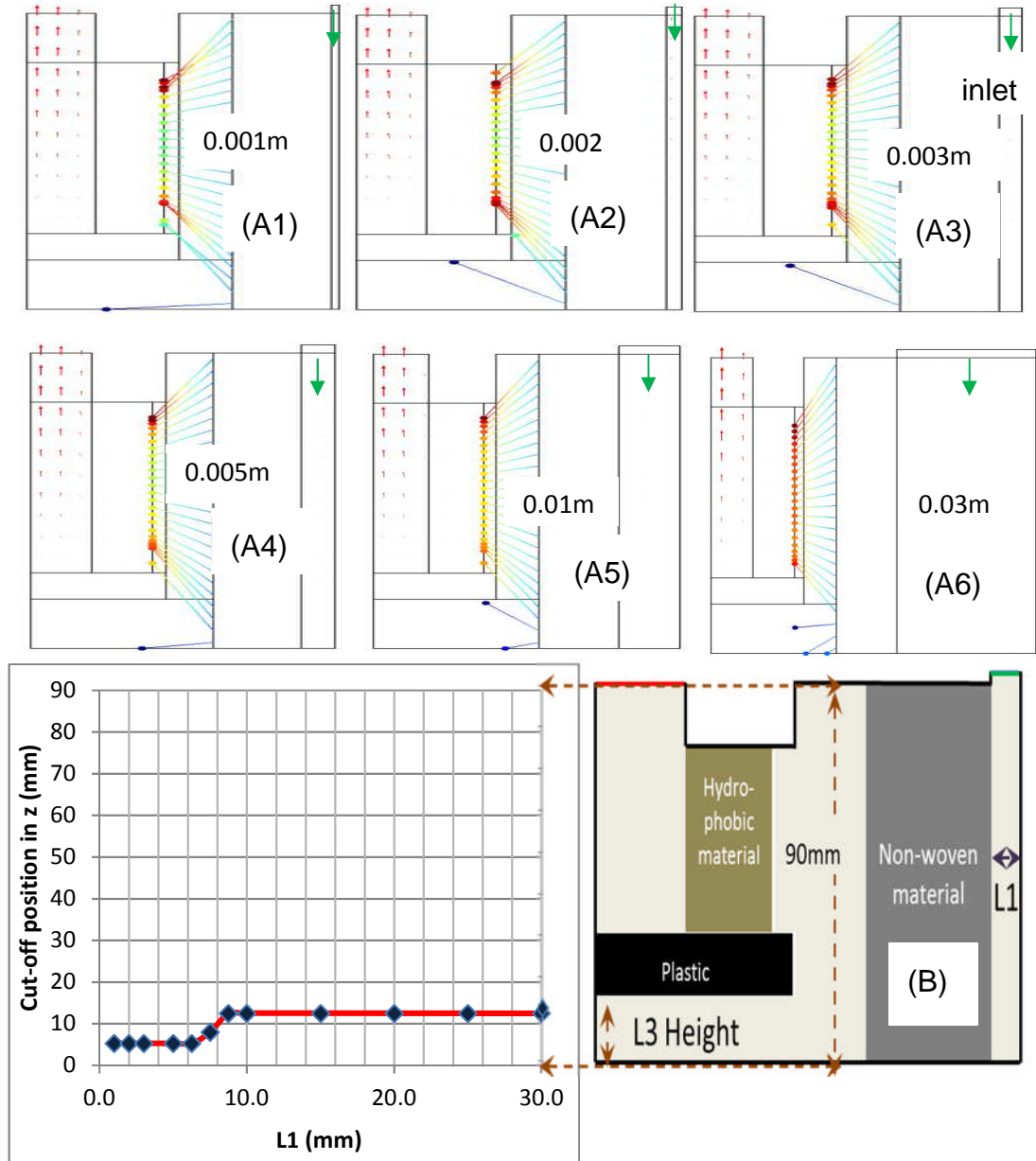


**Figure 3.6** (A 1-6) represents the Cmsol simulation results and (B) analysed results for L1 or inlet thickness variation..

### 3.5.3 Effect of L2 change in the filter cartridge

L2 is the width of the annulus downstream of the coalescing filter. The flow, after passing through the coalescing filter then allows separation of droplets by gravity in this region. Effect of the L2 is varied, with all other parameters kept constant as shown in Table 3.2.

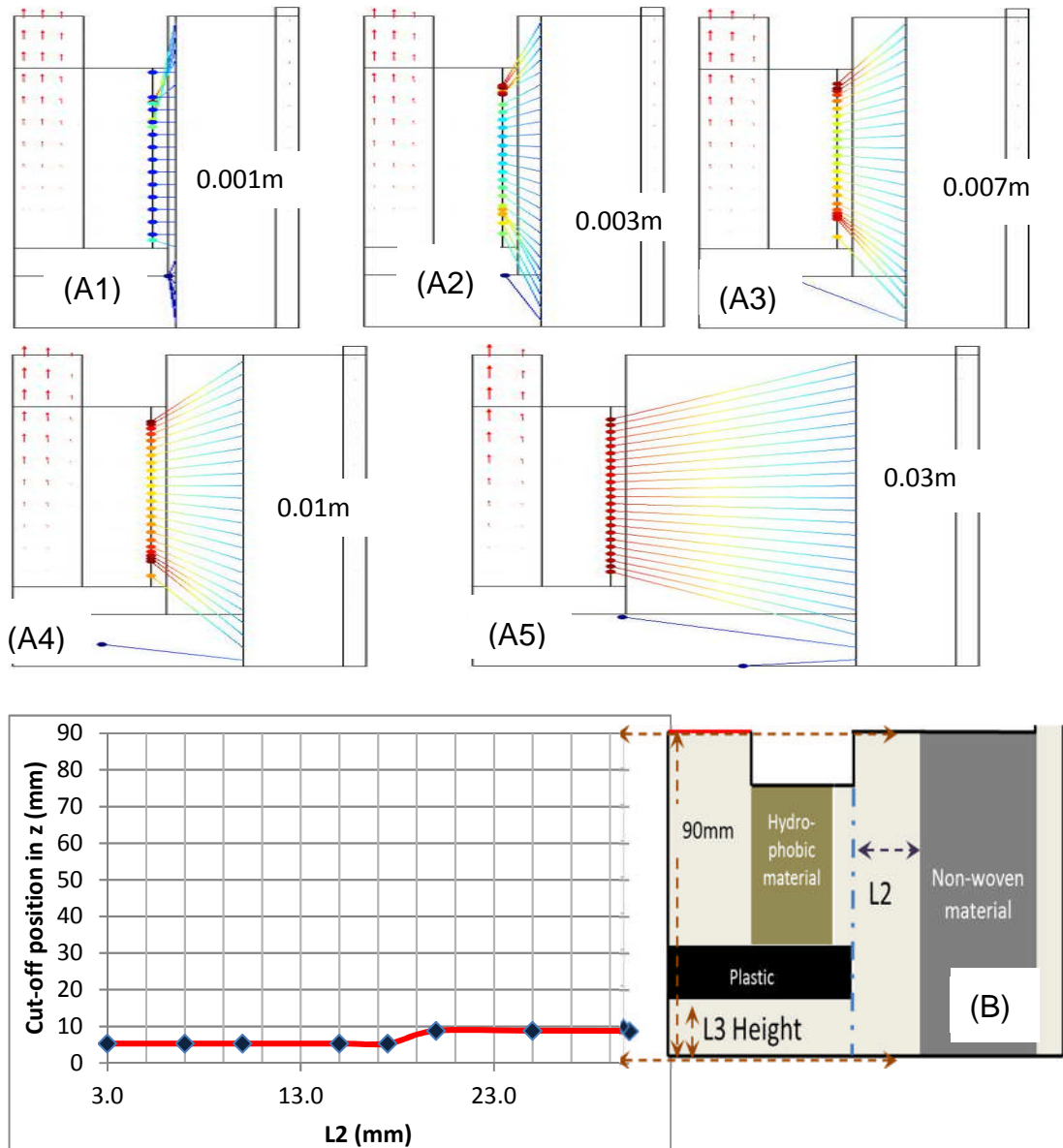


**Figure 3.7** (A1-5) represents the Comsol simulation results and (B) analysed results for L2 or free space thickness variation.

### 3.5.4 Effect of L3 change in the filter cartridge

L3 is the distance under the filter element. Effect of the L3 is varied, with all other parameters kept constant as shown in Table 3.2.

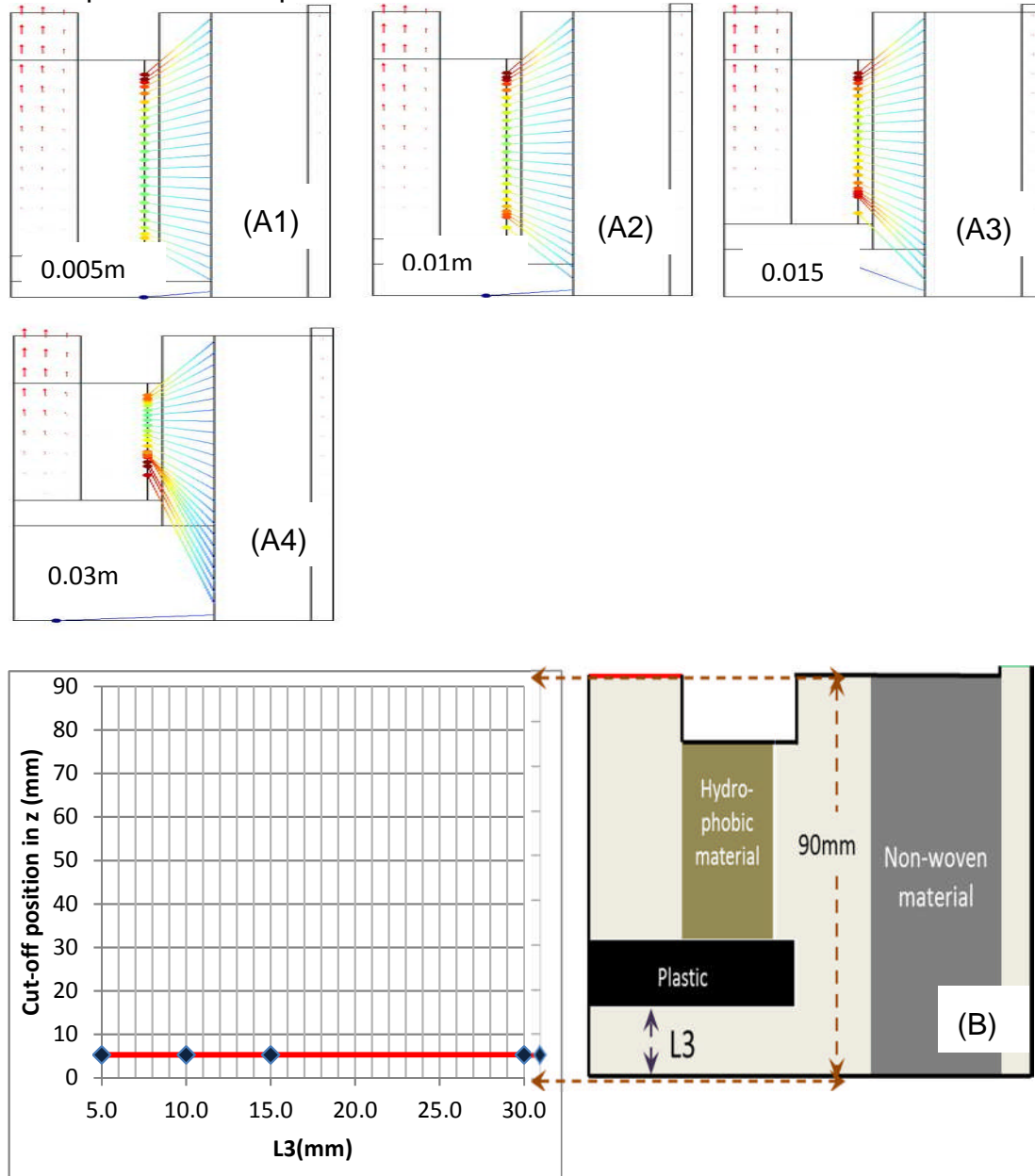


**Figure 3.8** (A 1-4) represents the Cofsol simulation results and (B) analysed results for L3 or free space height variation.

### **3.6 Discussion**

Figure 3.5 (A1-6) represents the Comsol simulation results and (b) analysed results for the water particle sizes variation. It is noticeable that in L3 height region the particle greater than 1mm would settle down the filter and particle sizes less than 1mm would flow through in the original filter dimension. A maximum cut of height of 25 mm in a 90mm filter was observed. Therefore it demonstrates the importance of the hydrophobic filter in the downstream. A droplet of 1 mm diameter was chosen for the rest of the simulations, as this is likely to be representative of a coalesced droplet size.

Figure 3.6 (A) represents the Comsol simulation results and (B) analysed results for L1 or inlet thickness variation. This also changes the inlet velocity, but the flow rate was remained constant as 3.7litres/min. Cut-off position has increased by 8% at 8.75mm of L1. This shows that increasing L1 has small effect on cut-off position.

Figure 3.7 (A) represents the comsol simulation results and (B) analysed results for L2 or free space thickness variation. At 20mm of L2, the cut-off position has increased by 3.9%.This suggest that increasing L2 has small effect on cut-off position.

Figure 3.8 (A) represents the comsol simulation results and (B) analysed results for L3 or free space height variation. This shows that cut-off line position has a fixed value for different L3. Changing L3 has no effects on Cut-off position. Therefore water particle would follow the diesel fluid direction.

### **3.6 Summary**

Droplet sizes below 1mm are commonly encountered within water in diesel mixtures. This brief study demonstrates that whilst small performance gains can be made through changing filter housing geometries, by far the most important part of the filter that can affect performance is the coalescence media. Understanding the performance of small droplets within the coalescing media cannot be studied using Comsol as it is challenging to study wetting processes. Computational fluid dynamic software is difficult to adopt for studying processes where wetting and contact angle dynamics

dominates the flow behaviour, as in droplet dominated processes. Therefore the next chapter looks into Lattice Boltzmann method, to understand the droplet coalescence behaviour.

A further observation from this work is the importance of the downstream hydrophobic filter. This is generally a woven filter (similar to a fine mesh) which does not allow water droplets through. The separation of these larger droplets, when compared to the coalescence of the finer droplets is a much easier process – so whilst this is interesting in its own right, the coalescing pack is the focus for the remainder of this thesis.

## **Chapter 4**

### **Lattice Boltzmann Method**

#### **4. Introduction**

Chapter 3 introduced numerical simulations of a coalescence filter in which the filter medium itself was represented as a continuous porous medium. Although this allowed a general picture of the flow through the system, it included no detail of the actual coalescence process, which takes place at the pore scale. Modelling coalescence filtration at the pore scale involves a number of challenges, such as two-phase flow with the tracking associated problem of interfaces, coalescence and break up of liquid, dynamic wetting (moving contact lines) and complex geometry. As briefly introduced in Section 2.13, molecular dynamics, conventional or traditional CFD and lattice Boltzmann method have been used to model multiphase flow. Molecular dynamics is a microscopic techniques and suitable for capturing the microscopic interactions of the interface, but they are generally limited in space and time scales and hence not suitable for simulating the flow in a coalescence filter. Conventional CFD, is able to handle macroscopic phenomena, and is useful for capturing the bulk flow (as seen in the last chapter). However, CFD becomes more difficult with topologically complex domain, and flows involving moving contact lines. The lattice Boltzmann method (LBM) has become a popular numerical technique for simulating many types of complex flows. The LBM, due to its kinetic nature, is termed a 'mesoscopic' method. It can incorporate many advantages of microscopic techniques while still efficiently simulating larger scale dynamics. This nature has made the LBM a useful tool for simulating multiphase multicomponent flows. Multiphase modelling in LBM is discussed in section 4.6. The method is easy to implement, and is able to simulate different multiphase problems, such as the droplet formation [144], breakup of a droplet in a wind tunnel, micro-droplet formation in the T-shape channel [145], thermal multiphase

flow such as boiling processes, wetting on solid surfaces, interfacial slip and capillary filling.

## 4.1 Lattice Boltzmann Method (LBM)

### 4.1.1 Discretization of the Boltzmann Equation

He & Luo [138] showed that the Lattice Boltzmann Equation (LBE) can be obtained from the continuum Boltzmann equation for discrete velocities by using a low Mach number expansion. Initially the Boltzmann equation has a collision integral and is hard to solve even in a simple system. Bhatnagar-Gross-Krook (BGK) in 1954 replaced the collision term in Boltzmann equation by a single-relaxation-time, giving the Boltzmann BGK equation[138]:

$$\frac{\partial f}{\partial t} + \xi \cdot \nabla f = -\frac{1}{\lambda} \left( f - f^{eq} \right) \quad \text{Equation 4.1}$$

where the single-particle distribution function is  $f \equiv f(\mathbf{x}, \xi, t)$ , microscopic velocity is  $\xi$ , relaxation time due to collision is  $\lambda$  and  $f^{eq}$  is the Maxwell-Boltzmann distribution function:

$$f^{eq} \equiv \frac{\rho}{(2\pi RT)^{D/2}} \exp\left(-\frac{(\xi - u)^2}{2RT}\right) \quad \text{Equation 4.2}$$

Here  $D$  is the dimension of space,  $R$  is the ideal gas constant, the macroscopic density of mass, velocity and temperature respectively as  $\rho$ ,  $u$  and  $T$ .  $RT = c_s^2$ , where  $c_s$  is the (pseudo)speed of sound. The macroscopic variables of  $\rho$ ,  $u$  and  $T$  are the moments of the distribution function  $f^{eq}$ .

$$\rho = \int f d\xi = \int f^{eq} d\xi \quad \text{Equation 4.3}$$

$$\rho u = \int \xi f d\xi = \int \xi f^{eq} d\xi \quad \text{Equation 4.4}$$

$$\rho \varepsilon = \frac{1}{2} \int (\xi - u)^2 f d\xi = \frac{1}{2} \int (\xi - u)^2 f^{eq} d\xi \quad \text{Equation 4.5}$$

Where the energy is  $\varepsilon = \frac{D_o}{2} RT$ .  $D_o$  is the number of degrees of freedom of a particle.

#### 4.1.2 Hydrodynamic Moments

Hydrodynamic moments of Equation 4.3- 4.5 can be approximated by quadrature up to a certain degree of accuracy,

$$\int \psi(\xi) f^{\text{eq}}(x, \xi, t) d\xi = \sum_{\alpha} W_{\alpha} \int \psi(\xi_{\alpha}) f^{\text{eq}}(x, \xi_{\alpha}, t) d\xi \quad \text{Equation 4.6}$$

Where  $\psi(\xi)$  is a polynomial of  $\xi$ ,  $W_{\alpha}$  is the weight coefficient of the quadrature and  $\xi_{\alpha}$  is the discrete velocity set of the quadrature. Hydrodynamic moments of Equation 4.3- 4.5 are,

$$\rho = \sum_{\alpha} f_{\alpha} = \sum_{\alpha} f_{\alpha}^{\text{eq}} \quad \text{Equation 4.7}$$

$$\rho u = \sum_{\alpha} \xi_{\alpha} f_{\alpha} = \sum_{\alpha} \xi_{\alpha} f_{\alpha}^{\text{eq}} \quad \text{Equation 4.8}$$

$$\rho \varepsilon = \frac{1}{2} \sum_{\alpha} (\xi_{\alpha} - u)^2 f_{\alpha} = \frac{1}{2} \sum_{\alpha} (\xi_{\alpha} - u)^2 f_{\alpha}^{\text{eq}} \quad \text{Equation 4.9}$$

Where

$$f_{\alpha} \equiv f_{\alpha}(x, t) \equiv W_{\alpha} f(x, \xi_{\alpha}, t) \quad \text{Equation 4.10}$$

$$f_{\alpha}^{\text{eq}} \equiv f_{\alpha}^{\text{eq}}(x, t) \equiv W_{\alpha} f^{\text{eq}}(x, \xi_{\alpha}, t) \quad \text{Equation 4.11}$$

$f_{\alpha}$  or  $f_{\alpha}^{\text{eq}}$  has the unit of  $f d\xi$  or  $f^{\text{eq}} d\xi$ . The Maxwell-Boltzmann distribution function (Equation 4.2) may be written as

$$f^{\text{eq}} = \frac{\rho}{(2\pi RT)^{D/2}} \exp\left(-\frac{(\xi)^2}{2RT}\right) \exp\left(\frac{(\xi \cdot u)}{RT} - \frac{(u \cdot u)}{2RT}\right), \quad \text{Equation 4.12}$$

and a small velocity expansion about  $u=0$  gives,

$$f^{\text{eq}} = \frac{\rho}{(2\pi RT)^{D/2}} \exp\left(-\frac{(\xi)^2}{2RT}\right) \times \left(1 + \frac{(\xi \cdot u)}{RT} + \frac{(\xi \cdot u)^2}{2(RT)^2} - \frac{(u \cdot u)}{2RT}\right) \quad \text{Equation 4.13}$$

Calculating the hydrodynamic moments of  $f^{eq}$  is equivalent to,

$$I = \int \psi(\xi) f^{eq} d\xi = \frac{\rho}{(2\pi RT)^{D/2}} \int \psi(\xi) \exp\left(-\frac{(\xi)^2}{2RT}\right) \times \left(1 + \frac{(\xi \cdot \mathbf{u})}{RT} + \frac{(\xi \cdot \mathbf{u})^2}{2(RT)^2} - \frac{(\mathbf{u} \cdot \mathbf{u})}{2RT}\right) d\xi$$

Equation 4.14

The above integral is seen to have the form

$$\int g(x) e^{-x^2} dx ,$$

Equation 4.15

which can be calculated numerically by Gauss-Hermite quadrature.

### 4.1.3 Equilibrium Distribution Function $f^{eq}$

Using the third-order Hermite formula, Equation 4.14 becomes,

$$I = \frac{\rho}{\pi} \sum_{i,j=1}^3 \omega_i \omega_j \psi(\xi_{i,j}) \times \left(1 + \frac{(\xi_{i,j} \cdot \mathbf{u})}{RT} + \frac{(\xi_{i,j} \cdot \mathbf{u})^2}{2(RT)^2} - \frac{(\mathbf{u} \cdot \mathbf{u})}{2RT}\right)$$

Equation 4.16

Where  $\xi_{i,j} = (\xi_i, \xi_j) = \sqrt{2RT}(\zeta_i, \zeta_j)$ . Therefore the equilibrium distribution function is,

$$f_{i,j}^{eq} = \frac{\omega_i \omega_j}{\pi} \times \rho \times \left(1 + \frac{(\xi_{i,j} \cdot \mathbf{u})}{RT} + \frac{(\xi_{i,j} \cdot \mathbf{u})^2}{2(RT)^2} - \frac{(\mathbf{u} \cdot \mathbf{u})}{2RT}\right)$$

Equation 4.17

The discretized velocities is  $\mathbf{e}_\alpha = (\xi_i, \xi_j)$  and weighting factor  $w_\alpha = \left(\frac{\omega_i \omega_j}{\pi}\right)$

expressed in Table 4.1. Finally substituting  $RT = c_s^2 = c^2/3$ , discretized distribution function is written as,

$$f_\alpha^{eq} = w_\alpha \times \rho \times \left(1 + \frac{3(\mathbf{e}_\alpha \cdot \mathbf{u})}{c^2} + \frac{9(\mathbf{e}_\alpha \cdot \mathbf{u})^2}{2(c)^4} - \frac{3(\mathbf{u} \cdot \mathbf{u})}{2c^2}\right)$$

Equation 4.18

The case with 2 Dimensional and 9 discrete velocities (having 2 Dimensional square lattices) is called the D2Q9 model. Cubic lattice models are used for 3 Dimensional space and currently D3Q15, D3Q19 and D3Q27 are commonly used. Illustrations of some models are shown in Figure 4.1

[131].The equilibrium distribution function  $f_{\alpha}^{eq}$  of D2Q9, D3Q15, D3Q19 and D3Q27 model are shown in Equation 4.18[138].

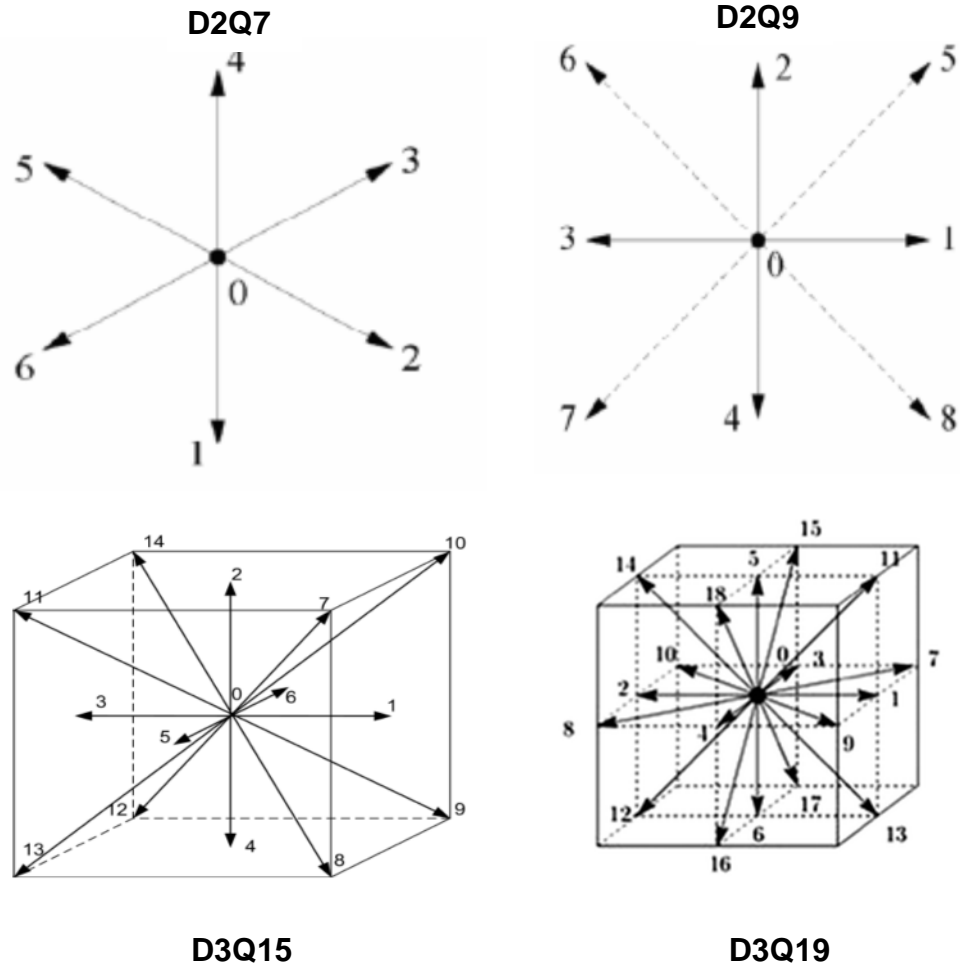


**Figure 4.1** Discrete velocity models used currently for 2 Dimensional and 3 Dimensional. D2Q7 model is rarely used.[131]

D2Q9 and D3Q19 models are often used in LB simulations. Therefore weighting factors of these models are written in Table 4.1 [138, 146].

**Table 4.1** D2Q9 and D3Q19 models discrete velocity, weighting factor and point in Figure 2.9.2 are labelled.

models	$e_{\alpha}$ - discrete velocity	$w_{\alpha}$ - <i>Weighting factor</i>	$\alpha$ -the point in Figure- -2.6.4.
D2Q9	(0,0)	4/9	0
	( $\pm 1,0$ )c, (0, $\pm 1$ )c	1/9	1,2,3,4;
	( $\pm 1,\pm 1$ )c	1/36	5,6,7,8;
D3Q19	(0,0,0)	1/3	0
	( $\pm 1,0,0$ )c, (0, $\pm 1,0$ )c, (0,0, $\pm 1$ )c	1/18	1,2,3,.....,6;
	( $\pm 1, \pm 1,0$ )c, ( $\pm 1,0,\pm 1$ )c, (0, $\pm 1,\pm 1$ )c	1/36	7,8,9,.....,18;

#### 4.1.4 Temporal Discretization

Equation 4.1 can be rewritten as an ordinary differential equation,

$$\frac{df}{dt} + \frac{1}{\lambda} f = \frac{1}{\lambda} f^{eq} \quad \text{Equation 4.19}$$

Where  $\frac{d}{dt} \equiv \frac{\partial}{\partial t} + \xi \cdot \nabla$  is the time derivative along the characteristic line  $\xi$ .

Following He and Luo (1997) Equation 4.19 is multiplied by  $\exp\left(\frac{t}{\lambda}\right)$  and integrated over a time step of  $\delta t$ .

$$f(x + \xi\delta t, \xi, t + \delta t) = \frac{1}{\lambda} e^{-\frac{\delta t}{\lambda}} \int_0^{\delta t} e^{\frac{t'}{\lambda}} f^{eq}(x + \xi t', \xi, t + t') dt' + e^{-\frac{\delta t}{\lambda}} f(x, \xi, t)$$

Equation 4.20

Assuming that  $\delta t$  is small enough and  $f^{eq}$  is smooth enough locally the approximation is ,

$$f^{\text{eq}}(x + \xi \delta t', \xi, t + t') = f^{\text{eq}}(x', \xi, t') + \frac{f^{\text{eq}}(x + \xi \delta t', \xi, t + \delta t') - f^{\text{eq}}(x', \xi, t')}{\delta t} + O(\delta t^2)$$

Equation 4.21

For  $0 \leq t' \leq \delta t$ , with this Equation 4.20 approximates too,

$$f(x + \xi \delta t, \xi, t + \delta t) - f(x, \xi, t) = \left( e^{-\frac{\delta t}{\lambda}} - 1 \right) [f(x, \xi, t) - f^{\text{eq}}(x, \xi, t)] + \left( 1 + \frac{\lambda}{\delta t} \left( e^{-\frac{\delta t}{\lambda}} - 1 \right) \right) [f^{\text{eq}}(x + \xi \delta t', \xi, t + \delta t') - f^{\text{eq}}(x', \xi, t')]$$

Equation 4.22

Taylor expansion of  $e^{-\frac{\delta t}{\lambda}}$  and neglecting terms of order  $O(\delta t^2)$  in Equation 4.23 gives,

$$f(x + \xi \delta t, \xi, t + \delta t) - f(x, \xi, t) = -\frac{1}{\tau} [f(x, \xi, t) - f^{\text{eq}}(x, \xi, t)]$$

Equation 4.23

Where  $\tau \equiv \lambda / \delta t$  is the non-dimensional relaxation time.

Density is measured by summing up the total number of distribution function at each node.

$$\rho(x, t) = \sum_i f_i(x, t)$$

Equation 4.24

Similarly momentum derivation is:

$$\rho(x, t)u(x, t) = \sum_i e_i \alpha_i f_i(x, t)$$

Equation 4.25

#### 4.1.5 kinematic viscosity ( $\nu$ )

In Equation 4.23,  $f^{\text{eq}}$  is the equilibrium (Maxwell-Boltzmann) distribution function and  $\tau$  is the relaxation time. The equilibrium distribution function (Equation 4.18) has velocity, weighting factor and density. The disadvantage of this method is that macroscopic parameters depend on  $\tau$  and lattice velocities set. The BGK model limits the flexibility of flow simulation due to the dependency of kinematic viscosity ( $\nu$ ) [144], which is related to relaxation time  $\tau$  via [131]:

$$v = \left( \tau - \frac{1}{2} \right) c_s^2 \Delta t \quad \text{Equation 4.26}$$

In Equation 4.26, the  $c_s$  represents the speed of sound and  $\Delta t$  is the time increment. LBM has been shown to be second order accurate in space in time and the representation of the kinematic viscosity for solving incompressible flow in LBGK, to have positive viscosity, the relaxation time should be greater than 0.5 ( $\tau > 1/2$ ) [131].

## 4.2 From the Lattice Boltzmann equation (LBE) to Navier Stokes equations (N-S).

### 4.2.1 Chapman-Enskog expansion

A Taylor expansion of Equation 4.23 produces the following:

$$\sum_{n=1}^{\infty} \frac{D^n}{n!} \varepsilon^n (f_i^{(0)} + \varepsilon f_i^{(1)} + \varepsilon^2 f_i^{(2)} + \dots) = - \frac{\sum_{n=1}^{\infty} \varepsilon^n f_i^{(n)}}{\tau} \quad \text{Equation 4.27}$$

Where  $D = \partial_t + e_{i\alpha} \partial_\alpha = \sum_{m=0}^{\infty} \varepsilon^m \partial_m + e_{i\alpha} \partial_\alpha$  Consecutive approximations in powers of  $\varepsilon$  are[147]:

$$\begin{aligned} \varepsilon^0 : f_i^{(0)} &= f_i^{(\text{eq})} \\ \varepsilon^1 : (\partial_t + e_{i\alpha} \partial_\alpha) f_i^{(0)} &= - \frac{f_i^{(1)}}{\tau} \\ \varepsilon^2 : \partial_t f_i^{(0)} + (\partial_{t0} + e_{i\alpha} \partial_\alpha) f_i^{(1)} + \frac{(\partial_{t0} + e_{i\alpha} \partial_\alpha)^2 f_i^{(0)}}{2} &= - \frac{f_i^{(2)}}{\tau} \end{aligned} \quad \text{Equation 4.28}$$

Where  $\varepsilon^0$  terms are taken from the fact that expansion is performed around the equilibrium function[144].

### 4.2.2 Lattice Boltzmann equation (LBE) to Navier-Stokes equations (N-S)

The Chapman-Enskog expansion is applied to the lattice BGK model in Equation 4.23 to derive the macroscopic equation of the model. The mass continuity equation is written [148](neglecting terms of order  $O(\delta t^2)$ ) as  $[\nabla]$  :

$$\frac{\partial \rho}{\partial t} + \nabla \cdot (\rho \mathbf{u}) = 0 \quad \text{Equation 4.29}$$

The Momentum equation is shown in Equation 4.30, with an error proportional to  $O(\text{Ma}^3)$  in space and  $O(\text{Ma} \cdot \Delta t)$  in time [148, 149].

$$\partial_t (\rho u_\alpha) + \partial_\beta (\rho u_\alpha u_\beta) = -\partial_\alpha (c^2 \rho) + \nu \partial_\beta (\rho \partial_\alpha u_\beta + \rho \partial_\beta u_\alpha) \quad \text{Equation 4.30}$$

In Equation 4.30, the pressure is  $p = \rho c_s^2$  (the equation of state (EOS)),  $c_s$  is

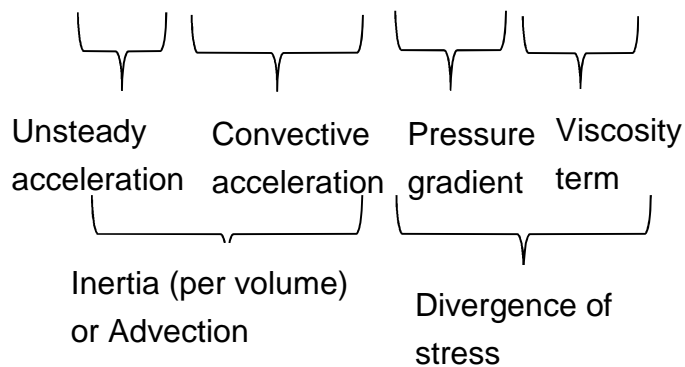
speed of sound  $c_s = \frac{c}{\sqrt{3}}$  and the kinematic viscosity is  $\nu = \left(\tau - \frac{1}{2}\right) c_s^2 \Delta t$ .

The macroscopic equation of LBGK represents the incompressible Navier-Stokes equation in the limit of  $\rho \rightarrow \rho_0$  is a constant and low Mach number (or Mach number approaches zero).

The exact solution of the incompressible Navier-Stokes equation is shown below in Equation 4.31 [134, 148, 149].

Since the density is constant, the continuity equation is  $\nabla \cdot (\mathbf{u}) = 0$ .

$$\rho \left( \partial_t (u_\alpha) + \partial_\beta (u_\alpha u_\beta) \right) = -\partial_\alpha (p) + \mu \partial_\beta \partial_\beta u_\alpha \quad \text{Equation 4.31}$$



In Equation 4.31,  $\rho$ ,  $u$  &  $p$  represent the density, velocity and pressure respectively, and  $\mu$  is the dynamic viscosity, which is the product of the density and the kinematic viscosity [148].  $\mu = \nu \rho$ .

### 4.3 LBM computer implementation process

The evolution of the lattice-BGK model is written as:

$$f_{\alpha}(x + e_{\alpha} \Delta t, t + \Delta t) = f_{\alpha}(x, t) - \frac{1}{\tau} \left[ f_{\alpha}(x, t) - f_{\alpha}^{\text{eq}}(x, t) \right] \quad \text{Equation 4.32}$$

Streaming

Collision

The  $f_{\alpha}(x,t)$  is non-equilibrium distribution function at node  $x$  and time  $t$  and  $f_{\alpha}^{\text{eq}}(x,t)$  is equilibrium distribution function at node  $x$  and time  $t$  [132]. The Equation 4.32 is solved using two steps: the collision step and the streaming step.

#### 4.3.1 Streaming step

The streaming step handles the spreading of particle. The streaming step is written as [131]:

$$f_{\alpha}(x + e_{\alpha} \Delta t, t + \Delta t) = f_{\alpha}^{+}(x, t) \quad \text{Equation 4.33}$$

Where  $f_{\alpha}^{+}(x,t)$  is post collision state of the distribution functions. Streaming is fundamentally data shifting as shown in Figure 4.2(b). However the streaming step involves computations. It is noticeable that boundary nodes do not have all neighbouring nodes and would therefore have some missing distribution functions after the streaming step is processed. Boundary conditions in the LBM involve specifying these missing distribution function in one of a number of ways (see section 4.4) [150].

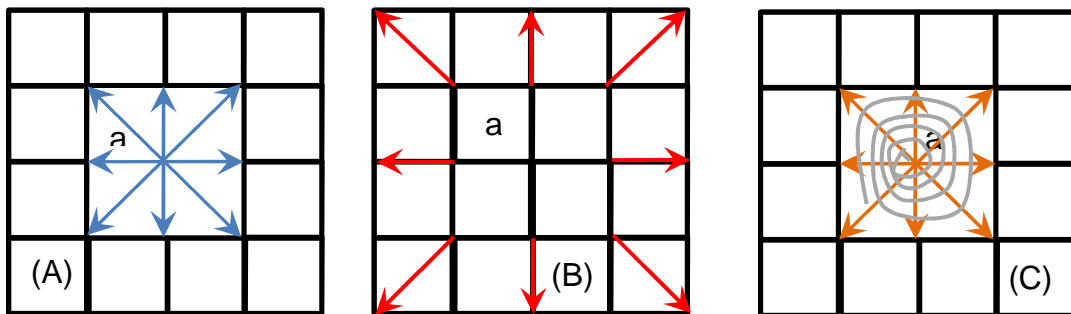


**Figure 4.2** Shows the initial step (a) of lattice node  $a$  (modelled as a fluid node), (b) is streaming step and (c) is collision step [150].

### 4.3.2 Collision step

Interactions between particles are handled through a collision step [151] during which the distribution functions relax towards the local equilibrium distribution, which in turn depends on the local velocity and density [152]. The collision steps formula is shown in Equation 4.34 [150]. The collision step is strictly local to node(x,t), as it involves no transfer of information between lattice cells [134]. Therefore, it is easy to implement in a parallel algorithm [150].

$$f_{\alpha}^{+}(x,t) = f_{\alpha}(x, t) - \frac{1}{\tau} \left[ f_{\alpha}(x, t) - f_{\alpha}^{\text{eq}}(x, t) \right] \quad \text{Equation 4.34}$$

Where  $f_{\alpha}(x,t)$ ,  $f_{\alpha}^{+}(x,t)$ ,  $f_{\alpha}^{\text{eq}}(x,t)$  and  $\tau$  are respectively pre, post collision state of distribution function, equilibrium distribution function and relaxation time.

## 4.4 Boundary condition

The boundary conditions set how the fluid flows in the simulations and correct implementation gives good accuracy and stability in the computation [131]. In the boundary nodes of the domain, the macroscopic quantities need to be transformed into the missing distribution functions. Normally periodic or constant pressure/velocity boundary conditions are used to solve these problems. In this section, the periodic, bounce back and Zou & He (pressure difference model) boundary models are discussed. LBM has the ability to incorporate complex boundaries like porous media fluid flow [153].

### 4.4.1 Periodic boundary conditions

Periodic boundary conditions are very easy to implement. They simply involve wrapping around opposite edges of the domain, as shown in Figure 4.3[150]. Distribution function values for the outwards pointing directions on the right-hand side of the domain are simply streamed to the corresponding node on the left-hand side of the domain, and vice versa. Hence fluid which leaves the domain reappears on the opposite side. [151].



**Figure 4.3** shows the periodic boundary condition from Right to Left .

#### 4.4.2 Bounce back Boundary conditions

The no-slip boundary condition is used in most CFD methods. In the LBM this is implemented through a bounce-back boundary condition. Based on reflection, there are two methods: full-way bounce back and half-way bounce back. This is shown in Figure 4.4 [154].

Full-way bounce back method skips the collision step at the wall boundary nodes and reverses the direction of the distribution functions for directions pointing into the wall. Then the streaming step is carried out. In the wall node, instead of the collision step the Equation 4.35 [131] is used.

$$f_{\tilde{\alpha}}^{\text{out}}(x,t) = f_{\alpha}^{\text{in}}(x,t) \quad \text{Equation 4.35}$$

$f_{\alpha}^{\text{in}}(x,t)$  is particle distribution function (PDF) entering boundary nodes and  $f_{\tilde{\alpha}}^{\text{out}}(x,t)$  is PDF leaving boundary nodes. Opposite directions are noted by  $\alpha$  and  $\tilde{\alpha}$ . The Full-way bounce back boundary conserves mass and momentum. It has first order accuracy at the boundaries. But LBM itself has a second order accuracy [153]. Second order accuracy at boundaries is achieved through a half-way bounce back condition and allows lower grid resolutions [151].

In the Half-way bounce back condition, the wall is placed in-between the fluid nodes and the bounce back node. This method applies the collision

step for every nodes[150]. Compared to other second order accuracy treatments, the half-way bounce condition doesn't need additional computation and is easy to implement.

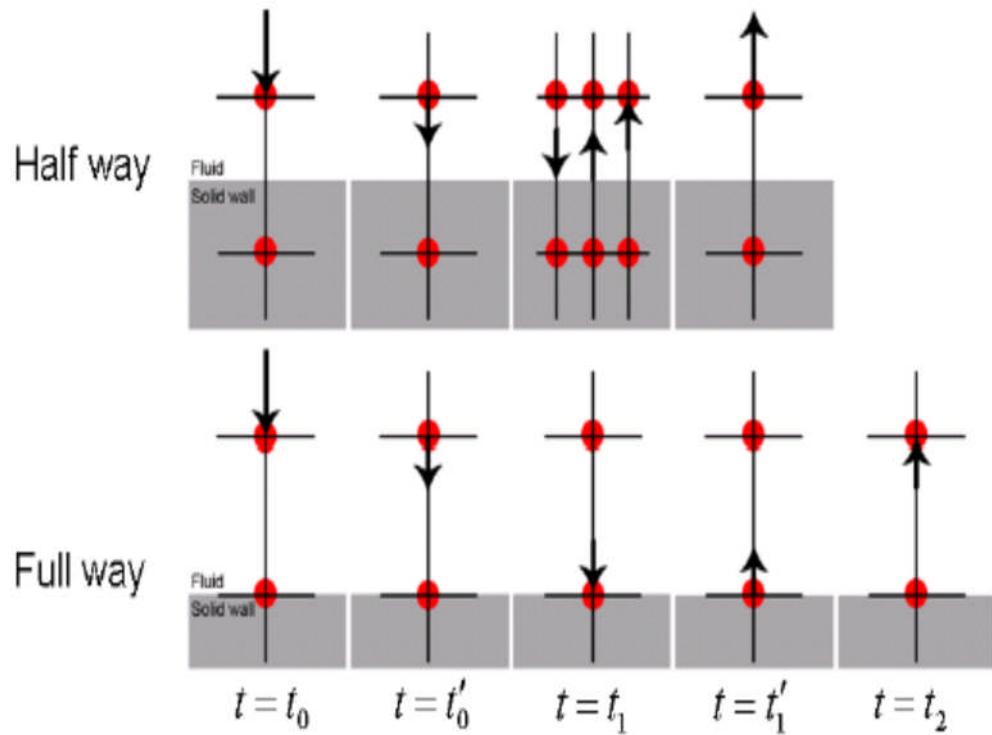


**Figure 4.4** Half-way and Full-way boundary conditions are shown. The  $t_1$ -denotes a time step after streaming step and  $t'_1$ -denotes the time step after boundary condition[154].

#### 4.4.3 Zou-He (pressure boundary)

Zou & He proposed a model in 1997 to handle both velocity and pressure boundary conditions. Pressure is given as a function of density (i.e. via the equation of state), therefore pressure boundaries are equivalent to density boundaries [151]. Identifying the distribution function that points from the inlet and the outlet into the domain is a problem in this method. Figure 4.5 shows an inlet boundary condition at one node. After the streaming step the distribution functions F1, F5 & F8 would be missing. These three unknown distribution functions and velocity are derived from the known distribution functions at the inlet. This model assumes the velocity tangential to the boundary is zero and velocity component is normal to boundary [153].

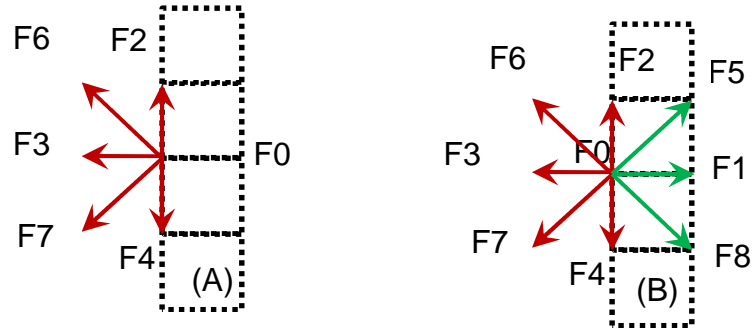


**Figure 4.5** Missing distribution function at the inlet boundary node (A) and unknown distribution function modelled with Zou & He method.

By using the macroscopic density and momentum equations (Equation 4.24 & 4.25 respectively), the following Equation 4.36-4.38 can be obtained.

$$\rho = \sum_i f_{\alpha}(x,t) = f_0 + f_1 + f_2 + f_3 + f_4 + f_5 + f_6 + f_7 + f_8 \quad \text{Equation 4.36}$$

$$\rho u_y = 0 = f_2 \cdot f_4 + f_5 + f_6 \cdot f_7 \cdot f_8 \quad \text{Equation 4.37}$$

$$\rho u_x = f_1 \cdot f_3 + f_5 \cdot f_6 \cdot f_7 + f_8 \quad \text{Equation 4.38}$$

Zou & He assumed that part of the distribution was reflected at the boundary and this is shown in :[151]

$$f_1 - f_1^{eq} = f_3 - f_3^{eq} \quad \text{Equation 4.39}$$

Then, the velocity and the three unknown distribution functions are obtained through a calculation from the above equations is shown [155].

$$u_x = 1 - \frac{f_0 + f_2 + f_4 + 2(f_3 + f_6 + f_7)}{\rho} \quad \text{Equation 4.40}$$

$$f_1 = f_3 + \frac{2}{3} \rho u_x \quad \text{Equation 4.41}$$

$$f_5 = f_7 - \frac{1}{2}(f_2 - f_4) + \frac{1}{6} \rho u_x \quad \text{Equation 4.42}$$

$$f_8 = f_6 + \frac{1}{2}(f_2 - f_4) + \frac{1}{6} \rho u_x \quad \text{Equation 4.43}$$

The Zou & He method is not efficient to handle the two-phase flow simulations [151] due to the equation of state. (pressure is related to the density).

#### 4.4.4 Force Equilibrium

This is a simple boundary condition that imposes the equilibrium distribution function on either the unknown or all distribution functions of boundary nodes and is used to set the velocity and density at boundary. This is shown in equation 4.44. Also it is general boundary condition. However it doesn't conserve mass, but is simple to implement .

$$f_i = f_i^{eq}(\rho, u) \quad \text{Equation 4.44}$$

#### 4.4.5 Zero gradient boundary (Neumann boundary condition)

The outflow boundary is critical in LBM and in the simulation in the rest of this thesis, the outlet boundary is located at  $x = N$  (corresponding to lattice nodes at  $x_N, y_j$ ), where the directional derivatives normal to the boundary of all the dependent variable are set to zero. The zero gradient boundary is written as [156]:

$$\frac{\partial \chi}{\partial x} = 0, \quad x = N \quad \text{Equation 4.45}$$

Where  $\chi$  is the dependent variables such as  $\rho, \rho u$  and etc. Implementation is [156]:

$$f_i(N, j, t) = f_i(N-1, j, t) \quad \text{Equation 4.46}$$

### 4.5 Summary of procedure

Lattice Boltzmann methods (LBMs) have a bottom-up approach, starting with a discrete microscopic model, which can yield the Navier-Stokes equations. LBM considers that the volume of fluid is made of a collection of particles, represented by distribution functions  $f_\alpha$  for each fluid component at each node of the domain. Macroscopic flow density is defined as sum of the distribution function at each node. Macroscopic velocity is an average of the microscopic velocities  $e_\alpha$  weighted by the directional densities  $f_\alpha$  . Collisions between molecules are handled through a relaxation time that brings the velocity distribution at each node towards a discrete version of the Maxwell-Boltzmann distribution. The most popular collision operator is the Bhatnagar-

Gross-Krook (BGK) method. The macroscopic equation of LBGK represents the incompressible Navier Stokes equation in the limit of  $\rho \rightarrow \rho_0$  is a constant and low Mach number (Section 4.2.2), therefore the particle densities that propagate along a lattice can be shown to also satisfy the macroscopic flow equations, making LBMs suitable for CFD. The relaxation time towards the equilibrium distribution determines the viscosity of the fluid. LBMs are typically implemented in a two-step process. In streaming step, densities propagate to adjacent nodes along the lattice directions; in the collision step, the velocity distribution at each node relaxes towards the equilibrium distribution. This process is highly adaptable to parallelization, a key advantage over other CFD methods, because no communication is required during the collision step, and communication with only the adjacent nodes is required for the streaming step.

#### **4.6 Multiphase flow modelling.**

A number of multiphase LBM models have been proposed in the literature. Among them, three representative models are the colour gradient model, the inter-particle potential model and the free-energy model [144, 157].

One of the first models for multiphase simulations implemented for the LBM was from the lattice gas colour gradient model [158, 159]. In this model, red and blue distribution functions  $f_\alpha^r$  and  $f_\alpha^b$  were used to represent the two different fluids. Each of the distribution functions is run by the usual Lattice Boltzmann implementation. The interface between two fluids is calculated at every time step. The surface tension is applied to the fluids as the external force. The original method allows to obtain sharp interfaces but it is computationally demanding due to calculation of the surface location and surface tension terms at every time step. Also, the model was unstable for large fluid density ratios due to the different sound speeds in the media [160] and spurious currents but using Multiple relaxation time these issues are solved [161]. Spurious current is a small-amplitude artificial velocity field which arises from an imbalance between discretized forces in multiphase/multi-component flows [162]. Therefore this method is not effective for simulating multiphase flows in porous media [163].

The inter-particle potential model was first proposed by Shan and Chen by introducing a velocity shift to implement the force term, which is the function utilizing the nearest node neighbours densities. Later named as the pseudopotential model, The Shan-Chen model has been widely applied in simulations of multiple component fluid flow and multi-phase flow [164]. The advantages of the Shan-Chen model are that it is easy to trace the motion of the interface between phases and to implement the forces in the model, such as buoyancy and interfacial tension. The main disadvantages of the Shan-Chen model are that the temperature is not introduced in the model directly, which is imitated by the strength of the inter-particle interaction  $G$  (discussed later in this chapter), and that unphysical spurious velocity was found on the interface [165], which eventually destroy the stability. Also gas-liquid density ratio is up to 60 – 70, the surface tension and the equation of state dependent on a inter-particle interaction  $G$ . The utilization of different equation of states (EOS) such as Peng-Robinson or Carnahan-Starling in the Shan-Chen pseudopotential allows to decrease spurious currents. From this, gas-liquid density ratio of a few thousand can be obtained with better thermodynamically consistent behaviour [144].

Swift et al [166] introduced the free energy model. The primary advantage of this model is that temperature was well-defined in the model. In addition, spurious velocity is almost negligible, due to the benefit of local momentum conservation [167]. The model is able to simulate not only gas-liquid systems but binary liquids with different viscosities [168]. The model is limited to small gas-liquid density ratio problems and small viscosity ratio. There are problems with the lack of Galilean invariance (it is non-physical) because of the unphysical viscous stresses which cannot be neglected [169]. However, this has been addressed in later development of the method.

In this study, the Shan-Chen inter-particle interaction pseudo-potential model is adopted. Mainly because, of its ease of implement and its ability to capture many fundamental physical properties of multiphase flow. Further details are described in the following sections.

## 4.7 Shan-Chen Multiphase Model

The Shan-Chen model is a common LBE model for multi-phase simulations. This model can simulate multiphase flow using a single component (liquid and vapour form of the same fluid). In single component multiphase flow simulations, the two phases have a large degree of mixing ability due to the phase transition at the gas-liquid interface. This can be solved using a two component version of the method (discussed in 4.8).

### 4.7.1 Phase separation

Multiphase flow and phase separation are captured by incorporating microscopic interactions between fluid through a non-ideal equation of state. Interfacial tension is captured by attractive or repulsive force between neighbours. Non-ideal effects are formed by inter-particle forces between nearest- neighbours of fluid and given by [153, 170]:

$$F(x,t) = -G\psi(x,t)\sum_{\alpha} w_{\alpha}\psi(x + e_{\alpha}\Delta t,t)e_{\alpha} \quad \text{Equation 4.47}$$

In Equation 4.47,  $G$ ,  $w_{\alpha}$ ,  $\psi$  and  $e_{\alpha}$  are respectively the interaction strength, weighting factor, pseudo-potential or effective density and discrete velocity. Negative  $G$ -interaction strength corresponds to attractive forces between the liquid molecules and positive interaction strength corresponds to repulsive forces between the gas and the liquid. The  $G$ -Interaction strength determines the Equilibrium phase densities, the level of mixing between different phases, the sharpness of the interface and the surface tension.

The initial Shan-Chen multiphase model was limited to low density ratios between different phases due to large parasitic velocities along the interface and numerical instabilities. The density ratio could be increased by  $\psi$  - pseudo-potential and written in[171]:

$$\psi(\rho) = \rho_o \left[ 1 - \exp\left(\frac{-\rho}{\rho_o}\right) \right] \quad \text{Equation 4.48}$$

Where  $\rho_o=1$ .

#### 4.7.2 Wetting boundary condition

The surface wettability or wall-fluid force is represented by imposing the density of the fluid at the wall via a 'surface affinity' parameter or wettability coefficient,  $\phi$ . This parameter is defined in the range of 0 to 1 by [172]

$$\phi = \frac{\rho_{wall} - \rho_l}{(\rho_h - \rho_l)}$$

where,  $\rho_h$  and  $\rho_l$  are the densities of the heavy phase and light phase respectively, and  $\rho_{wall}$  is the fluid density at the wall. Inverting this expression allows the wall density to be expressed as:

$$\rho_{wall} = \phi * (\rho_h - \rho_l) + \rho_l \quad \text{Equation 4.49}$$

$\rho_{wall}$  (density of wall) is similar to the density of the liquid ( $\rho_h$ ), i.e.  $\phi \sim 1$ , then the wall is hydrophilic with small contact angle ( $0^\circ$ ) and if  $\rho_{wall}$  is similar value to density of gas ( $\rho_l$ ), i.e.  $\phi \sim 0$ , the wall would have hydrophobic behaviour with large contact angle ( $180^\circ$ ) [170].

#### 4.7.3 Force inclusion

Gravitational force calculation is shown in:

$$F^{gra} = \rho g \quad \text{Equation 4.50}$$

Where  $\rho$  is the density and  $g$  is the gravitational acceleration.

The total forces for this model are the sum of inter-particle force  $F(x,t)$ , wall adhesion forces  $F^{ads}$  and gravitational forces  $F^{gra}$ . This is shown in Equation 4.51 [97, 173].

$$F^{tot} = F(x,t) + F^{gra} + F^{ads} \quad \text{Equation 4.51}$$

The total force term  $\tau F^{tot}$  is added to the momentum density  $\rho u'$  to obtain the velocity to use in  $f^{eq}$ , i.e [153]:

$$\rho u = \rho u' + \tau F^{tot} \quad \text{Equation 4.52}$$

The velocity used in the equilibrium distribution function  $f^{eq}$  Equation 4.18 is therefore:

$$u = u' + \frac{\tau F^{tot}}{\rho} \quad \text{Equation 4.53}$$

The velocity ( $U$ ) of the flow is calculated by averaging the moments before and after collision [131].

$$U = u + \frac{F^{tot}}{2\rho} \quad \text{Equation 4.54}$$

The direct body approach is another way of incorporating fluid-fluid interactions. Fluid-fluid interactions are linked with the body force term in the Boltzmann equation, where additional terms are added after the collision step [131, 149].

#### 4.7.4 Equation of state (EOS)

The non-linear equation of state is show in Equation 4.55 [153, 173, 174].  $p, G, \psi(\rho)$  and  $\rho$  are respectively the pressure, interaction strength of the inter-particle forces, pseudo-potential and density.

$$p = \frac{\rho}{3} + \frac{G}{6} \psi^2(\rho) \quad \text{Equation 4.55}$$

### 4.8 Shan-Chen Multicomponent Multiphase model

This model can simulate multiphase flow involving a multiple components (i.e.different fluids), components which are immiscible.

#### 4.8.1 Phase separation

Interfacial tension is captured by attractive or repulsive forces between neighbours. Non-ideal effects are formed by inter-particle forces between nearest- neighbours of fluid and shown in Equation 4.56 [146, 153, 170].

$$F(x,t) = -G\rho_\sigma(x,t)\sum_{\alpha} w_{\alpha}\rho_{\sigma}^{-}(x + e_{\alpha}\Delta t,t)e_{\alpha} \quad \text{Equation 4.56}$$

In Equation 4.56,  $G, w_{\alpha}, e_{\alpha}, \rho_{\sigma}$  and  $\rho_{\sigma}^{-}$  are respectively the interaction strength, weighting factor, discrete velocity, density of fluid component 1 (water) and density of fluid component 2 (oil). The  $G$ -interaction strength corresponds to the strength of the cohesion force between the liquid molecules, and determines the liquid phase equilibrium densities, level of mixing between different components, the sharpness of the interface and the interfacial tension.

The Shan-Chen Multicomponent multiphase model is limited to low density ratios between different phases due numerical instabilities.  $\psi$  - pseudo-potential and written in [146, 171]:

$$\psi(\rho) = \rho \quad \text{Equation 4.57}$$

#### 4.8.2 Wetting boundary condition

The wettability of solid boundaries is represented in the same way as described in section 4.7.2 except that two densities need to be specified for the two components. The surface wetting or the wall-fluid force is represented through a surface affinity parameter. The wettability coefficient is fixed at wall nodes and defined in the range of 0-1 by Equation 4.58 [172].  $\rho_1$  and  $\rho_2$  are respectively liquid1 density (heavy component) , liquid 2 density (light component). In relation they also have dissolved density 1( $\overline{\rho_1}$ ) and dissolve density 2( $\overline{\rho_2}$ ). Dissolved density is an arbitrary value.

$$\begin{aligned} \rho_{1w} &= \phi * (\overline{\rho_1} - \rho_1) + \overline{\rho_1} \\ \rho_{2w} &= \phi * (\overline{\rho_2} - \rho_2) + \rho_2 \end{aligned} \quad \text{Equation 4.58}$$

Parameter  $\rho_{wall}$  can be modified to control the equilibrium contact angle at wall boundary. If  $\rho_{1w}$  (density of wall) is similar to the density of the liquid1 ( $\rho_1$ ) then the wall is hydrophilic behaviour with small contact angle and if  $\rho_{1w}$  is similar value to density of dissolved liquid1 would have hydrophobic

with large contact angle [170]. Visa versa for  $\rho_{2w}$  (density of component 2 at the wall).

### 4.8.3 Force inclusion

Gravitational force and Total forces calculation are same as in section 4.7.3 [97, 173].  $\rho_\sigma$  is the density of the  $\sigma^{\text{th}}$  component can be obtained from

$\rho_\alpha = \sum_a f_a^\sigma$ . The total force term  $\tau F^{\text{tot}}$  is added to the momentum  $\rho_\sigma u'_\sigma$  to

obtain the velocity to use in  $f^{\text{eq}}$  in Equation 4.18 . Equation 4.59 shows the formula for momentum [146, 153].

$$\rho_\sigma u_\sigma^{\text{eq}} = \rho_\sigma u'_\sigma + \tau F^{\text{tot}} \quad \text{Equation 4.59}$$

The velocity common to the various components is defined as  $u'$  in:

$$u' = \frac{\sum_\sigma \left( \frac{\sum_a f_a^\sigma e_a}{\tau_\sigma} \right)}{\left( \frac{\sum_\sigma \rho_\sigma}{\tau_\sigma} \right)} \quad \text{Equation 4.60}$$

Velocity (U) of the flow is calculated by averaging the moments before and after collision. Shown in Equation 4.61 [131]:

$$U = u^{\text{eq}} + \frac{F^{\text{tot}}}{2\rho} \quad \text{Equation 4.61}$$

The overall density of the fluids in the domain are  $\rho_i = \sum_\sigma \rho_\sigma$  or  $\rho_1(x) + \rho_2(x)$ .

### 4.8.4 Equation of state (EOS)

The non-linear equation of state is shown in Equation 4.62 [146, 153, 173, 174].  $p, G, \rho_1$  and  $\rho_2$  are respectively the pressure, interaction strength of the inter-particle forces, density liquid1 density and liquid 2 density.

$$p(x) = \frac{\rho_1(x) + \rho_2(x)}{3} + \frac{G(\rho_1(x) + \rho_2(x))}{6} \quad \text{Equation 4.62}$$

## 4.9 Parallel computing

The LBM has the main advantages, including a simple algorithm, easy treatment of complicated boundary condition and parallel computing. Parallel computation reduces the calculation time. Increasing simulation speed without a large increase in cost, Compute Unified Device Architecture (CUDA) technique for issuing and managing computations on a graphic processor unit (GPU) can be used to exploit a GPU as a data- parallel computing device. GPU is designed such that more transistors are allocated to data processing in place of temporary storing data and flow control. The typical programming pattern is [154]:

1. Load the data from host (device memory) to GPU (shared memory)
2. Process the data in GPU
3. And write the results back to the host

The LBM simulation requires to solve the collision step and streaming step (Equation 4.33-4.34). During collision step, updating the value on one grid only needs its own previous data. But streaming step needs the data of other grids nearby it [154, 175].

## 4.10 LB Unit conversion

LBM simulations deal with dimensionless lattice units. Therefore it is necessary to give a conversion factor to the physical units. The value used in LBM simulations requires to be multiplied by a suitable combination of conversion factors,  $\Delta x$  (length)  $\Delta t$  (time)  $\Delta m$  (mass), and from this physical units are achieved. Experimentally known values of  $\rho_{actual} [kg/m^3]$ , viscosity  $\nu_{actual} [m^2/s]$  and interfacial tension  $\sigma_{actual} [kg/s^2]$  of the liquid. These parameters are related to the corresponding lattice Boltzmann variables  $\rho_{LB}$ ,  $\nu_{LB}$  and  $\sigma_{LB}$ . LB unit conversion are shown in Table 4.2:

**Table 4.2** LB unit conversion.

Velocity	Viscosity	Interfacial tension
$V_{actual} [m/s] = V_{LB} \times \frac{\Delta x}{\Delta t}$	$\nu_{actual} [m^2/s] = \nu_{LB} \times \frac{\Delta x^2}{\Delta t}$	$\sigma_{actual} [kg/s^2] = \sigma_{LB} \times \frac{\Delta m}{\Delta t^2}$

Solving this system equations for  $\Delta x$ (length) and  $\Delta t$ (time),  $\Delta m$  (mass) are [176]:

$$\Delta x = \frac{L}{N} = \frac{\text{Diameter of actual droplet or fibre}}{\text{number of lattice nodes across droplet or fibre}} \quad \text{Equation 4.63}$$

$$\Delta t = \left( \frac{\rho_{actual}}{\rho_{LB}} \right)^2 \times \left( \frac{\nu_{actual}}{\nu_{LB}} \right)^3 \times \left( \frac{\sigma_{LB}}{\sigma_{actual}} \right)^2 \quad \text{Equation 4.64}$$

$$\Delta m = \left( \frac{\rho_{actual}}{\rho_{LB}} \right)^4 \times \left( \frac{\nu_{actual}}{\nu_{LB}} \right)^6 \times \left( \frac{\sigma_{LB}}{\sigma_{actual}} \right)^3 \quad \text{Equation 4.65}$$

## 4.11 Fluid flow parameters

The Mach number is the ratio between the fluid speed and speed of sound:

$$Ma = \frac{u}{c_s} \quad \text{Equation 4.66}$$

Laminar flow in porous media usually has a very low Mach number. Also LBGK represents the incompressible flow at low Mach number.

The Reynolds number of a fluid is given as:

$$Re = \frac{UL}{\nu} \quad \text{Equation 4.67}$$

Where  $U$  ,  $L$  and  $\nu$  are the characteristic velocity, length and kinematic viscosity.

Weber number represents the ratio of disruptive hydrodynamic forces to the stabilizing surface tension force:

$$We = \frac{\rho U^2 L}{\sigma} \quad \text{Equation 4.68}$$

Where  $\rho$ ,  $U$ ,  $L$  and  $\sigma$  are the density of fluid, characteristic velocity, length and Interfacial tension.

Kinematic viscosity is related to relaxation time (Equation 4.26), but relaxation time in Shan-Chen MCMP model is limited to a range between  $0.64 < \tau < 1.81$ . This is sufficient for representing diesel and water viscosities.

### 4.12 LBM algorithm flow chart

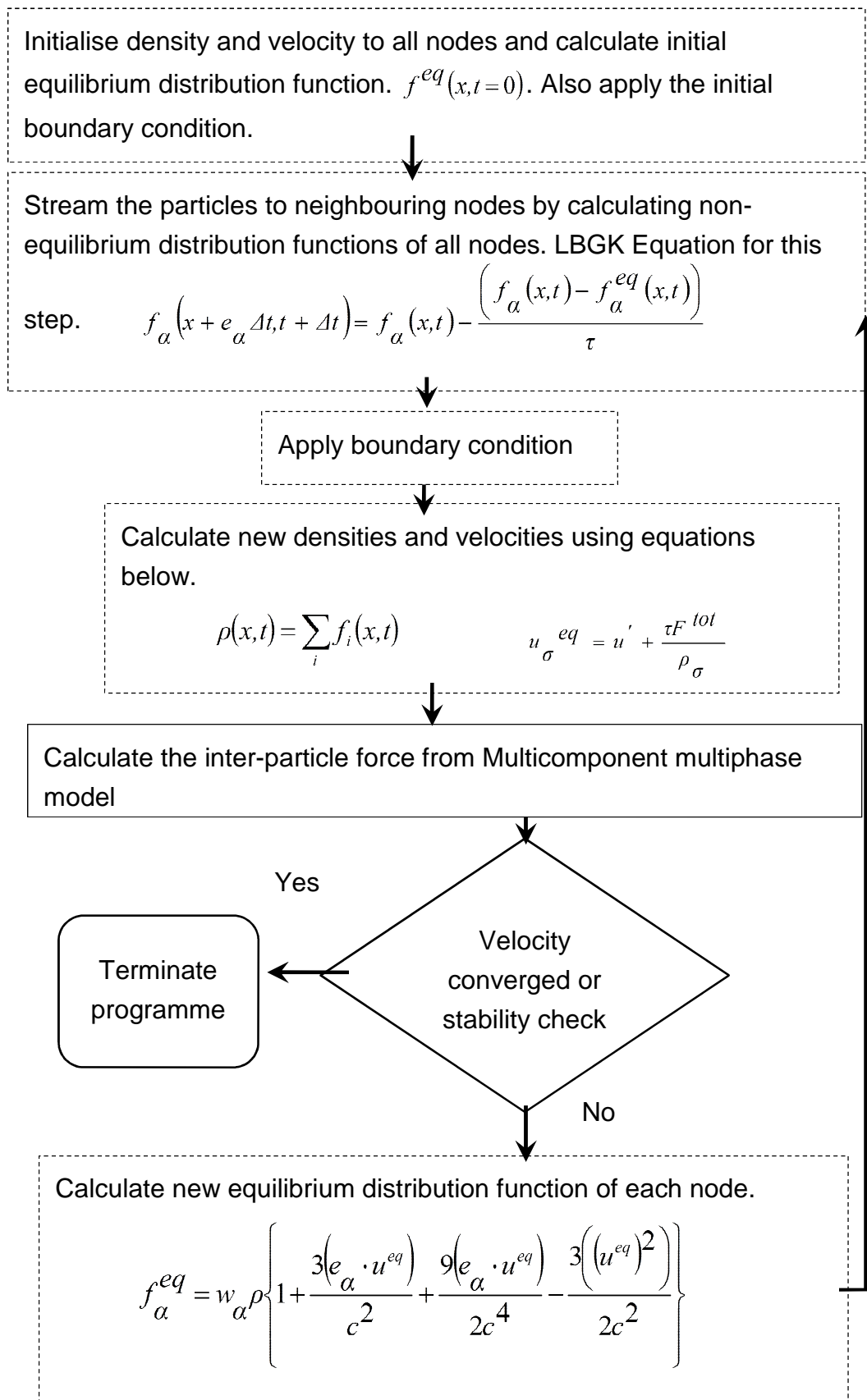


Figure 4.6 LBM programming flow chart.

### **4.13 Summary**

This chapter presented the key ideas behind the lattice Boltzmann method, including the application of boundary conditions and incorporation of multiphase flow. To represent the diesel and water flow in a coalescence filter, the multicomponent multiphase Shan-Chen is chosen. The wettability of the solid surfaces (i.e. filter fibres) is represented by specifying the density of the fluids on the solid surfaces in terms of a 'surface affinity' parameter or 'wettability coefficient' with a value between 0 and 1, corresponding to contact angles between  $180^\circ$  and  $0^\circ$ . The highly local nature of the lattice Boltzmann algorithm (i.e. involving information exchange just between adjacent nodes in the lattice) makes it ideal for parallel computation. The next chapter tests the predictions of the lattice Boltzmann simulations against previously published work, and the method is then used to explore coalescence filtration process in Chapter 6.

## Chapter 5 Sensitivity & Validation studies

### 5.1 Introduction

This chapter presents several sensitivity and validation studies to establish the reliability of the multicomponent multiphase (MCMP) Shan-Chen lattice Boltzmann method described in the previous chapter. Particular aspects considered are the appropriate domain size, calibration of the model parameters to achieve the correct fluid properties and contact angles, and testing of model predictions against previously published work.

### 5.2 Sensitivity studies

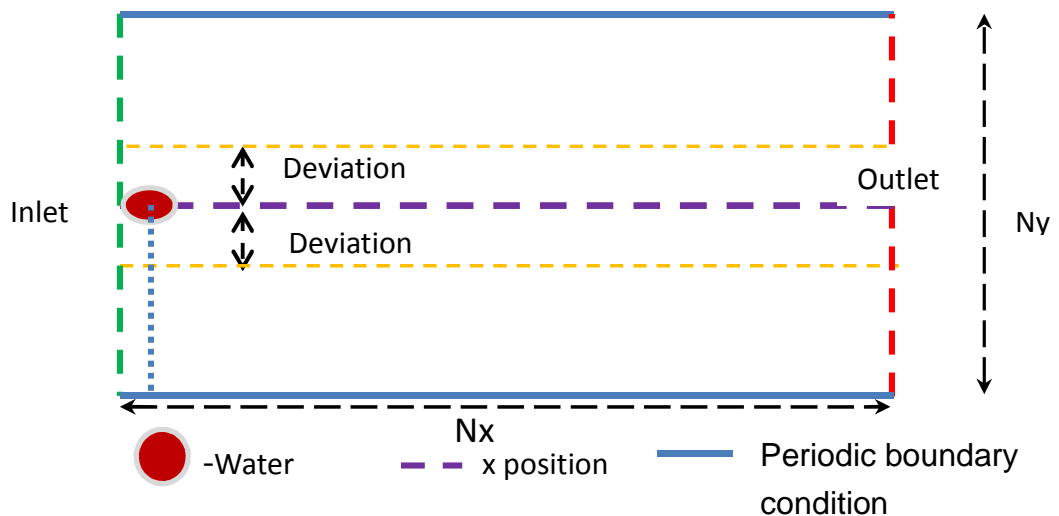


**Figure 5.1** represents the inlet, outlet region with a droplet in centre of  $N_y$  and equivalent radius away from inlet boundary for  $N_x$  centre. This system was studied for square domain size.

This section examines the size of the domain to minimise unphysical diffusion of droplets. This will be done initially for a square domain, before examining a rectangular domain. Figure 5.1 shows a general figure illustrating this.  $N_x$  is the domain length,  $N_y$  the domain height both in terms of the number of lattice units.

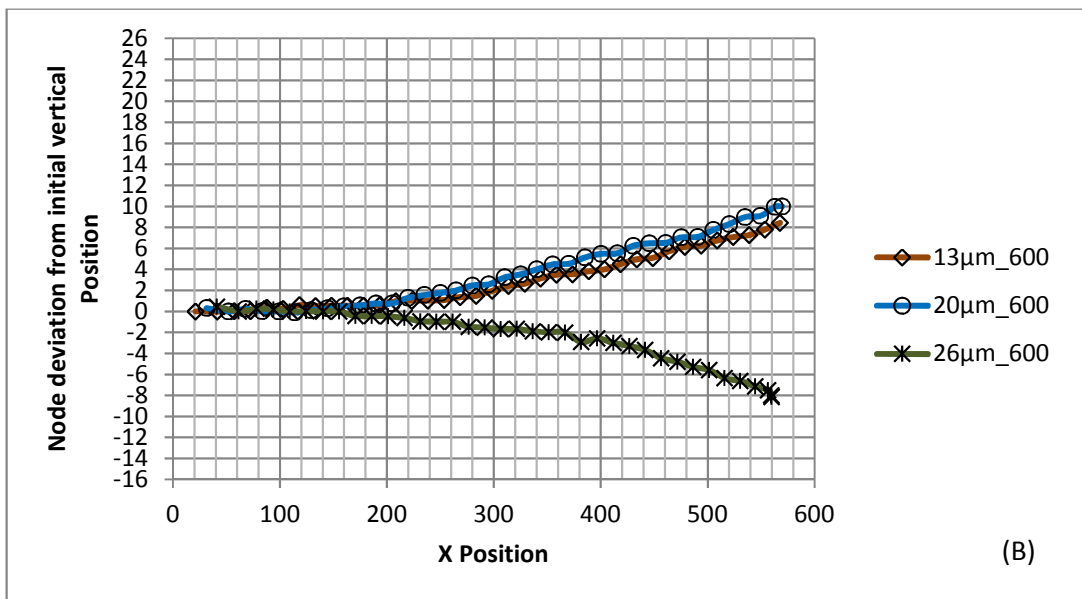
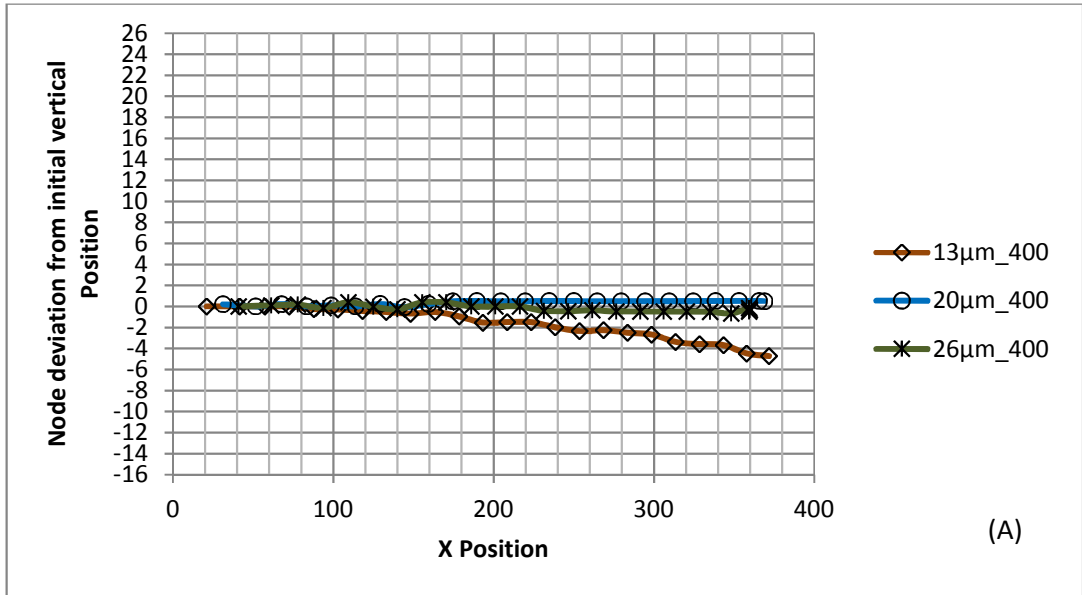
### 5.2.1 Domain Size

#### ***The influence of Domain size on Droplet flow: Square domain (NX=NY).***

Figure 5.1 represents the inlet and outlet region with a droplet in centre of NY for y coordinate and equivalent radius away from the inlet boundary for x coordinate. The main purpose of the study is to identify the NX domain length, where the droplet flows through the domain with small amounts of numerical diffusion. Diffusion is observed where the initial droplet radius shrink in the flow with an uneven interface reduction, and effects a shift in the centre position of the droplet. Therefore different domain sizes were studied to minimise the effects of diffusion of droplet. Initially domain sizes of 400×400,600×600,800×800 and 1000×1000 were simulated as shown in Figure 5.1 with a velocity boundary condition. The inlet has a force equilibrium velocity and zero gradient at the outlet (explained in section 4.4.4 and 4.4.5). Droplets with radii of 20, 30 and 40 LB units were studied, in real terms droplet radius are 13µm, 20µm and 26µm.

The density ratio of water to diesel was 1.2, dynamic viscosity ratio of diesel to water was 2 and a square domain size (NX=NY) was used. Also Gww(water)-interaction potential of 0.80 and Goo(diesel)-interaction potential of 0.44 (discussed in section 4.8.2) were used. An inlet velocity of 0.019 LB units were simulated, corresponding to a velocity 0.15m/s. Actual filtration face velocity is below 0.003m/s, but this model only able to deal with part of a real parameter range. Mainly because droplets velocity lower than 0.019 LB units tends to diffuse unpredictably in most of the domain sizes. Simulation were run for 800000 time steps, these number of time steps were chosen for droplet to reach the outlet boundary and disappear. The “imfindcircles” matlab function was used to analyse the results, where it provides the radius and the centre of droplet location. Ideally in the absence of any error, the droplet should have a zero node deviation from initial vertical position, suggests that the droplet follows the streamline. Figure 5.2 (A),(B),(C) and (D) shows that domain size 1000×1000 has less diffusion or node deviation of droplet and follows the streamline. This suggests that

water (Gww) and diesel (Goo) interaction potential values have an influence on droplet diffusion for a particular domain size.



The caption for the graphs above (A & B) are in Figure 5.2 on next page.

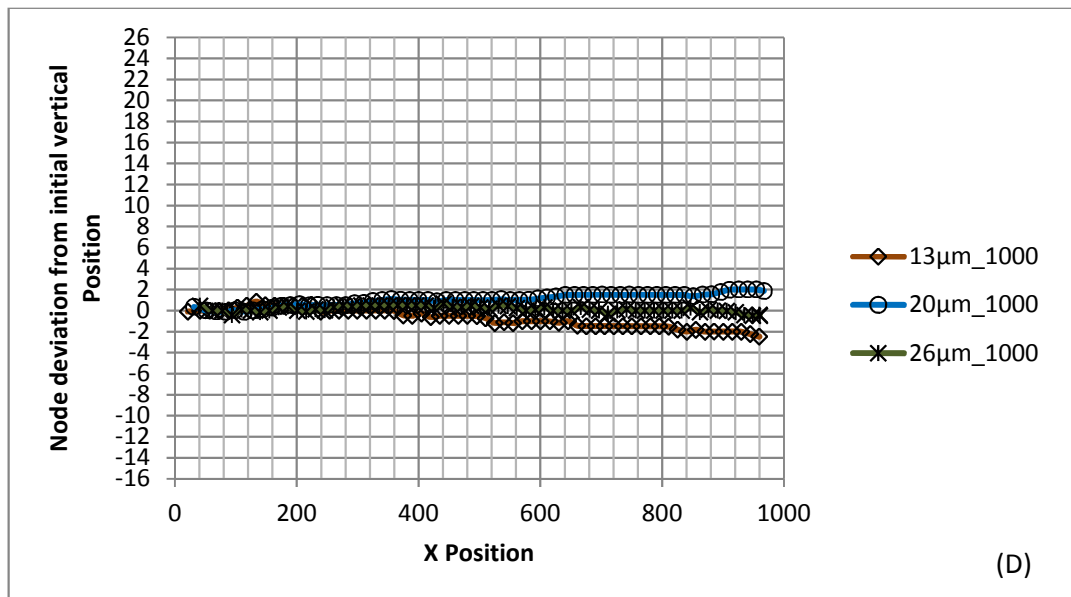
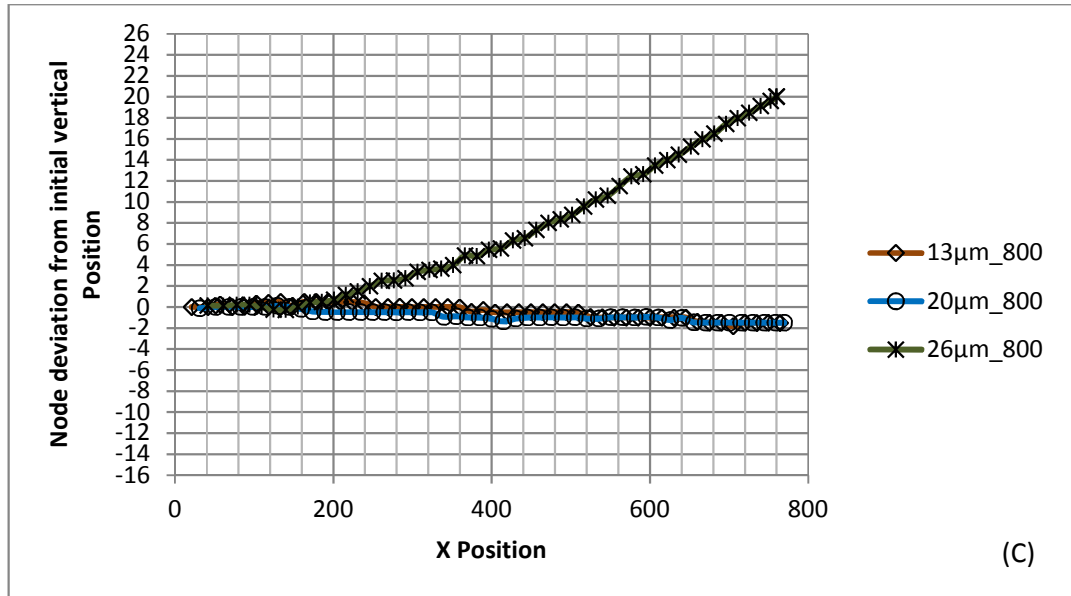
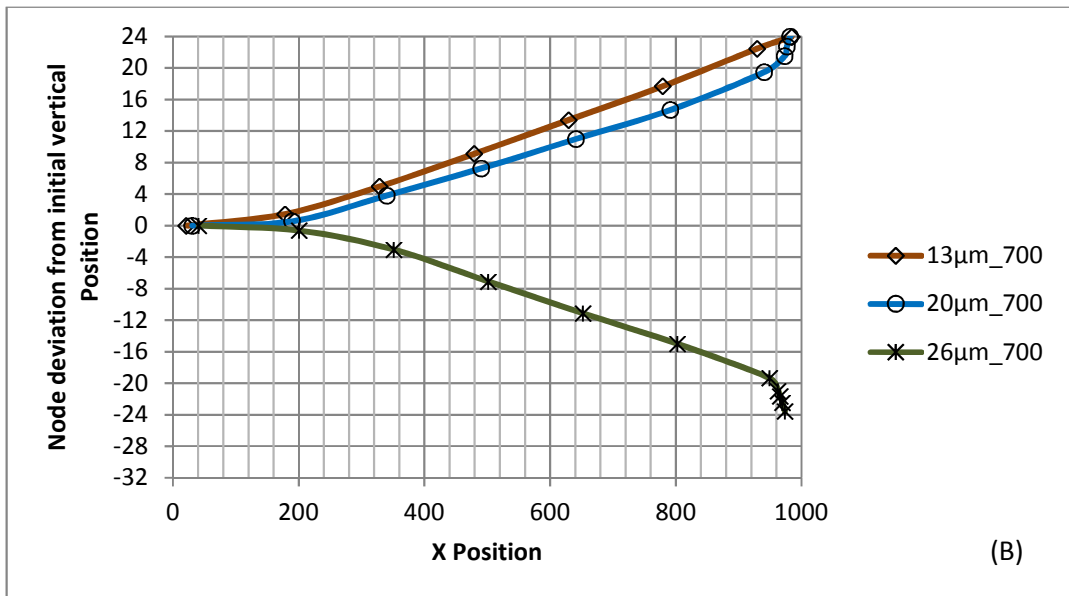
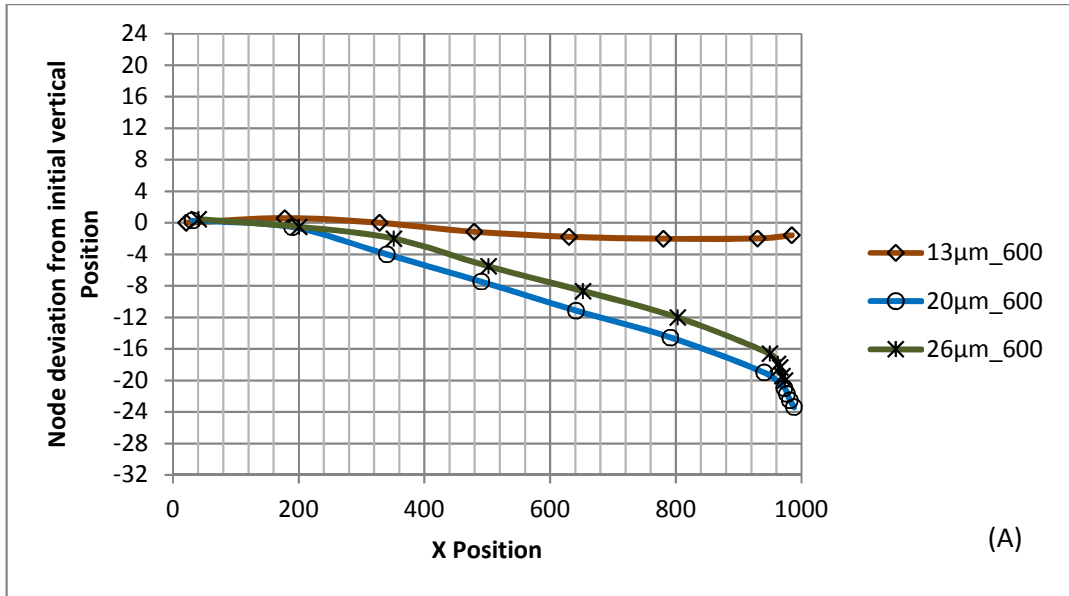


**Figure 5.2** Node deviation from initial vertical position versus x position in the domain for droplet sizes of 20,30 and 40 (respectively 13, 20 and 26  $\mu\text{m}$ ). (A) of 400x400, (B) OF 600x600, (C) of 800x800 and (D) of 1000x1000 domain size.

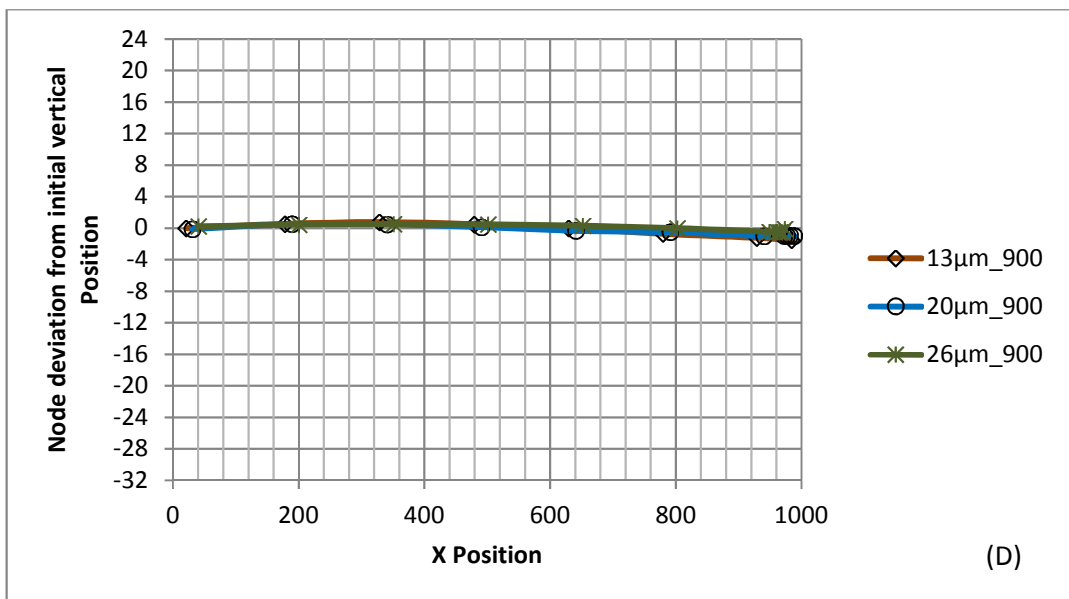
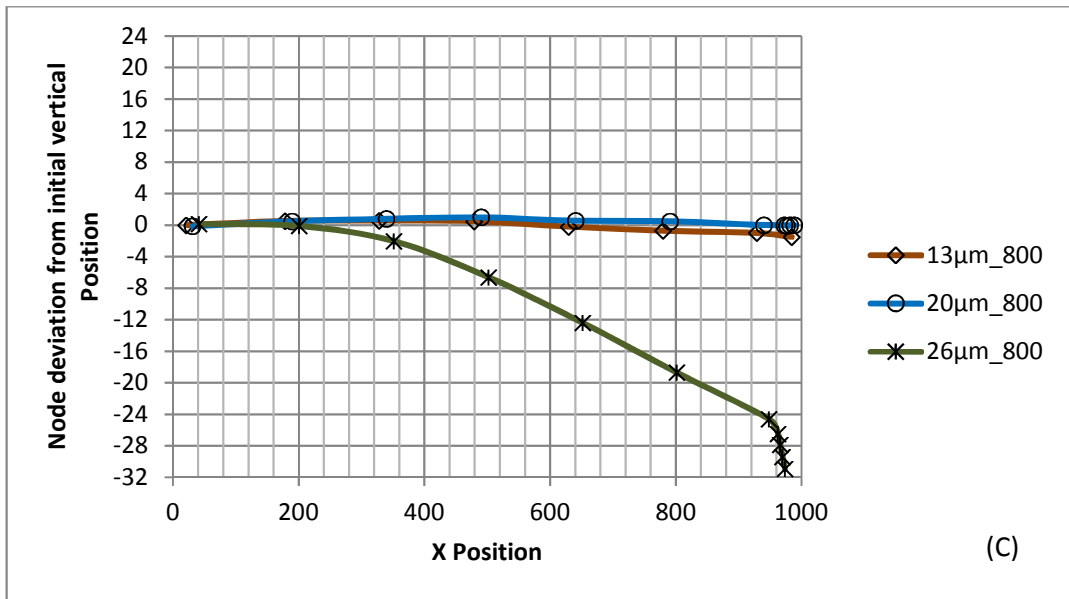
***Rectangular domain (Same NX=1000) size influence in the droplet flow***

Minimising the droplet diffusion is an essential criteria for simulation, therefore NY Domain size of 600,700,800, 900 and 1000 were simulated for same conditions and parameters as the Square Domain (NX=NY) size (section 5.2.1). Figure 5.3 (A), (B), (C), (D) and (E) respectively has NY domain size of 600, 700, 800, 900 and 1000. The results suggest that 1000x

900 (D) has less diffusion or node deviation of droplet and droplet follows the expected streamline.



The caption for the graphs above (A & B) are in Figure 5.3 on page 107.



The caption for the graphs above (C & D) are in Figure 5.3 on next page.

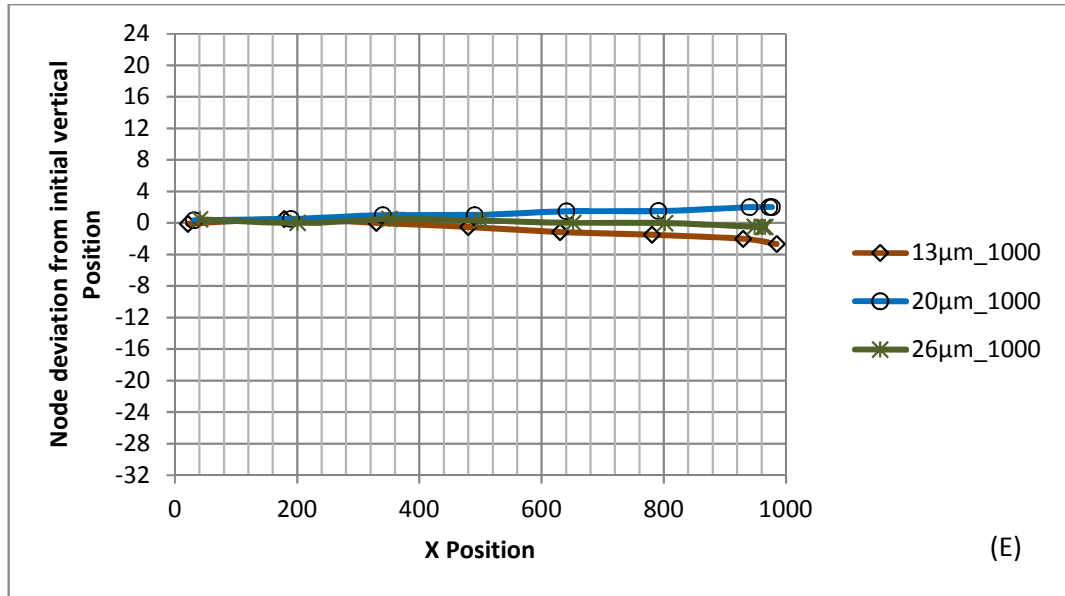


**Figure 5.3** Node deviation from initial vertical position versus x position in the domain for droplet sizes of 20,30 and 40 (respectively 13, 20 and 26  $\mu\text{m}$ ).  $N_X=1000$  and  $N_Y$  Domain size of (A) 600, (B) 700, (C) 800, (D) 900 and (E) 1000 were simulated for same conditions & parameters as Square Domain ( $N_X=N_Y$ ).

### ***Droplet sizes diffusion in domain size of 1000x 900***

Within the MCMP Shan-Chen model diffusion is inevitable. Therefore droplet diffusion in nodes is compared near the outlet boundary to its original droplet size. Figure 5.4 shows that as the droplet radius size increase the diffusion rate (in nodes) measured will decrease. Also notice that diffusion happens mostly on the initialisation time step in this domain size. Therefore initial radius specified in the programme (LBM algorithm) is not the actual radius in the flow, due to the diffusion or shrinkage of the droplet. This suggest that initialisation of droplet require a certain number of time steps for droplet to reach its equilibrium radius.

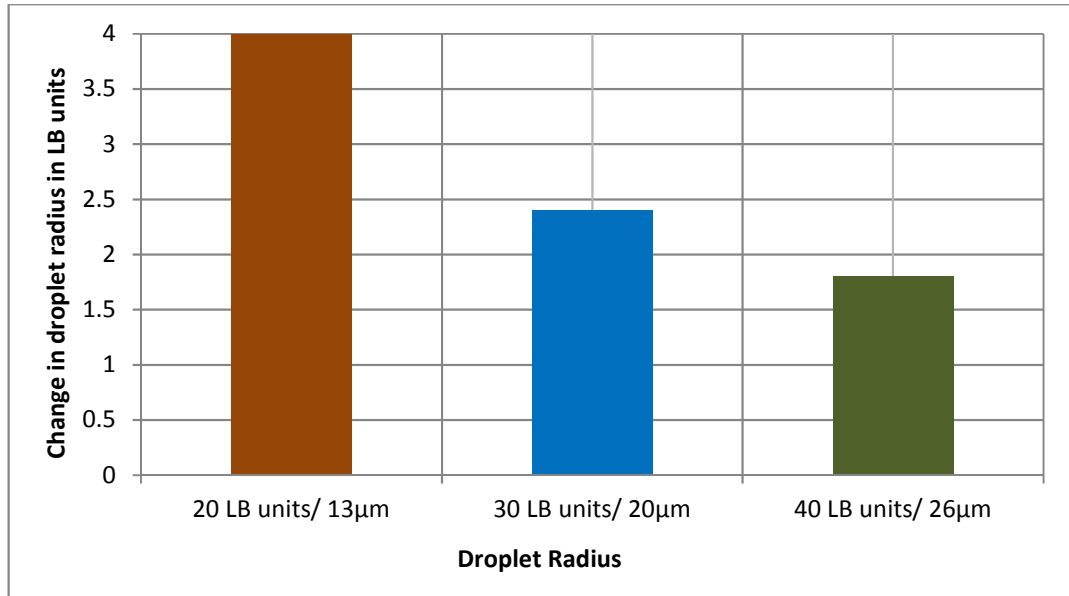
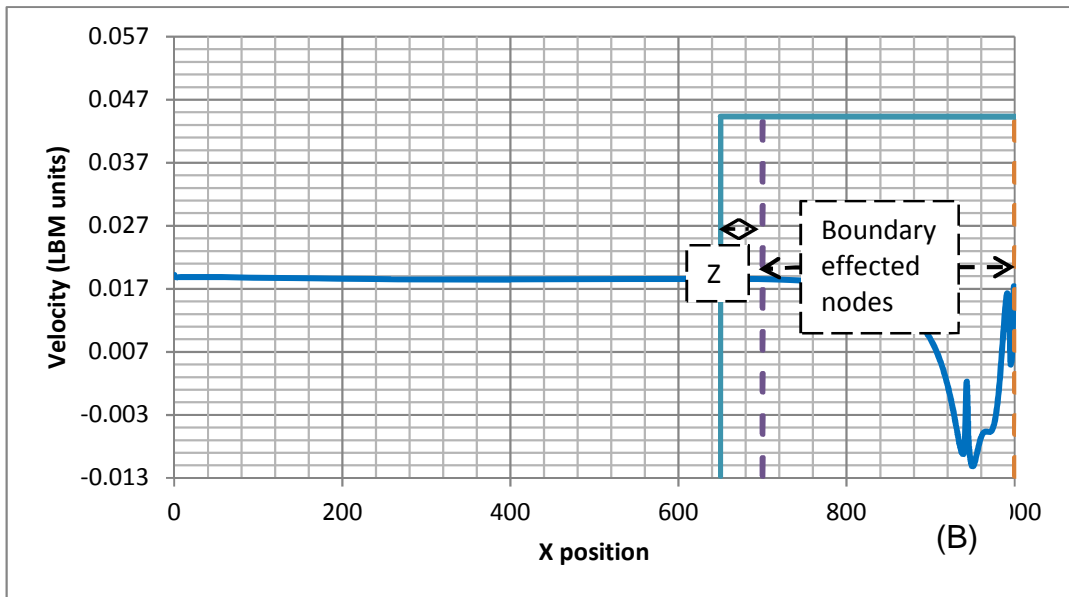
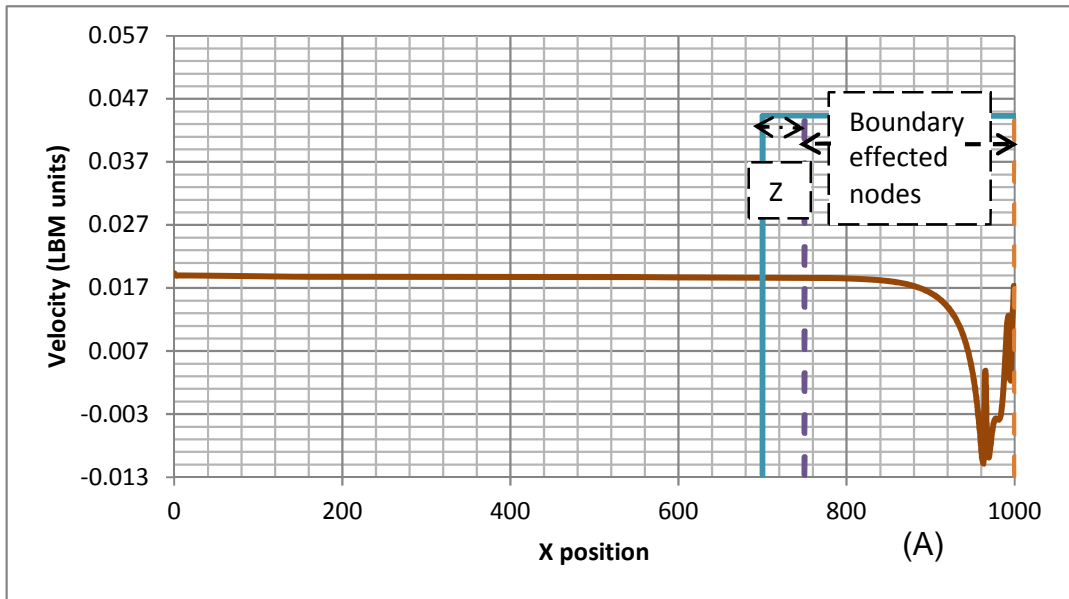


**Figure 5.4** Comparison of change in droplet radius in LB units near inlet and outlet for different droplet sizes.

### 5.2.2 Influence of outlet Boundary condition

A zero gradient condition (explained in section 4.4.5) was used as the outlet boundary condition. Outlet conditions are problematic for multiphase flow, when a drop goes through, gradient (&pressure)  $\neq 0$ . Hence there was an effect on the flow velocity as the droplet reaches the outlet boundary. Therefore domain size of 1000×900 were simulated for same conditions with other set as for section 5.2.1. Figure 5.5 (A), (B) and (C) shows the nodes which have been affected for a droplet size of 20 LB units (13µm), 30 LB units (20µm) and 40 LB units (26µm) with a inlet velocity of 0.019 LB units ( 0.15m/s). Z in Figure 5.5 (A), (B) and (C) is the length of the buffer region between the steady velocity and the unsteady velocity or boundary effected region. 50 nodes were selected for the intermediate region Z as a results of this work. Finally droplet sizes of 20, 30 and 40 LB units would have a same inlet velocity region of 700, 650 and 600 LB nodes respectively.



The caption for the graphs above (A & B) are in Figure 5.5 on next page.

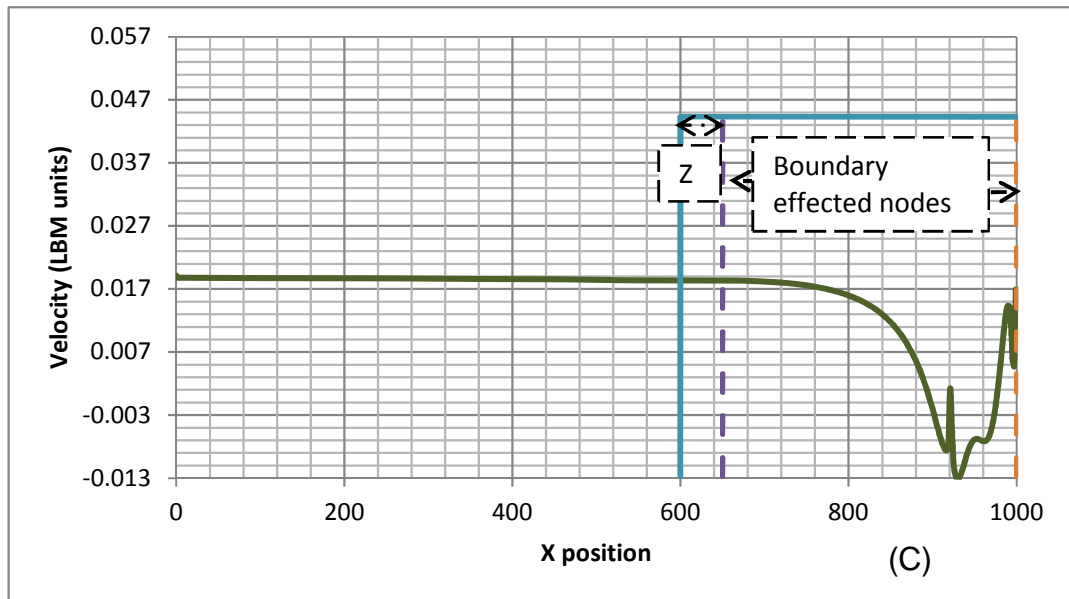


**Figure 5.5** Figure 5.5 (A), (B) and (C) shows the nodes, which has been effected for a droplet size of 20 LB units/ 13 $\mu\text{m}$ , 30 LB units/ 20 $\mu\text{m}$  and 40 LB units/ 26 $\mu\text{m}$  in a velocity profile.

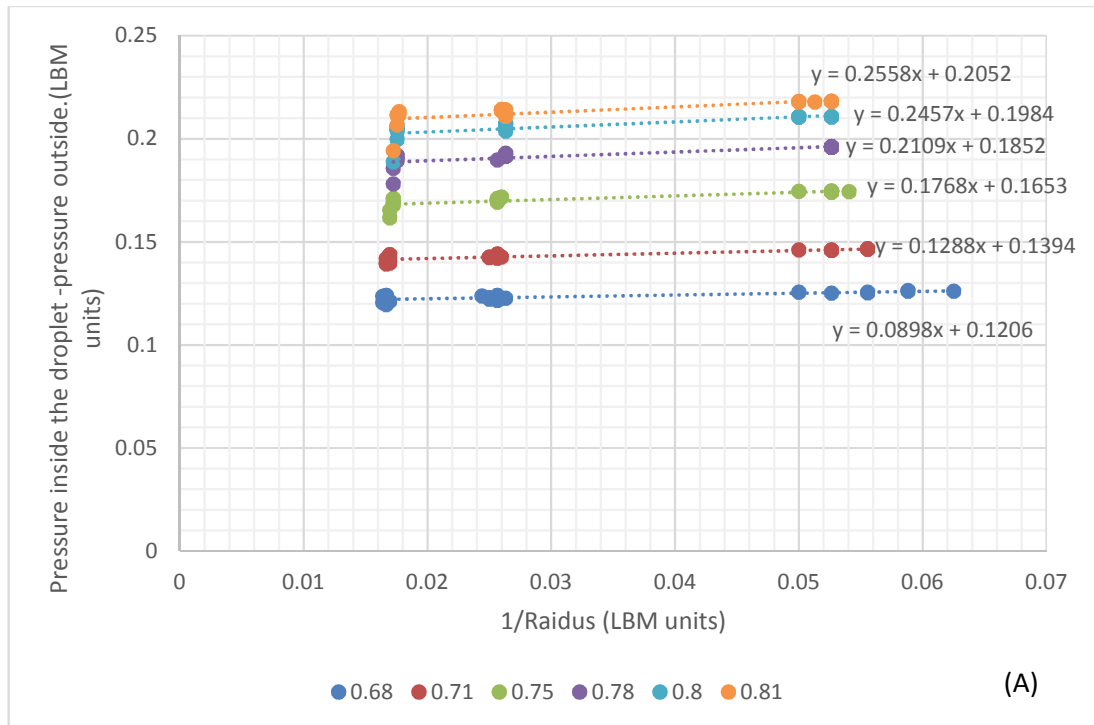
### 5.2.3 Laplace Law for Interfacial tension

The Laplace law is an important benchmark for droplets in equilibrium. For a two-dimensional simulation, this reads:

$$\Delta P = \frac{\sigma}{R} \quad \text{Equation 5.1}$$

where  $\sigma$  is the surface tension and  $R$  (measured in dense phase) is the droplet radius in LB units and  $\Delta P$  is the difference in pressure inside and outside the droplet. 2D simulations are performed in a 1000 $\times$ 900 (LBM units) domain size, the periodic boundary condition was applied to domain boundaries. Droplets of 20, 40 and 60 radii (LB units) were simulated for G<sub>ww</sub>- interaction potential of 0.68, 0.71, 0.75, 0.78, 0.80 and 0.81 and a range of diesel: water dynamic viscosity ratios, namely 2,3,4 and 5. The viscosity ratios were achieved by fixing the relaxation time, tau ( $\tau$ ), for water at 0.71 and varying tau for diesel (values:1.00,1.26,1.51,1.76). The interfacial tension can be determined simply by measuring the radii and inside and outside pressures of the droplets after 50000 time steps. These number of time steps were chosen to determine the variation of pressure difference with time. It was observed that variation in pressure difference

with time was negligible. Figure 5.6 (A) shows a gradient of 0.09, 0.129, 0.177, 0.211, 0.245 and 0.255 LB units [146]. After converting the LB units into real values, the respective interfacial tension are 0.01, 0.015, 0.020, 0.025, 0.028 and 0.03 (N/m). Also (B) shows a gradient of 0.246, 0.24, 0.25 and 0.25 LB units; these correspond to a real interfacial tension value of 0.0285 (N/m). Since using different tau values for diesel and water has an effect on initialisation time step, therefore it produces an offset pressure initially which can be noticed through interception values in Figure 5.6 (A)&(B).



The caption for the graph above (A) is in Figure 5.6 on next page.

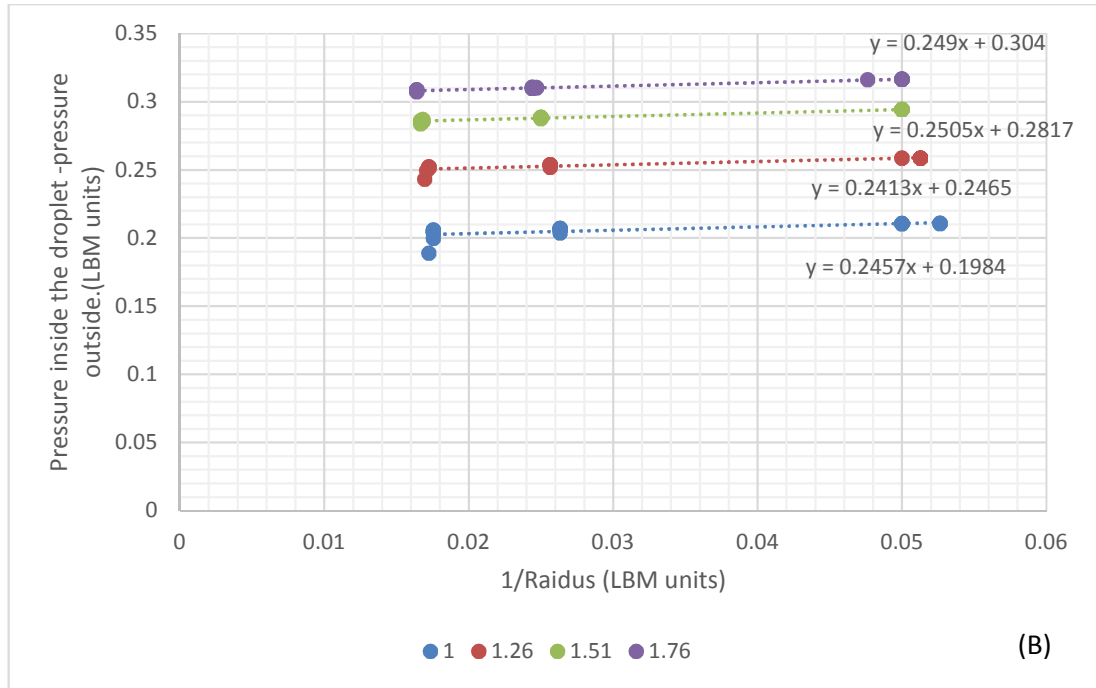


**Figure 5.6** Droplets of 20, 40 and 60 radii were simulated for (A) Gww-interaction potential of 0.68, 0.71, 0.75, 0.78, 0.80 and 0.81, (B) different diesel tau values and respectively are 1.00 , 1.26, 1.51 and 1.76 ( fixed water tau value is 0.71 ).

### 5.2.4 Contact Angle behaviour

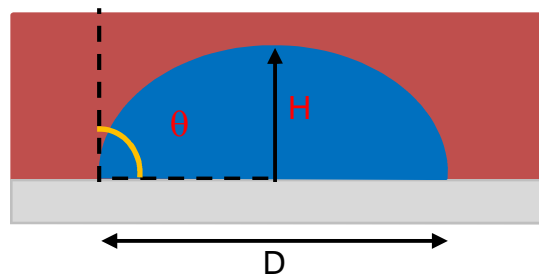
Geometrically, the contact angle can be calculated by measuring the drop diameter and the height of the apex (Figure 5.7).

$$\frac{\theta}{2} = \tan^{-1}\left(\frac{H}{D}\right) \quad \text{Equation 5.2}$$

This method yields reasonable results when the liquid drop is extremely small. However, the spherical shape assumption cannot be applied if the drop shape is large enough to be affected by gravity (Bond number).

As explained in section 4.8.3, the wettability of the solid surface is incorporated in the model by specifying the density at the wall in terms of a normalised wettability coefficient. To calibrate the wettability coefficient in terms of the corresponding contact angle, 2D simulations were performed in a 2000x2000 (LBM units) domain size, the periodic boundary condition was applied to domain boundaries. Solid wall of 2000x10 (LBM units) was initialised at the centre of the domain. Then circular (water) droplet was deposited on top of the solid wall as shown in Figure 5.8(A). Simulations

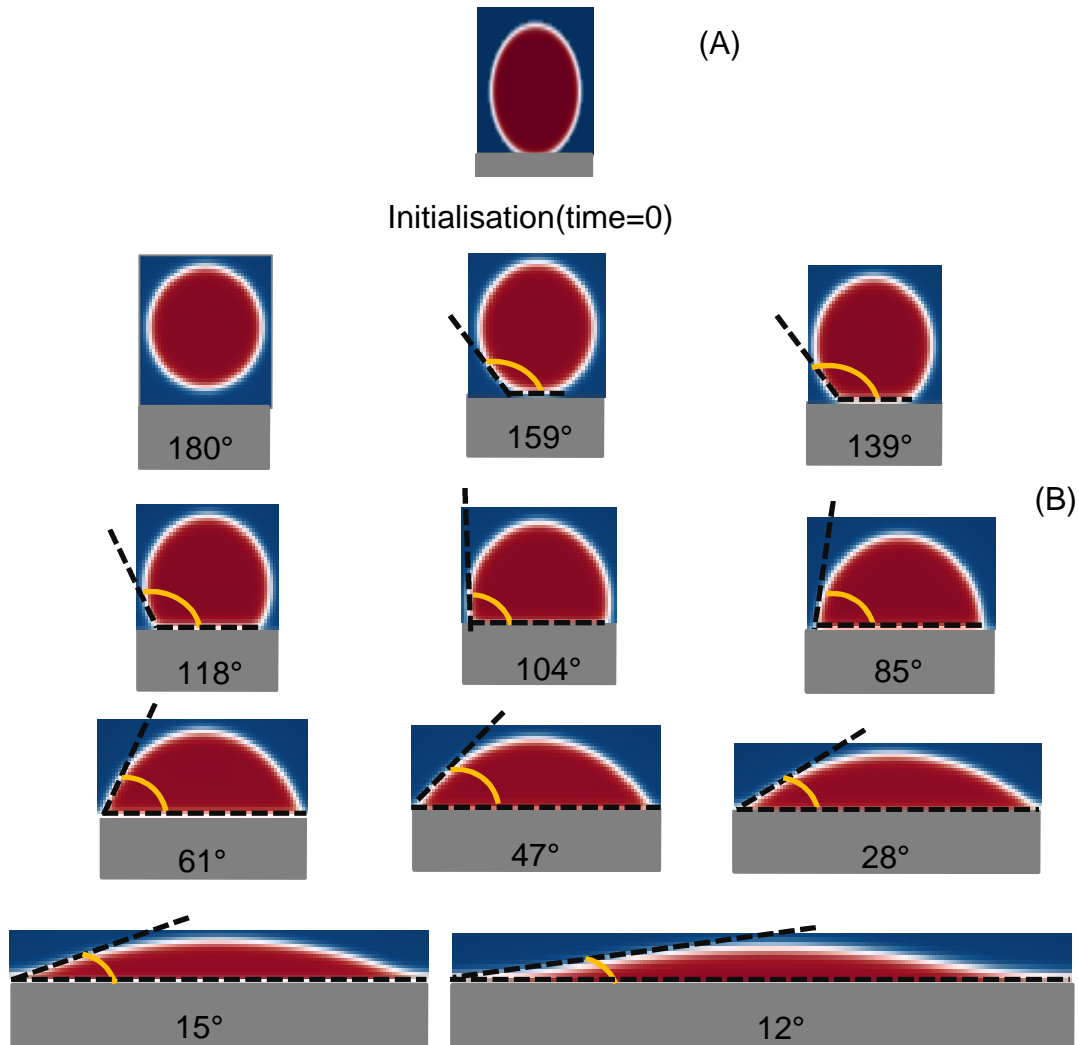
were analysed at 50000 time step (LBM units). These number of steps were chosen to determine the variation of the droplet diameter and height of the apex. Finally notice that after initialisation time step the variation were negligible. The effect of droplet size, interfacial tension and dynamic viscosities for contact angle were measured. Matlab “boundary function” was used to quantity the height and diameter. These values were used in Equation 5.2[99, 177, 178] to calculate the contact angle. Figure 5.8(B) represents the analysed contact angles for a droplet radius of 40 (LBM units) with the dynamic viscosity ratio of diesel to water being 2.



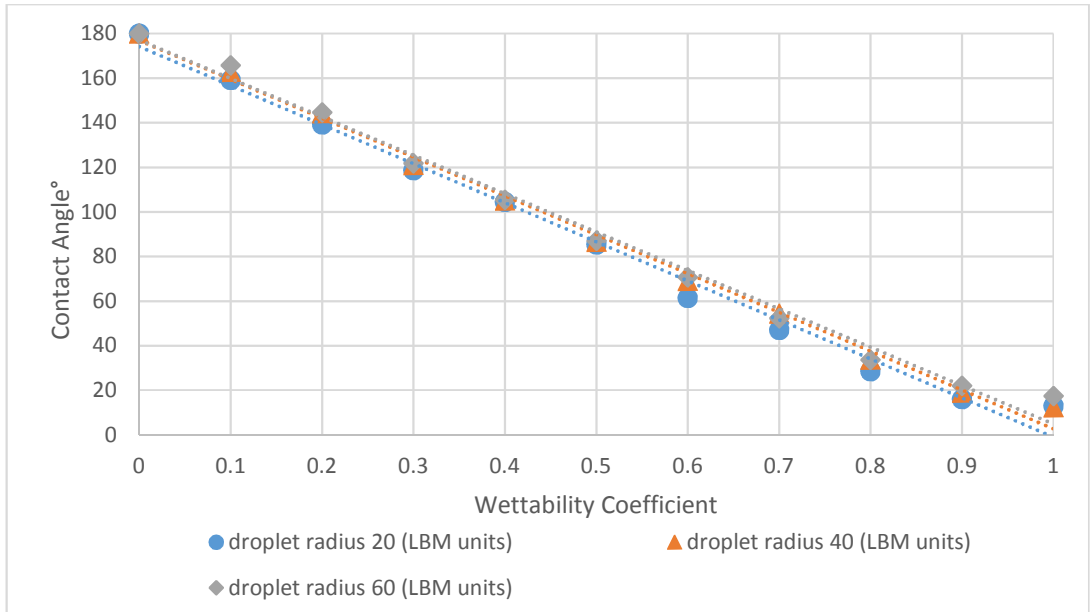
**Figure 5.7** Demonstration of the  $\theta/2$  method according to Equation 5.2.

Figure 5.9 shows the 20 , 40 and 60 LBM unit radius of droplets with an actual radius of  $13\mu\text{m}$ ,  $26\mu\text{m}$  and  $40\mu\text{m}$ . Water and diesel dynamic viscosities were respectively 0.001 Pa.s and 0.002 Pa.s. Figure 5.10 shows the effect of 40 LB unit radius of droplet was simulated for Gww-interaction potential values of 0.68, 0.71, 0.75, 0.78, 0.80 and 0.81. These respectively correspond to interfacial tension of 0.01, 0.015, 0.02, 0.025, 0.0285 and 0.03 N/m. The water and diesel dynamic viscosities were respectively 0.001 Pa.s and 0.002 Pa.s. Figure 5.11 shows the effect of 40 LB unit radius of droplet was simulated by fixing the relaxation time/tau ( $\tau$ ) for water at 0.71 and varying tau for diesel at 1.00, 1.26, 1.51 and 1.76. These respectively correspond to dynamic viscosity of water as 0.001(Pa.s) and diesel as 0.002, 0.003, 0.004 and 0.005 (Pa.s). Line of best fit are included in figure 5.9-5.11, all showing a negative gradient and indicating that the relationship between wetting coefficient and contact angle is approximately linear and is little influenced by droplet size, interfacial tension or viscosity ratio. The

variation of contact angle at equivalent wettability coefficient with these three factors is  $\pm 2.5^\circ$ ,  $\pm 6.5^\circ$  and  $\pm 5.0^\circ$  respectively.



**Figure 5.8** (A) shows the initialisation time step and (B) is the different contact angle of 40 LBM unit radius droplet with a dynamic viscosity ratio of diesel to water is 2.



**Figure 5.9** Calibration of wettability coefficient with contact angle for different droplet radii and diesel: water dynamic viscosity ratio 2.

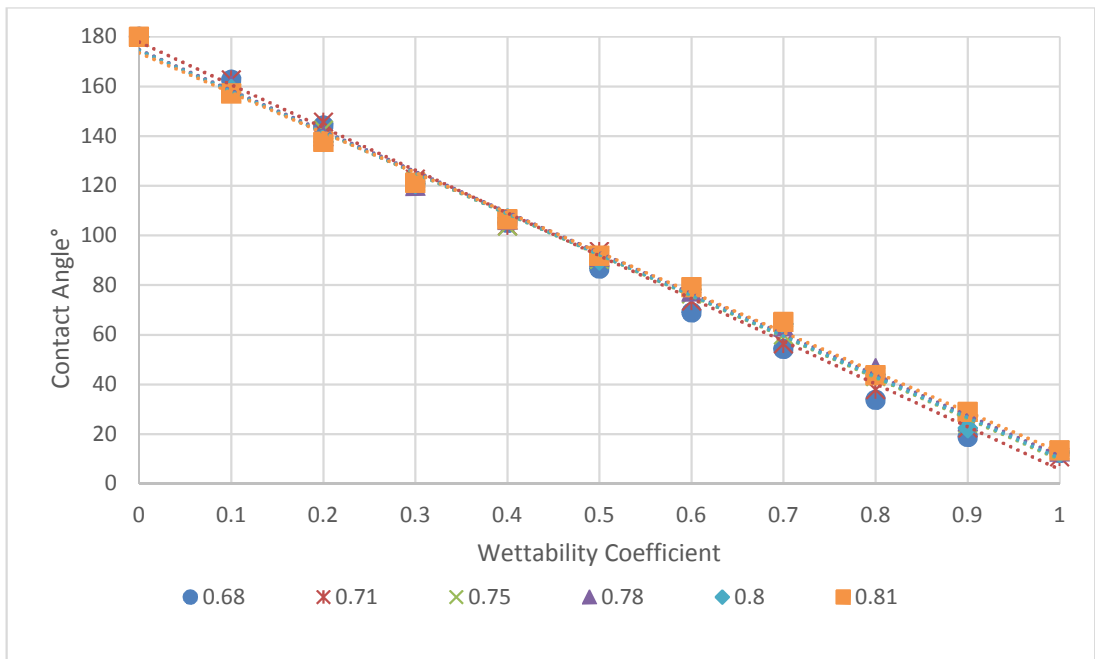


**Figure 5.10** Calibration of wettability coefficient with contact angle for different  $G_{ww}$ -interaction potential values are 0.68, 0.71, 0.75, 0.78, 0.80 and 0.81 and diesel: water dynamic viscosity ratio 2.

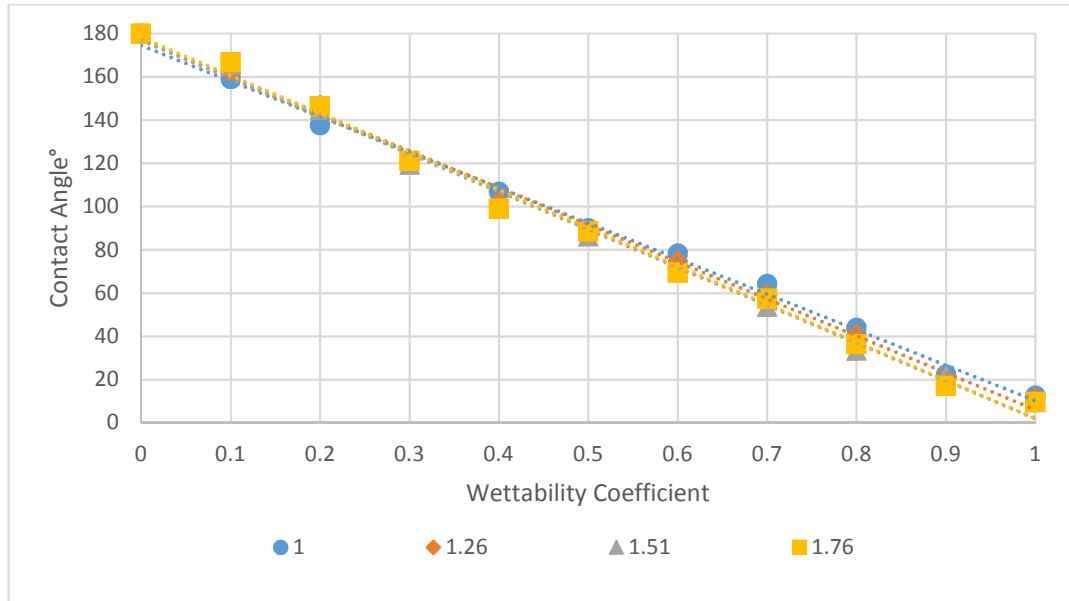


**Figure 5.11** Calibration of wettability coefficient with contact angle for different relaxation values for diesel are 1, 1.26, 1.51 and 1.76. Respective diesel: water dynamic viscosity ratio are 2, 3, 4 and 5.

### 5.2.5 Summary

The results suggest that domain size of 1000x 900 in Figure 5.3 (D) has less diffusion (initial droplet radius shrink with an uneven interface reduction, and effects a shift in the centre position of the droplet) of droplets and the droplet follows the streamline. Figure 5.4 shows that as the droplet radius size increases, the diffusion rate in nodes will decrease. It was also noticed that diffusion happens mostly on the initialisation time step in this domain size. The outlet boundary condition affect the useful domain size for different droplet sizes. For example droplet of 20, 30 and 40 LB units require domain sizes of respectively NX= 700, 650 and 600 LB nodes. Using different tau values (different dynamic viscosity) for diesel and water has an effect on initialisation time step, therefore it produces an offset pressure initially, which is noticed through interception values in Figure 5.6 (A)&(B).

### 5.3 Validation against FVM/VOF simulations of free droplet coalescence.

Mohammadi et al[179] used the finite volume numerical method (FVM) in conjunction with volume of fluid (VOF) approach for interface capturing method to model water droplets coalescence behaviour in diesel. Mohammadi et al[179], initially simulated the tetradecane droplet coalescence in nitrogen gas and validated that with experimental results from Qian and Law (1997) (Where the coalescence behaviour and time were validated). Then Mohammadi et al modelled a film of continuous phase(diesel) which is trapped between two droplets (water) as shown in Figure 5.12 , and as the both droplets are close to each other, continuous phase should be drained out to allow the droplets to reach each other. And then both droplets coalesce. Note, the coalescence time doesn't have a unique definition from literature or Mohammadi et al[179] it will be described later.

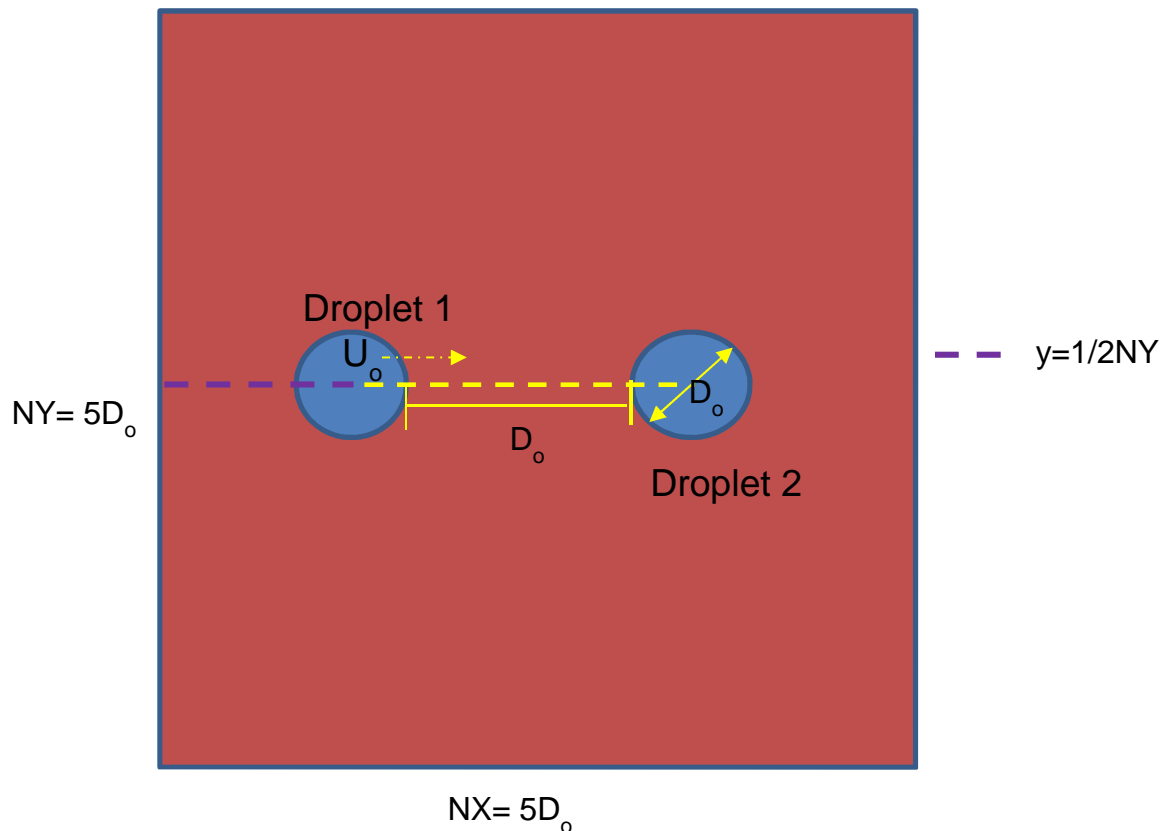


**Figure 5.12** Domain size and droplet separation for simulation cases. Water droplets are in blue and diesel the continuous phase in red.

Figure 5.12 shows two water droplets of the same diameter in diesel separated by one droplet diameter between them for simulation for coalescence behaviour. A pair of droplets with the same diameters of  $D_0$  was identified in which the left droplet (droplet 1) starts its movement with a specified velocity of  $u_0$  towards the stagnant droplet (droplet2). The domain size has a dimension of  $5D_0 \times 5D_0$  with outer wall as periodic boundary condition. The conditions applied for the simulations are presented in Table 5.1.

### 5.3.1 Analysis method for stage 1 & 2 Coalescence time

Stage 1 coalescence time from Mohammadi et al[179] defined as “the time it takes for a pair of droplets with the same diameters of  $D_0$  and initial separation distance of  $D_0$  with a relative initial velocity of  $u_0$  move towards each other until the film of continuous phase moves out and the droplets coalesce”. Visual representation of Stage 1 coalescence time is shown in Figure 5.13.

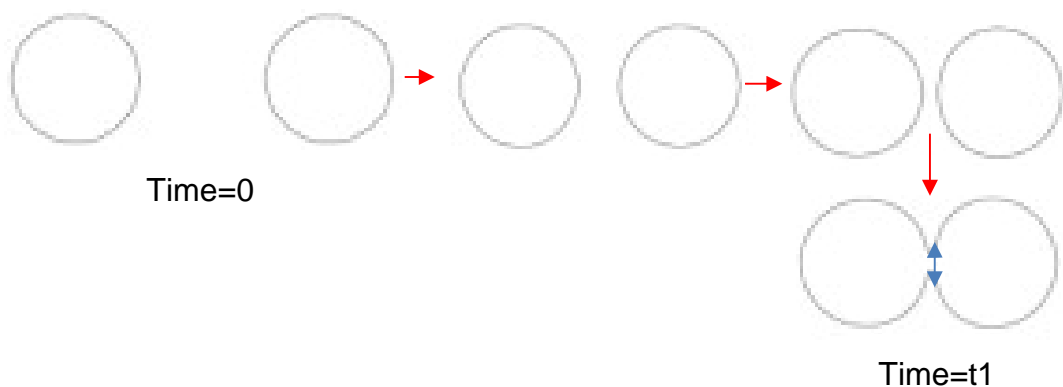


**Figure 5.13** Visual representation of stage 1 coalescence time at time=0 to time=t1.

In LBM simulation, the Stage 1 coalescence time from Mohammadi et al[179] is followed with an additional quantifying method. In Figure 5.14, (A) shows the initial time stage for simulation and (B) is during the coalescence time stage. In (C), the density profile has been plotted along the horizontal centerline of the domain ( $y=1/2NY$ ). Also the red and yellow lines in (B) are respectively the vertical distance and horizontal distance during the coalescence time stage. Figure 5.15 (A) shows the density profile along the

horizontal centreline of the domain ( $y=1/2NY$ ), (B) shows the density profile along the vertical axes at coalescence time stage (Figure 5.14 (B) red line position for  $x$ ). Red and yellow lines had a distance of 40 LB units. 40 LB units was chosen because 30 and 50 LB units roughly had a difference of  $\pm 0.01$  millisecond in coalescence timing stage.

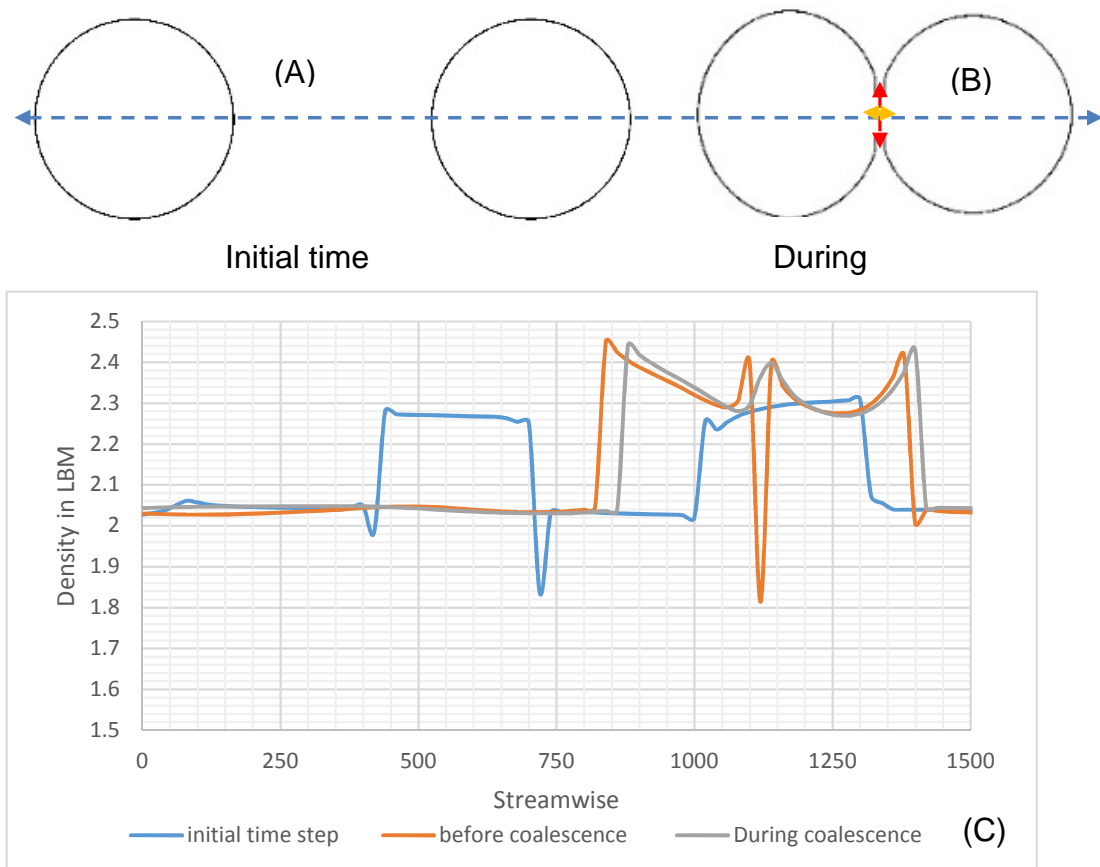


**Figure 5.14** (A):the initial time step,(B)during the coalescence stage. Where the blue dotted line represents the horizontal centreline of the domain ( $y = 1/2NY$ ). And (C) is the density profile plotted at  $y = 1/2NY$ . Also the red and yellow lines in (B) are respectively the vertical distance and horizontal distance during the coalescence time stage.

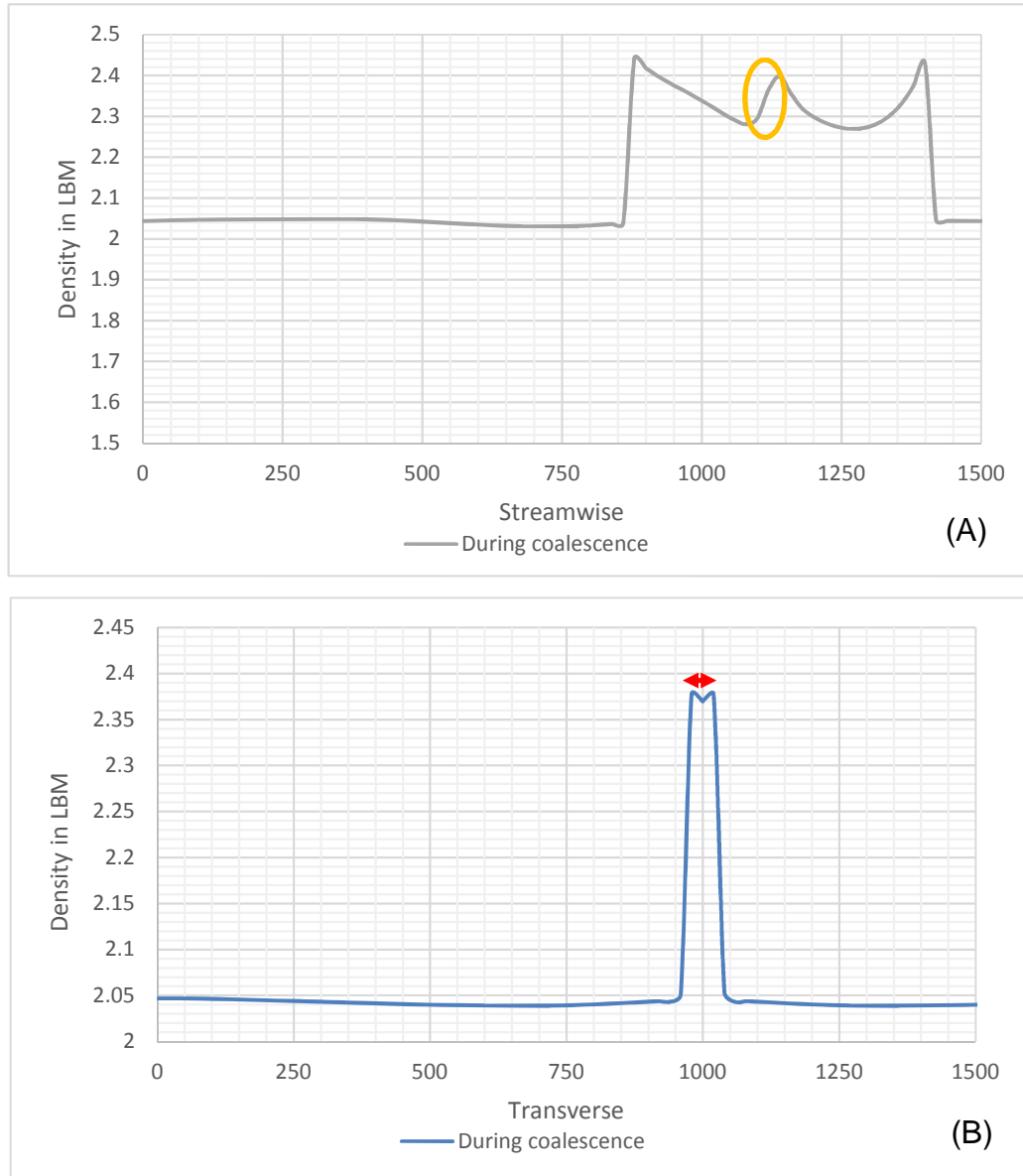


**Figure 5.15** (A):is during coalescence time stage, shows the density profile along the horizontal centreline of the domain ( $y = 1/2NY$ ). (B):is the density profile along the vertical axes at coalescence time stage (Figure 5.14 (B) red line position for x).

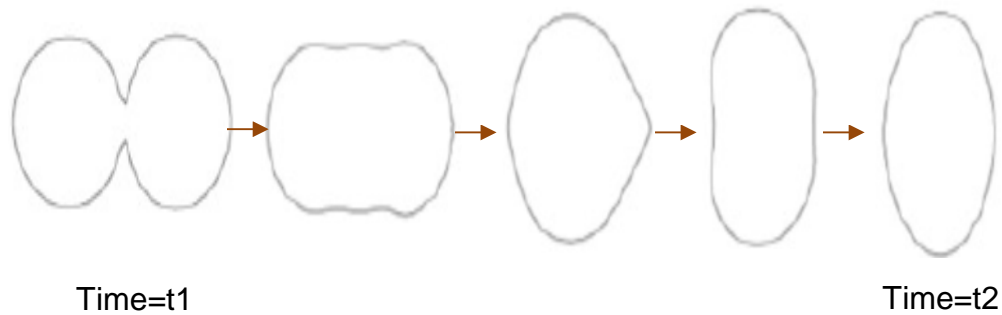


**Figure 5.16** Stage 2 coalescence time is shown in these images. Coalescence time is the difference of  $t_2$  &  $t_1$  .

Figure 5.16 shows stage 2 coalescence time in Mohammadi et al[179] and LBM simulation. This method is useful for interfacial tension variation and stage 2 coalescence timing is the difference of  $t_2$  and  $t_1$ . Time=  $t_1$  is explained in stage 1 coalescence time (Figure 5.13). Time= $t_2$  is chosen at that particular image due to the available data in Mohammadi et al[179] for the smallest interfacial tension (0.01N/m). Interfacial tension is effective for how fast the droplets coalesce. Therefore stage 1 coalescence timing doesn't influence the interfacial tension.

### 5.3.2 Results for speed

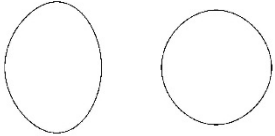
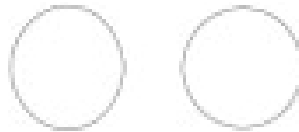
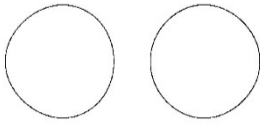
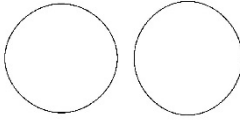
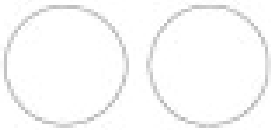
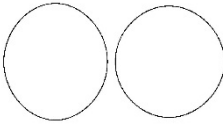
Mohammadi et al[179] studied five different collision velocities of 0.75, 1.0, 1.25, 1.5, and 2.0 m/s for a system consisting of two water droplets in stagnant diesel as in Figure 5.12. Here, velocities of 0.75, 1.0 and 1.25 m/s studied using LBM simulations. Velocities higher than 1.25 m/s were not possible due to limitation on the speed for incompressible flow in LBM. Stage 1 coalescence timing was studied for different collision velocity. The operating conditions and two phase properties were considered as provided in Table 5.1 for simulations 1–3. Table 5.2 -5.4 shows the snapshots of the coalescence progress for each simulation (collision velocity) in LBM validation with Mohammadi et al[179] model. First and second column of time represents respectively the Mohammadi et al[179] time and LBM simulation time. Figure 5.17 shows the stage 1 coalescence time as a function of collision velocity as calculated from the present LBM simulations

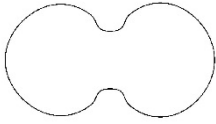
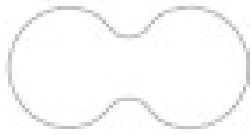
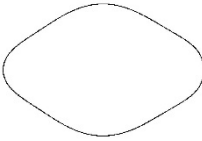
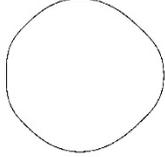
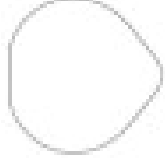
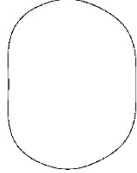
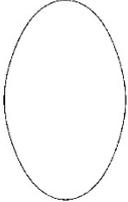
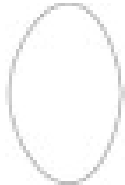
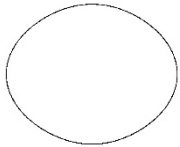
and in Mohammadi et al. Then curves(power-law) of best fit are included in Figure 5.17. Good agreement is seen.

**Table 5.1** The operating conditions and two phase properties for different velocity. (l.b.u= lattice Boltzmann units)

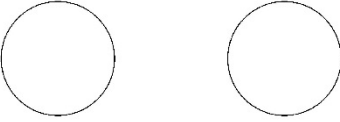
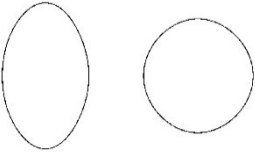
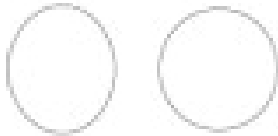
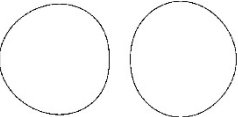
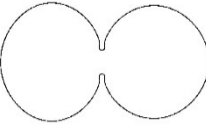
	Simulation 1		Simulation 2		Simulation 3	
	Mohammadi value	LB value	Mohammadi value	LB value	Mohammadi value	LB value
Reynolds	65.6	65.7	87.5	87.3	109.4	109.8
Weber	4.01	4.02	7.14	7.10	11.16	11.23
face velocity	0.75 (m/s)	0.0365 (l.b.u)	1 (m/s)	0.048 (l.b.u)	1.25 (m/s)	0.061 (l.b.u)
			Common parameters			
			Mohammadi value		Corresponding values l.b.u	
Density of water			1000 (kg/m <sup>3</sup> )		2.47	
Density of diesel			875 (kg/m <sup>3</sup> )		2.043	
Dynamic viscosity of water			0.001 (Pa.s)		0.173	
Dynamic viscosity of diesel			0.002 (Pa.s)		0.341	
Kinematic viscosity of water			1.00×10 <sup>-06</sup> (m <sup>2</sup> /s)		0.07	
Kinematic viscosity of diesel			2.29×10 <sup>-06</sup> (m <sup>2</sup> /s)		0.167	
Diameter of droplet			200 (µm)		300	
surface tension			0.028 (N/m)		0.246	

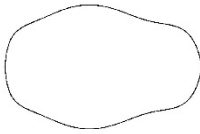
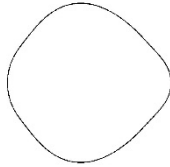
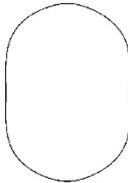
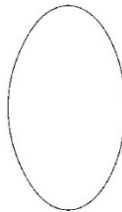
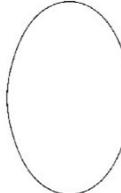
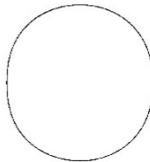
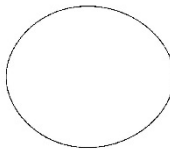
**Table 5.2** shows the snapshots of the coalescence progress for each simulation 1 ( 0.75 m/s collision velocity) in LBM validation with Mohammadi et al[179] model. First and second column of time represents respectively the Mohammadi et al time and LBM simulation time.

		Simulation 1		Mohammadi et al
Reynolds		65.7		65.6
Weber		4.02		4.01
Speed LB Time		0.0365 (Lb units)		0.75 (m/s)
		$\Delta x$	$6.667 \times 10^{-07}$	
		$\Delta t$	$1.15 \times 10^{-08}$	
0	0			
0.3ms	18000			
-	time steps - 0.21ms			
0.4ms	26000			
-	time steps - 0.30ms			
0.5ms	34700			
-	time steps - 0.40ms			
0.6ms	43400			
-	time steps - 0.50ms			

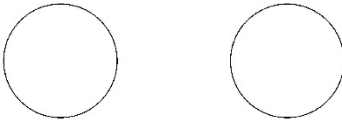
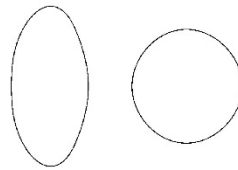
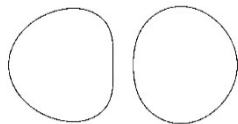
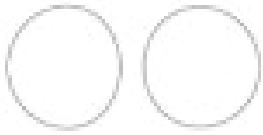
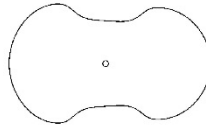
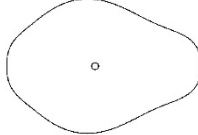
0.7ms -	57200 time steps - 0.66ms		
0.8ms -	61100 time steps - 0.70ms		
0.9ms -	65200 time steps - 0.75ms		
1.0ms -	69800 time steps - 0.80ms		
1.1ms -	73600 time steps- 0.85ms		
1.2ms -	85500 time steps - 0.98ms		
1.5ms -	101900ti me steps- 1.17ms		

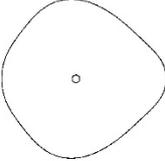
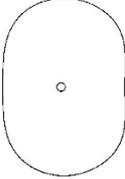
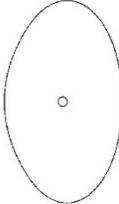
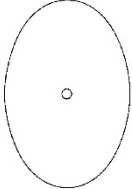
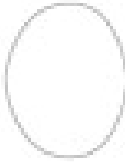
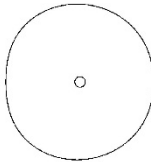
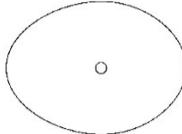
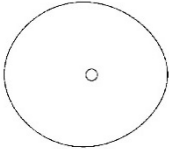
**Table 5.3** shows the snapshots of the coalescence progress for simulation 2 ( 1.00 m/s collision velocity) in LBM validation with Mohammadi. et al (2012)[179] model. First and second column of time represents respectively the Mohammadi et al time and LBM simulation time.

		Simulation 2		Mohammadi et al
Reynolds		87.3		87.5
Weber		7.10		7.14
Speed LB Time		0.0485(Lb units)		1 (m/s)
		$\Delta x$	$6.667 \times 10^{-07}$	
		$\Delta t$	$1.15 \times 10^{-08}$	
0	0			
0.3ms -	16600 time steps - 0.19ms			
0.4ms -	28000 time steps - 0.32ms			
0.5ms -	42000 time steps - 0.48ms			
0.6ms -	46400 time steps - 0.53ms			

0.7ms -	48800 time steps - 0.56ms		
0.8ms -	54700 time steps - 0.63ms		
0.9ms -	59700 time steps - 0.69ms		
1.0ms -	69300 time steps - 0.80ms		
1.1ms -	73200 time steps - 0.84ms		
1.2ms -	81000 time steps - 0.98ms		
1.5ms -	101900ti me steps -1.17ms		

**Table 5.4** shows the snapshots of the coalescence progress for simulation 3 ( 1.25 m/s collision velocity) in LBM validation with Mohammadi et al model. First and second column of time represents respectively the Mohammadi et al time and LBM simulation time.

		Simulation 3		Mohammadi et al
Reynolds		109.8		109.4
Weber		11.23		11.16
Speed LB Time		0.061(Lb units)		1.25(m/s)
		$\Delta x$	$6.667 \times 10^{-07}$	
		$\Delta t$	$1.15 \times 10^{-08}$	
0	0			
0.3ms	18500			
-	time steps - 0.21ms			
0.4ms	28000			
-	time steps - 0.32ms			
0.5ms	43400			
-	time steps - 0.50ms			
0.6ms	49000			
-	time steps - 0.56ms			

0.7ms -	53600 time steps - 0.62ms		
0.8ms -	59300 time steps - 0.68ms		
0.9ms -	67900 time steps - 0.78ms		
1.0ms -	72900 time steps - 0.84ms		
1.1ms -	80500 time steps - 0.93ms		
1.2ms -	89900 time steps - 1.04ms		
1.5ms -	101900 time steps - 1.17ms		

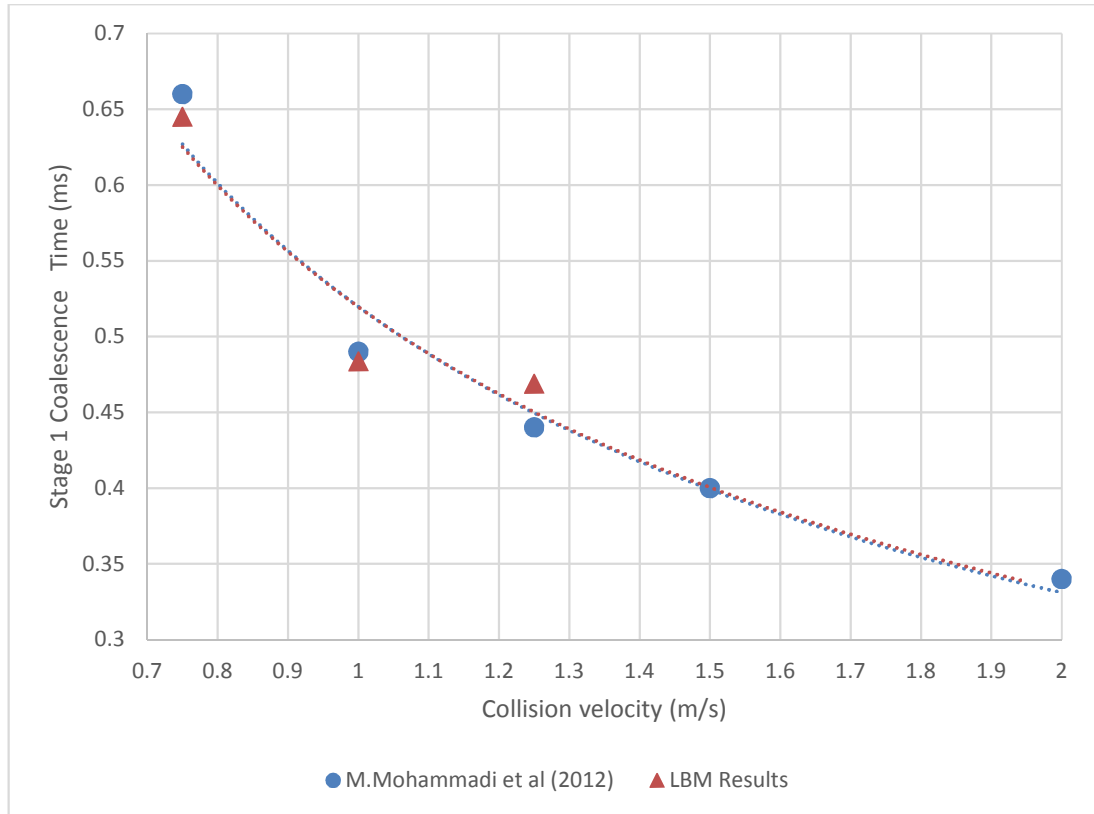


**Figure 5.17** the stage 1 coalescence time versus the collision velocity.

### 5.3.3 Results for Dynamic viscosity

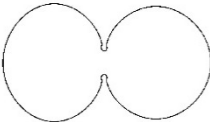
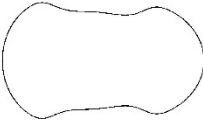
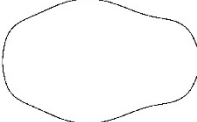
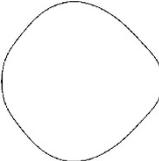
Diesel viscosity determines the resistant force against the approaching movement of the water droplets. When the diesel viscosity is reduced at higher temperatures, the resistant force declines and water droplets coalesce easier. Therefore, diesel viscosity is one of the most important factors influencing the stage 1 coalescence time of water droplets in the diesel. Four different diesel viscosities were simulated: 0.002, 0.003, 0.004 & 0.005 (Pa.s), with corresponding diesel: water dynamic viscosity ratios of 1.97, 2.99, 3.97 & 5.07 respectively, for a system consisting of two water droplets in stagnant diesel (Figure 5.12). The operating conditions and two phase properties were considered as provided in Table 5.5 for simulations 4–7. Table 5.6–5.8 shows the snapshots of the coalescence progress for each simulation (dynamic viscosities) in LBM. LBM simulation 4 and 6 are validated with the Mohammadi et al [179] model. The LBM model is restricted to a dynamic viscosity of 5 due to the relaxation time (which needs to be in the range 0.65 to 1.85). The first and second columns represent respectively the Mohammadi et al [179] time and LBM simulation time. Figure

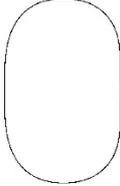
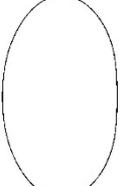
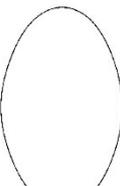
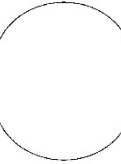
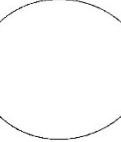
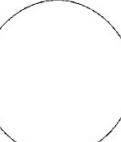
5.18 shows the stage 1 coalescence time as a function of viscosity ratio as calculated from the present LBM simulations and in Mohammadi et al. Then exponential curves of best fit are included in Figure 5.18. Good agreement is seen.

**Table 5.5** The operating conditions and two phase properties for different dynamic viscosities of diesel. (l.b.u= lattice Boltzmann units)

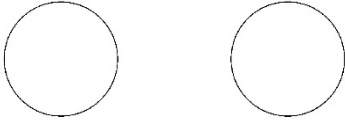
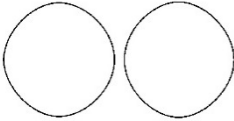
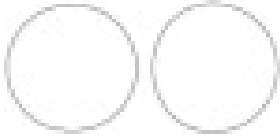
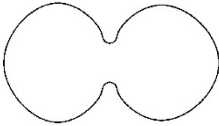
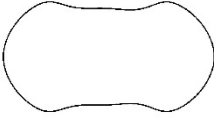
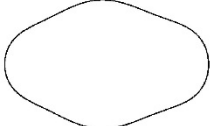
	Simulation 4		Simulation 5		Simulation 6		Simulation 7	
	Mohammadi value	LB value	-----	LB value	Mohammadi value	LB value	-----	LB value
Reynold	87.5	87.3	58.3	57.4	43.8	43.2	35.0	34.6
Weber	7.14	7.10	7.14	7.23	7.15	6.99	7.14	6.85
Dynamic viscosity of diesel	0.002 (Pa.s)	0.340 (l.b.u)	0.003 (Pa.s)	0.517 (l.b.u)	0.004 (Pa.s)	0.688 (l.b.u)	0.005 (Pa.s)	0.858 (l.b.u)
Dynamic viscosity ratio (diesel/water)	2.0	1.97	3.0	2.99	4.0	3.97	5.0	5.07
Kinematic viscosity of diesel	$2.29 \times 10^{-06}$ (m <sup>2</sup> /s)	0.167 (l.b.u)	$3.43 \times 10^{-06}$ (m <sup>2</sup> /s)	0.253 (l.b.u)	$4.57 \times 10^{-06}$ (m <sup>2</sup> /s)	0.337 (l.b.u)	$5.71 \times 10^{-06}$ (m <sup>2</sup> /s)	0.42 (l.b.u)
			Common parameters					
			Mohammadi value			Corresponding values l.b.u		
Density of water			1000 (kg/m <sup>3</sup> )			2.47		
Density of diesel			875 (kg/m <sup>3</sup> )			2.043		
Dynamic viscosity of water			0.001 (Pa.s)			0.173		
Kinematic viscosity of water			$1.00 \times 10^{-06}$ (m <sup>2</sup> /s)			0.07		
Diameter of droplet			200 (µm)			300		
surface tension			0.028 (N/m)			0.246-0.250		
face velocity			1.0 (m/s)			0.0485		

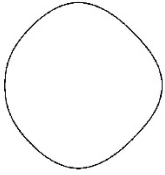
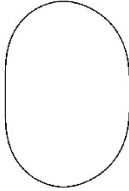
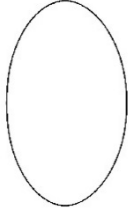
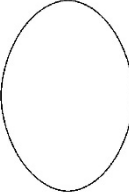
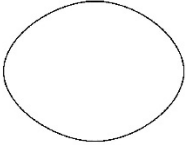
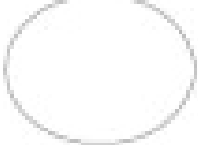
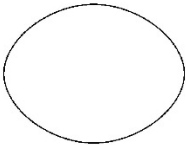
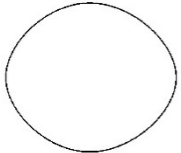
**Table 5.6** shows the snapshots of the coalescence progress for simulation 4 ( 1.97 Dynamic viscosity ratio) in LBM validation with Mohammadi et al[179] model. First and second column of time represents respectively the Mohammadi et al time and LBM simulation time.

		Simulation 4		Mohammadi et al
Reynolds		87.5		87.3
Weber		7.14		7.10
Dynamic viscosity ratio Time		1.97		2
		$\Delta x$	$6.67 \times 10^{-07}$	
		$\Delta t$	$1.15 \times 10^{-08}$	
0	0			
0.5ms -	42000 time steps - 0.48ms			
0.6ms -	45900 time steps - 0.53ms			
0.7ms -	48900 time steps - 0.56ms			
0.8ms -	54900 time steps - 0.63ms			

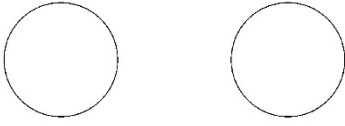
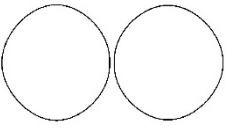
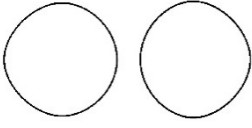
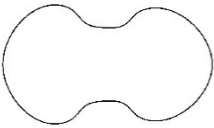
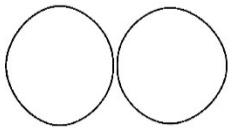
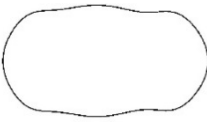
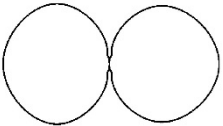
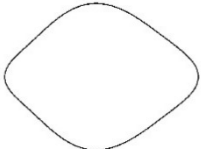
0.9ms -	62300 time steps - 0.72ms		
1.0ms -	67000 time steps - 0.77ms		
1.1ms -	71200 time steps - 0.82ms		
1.2ms -	80800 time steps - 0.93ms		
1.5ms -	101900 time steps- 1.17ms		
1.6ms -	103800 time steps - 1.20ms		
1.7ms -	130700 time steps- 1.51ms		

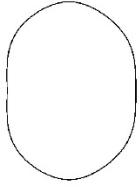
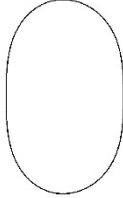
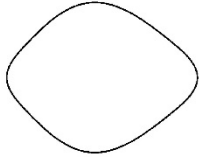
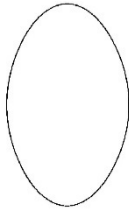
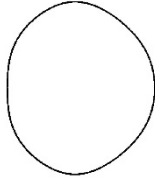
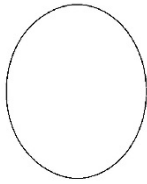
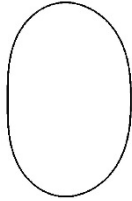
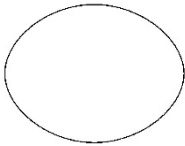
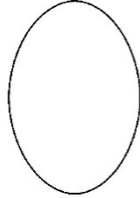
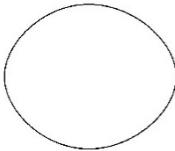
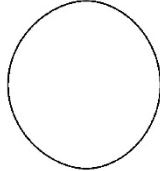
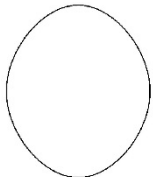
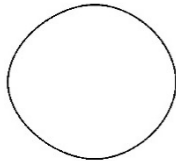
**Table 5.7** shows the snapshots of the coalescence progress for simulation 6 ( 3.97 Dynamic viscosity ratio) in LBM validation with Mohammadi et al[179] model. First and second column of time represents respectively the Mohammadi et al time and LBM simulation time.

		Simulation 6		Mohammadi et al
Reynolds		43.22		43.8
Weber		6.99		7.15
Dynamic viscosity ratio Time		3.97		4
		$\Delta x$	$6.67 \times 10^{-07}$	
		$\Delta t$	$1.40 \times 10^{-08}$	
0	0			
0.5ms	31700			
-	time steps - 0.44ms			
0.6ms	42200			
-	time steps - 0.59ms			
0.7ms	45600			
-	time steps - 0.64ms			
0.8ms	49000			
-	time steps - 0.69ms			

0.9ms -	54500 time steps - 0.76ms		
1.0ms -	59200 time steps - 0.83ms		
1.1ms -	65500 time steps - 0.91ms		
1.2ms -	71000 time steps - 0.99ms		
1.5ms -	85500 time steps- 1.19ms		
1.6ms -	90000 time steps - 1.26ms		
1.7ms -	95000 time steps- 1.33ms		

**Table 5.8** shows the snapshots of the coalescence progress for simulation 5 and 7, respectively with a 2.99 and 5.07 Dynamic viscosity ratio in LBM .First and second column of time represents respectively the Mohammadi et al[179] time and LBM simulation time.

		Simulation 5		LBM time	Simulation 7	
Reynolds		58.3			34.6	
Weber		7.14			6.85	
Dynamic viscosity ratio Time		2.99			5.07	
		$\Delta x$	$6.67 \times 10^{-07}$	$\Delta x$	$6.67 \times 10^{-07}$	
		$\Delta t$	$1.26 \times 10^{-08}$	$\Delta t$	$1.65 \times 10^{-08}$	
0	0			0		
0.5 ms -	36500 time steps - 0.46ms			25400 time steps - 0.42m s		
0.6 ms -	44400 time steps - 0.56ms			37500 time steps - 0.62m s		
0.7 ms -	47600 time steps - 0.6ms			41200 time steps - 0.68m s		
0.8 ms -	52300 time steps - 0.66ms			43600 time steps - 0.7ms		

0.9 ms -	58700 time steps - 0.74ms		47200 time steps - 0.78m s	
1.0 ms -	63400 time steps - 0.80ms		52100 time steps - 0.86m s	
1.1 ms-	69000 time steps - 0.87ms		56300 time steps - 0.93m s	
1.2 ms-	76100 time steps - 0.96ms		61700 time steps - 1.02m s	
1.5 ms-	93600 time steps- 1.18ms		72700 time steps- 1.2ms	
1.6 ms-	97600 time steps - 1.23ms		78100 time steps - 1.29m s	
1.7 ms-	116100 time steps- 1.46ms		82000 time steps- 1.35m s	

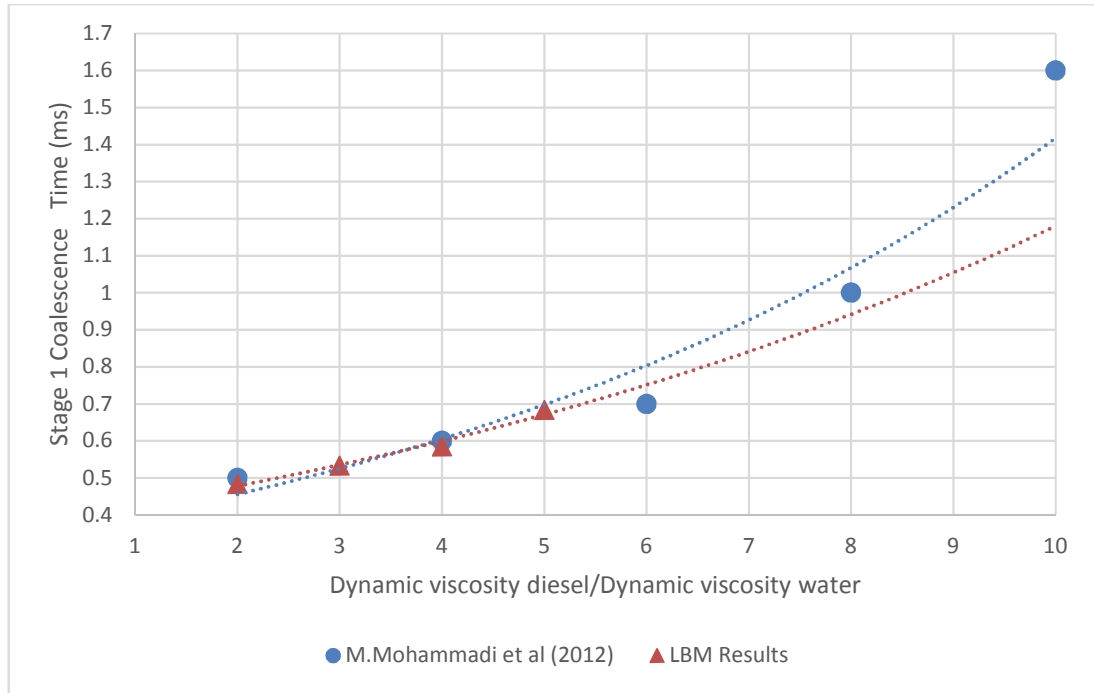


**Figure 5.18** the stage 1 coalescence time versus the dynamic viscosity ratio of Diesel/water.

### 5.3.4 Results for Interfacial tension

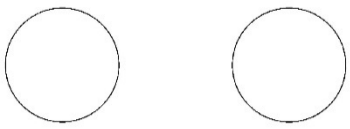
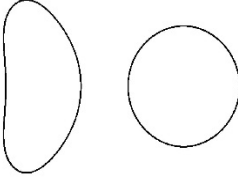
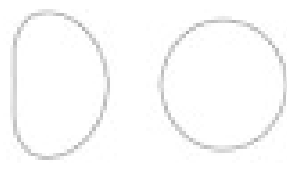
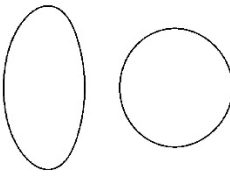
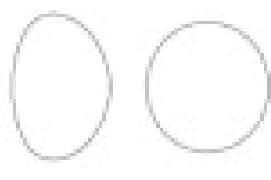
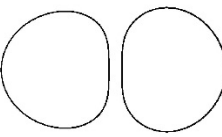
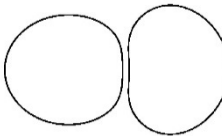
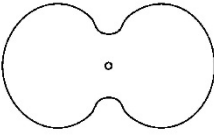
Six different interfacial tensions were simulated, namely 0.01, 0.015, 0.02, 0.025, 0.028 and 0.03 (N/m) for a system consisting of two water droplets in stagnant diesel (Figure 5.12). The operating conditions and two phase properties were considered as provided in Table 5.9 for simulations 8–13. Table 5.10–5.14 shows the snapshots of the coalescence progress for each simulation (interfacial tension) in LBM. LBM simulation 8, 10, 12 and 13 are validated with the Mohammadi et al (2012)[179] model. LBM model is restricted to an interfacial tension up to 0.03 (N/m) due to Shan-Chen LBM model, in which the interaction potential controls both the density ratio and interfacial tension. The first and second columns represent respectively the Mohammadi et al[179] time and LBM simulation time. Figure 5.19 and 5.20 shows respectively the stage1 coalescence time and stage 2 coalescence time as a function of water-diesel interfacial tension (N/m) as calculated from the present LBM simulations and in Mohammadi et al. Then curves(power-law) of best fit are included in Figure 5.19 and 5.20. Good agreement is seen for stage 1 coalescence time. Stage 2 coalescence time in LBM is faster to coalesce compared to Mohammadi et al, it is mainly

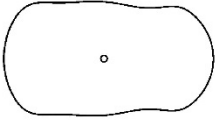
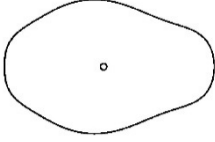
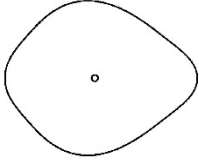
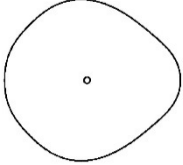
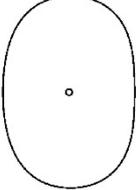
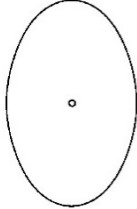
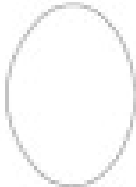
because of the different approach to reach Navier-Stokes equation(Figure 2.25) and there is a variation in time due to oscillation of merged droplet time.

**Table 5.9** The operating conditions and two phase properties for different Interfacial tension. (l.b.u= lattice Boltzmann units)

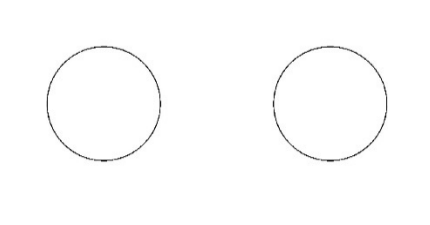
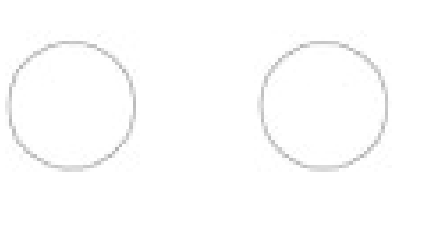
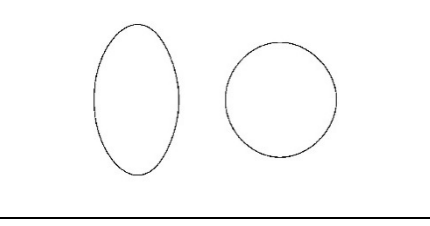
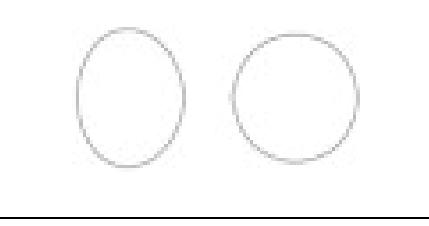
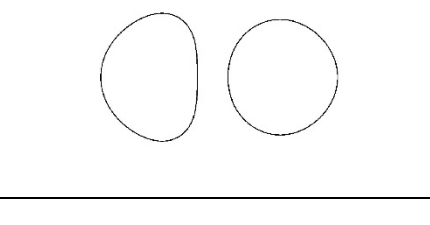
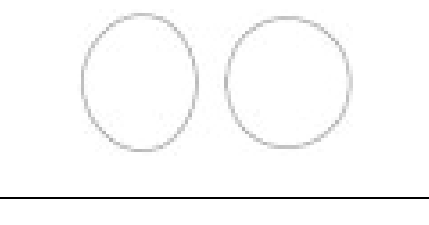
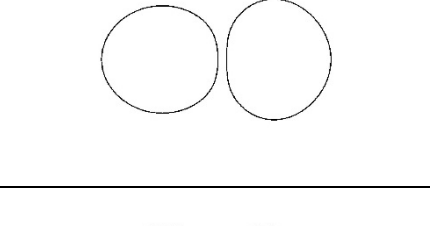
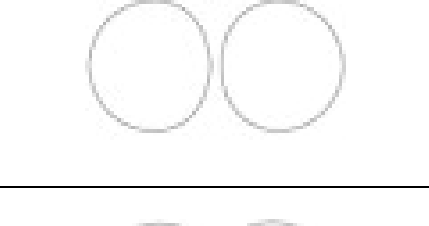
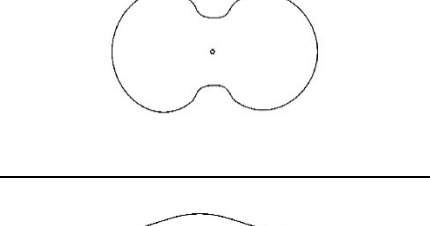
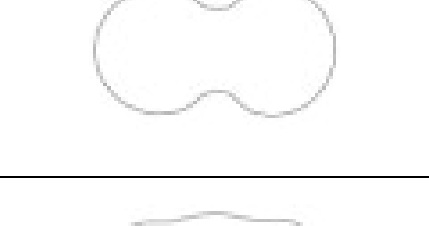
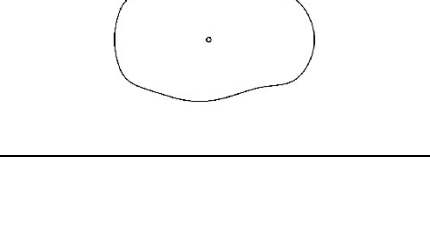
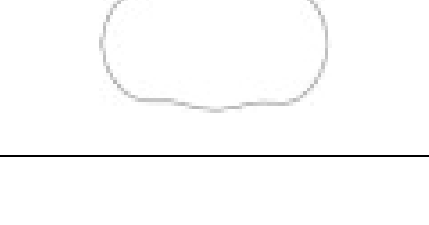
		Weber	Density of water $\rho_w$	surface tension $\sigma$
Simulation 8	Validation value	20.0	1000 (Kg/m <sup>3</sup> )	0.01 N/m
	LB value	17.0	2.17 (l.b.u)	0.09 (l.b.u)
Simulation 9		13.3	1000 (Kg/m <sup>3</sup> )	0.015 N/m
	LB value	12.3	2.24 (l.b.u)	0.129 (l.b.u)
Simulation 10	Validation value	10.0	1000 (Kg/m <sup>3</sup> )	0.02 N/m
	LB value	9.35	2.34 (l.b.u)	0.177 (l.b.u)
Simulation 11		8.0	1000 (Kg/m <sup>3</sup> )	0.025N/m
	LB value	8.10	2.42 (l.b.u)	0.211 (l.b.u)
Simulation 12	Validation value	7.14	1000 (Kg/m <sup>3</sup> )	0.028 N/m
	LB value	7.10	2.47 (l.b.u)	0.246 (l.b.u)
Simulation 13	Validation value	6.89	1000 (Kg/m <sup>3</sup> )	0.03N/m
	LB value	6.67	2.51 (l.b.u)	0.256 (l.b.u)
Common parameters				
		Mohammadi et alvalue		Corresponding values l.b.u
Reynold		87.5		87.3
Density of water $\rho_w$		1000 (kg/m <sup>3</sup> )		2.17-2.51
Density of diesel		875 (kg/m <sup>3</sup> )		2.043
Dynamic viscosity of water		0.001 (Pa.s)		0.173
Dynamic viscosity of diesel		0.002 (Pa.s)		0.340
Kinematic viscosity of water		$1.00 \times 10^{-06}$ (m <sup>2</sup> /s)		0.07
Kinematic viscosity of diesel		$2.29 \times 10^{-06}$ (m <sup>2</sup> /s)		0.167
Diameter of droplet		200 ( $\mu$ m)		300
face velocity		1.0 (m/s)		0.0485

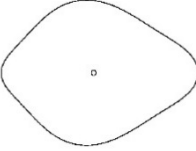
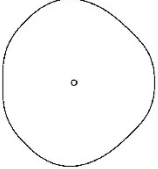
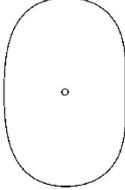
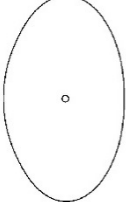
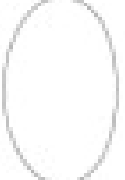
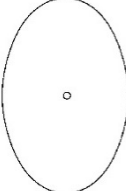
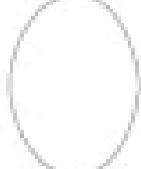
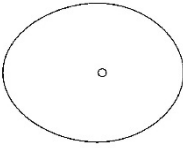
**Table 5.10** shows the snapshots of the coalescence progress for simulation 8 ( 0.01 N/m interfacial tension) in LBM validation with Mohammadi et al model. First and second column of time represents respectively the Mohammadi et al time and LBM simulation time.

		Simulation 8		Mohammadi et al
Reynolds		87.5		87.3
Weber		17.0		20.0
surface tension Time		0.09		0.01 N/m
		$\Delta x$	$6.67 \times 10^{-07}$	
		$\Delta t$	$1.15 \times 10^{-08}$	
0	0			
0.3ms -	20000 time steps - 0.23ms			
0.4ms -	27200 time steps - 0.31ms			
0.5ms -	40800 time steps - 0.47ms			
0.6ms -	46000 time steps - 0.53ms			
0.7ms -	59900 time steps - 0.69ms			

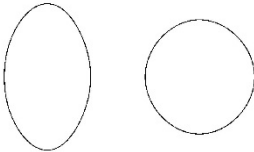
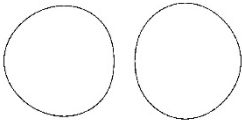
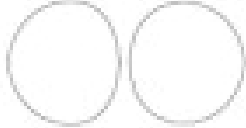
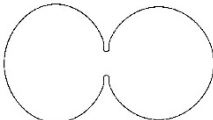
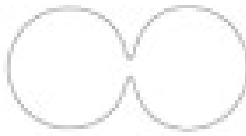
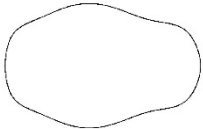
0.8ms -	65900 time steps - 0.76ms		
0.9ms -	70000 time steps - 0.81ms		
1.0ms -	76000 time steps - 0.88ms		
1.1ms -	78000 time steps- 0.90ms		
1.2ms -	98000 time steps- 1.13ms		
1.5ms -	101900 time steps- 1.17ms		

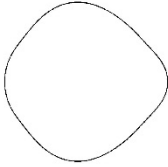
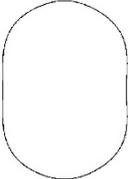
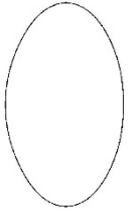
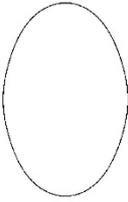
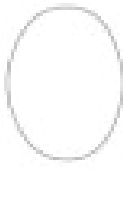
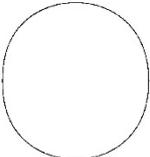
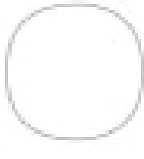
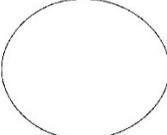
**Table 5.11** shows the snapshots of the coalescence progress for simulation 10 ( 0.02 N/m interfacial tension) in LBM validation with Mohammadi et al model. First and second column of time represents respectively the Mohammadi et al time and LBM simulation time.

		Simulation 10		Mohammadi et al
Reynolds		87.5		87.3
Weber		9.35		10.0
surface tension Time		0.177		0.02 N/m
		$\Delta x$	$6.67 \times 10^{-07}$	
		$\Delta t$	$1.15 \times 10^{-08}$	
0	0			
0.3ms -	20000 time steps - 0.23ms			
0.4ms -	27200ti me steps - 0.31ms			
0.5ms -	35500 time steps - 0.41ms			
0.6ms -	47800 time steps - 0.55ms			
0.7ms -	53500 time steps - 0.62ms			

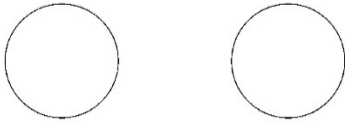
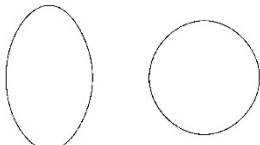
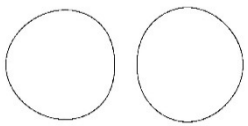
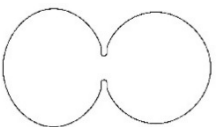
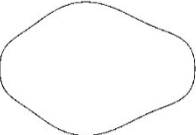
0.8ms -	57400 time steps - 0.66ms		
0.9ms -	62400 time steps - 0.72ms		
1.0ms -	70000 time steps - 0.81ms		
1.1ms -	77000 time steps- 0.89ms		
1.2ms -	82000 time steps- 0.94ms		
1.5ms -	101900 time steps- 1.17ms		

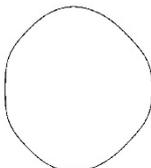
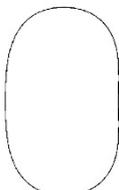
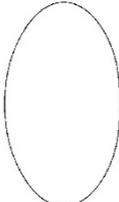
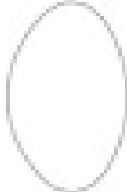
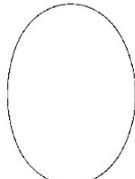
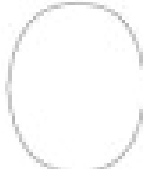
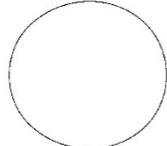
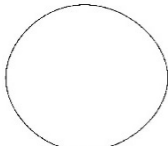
**Table 5.12** shows the snapshots of the coalescence progress for simulation 12 ( 0.028 N/m interfacial tension) in LBM validation with Mohammadi et al model. First and second column of time represents respectively the Mohammadi et al time and LBM simulation time.

		Simulation 12		Mohammadi et al
Reynolds		87.5		87.3
Weber		7.14		7.10
surface tension Time		0.246		0.028 N/m
		$\Delta x$	$6.67 \times 10^{-07}$	
		$\Delta t$	$1.15 \times 10^{-08}$	
0	0			
0.3ms -	16600 time steps - 0.19ms			
0.4ms -	28000 time steps - 0.32ms			
0.5ms -	42000 time steps - 0.48ms			
0.6ms -	46400 time steps - 0.53ms			
0.7ms -	48800 time steps - 0.56ms			

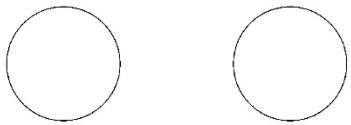
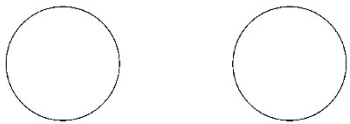
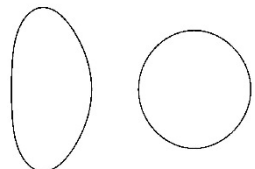
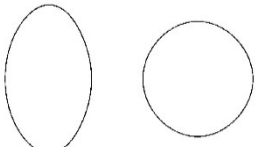
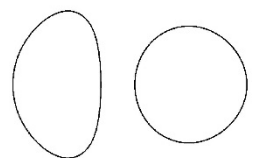
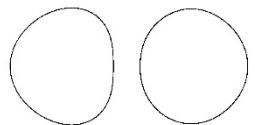
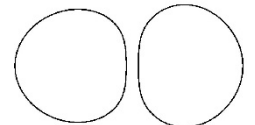
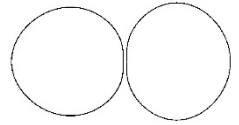
0.8ms -	54700 time steps - 0.63ms		
0.9ms -	59700 time steps - 0.69ms		
1.0ms -	69300 time steps - 0.80ms		
1.1ms -	73200 time steps- 0.84ms		
1.2ms -	81000 time steps- 0.98ms		
1.5ms -	101900 time steps- 1.17ms		

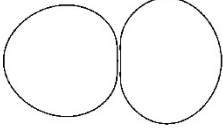
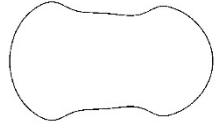
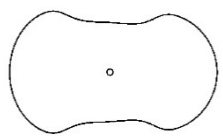
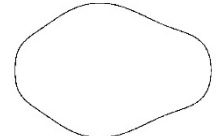
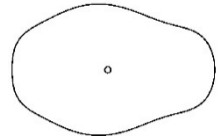
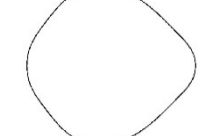
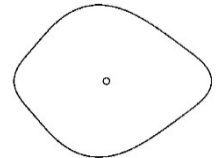
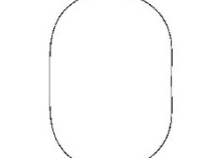
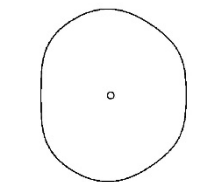
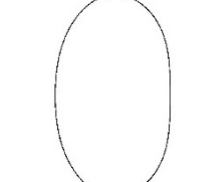
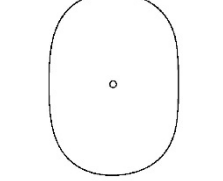
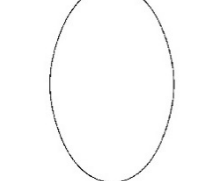
**Table 5.13** shows the snapshots of the coalescence progress for simulation 13 ( 0.03 N/m interfacial tension) in LBM validation with Mohammadi et al model. First and second column of time represents respectively the Mohammadi et al time and LBM simulation time.

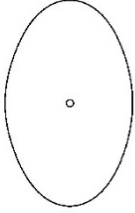
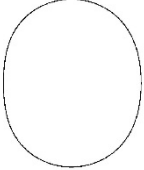
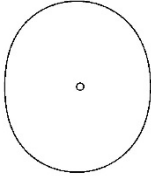
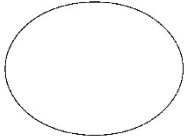
		Simulation 13		Mohammadi et al
Reynolds		87.5		87.3
Weber		6.67		6.89
surface tension Time		0.256		0.03 N/m
		$\Delta x$	$6.67 \times 10^{-07}$	
		$\Delta t$	$1.15 \times 10^{-08}$	
0	0			
0.3ms	16100 - time steps - 0.19ms			
0.4ms	27200 - time steps - 0.31ms			
0.5ms	41600 - time steps - 0.48ms			
0.6ms	46200 - time steps - 0.53ms			
0.7ms	49600 - time steps - 0.57ms			

0.8ms -	55300 time steps - 0.64ms		
0.9ms -	62400 time steps - 0.72ms		
1.0ms -	67000 time steps - 0.77ms		
1.1ms -	74200 time steps- 0.85ms		
1.2ms -	82000 time steps- 0.94ms		
1.5ms -	101900 time steps- 1.17ms		

**Table 5.14** shows the snapshots of the coalescence progress for simulation 9 and 11, respectively with a 0.015 and 0.025 (N/m) Interfacial tension in LBM .First and second column of time represents respectively the Mohammadi et al time and LBM simulation time.

		Simulation 9		LBM time	Simulation 11	
Reynolds		87.5			87.5	
Weber		12.3			8.10	
surface tension Time		0.129			0.211	
		$\Delta x$	$6.67 \times 10^{-07}$	$\Delta x$	$6.67 \times 10^{-07}$	
		$\Delta t$	$1.15 \times 10^{-08}$	$\Delta t$	$1.15 \times 10^{-08}$	
0	0			0		
0.3 ms -	20000 time steps -			18000 time steps - 0.21m s		
0.4 ms -	27200 time steps -			27200 time steps - 0.31m s		
0.5 ms -	37500 time steps -			38500 time steps - 0.44m s		

0.6 ms - 0.54m s	46900 time steps - 0.54m s		47000 time steps - 0.54m s	
0.7 ms - 0.65m s	56700 time steps - 0.65m s		51500 time steps - 0.59m s	
0.8 ms - 0.71m s	61600 time steps 0.71m s		56300 time steps - 0.65m s	
0.9 ms- 0.76m s	66200 time steps - 0.76m s		62400 time steps - 0.72m s	
1.0 ms- 0.84m s	73000 time steps - 0.84m s		68500 time steps - 0.79m s	
1.1 ms- 0.89m s	77500 time steps- 0.89m s		75600 time steps- 0.87m s	

1.2 ms-	90000 time steps-1.04ms		82000 time steps-0.94ms	
1.5 ms-	101900 time steps-1.17ms		101900 time steps-1.17ms	

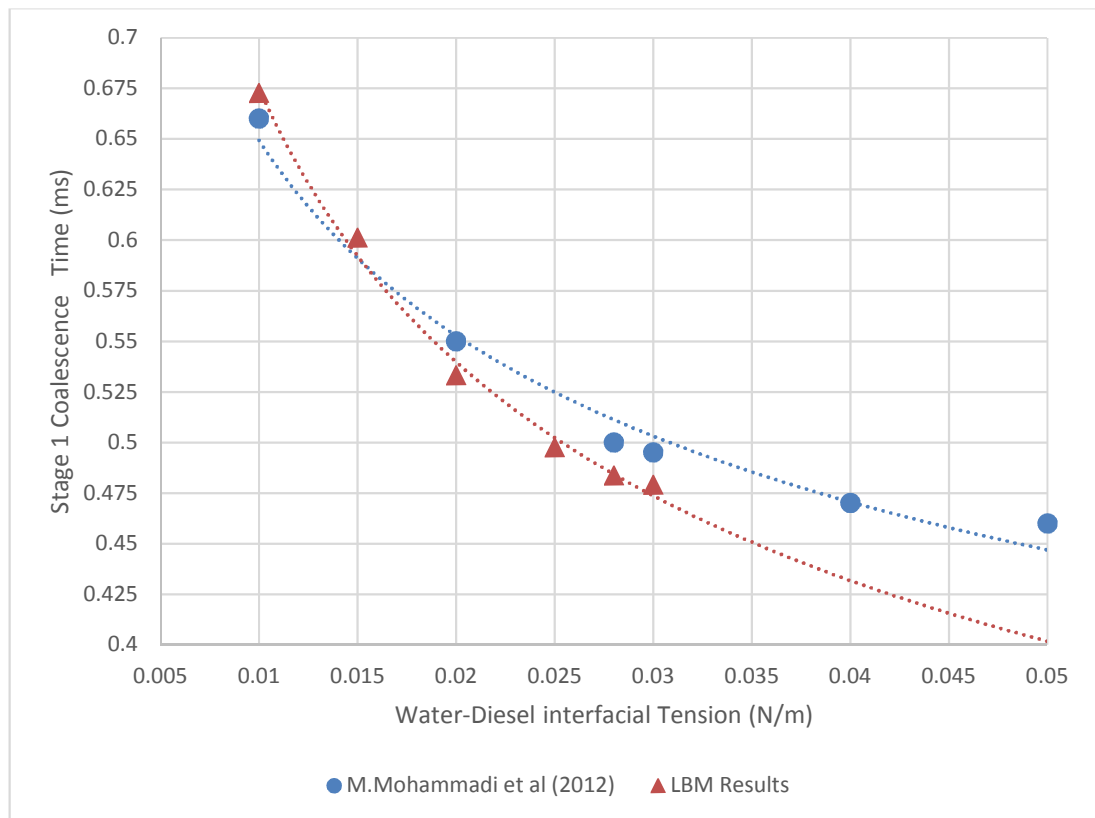


**Figure 5.19** the stage 1 coalescence time versus the water-diesel interfacial tension (N/m).

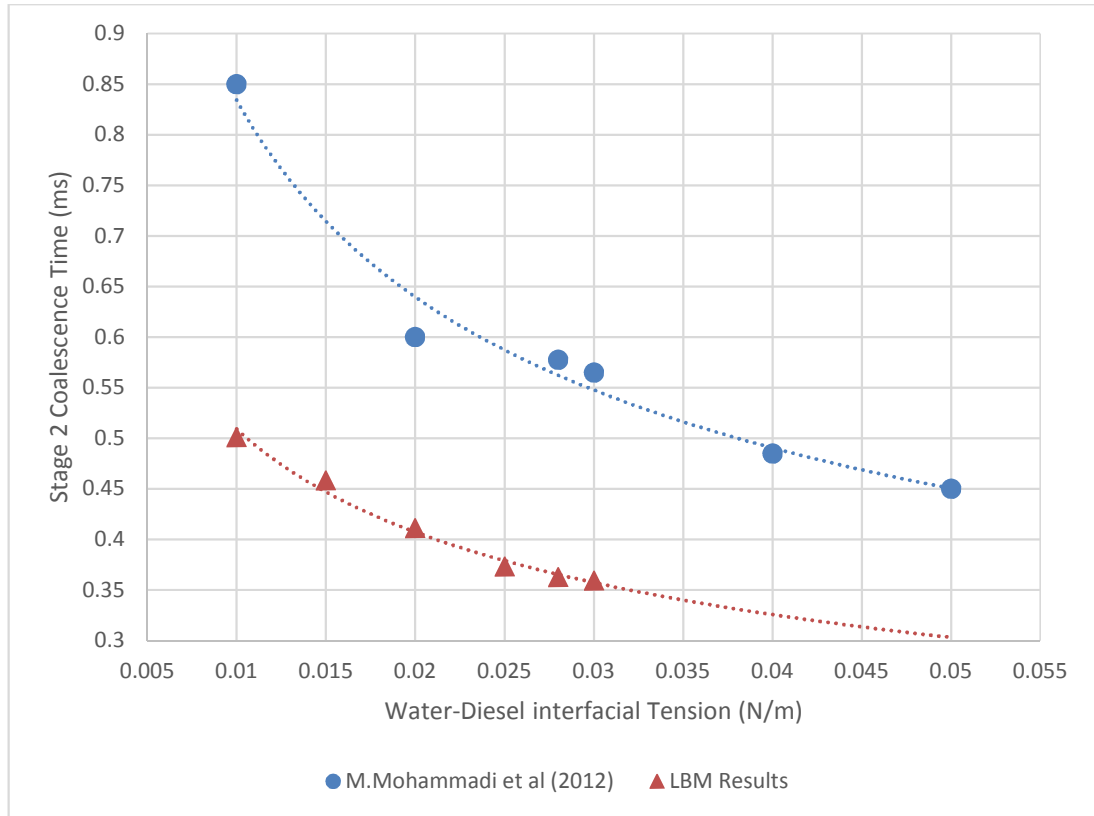


**Figure 5.20** the stage 2 coalescence time versus the water-diesel interfacial tension (N/m).

### 5.3.5 Discussion

#### *Results for speed*

Table 5.1, LBM values of Reynolds number and weber number were matched with Mohammadi et al values. Table 5.2 -5.4 shows the snapshots of the coalescence progress for each velocity simulation in LBM validating with Mohammadi et al model. At Time of 0.5 ms, for the collision velocity of 0.75 m/s, the moving droplet has not reached to the stationary droplet. while for the velocity of 1 m/s, the moving droplet has just met the other one. And for the velocity of 1.25 m/s the droplets have passed the coalescence stage. Figure 5.17 shows as expected, increasing the collision velocity resulted in stage 1 coalescence time reduction due to increased kinetic energy. It suggests that lower velocity is much more beneficial in the coalescence process. Also stage 1 coalescence timing for Mohammadi et al values and LBM values agrees closely.

### ***Results for Dynamic viscosity***

Table 5.5, LBM values of Reynolds number were matched with Mohammadi et al values, but similar weber number was able to simulate due to fluid-fluid (Gww or Goo) interaction potential value controlling the density and interfacial tension values. Table 5.6 -5.7 shows the snapshots of the coalescence progress for each dynamic viscosity ratio simulation in LBM validating with Mohammadi et al model. At Time of 0.5 ms, for the dynamic viscosity ratio of 2, the moving droplet has just met the other one, while for the dynamic viscosity ratio of 3, 4 and 5, the moving droplet has not reached the stationary droplet and the thin diesel film distance is increasing. This is mainly because of the slower drainage of the diesel film. Figure 5.18 shows, increasing the dynamic viscosity of diesel resulted in a stage 1 coalescence time increment due to the higher force required to displace the thin film of diesel between water droplets. The stage 1 coalescence timing for Mohammadi et al values and LBM values agree closely. Finally, increasing the diesel dynamic viscosity in LBM will increase the  $\Delta t$  value to calculate the real time from the Mohammadi et al. LBM time has a maximum error of 22% compared to the time from Mohammadi et al. The difference in time was observed because of two different computational methods, and the approach used to solve the Navier-Stokes equation (Figure 2.25). Therefore it is difficult to validate the time without experimental data.

### ***Results for interfacial tension***

Table 5.9, LBM values of Reynolds number and weber number were matched with Mohammadi et al values. Table 5.10 -5.13 shows the snapshots of the coalescence progress for each water-diesel interfacial tension simulation in LBM validating with Mohammadi et al model. At Time of 0.5 ms, with interfacial tension values of 0.0285 and 0.03 N/m, the droplets have started to coalesce, while with lower values of interfacial tension (0.01, 0.015, 0.02 and 0.025 N/m), they have not reached each other yet. Figure 5.19 shows that the stage1 coalescence time decreases as the water-diesel interfacial tension increase. Also stage 1 coalescence timing for Mohammadi et al values and LBM values agrees closely. Figure 5.20 shows

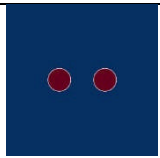
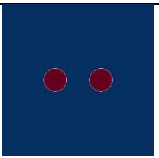
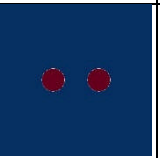
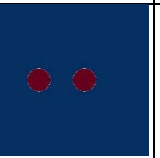
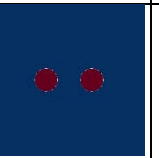
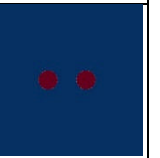
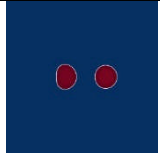
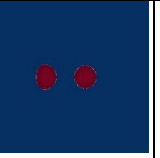
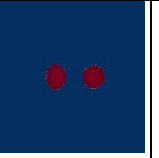
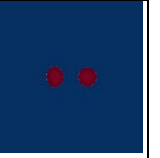
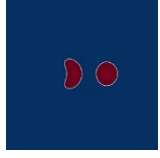
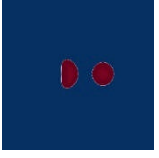
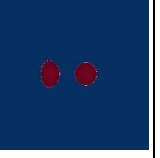
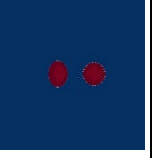
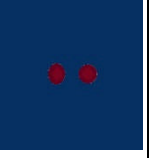
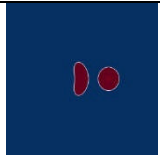
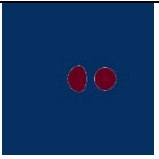
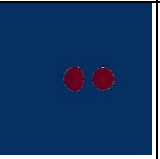
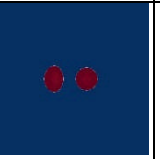
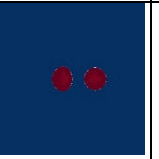
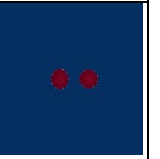
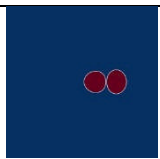
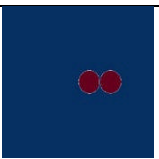
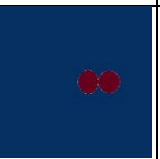
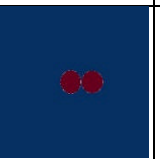
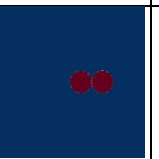
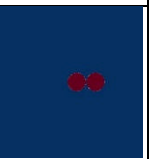
that the stage 2 coalescence time decreases as the water-diesel interfacial tension increases. It suggests that higher interfacial tension are much more easy to coalesce compared to lower interfacial tension. Stage 2 coalescence time in Mohammadi et al results are higher than LBM results. This suggest that droplets coalesce faster in LBM due to streaming and collision step.

LBM time has under predicted the time from Mohammadi et al. This is because of different computational method to solve Navier-Stokes equation.

### **5.3.6 Effect of Lattice Resolution**

A system consisting of two water droplets in stagnant diesel as in Figure 5.12 is studied for lattice resolutions of ( $N_x=N_y$ ) of 500, 1000, 1500, 2000, 2500 and 3000 with respective droplet size of 75, 150, 225, 300, 375 and 450 in LB units. All the simulations were performed for a Reynolds number of 65.6 (same common parameter as Table 5.1). Table 5.15 shows the snapshots of the each domain sizes droplet behaviour at  $d$  (distance of separation for the two droplets). It is noticeable that lattice resolution  $\geq 1000$  has the same effect on droplets shape compared to 500 lattice resolution. In 500 lattice resolution,  $d=0.5$  and  $0.75$  the moving droplets shape is evident.

**Table 5.15** shows the snapshots of the lattice resolution for a Reynolds number of 65.6 and  $d$  is the distance of separation for the two droplets

d	Domain size (Nx=Ny)					
	500	1000	1500	2000	2500	3000
1						
0.2 5						
0.5						
0.7 5						
1.0						

## **5.4 Sensitivity study for critical droplet detachment velocity**

In the coalescence filtration process the droplet's contact angle on fibres is a key aspect, where fibre properties could be changed with their respective contact angle with the droplets. Therefore critical droplet detachment velocity from each fibre properties (contact angle) is vital because it determines the maximum useful flow rate in filtration media. (above maximum flow rate, coalescence will be hampered).

### **5.4.1 Simulation setup**

Figure 5.21 shows the geometry studied, the inlet velocity boundary is force equilibrium and the outlet is zero gradient boundary. The purpose of this study is to investigate the influence of periodic versus bounce back condition on the prediction of the model. The top and bottom boundaries were set to either bounce back condition or periodic condition. A rectangular domain of 500 x 250 was created and a fibre radius (25 LB unit) was positioned with centre at x:125, y:125 in the lattice nodes. After that a droplet radius was positioned with centre at x: (125+fibre radius+ droplet radius), y:125 in the lattice nodes (as shown in Figure 5.21). Due to symmetry the domain y coordinate will remain the same. For example, a 50 LB unit droplet radius was created at centre at x: 200, y: 125 in the domain. Combination of contact angle with interfacial tension or droplet size or dynamic viscosity ratio were varied. Table 5.16 shows the combination of parameter change. Inlet velocity was increased by every 0.01 LB units in speed till the droplet detached from the fibre. Droplet detachment from fibre is shown in Figure 5.22.

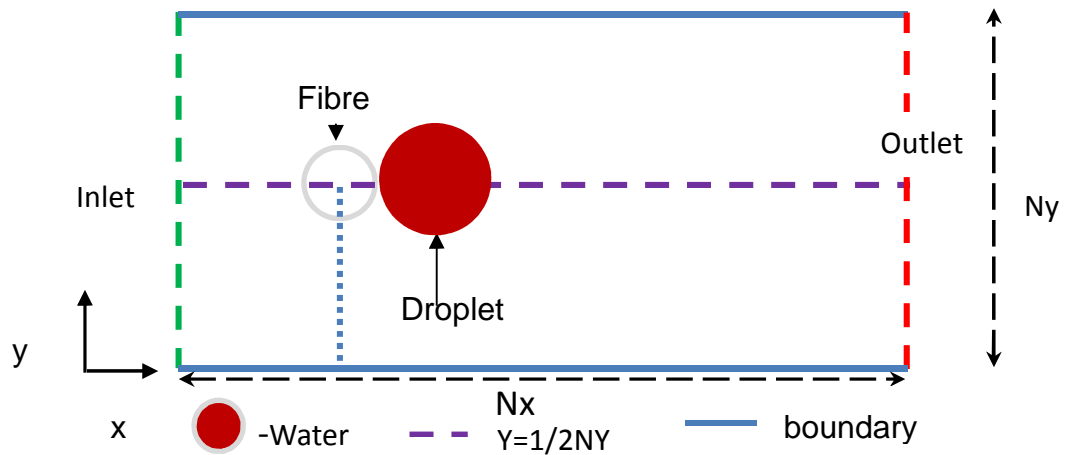


**Figure 5.21** represents the inlet, outlet region with a droplet and a fibre. This system was studied for rectangular domain size.

**Table 5.16** parametric studies for the droplet detachment velocity.

	Droplet Radius size	Fibre radius size	Interfacial tension	boundary condition	Dynamic viscosity ratio
Simulation 1	33µm	16 µm	20mN/m	Bounce back	2.0
Simulation 2	33µm	16 µm	28.5mN/m	Bounce back	2.0
Simulation 3	33µm	16 µm	20mN/m	Periodic condition	2.0
Simulation 4	33µm	16 µm	28.5mN/m	Periodic condition	2.0
Simulation 5	16 µm	16 µm	28.5mN/m	Periodic condition	2.0
Simulation 6	26 µm	16 µm	28.5mN/m	Periodic condition	2.0
Simulation 7	50 µm	16 µm	28.5mN/m	Periodic condition	2.0
Simulation 8	66 µm	16 µm	28.5mN/m	Periodic condition	2.0
Simulation 9	33µm	16 µm	28.5mN/m	Periodic condition	3.0
Simulation 10	33µm	16 µm	28.5mN/m	Periodic condition	4.0
Simulation 11	33µm	16 µm	28.5mN/m	Periodic condition	5.0

#### 5.4.2 Results of Contact angle.

Figure 5.22 (A),(B) and (C) shows the droplets detachment at fibre contact angle of  $78^\circ$ ,  $90^\circ$  and  $120^\circ$  respectively for all the simulations in the Table 5.16. It was noticeable that for smaller contact angle ( $\theta < 90^\circ$ ) the initially attached droplet tends to split into two droplets as shown in Figure 5.22 (A). Major part of the droplets follows the streamline but a small radius droplet tends to stick with the fibre. Also (B), and (C) shows that there is no split of the original droplet, for higher contact angles ( $\theta > 90^\circ$ ).

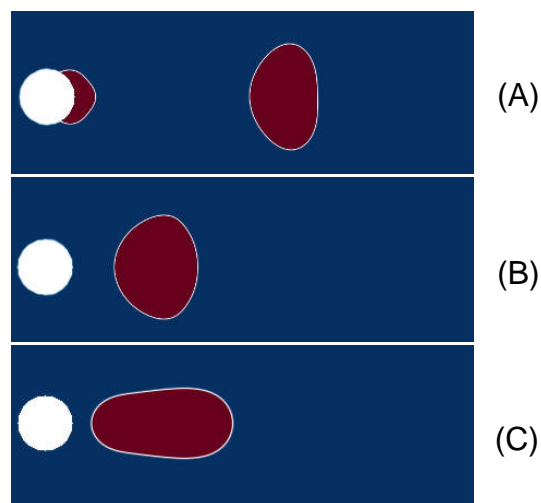


**Figure 5.22** (A),(B) and (C) shows the droplets detachment at fibre contact angle of  $78^\circ$ ,  $90^\circ$  and  $120^\circ$ .

#### 5.4.3 Results for different Boundary condition & interfacial tension

The operating conditions and two phase properties were considered as provided in Table 5.16 for simulations 1–4. Figure 5.23 shows the detachment velocity versus contact angle for different boundary condition at the top and bottom wall. Also the influence of interfacial tension.  $\Delta x$  is  $6.67 \times 10^{-07}$  m and  $\Delta t$   $5.19 \times 10^{-08}$  s used to convert LBM units into real values. Contact angle  $\theta < 78^\circ$  tends to split the droplet as Figure 5.22 (A) and contact angle  $\theta > 78^\circ$  detaches the original size of the droplet shown in Figure 5.22 (B) and (C).

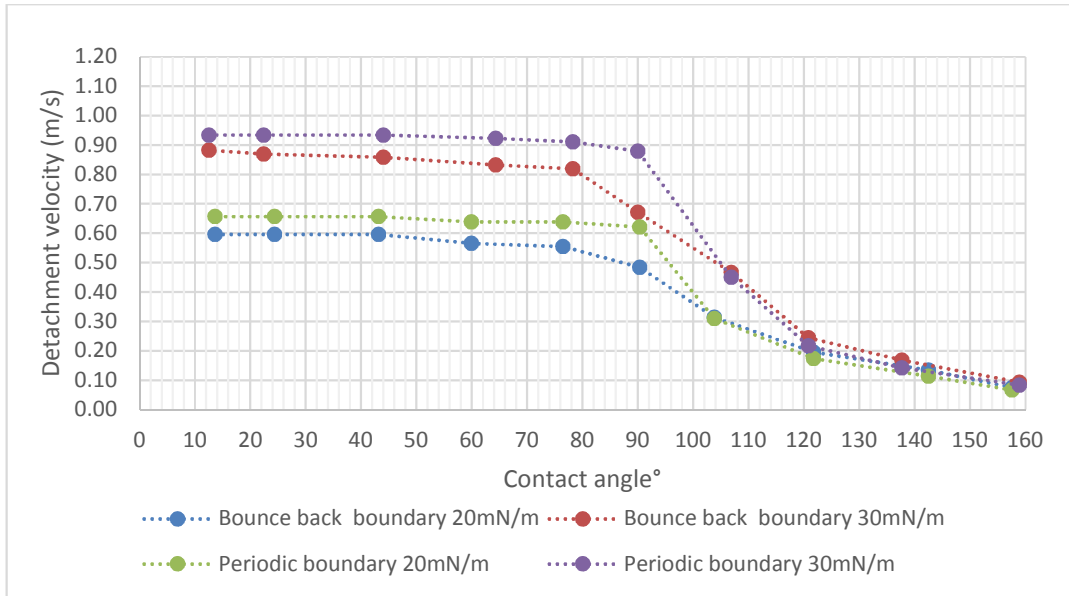


**Figure 5.23** the detachment velocity versus contact angle, bounce back and periodic boundary condition to different interfacial tension.

#### 5.4.4 Results for Different droplet diameter

The operating conditions and two phase properties were considered as provided in Table 5.16 for simulations 4-8. Figure 5.24 shows the detachment velocity versus contact angle for different diameter of droplet.  $\Delta x$  is  $6.67 \times 10^{-07}$  m and  $\Delta t$  is  $5.19 \times 10^{-08}$  s used to convert LBM units into real values.

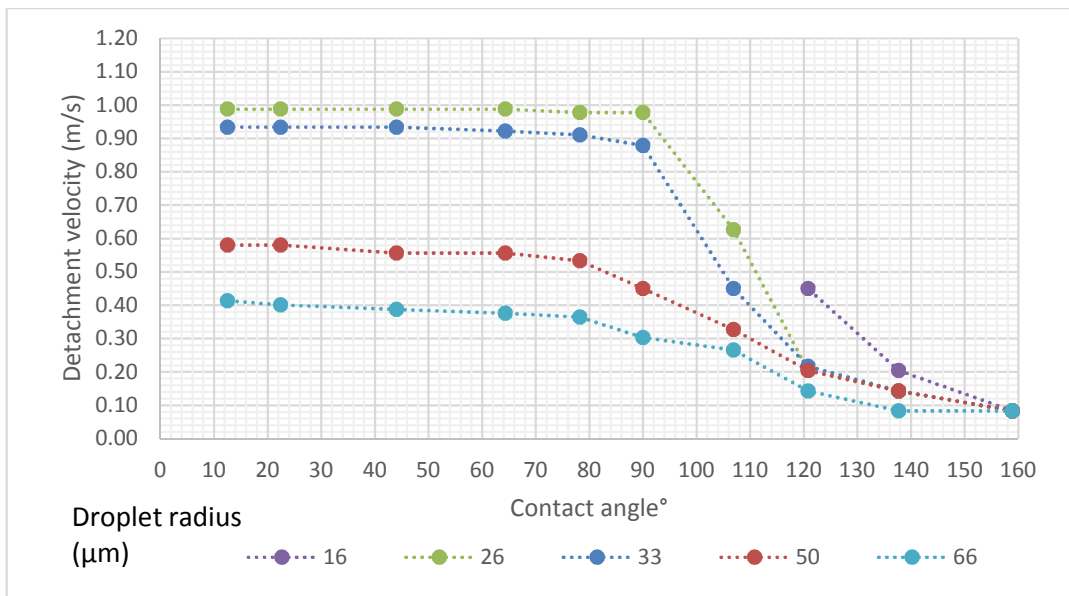


**Figure 5.24** the detachment velocity versus contact angle for different diameter of droplet.

### 5.4.5 Results for Dynamic viscosity

The operating conditions and two phase properties were considered as provided in Table 5.16 for simulations 4 & 9-11. Figure 5.25 shows the detachment velocity versus contact angle for different dynamic viscosity ratios. Dynamic viscosity ratios are 2, 3, 4 and 5 and their respective  $\Delta t$  values are  $5.19 \times 10^{-08}$ ,  $6.39 \times 10^{-08}$ ,  $9.99 \times 10^{-08}$ ,  $1.15 \times 10^{-07}$  s. Also  $\Delta x$  is  $6.67 \times 10^{-07}$  m.  $\Delta x$  and  $\Delta t$  are used to convert LBM units into real values.

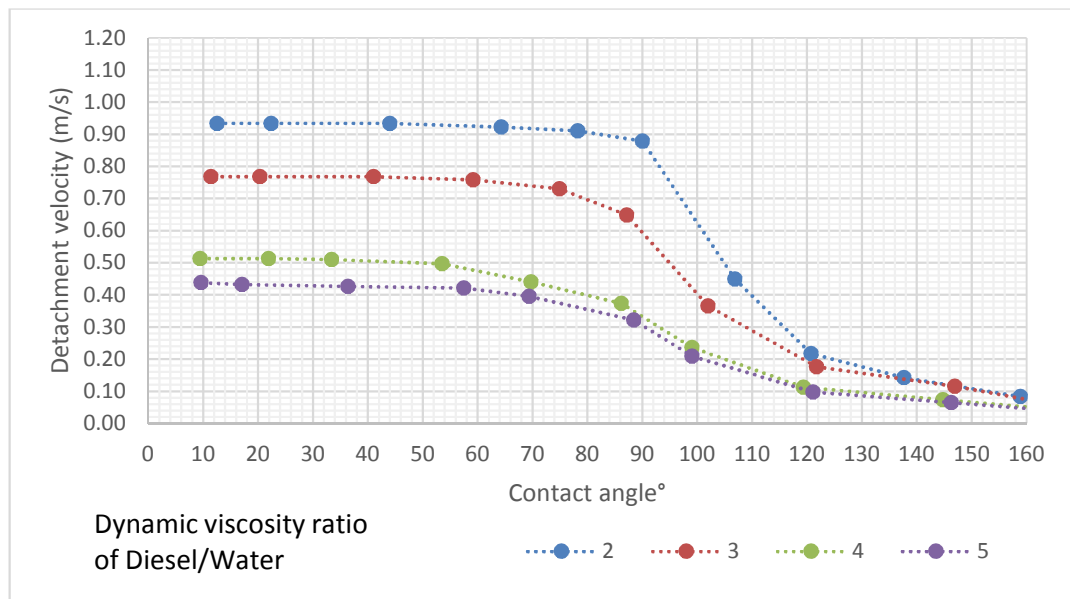


**Figure 5.25** the detachment velocity versus contact angle for different dynamic viscosity ratios.

### 5.4.6 Discussion

The plots in Figures 5.23 to 5.25 all exhibit a similar form in that there is a plateau at low contact angles ( $\theta < 90^\circ$ ) and another at high contact angles ( $\theta > 120^\circ$ ), with a steep gradient in-between. The reason for this is attributed to the change in the area of contact between the droplet and the fibre as the contact angle is changed. This is illustrated in Figure 5.26 which shows how a droplet of fixed volume sits on a fibre under quiescent conditions for different contact angles.

As can be seen, the area of contact changes only a little with contact angle when the contact angle is either large or small, due to the curvature of the

fibre. For intermediate contact angles, however, changing contact angle has a more pronounced effect on the contact area, and hence greater sensitivity of detachment velocity to contact angle can be expected in this range.

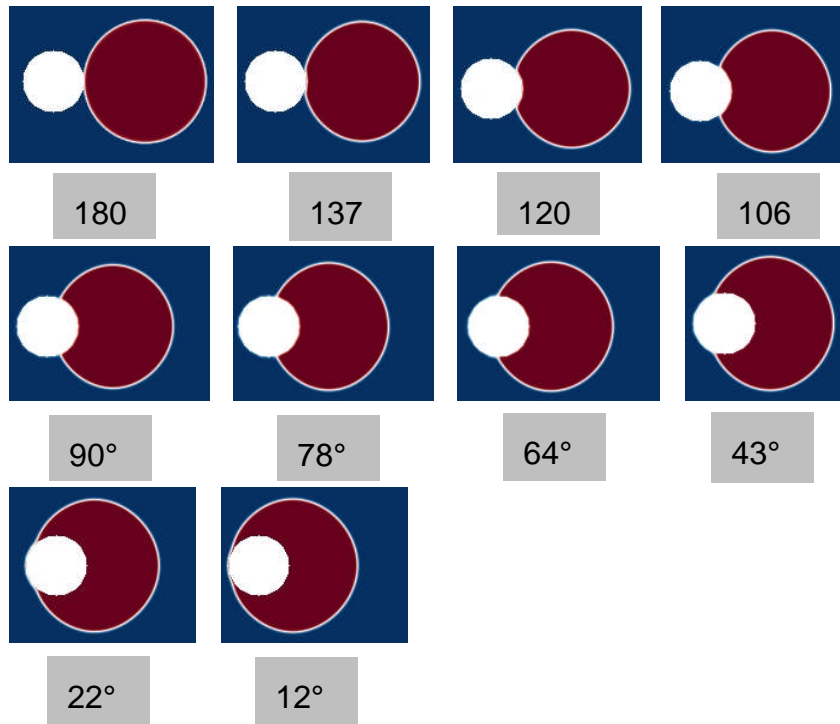


**Figure 5.26** Droplets of equal volumes sitting on a fibre in quiescent conditions with different contact angles between 12 and 180 degrees.

### ***Results for different boundary condition & interfacial tension***

The hydrodynamic force acting on a droplet must overcome the adhesion force between the droplet and fibre before detachment occurs[112], which is related to critical detachment velocity. For smaller contact angle ( $\theta < 78^\circ$ ) the initially attached droplet tends to split into two droplets as shown in Figure 5.22 (A). Major part of the droplets follows the streamline but a small radius droplet tends to stick with the fibre. Also (B), and (C) shows that there is no split of the original droplet, for higher contact angles ( $\theta > 78^\circ$ ). Figure 5.23 shows that having a bounce back wall condition would require a lesser critical detachment velocity compared to periodic boundary for a particular interfacial tension value. Mainly because the bounce back condition has a slightly higher Poiseuille velocity profile between the fibre and wall boundary compared to periodic condition. Increasing interfacial tension has a higher critical detachment velocity. Mainly because higher interfacial tension tends

to have a high molecular interaction strength towards each other and a higher adhesion force towards the fibre [180]. Li et al [181] concluded that dependence of dynamic wetting is affected by lower surface tension of liquid and this was noticeable in Figure 5.23. It is noticeable that contact angle  $\theta < 80^\circ$  have a similar critical detachment velocity,  $80^\circ < \theta < 120^\circ$  have a negative gradient for the velocity and  $120^\circ < \theta$  have a low velocity. In other words droplet contact line on fibre influences the critical detachment velocity. Also Figure 5.23- 5.25 have a trend as the contact angle increases the critical detachment velocity decreases.

### ***Results for Droplet diameter***

Figure 5.24 shows that increasing droplet diameter reduces the critical detachment velocity. At  $16\mu\text{m}$  droplet,  $\theta < 120^\circ$  the critical detachment velocity was out of the velocity range in LBM simulation due to the lattice resolution. As droplet area is increased the diesel flow velocity required to initiate motion decreases. Because larger diameter droplets have a greater surface area in contact with the diesel flowing past the fibre and so experience higher shear. This behaviour is consistent with that observed by Fan et al [182] where increasing the droplet size reduced the shearing air flow velocity required for motion to occur.

### ***Results for Dynamic viscosity ratio***

Figures 5.25 shows the effect of varying the simulated fluid viscosity. The lower the dynamic viscosity ratio of Diesel/water requires a higher critical detachment velocity. This behaviour is consistent with that observed by Li et al [181] where increasing the dynamic viscosity reduced the imbibition rate or velocity. As the viscosity increases, higher force resistance needed for drop to hold on to fibre [116]. Therefore droplets are easy to detach at lower viscosity range.

## **5.5 Summary and Conclusion**

Domain size of  $1000 \times 900$  has less diffusion of droplets and the droplet follows the streamline. The diffusion rate in nodes will decrease with

increase of droplet size. It was also noticed that diffusion happens mostly on the initialisation time step in this domain size. The outlet boundary condition affect the useful domain size for different droplet sizes. For example droplet of 20, 30 and 40 LB units require domain sizes of respectively  $NX= 700$ , 650 and 600 LB nodes.

Shan-Chen multicomponent multiphase validation against finite volume numerical method (FVM) in conjunction with volume of fluid (VOF) approach (Mohammadi et al) simulations of free droplet coalescence agree closely with speed, dynamic viscosity ratio and Interfacial tension. Therefore LBM code is suitable for exploring more about the coalescence process.

- Increasing the collision velocity resulted in stage 1 coalescence time reduction due to increased kinetic energy. It suggests that lower velocity is much more beneficial in the coalescence process.
- Increasing the dynamic viscosity of diesel resulted in a stage 1 coalescence time increment due to the higher force required to displace the thin film of diesel between water droplets.
- The stage 2 coalescence time decreases as the water-diesel interfacial tension increases. It suggests that higher interfacial tension are much more easy to coalesce compared to lower interfacial tension.
- LBM time was under predicting the time from Mohammadi et al and has a maximum error of 22%.
- In fibre with droplet studies, the effect of periodic condition and bounce back condition for top and bottom wall had a less variation in critical detachment velocity.
- Contact angle  $\theta < 80^\circ$  have a similar critical detachment velocity,  $80^\circ < \theta < 120^\circ$  have a negative gradient for the velocity and  $120^\circ < \theta$  have a low velocity. In other words droplet contact line on fibre influences the critical detachment velocity. As the contact angle increases the critical detachment velocity decreases. Also higher interfacial tension has a higher critical detachment velocity. Then large droplet diameter reduces the critical detachment velocity. The lower the dynamic viscosity ratio of Diesel/water requires a higher critical detachment velocity.

## **Chapter 6**

### **Interaction of water droplets with filter fibres**

#### **6.1 Introduction**

Coalescence filtration processes are divided into three main steps; droplet attachment onto a fibre, coalescence of droplets on a fibre and droplet detachment from a fibre. In the previous chapter the droplet detachment from a fibre is studied. This chapter considers the attachment of a passing droplet to a fibre, followed by the coalescence of a second droplet with that captured by the fibre and the continuous droplets on fibres. Particular aspects considered are the speed of the flow and the effects of different droplet diameters, fibre diameter and dynamic viscosity ratios.

#### **6.2 Droplet attachment on a single fibre**

In the absence of suspended water droplets, the streamlines of the diesel flow past a fixed cylindrical fibre will naturally curve around the fibre. Hence there will be a tendency for water droplets in the fuel to be steered around the fibre without making contact with it. However, the finite size of such water droplets will distort the flow local to the droplet, leading to the expectation that droplets passing sufficiently close to the fibre will make contact with the fibre and consequently be able to attach to the fibre. Figure 6.1 shows a sketch of the flow past a single fibre, with the fibre positioned along the horizontally aligned centreline of the domain (i.e. the line  $y = Ny/2$ ). A water droplet is initially placed upstream of the fibre such that the horizontal distance between the droplet and the fibre is equal to 50 LB unit or  $33\mu\text{m}$ . The droplet is also given a (centre-to-centre) lateral offset of  $h$  (see Figure 6.1). It is expected that there will be a critical value of  $h$ , denoted as  $h^*$ , below which the droplet will adhere to the fibre and above which the droplet will pass the fibre. This critical value of  $h$  is also expected to depend on the various parameters, e.g. speed, of the system mentioned above. This is explored in the following sub-sections.

### 6.2.1 Simulation setup

The multicomponent multiphase(MCMP) Shan-Chen lattice Boltzmann method was used and Figure 6.1 shows the geometry studied. The inlet velocity condition was imposed by forcing the distribution functions at inlet nodes to the equilibrium distribution functions corresponding to desired flow velocity. The outlet was a zero gradient boundary, while the top and bottom boundaries were linked together in a set periodic condition. A rectangular domain of 1000 x 900 was created and a fibre was positioned with a centre at x:500, y:450 in the lattice nodes. After that a droplet radius was positioned with a centre at x: (500-(fibre radius+50LB unit +droplet radius)), y: (450+h distance) in the lattice nodes (as shown in Figure 6.1). For example, a 25 LB unit droplet radius was created at centre at x: 400, y: 470 in the domain for a h distance of 20 LB unit. Combination of contact angle with speed and droplet size and fibre size were varied. Distance between water droplet and fibre is 50 LB unit, this distance was chosen to allow for the droplet to diffuse and settle during the initialisation step. Table 6.1 shows the combinations of parameters considered. In LBM simulation, the droplet adhering to the fibre is analysed using Figure 6.2. The Figure 6.2 shows a droplet and fibre of 16 $\mu\text{m}$  with a h distance of zero. (A) is the initialisation step, (B) is during the position of  $x=1/2 N_x$ , at 15000 time step and (C) is the final position at 35000 time step. are the droplet sticking to the fibre. The offset h was increased in steps of 1 LB unit( i.e. by one node each time) till the droplet did not adhere to the fibre.

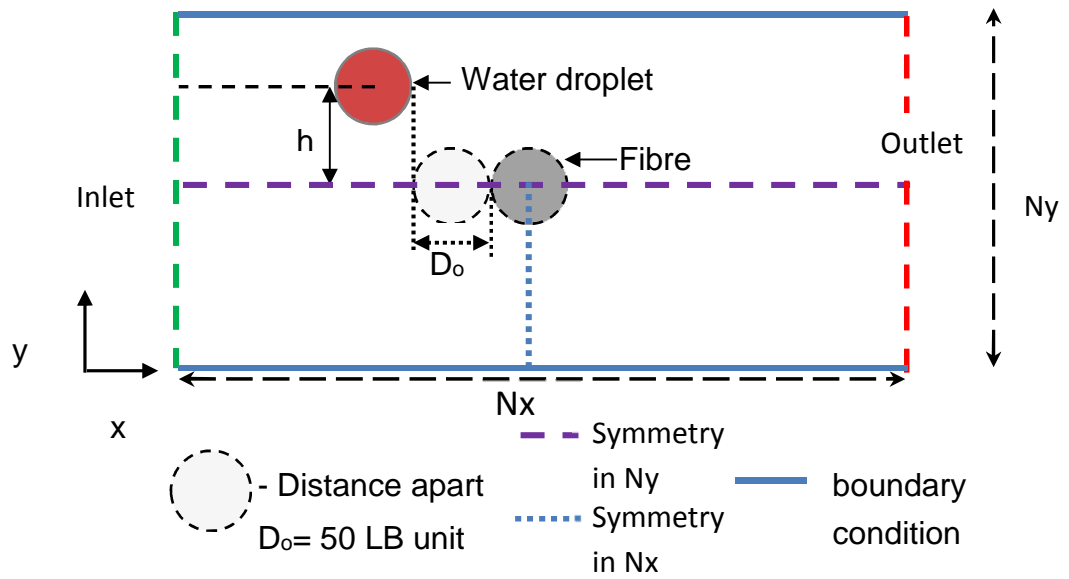


**Figure 6.1** Represents the inlet, outlet region with a droplet and a fibre. This system was studied for rectangular domain size.

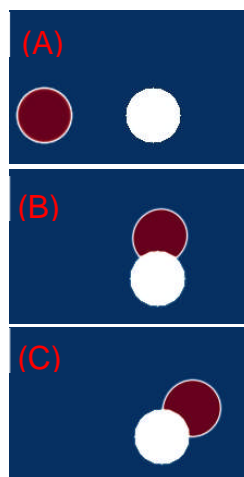


**Figure 6.2** Visual representation of droplet adhering to fibre surface. (A) shows the initialisation step, (B) is during the position of  $x = 1/2 N_x$ , at 15000 time step and (C) is at 35000 time step (final position).

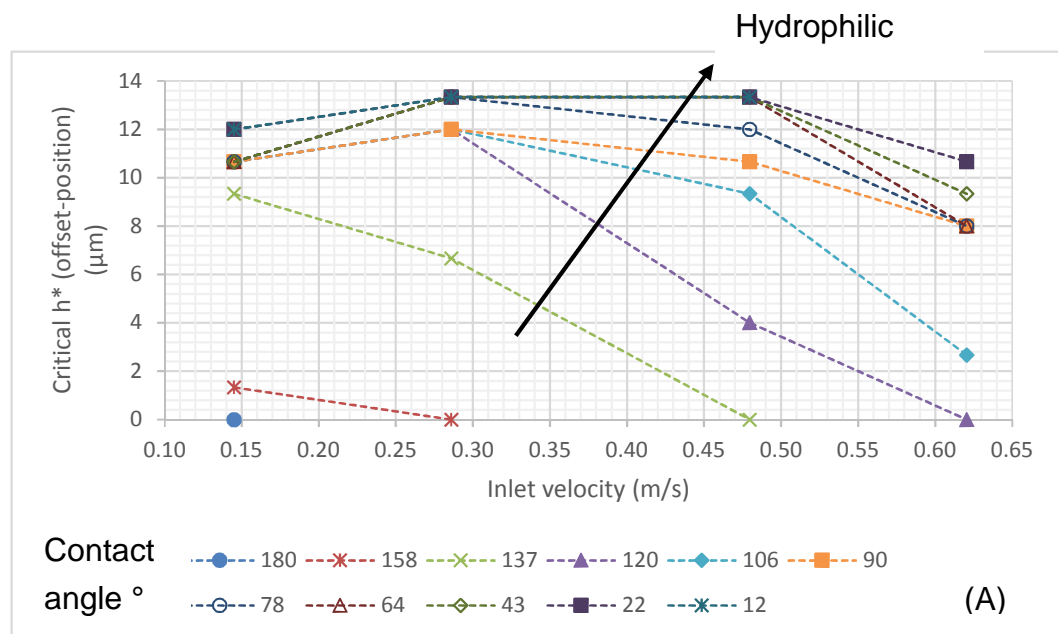
**Table 6.1** Parameters for the studies exploring the maximum offset  $h$  resulting in attachment of a droplet on a fibre.

	Droplet radius	Fibre radius	Inlet Speed (m/s)	Contact angle
Simulation 1	16 $\mu\text{m}$	16 $\mu\text{m}$	0.15	0°-180°
Simulation 2	16 $\mu\text{m}$	16 $\mu\text{m}$	0.29	0°-180°
Simulation 3	16 $\mu\text{m}$	16 $\mu\text{m}$	0.48	0°-180°
Simulation 4	16 $\mu\text{m}$	16 $\mu\text{m}$	0.62	0°-180°
Simulation 5	16 $\mu\text{m}$	16 $\mu\text{m}$	0.15	90°
Simulation 6	25 $\mu\text{m}$	16 $\mu\text{m}$	0.15	90°
Simulation 7	33 $\mu\text{m}$	16 $\mu\text{m}$	0.15	90°
Simulation 8	42 $\mu\text{m}$	16 $\mu\text{m}$	0.15	90°
Simulation 9	16 $\mu\text{m}$	16 $\mu\text{m}$	0.15	90°
Simulation 10	16 $\mu\text{m}$	33 $\mu\text{m}$	0.15	90°
Simulation 11	16 $\mu\text{m}$	50 $\mu\text{m}$	0.15	90°
Simulation 12	16 $\mu\text{m}$	66 $\mu\text{m}$	0.15	90°

### 6.2.2 Effect of flow speed and contact angle

To observe the effect of speed, four different inlet velocities were simulated as indicated in Table 6.1 (simulations 1-4), with the properties of the two phases being a dynamic viscosity ratio (diesel:water) of 2 and an interfacial tension of 28.5mN/m. The wettability of the fibre was also varied by imposing a wide range of contact angles on the fibre. Figure 6.3(A) shows the resulting critical offset distance  $h^*$  versus velocity for the full range of contact angle. For a completely non-wetting fibre (i.e. with contact angle 180°), attachment of a droplet to the fibre is not possible even if the droplet is aimed directly at the fibre (i.e. there is no lateral offset), and the speed is sufficiently small (see the single point at the bottom-left of the plot in Figure 6.3(A)). If the contact angle is reduced to 158°, droplets with a very small offset (1.33 $\mu\text{m}$ ) can be captured by the fibre, but only at low speeds; beyond

a speed of 0.29 m/s capture is not possible. Reducing the contact angle further increases both the offset distance and the speed at which the droplet can be captured by the fibre, as can be seen in the data points corresponding to a contact angle of 137°, however there is still a maximum speed beyond which capture is not possible, even with zero offset. Considering now the very low contact angle cases, corresponding to a highly wettable fibre, the results indicate that speed has little effect on the critical offset, and droplets can be capture with offsets up to 80% of the droplet radius. There is a small reduction in  $h^*$  at high speeds. It is possible that if the speed could be increased further a maximum speed for successful capture might be found, but this could not be established within the restrictions of the simulation approach. Between these two extremes of contact angle lies an intermediate range, the results for which are shown separately in Figure 6.3(B) for clarity.



The caption for the graph above (A) is in Figure 6.3 on next page.

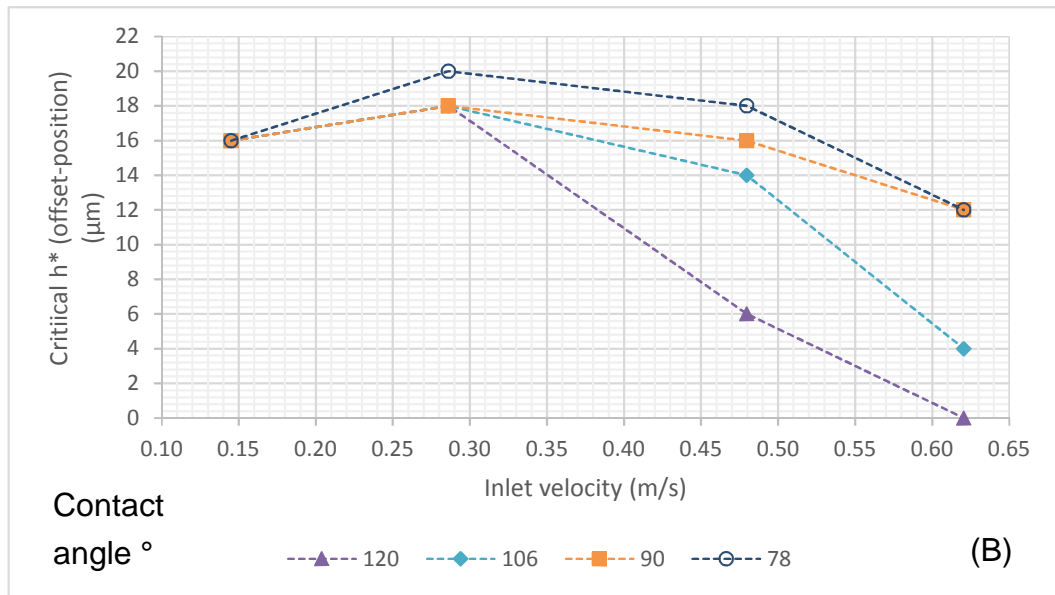


**Figure 6.3** The critical  $h^*$  (offset-position) versus velocity for (A) shows contact angle range of  $0^\circ$  to  $180^\circ$  and (B) for intermediate contact angle range of  $78^\circ$ - $120^\circ$ .

### 6.2.3 Effect of droplet size

Simulations 5-8 listed in Table 6.1 explored the effect of varying the size of the droplet approaching the fibre on the critical offset distance. Here the contact angle was set at  $90^\circ$  and the speed at 0.15 m/s. As before, the diesel:water dynamic viscosity ratio was 2 and the interfacial tension was 28.5mN/m. Figure 6.4 shows the critical  $h^*$ (offset-position) versus droplet radius. There is an approximately linear relationship, showing that  $h^*$  increases roughly in proportion to the increase in droplet radius. However, if  $h^*$  is expressed as a fraction of the distance  $r_d+r_f$ , i.e. the sum of the droplet radius and fibre radius, this corresponds to an increase in  $h^*$  from 35% of  $r_d+r_f$  for  $r_d = 16 \mu\text{m}$  to over 70% of  $r_d+r_f$  when  $r_d = 42 \mu\text{m}$ .

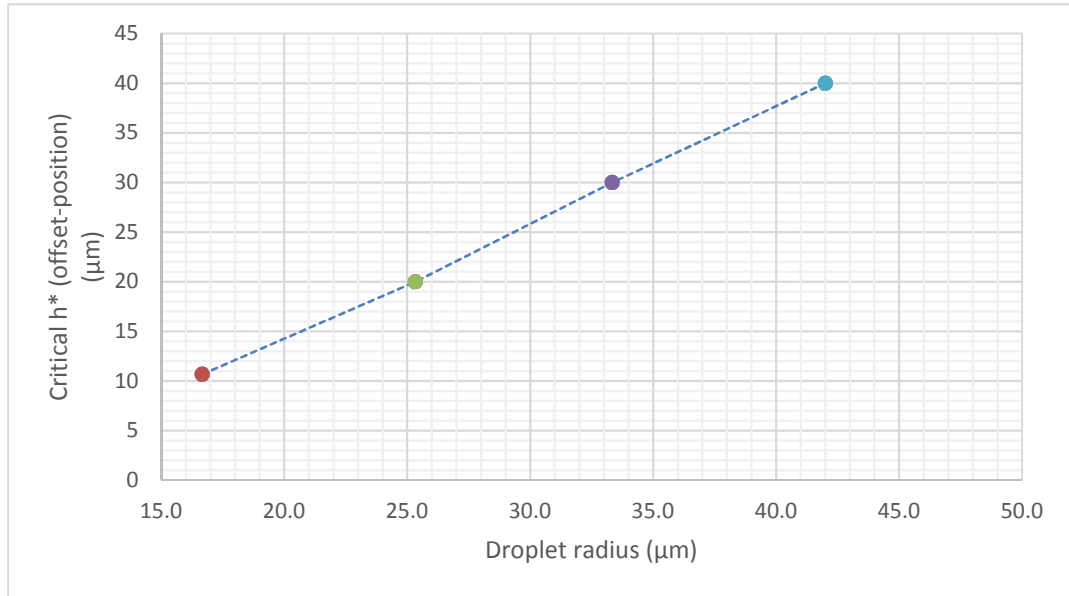


**Figure 6.4** The critical  $h^*$  (offset-position) versus droplet radius.

#### 6.2.4 Effects of fibre size

Under the same viscosity ratio, interfacial tension, contact angle and speed conditions as in the previous section, and with a fixed droplet diameter of  $16\mu\text{m}$ , the effect of varying the fibre radius on the critical offset is shown in Figure 6.5. Again an approximately linear increase in  $h^*$  is seen as the fibre radius increases, however the increase in  $h^*$  is much smaller than when the droplet size was increased.

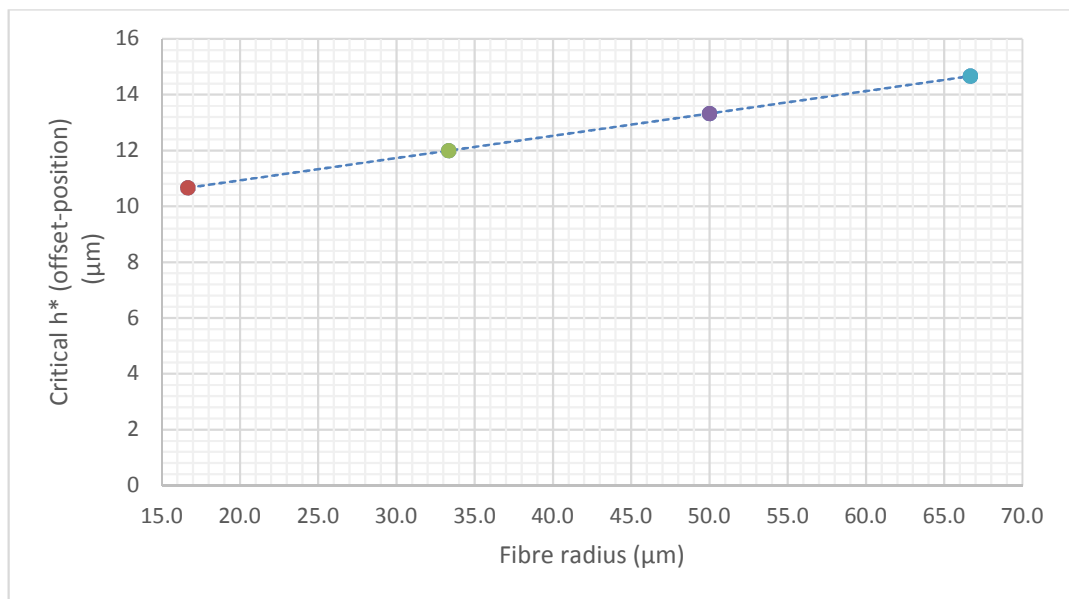


**Figure 6.5** The critical  $h^*$  (offset-position) versus fibre radius.

### 6.2.5 Discussion

The critical  $h^*$  defines the maximum offset position for a droplet to attach onto a fibre. Therefore values below the critical  $h^*$  would adhere to the fibre. Figure 6.3 (A) shows that increasing the velocity would decrease the effect of certain contact angles (mostly super hydrophobic). For example at 0.62 m/s, the contact angles of  $137^\circ$ ,  $158^\circ$  and  $180^\circ$  do not attach on to the fibre. This suggests that at these particular contact angles, the drag force is higher than the adhesion force between droplet and fibre. Also, at 0.15 m/s, as the contact angle increases ( $0^\circ < \theta < 180^\circ$ ),  $h^*$  decreases and all the contact angles have an effect on  $h^*$  at this velocity. Therefore this speed was considered for most of the remaining simulations in this chapter. Figure 6.3 (B) shows that velocity 0.15 and 0.29 m/s tend to have no or less variation in critical  $h^*$  for intermediate contact angle. Figure 6.4 shows that larger droplets have a higher critical  $h^*$  distance, suggesting that streamlines affect the droplet attachment on the fibre. Also larger droplets are easily attached onto a small fibre. This is consistent with the expectation that a larger droplet will produce a larger local distortion of the streamlines around the fibre, meaning that a larger droplet is less able to be 'steered around' the fibre by the flow. Figure 6.5 shows that larger fibres produce only a small variation ( $4\mu\text{m}$  variation) in critical  $h^*$  for a small droplet, again consistent with the fact that distortion of the flow field by the moving droplet is more important in ensuring the capture of a droplet by a fibre. Hence larger fibres are not effective for small droplets. The values of the critical  $h^*$  for droplet and fibre change could be normalised with respect to their radius. Therefore critical  $h^*$  remains in the same ratio.

### 6.3 Two droplets coalescing on a single fibre

In the coalescence filtration process it is important that droplets are captured and held by the fibres so that subsequent droplets can coalesce with the held droplets to form larger droplets that will eventually become large enough to be carried away by the flow and then to settle out of the fuel under

gravity. Hence this section investigates the coalescence of a droplet passing another one that is held on a fibre. Again, a critical offset distance,  $h^*$ , will be considered. Figure 6.6 shows the initial configuration of the simulations. One droplet starts in contact with the fibre and located at the top centre of the fibre. A second droplet is position upstream with a streamwise separation equal to the fibre diameter and a lateral (centre-to-centre) offset of  $h$ , as shown in Figure 6.6.

### 6.3.1 Simulation setup

The simulation step was same as in section 6.2.1, but additionally a droplet was attached on top of the fibre as shown in Figure 6.6. Simulations were performed for an inlet speed of 0.15 m/s.

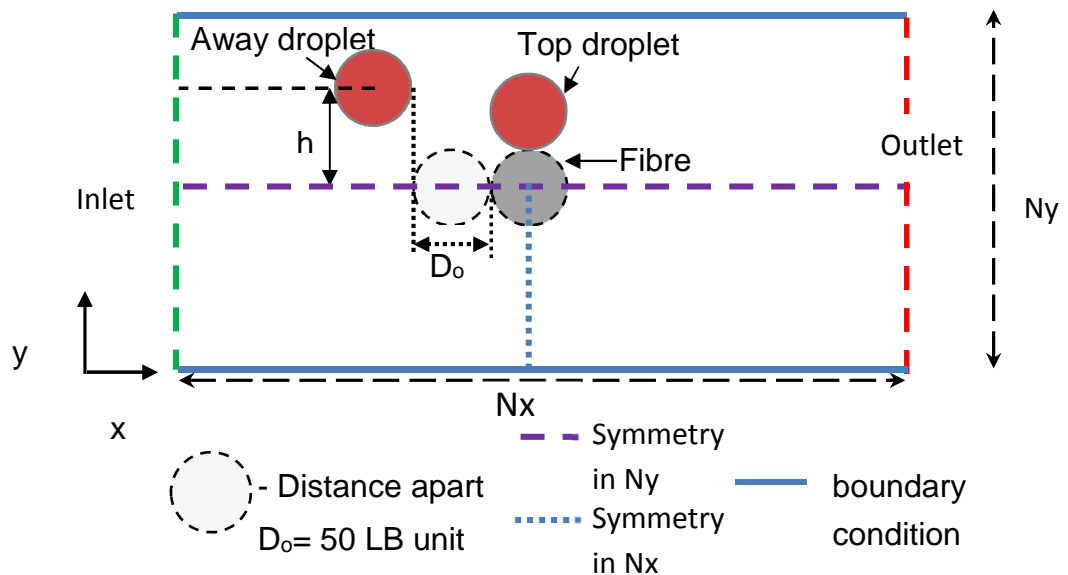


**Figure 6.6** Represents the inlet, outlet region with two droplets and a fibre. This system was studied for rectangular domain size.

The Figure 6.7 shows a droplet and fibre of  $16\mu\text{m}$  with a  $h$  distance of  $8\mu\text{m}$ . (A) is the initialisation step, (B) is initial droplet on the fibre has reached an equilibrium position and the second droplet has reached the position  $x=N_x/2$  and (C) is the final position at 50000 time step.

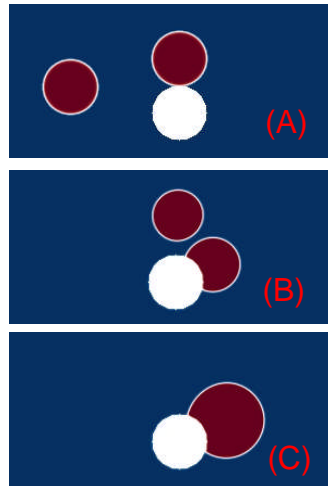


**Figure 6.7** Visual representation of droplet coalescing a different droplet on a fibre surface.(A) shows the initialisation step, (B) is before two droplets coalescence and (c) is coalesced droplet on a fibre.

**Table 6.2** Parameter studies for maximum h distance.

	Top Droplet radius	Away Droplet radius	Fibre radius	Contact angle	Dynamic viscosity ratio (D/w)
Simulation 1	16 $\mu$ m	16 $\mu$ m	16 $\mu$ m	0°-180°	2
Simulation 2	16 $\mu$ m	16 $\mu$ m	16 $\mu$ m	90°	2,3,4&5
Simulation 3	16 $\mu$ m	16 $\mu$ m	16 $\mu$ m	90°	2
Simulation 4	16 $\mu$ m	25 $\mu$ m	16 $\mu$ m	90°	2
Simulation 5	16 $\mu$ m	33 $\mu$ m	16 $\mu$ m	90°	2
Simulation 6	16 $\mu$ m	42 $\mu$ m	16 $\mu$ m	90°	2
Simulation 7	16 $\mu$ m	16 $\mu$ m	16 $\mu$ m	90°	2
Simulation 8	25 $\mu$ m	16 $\mu$ m	16 $\mu$ m	90°	2
Simulation 9	33 $\mu$ m	16 $\mu$ m	16 $\mu$ m	90°	2
Simulation 10	42 $\mu$ m	16 $\mu$ m	16 $\mu$ m	90°	2
Simulation 11	50 $\mu$ m	16 $\mu$ m	16 $\mu$ m	90°	2
Simulation 12	16 $\mu$ m	16 $\mu$ m	16 $\mu$ m	90°	2
Simulation 13	16 $\mu$ m	16 $\mu$ m	25 $\mu$ m	90°	2
Simulation 14	16 $\mu$ m	16 $\mu$ m	33 $\mu$ m	90°	2
Simulation 15	16 $\mu$ m	16 $\mu$ m	42 $\mu$ m	90°	2
Simulation 16	16 $\mu$ m	16 $\mu$ m	50 $\mu$ m	90°	2

### 6.3.3 Effect of contact angle

The operating conditions are provided in Table 6.2 for simulation 1, the two phase property with an interfacial tension of 28.5mN/m. Table 6.3 shows the snapshots of a droplet coalescing with a different droplet on a fibre, for a contact angle of 0°-180° at h distance of 16µm. After that Table 6.4 shows the snapshots of h distance at 16.7µm for contact angles of 120°, 106°, 90°, 78° and 64°. Figure 6.8 shows the critical  $h^*$  (offset-position) versus contact angle. In Table 6.4 contact angle 90°, the droplets do not coalesce due to the initial droplet on a fibre oscillates as the second droplet approaches.

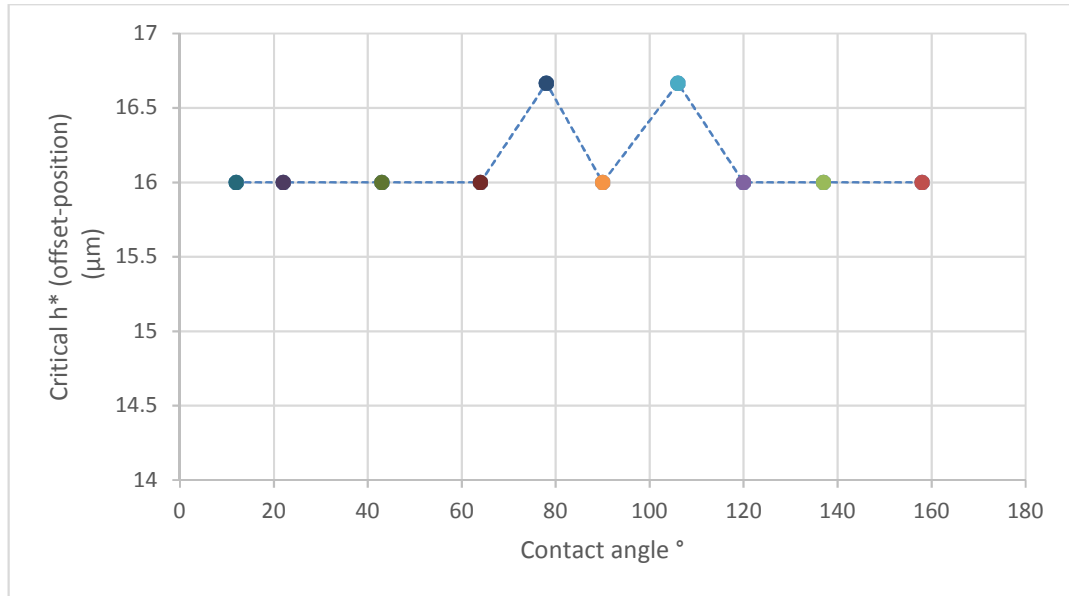
**Table 6.3** shows the snapshots of a droplet coalescing with a different droplet on a fibre (for different contact angle) at h distance (offset-parameter) of 16µm.

Contact angle	Time (lattice Boltzmann units (l.b.u))		
	Time=18000	Time=19000	Time=30000
158°			
137°	Time=17000	Time=18000	Time=30000
120°	Time=16000	Time=17000	Time=30000
106	Time=14000	Time=15000	Time=30000
90	Time=15000	Time=16000	Time=30000
	Time=14000	Time=15000	Time=30000

78			
	Time=13000	Time=14000	Time=30000
64			
	Time=12000	Time=13000	Time=30000
43			
	Time=12000	Time=13000	Time=30000
22			
	Time=10000	Time=11000	Time=30000
12			

**Table 6.4** shows the snapshots of a droplet coalescing with a different droplet on a fibre for contact angles of  $120^\circ$ ,  $106^\circ$ ,  $90^\circ$ ,  $78^\circ$  and  $64^\circ$  at h distance (offset-parameter) of 25.

Contact angle	Time (lattice Boltzmann units (l.b.u))		
	Time=14000	Time=15000	Time=20000
$120^\circ$			
$106^\circ$	Time=14000	Time=15000	Time=20000
$90^\circ$	Time=15000	Time=16000	Time=20000
$78^\circ$	Time=14000	Time=15000	Time=20000
$64^\circ$	Time=13000	Time=14000	Time=20000

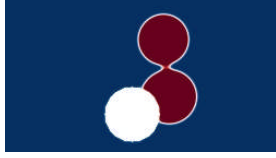
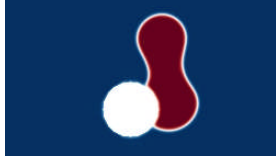


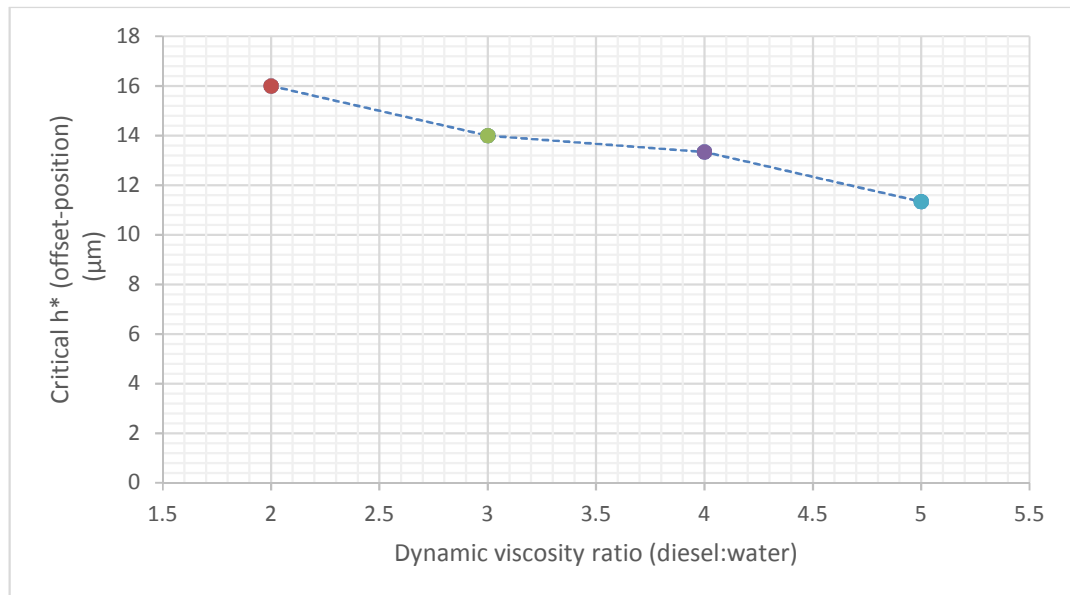
**Figure 6.8** The critical  $h^*$  (offset-position) versus contact angle.

### 6.3.4 Effect of dynamic viscosity ratio

Table 6.2 for simulation 2 provides the operating condition, with an interfacial tension of 28.5mN/m. Table 6.5 shows the snapshot of a droplet coalescing with a different droplet on a fibre (contact angle of 90°), at an initial coalescence stage for a different dynamic viscosity ratio. Figure 6.9 shows the critical  $h^*$  (offset-position) versus dynamic viscosity ratio.

**Table 6.5** shows the snapshots of a droplet coalescing with a different droplet on a fibre for different dynamic viscosity ratio.

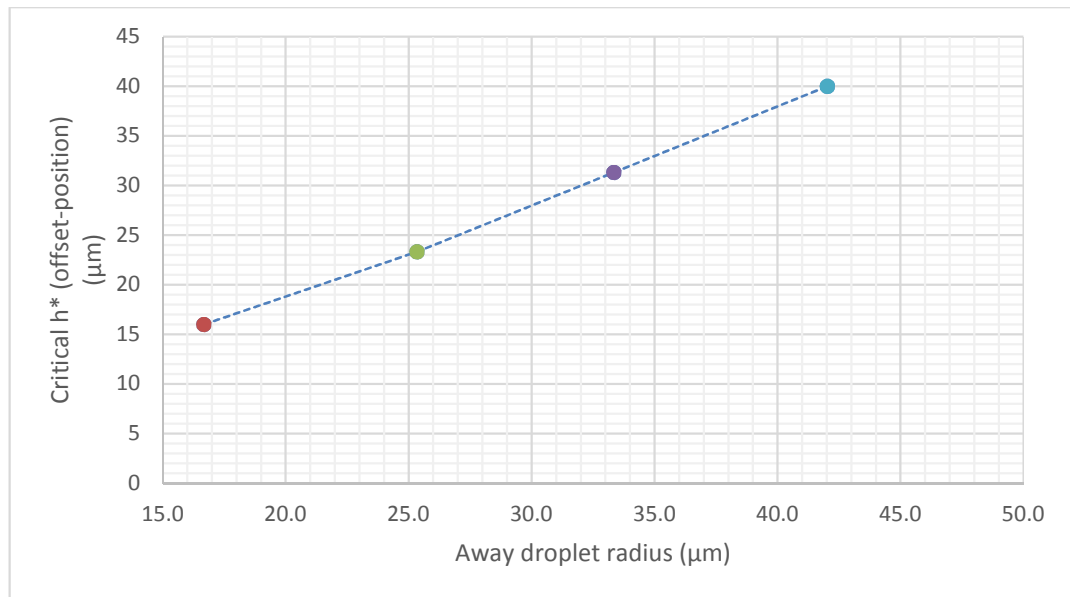
Dynamic viscosity ratio (Diesel: water)	At critical $h^*$ distance	Time step (LB units)
2		Time=16000
3		Time =17000
4		Time =19000
5		Time =20000



**Figure 6.9** The critical  $h^*$ (offset-position) versus dynamic viscosity ratio.

### 6.3.5 Effect of second droplet size

Simulations 3-6 in Table 6.2 were performed to explore the effect of changing the size of the second drop (i.e. initially away from the fibre) on the coalescence of this drop with one already held by the fibre. The interfacial tension was 28.5mN/m and the contact angle of the fibre was 90°. Figure 6.10 shows the critical  $h^*$  (offset-position) versus the second droplet radius.

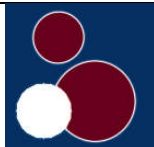
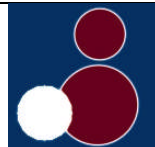
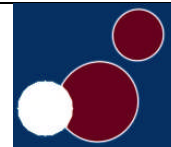
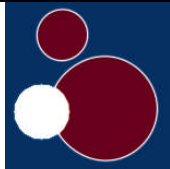
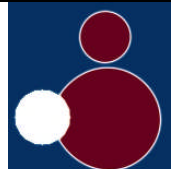
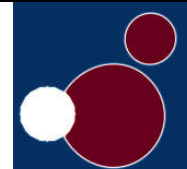
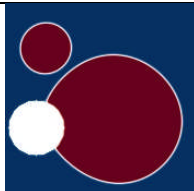
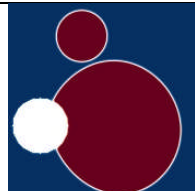
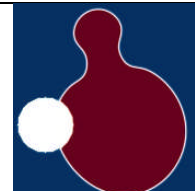
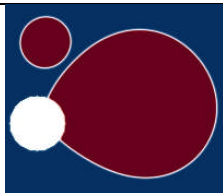
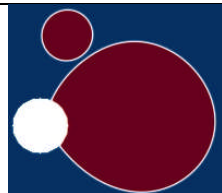
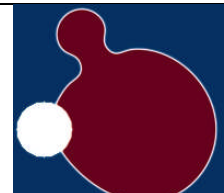


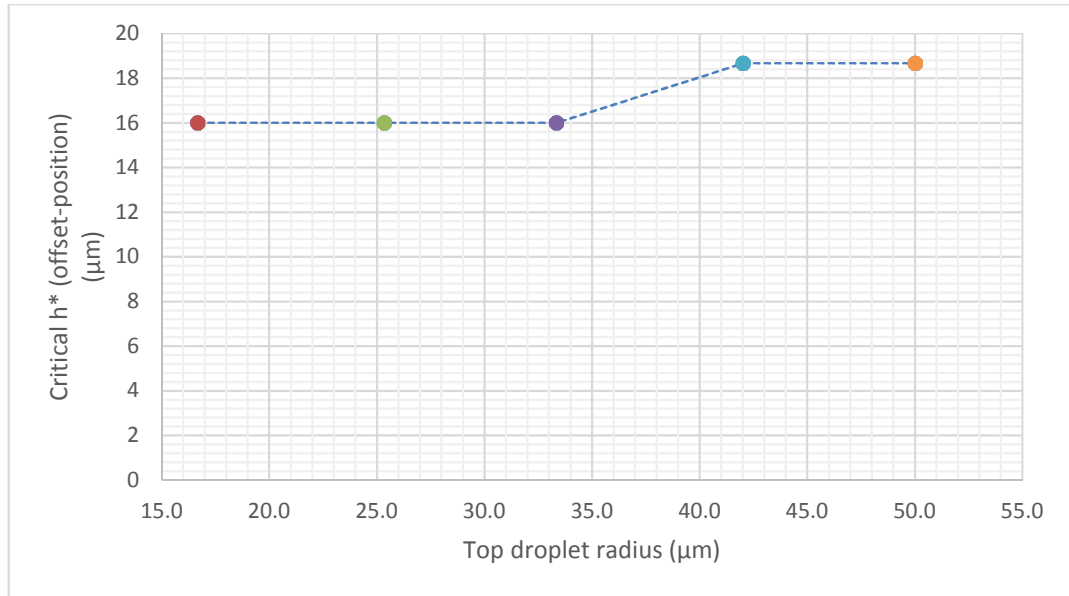
**Figure 6.10** The critical  $h^*$ (offset-position) versus away droplet radius.

### 6.3.6 Effect of the held droplet size

Table 6.2 for simulations 7-11 were executed to explore the effect of changing the size of the droplet holding on a fibre (Figure 6.6), with an interfacial tension of 28.5mN/m. Table 6.6 shows the snapshots of a droplet coalescing with a different droplet on a fibre, for a contact angle of 90° at h distance of 16.7 $\mu\text{m}$ . Figure 6.11 shows the critical  $h^*$ (offset-position) versus top droplet radius.

**Table 6.6** shows the snapshots of a droplet coalescing with a different droplet on a fibre (for  $90^\circ$  contact angle) at  $h$  distance (offset-parameter) of 25.

Top droplet radius	Time (lattice Boltzmann units (l.b.u))		
	Time=15000	Time=16000	Time=20000
16 $\mu\text{m}$			
	Time=15000	Time=18000	Time=20000
25 $\mu\text{m}$			
	Time=15000	Time=19000	Time=23000
33 $\mu\text{m}$			
	Time=15000	Time=18000	Time=19000
42 $\mu\text{m}$			
	Time=16000	Time=14000	Time=20000
50 $\mu\text{m}$			

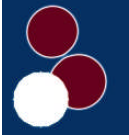
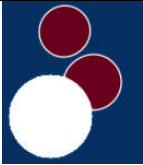
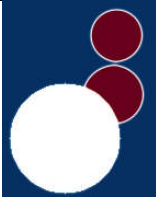
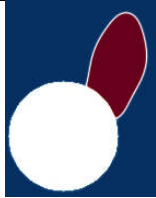
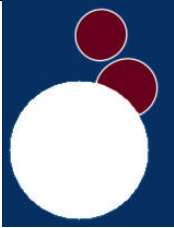
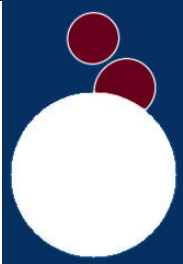


**Figure 6.11** The critical  $h^*$ (offset-position) versus top droplet radius.

### 6.3.7 Effect of fibre size

Simulations 12-16 in Table 6.2 are simulated to explore the effect of fibre size, with conditions similar to the previous simulation. Table 6.7 shows the snapshots of a droplet coalescing with a different droplet on different fibre size, for a contact angle of  $90^\circ$ . Figure 6.12 shows the critical  $h^*$ (offset-position) versus fibre radius.

**Table 6.7** shows the snapshots of a droplet coalescing with a different droplet on a different fibre radius (for 90° contact angle).

Fibre size	At critical $h^*$ distance	
	Before coalescence	After coalescence
16		
25		
33		
42		
50		

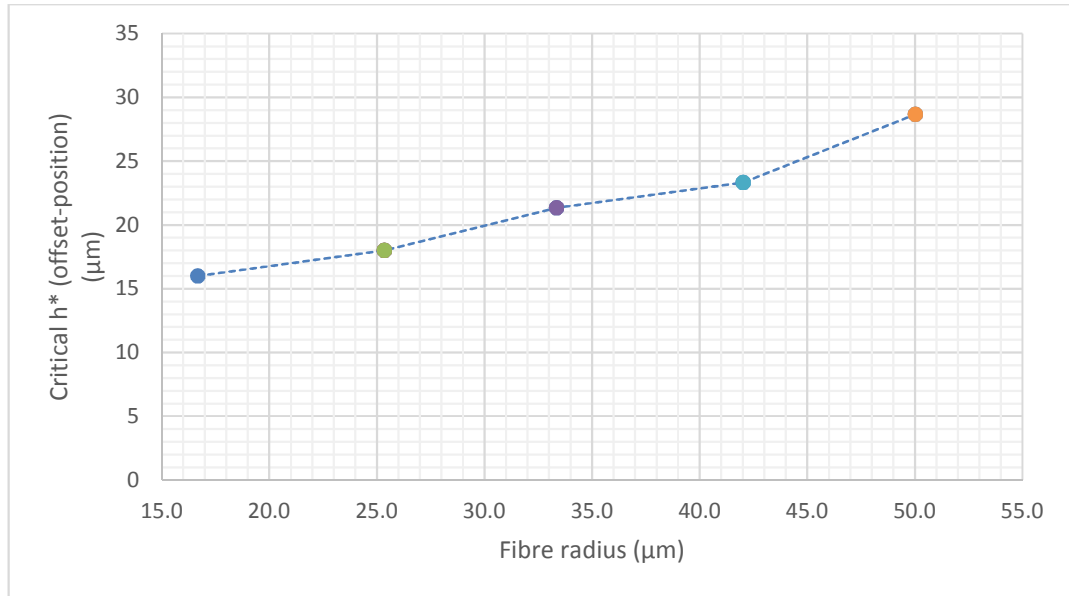


**Figure 6.12** shows the critical  $h^*$ (offset-position) versus fibre radius.

### 6.3.8 Discussion

#### ***Effect of contact angle***

Table 6.3 and Figure 6.8 shows that all the contact angles are useful below critical  $h^*$  of  $16\mu\text{m}$  for a droplet to coalesce with a droplet held on a fibre. From Table 6.3, it is noticeable that as the contact angle decreases ( $158^\circ > \theta$ ) the initial point for both droplets to meet each other tends to be in early stage (time) of the simulation, therefore the distance travelled by the droplets tends to decrease as well. Finally Table 6.3, last column shows the snapshots of different contact angles for droplets on a fibre, these visual representation provides a better understanding in a droplet contact line location for different contact angle. Figure 6.8 shows that contact angle of  $78^\circ$  and  $106^\circ$  tends to have an advantage of higher critical  $h^*$  compared to other contact angles. Table 6.4 provides the snapshots of both droplets meeting point, suggesting that the location of the droplet hanging on a fibre with the respective contact line is important for the coalescence process.

#### ***Effect of dynamic viscosity ratio***

Table 6.5 suggests that higher dynamic viscosity ratio leads to a longer time for a droplet to reach a different droplet on a fibre. This behaviour was observed in the earlier chapter (chapter 5). Figure 6.9 shows that a decrease in critical  $h^*$  for a higher dynamic viscosity ratio of diesel:water. Mainly

because it takes a longer time to drain the thin film between both droplets and drag force tends to push the moving droplet in the streamline direction.

***Effect of second droplet size***

Figure 6.10 shows that increasing the away droplet radius will increase the critical  $h^*$  distance. This suggests that larger droplets coalesce with a smaller droplet on a fibre and hangs on to the fibre. Therefore smaller fibres are essential in the filtration process for droplets to adhere on a fibre.

***Effect of the held droplet size***

Figure 6.11 shows that top droplet radius change will have a small variation in critical  $h^*$  distance, to understand this better, Table 6.6 shows snapshots of droplet approaching a different droplet on a fibre at  $16.7\mu\text{m}$  of  $h$  distance. It is noticeable that the top droplets of radius of 16, 25 and  $33\mu\text{m}$  do not coalesce with the moving droplet. The reason behind this could be that droplet on a fibre, changes the streamlines of the flow.

***Effect of fibre size***

Figure 6.12 shows that increasing the fibre size will increase the critical  $h^*$  distance. Also Table 6.7 shows the snapshots of critical  $h^*$  distance of different fibres. Increasing fibre size will change the streamlines of the flow and in Table 6.7, it is noticeable in the before coalescence column that the position of the droplet on the fibre has varied with the fibre size. Larger fibre size will have a droplet attached near the longitudinal fibre radius.

## 6.4 Continuous droplets on fibres

In coalescence filtration, the inlet layer and exit layer of fibres are critical to define the capture efficiency of the filter. Therefore fibres with different porosity and contact angles are studied in this section. From previous results, it suggest that interfacial tension and dynamic viscosity ratio of diesel:water influence the capture efficiency of the water droplets coalesced in filtration. These key parameters were varied. Figure 6.12 (A) shows a sketch of 3D fibres top view, (B) is the boundary condition in 2D view and (C) is the effective parameter change for porosity. Water droplets are initially placed upstream of the fibre such that the horizontal distance between the droplet layer and the fibre layer is equal to 50 LB unit or  $33\mu\text{m}$ . In droplet layer, one droplet diameter separates the two droplets. Also two fibres and two fibre layers centre position are separated through a distance  $L$  (Figure 6.12 (C)). The odd number fibre layer has an offset of  $0.5L$ . Finally the  $y=1/2 N_y$ , the symmetry of fibres and droplets were maintained for all the simulations(Figure 6.12 (B)).

### 6.4.1 Simulation setup

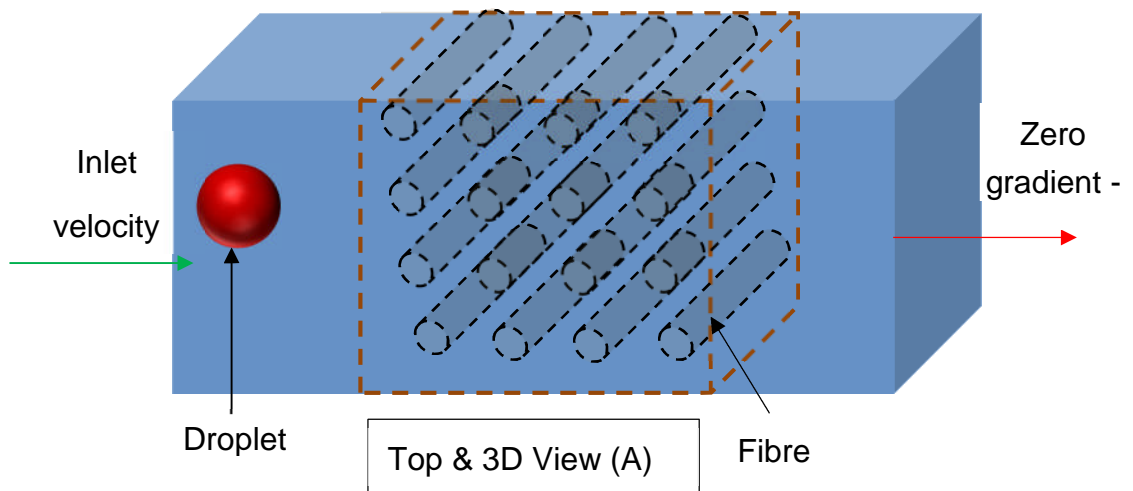
The multicomponent multiphase(MCMP) Shan-Chen lattice Boltzmann method was used and Figure 6.13 (B) shows the geometry studied (still 2D). The inlet velocity condition was imposed by forcing the distribution functions at inlet nodes to the equilibrium distribution functions corresponding to desired flow velocity. The outlet was a zero gradient boundary, while the top and bottom boundaries were linked together in a set periodic condition. A rectangular domain of  $1400 \times 900$  was created and a fibre was positioned with a centre at  $x: (200+25+\text{fibre radius})$ ,  $y:450$  in the lattice nodes. Then a  $L$  distance was varied between two fibres and two fibre layers centres. Eventually the maximum number of fibre layers were added till  $x=800$  LB unit (Figure 6.13 (c)), due to the useful domain size (check section 5.2.1). After that a droplet radius was positioned with a centre at  $x: (200-(25+\text{droplet radius}))$ ,  $y: 450$  in the lattice nodes (as shown in Figure 6.13 (B)). In the droplet layer, two droplets are distanced via a droplet diameter. Seven droplets were added at every 10000 time step, until the 340000 time step. In total 126 droplets were added to 400000 time step simulations. Seven

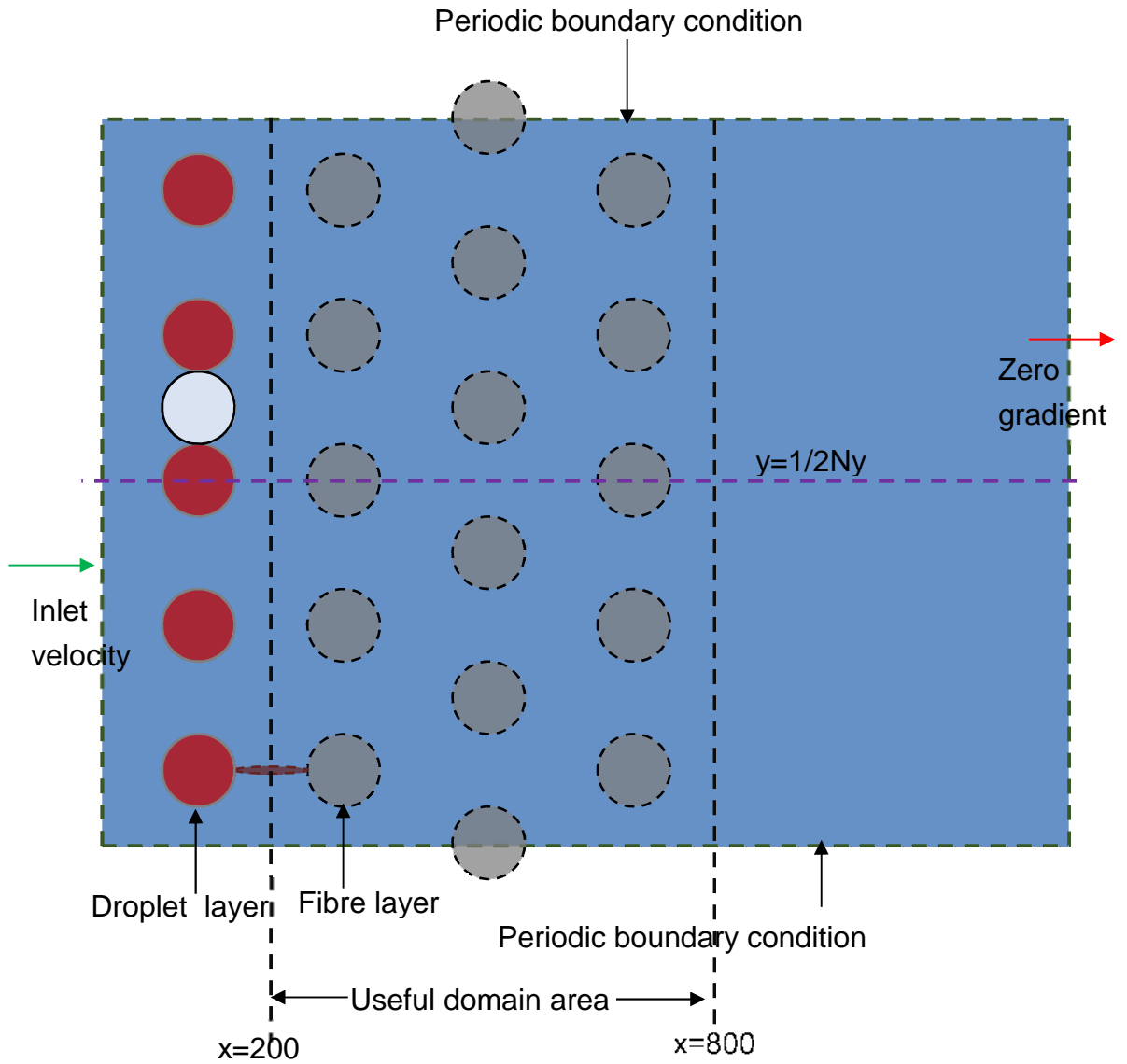
droplets were chosen to avoid the influence of periodic boundary condition and 10000 time step is because most of the droplet have passed the first fibre layer at that time. Combination of contact angle with porosity and interfacial tension and dynamic viscosity ratio were varied. Distance between water droplet and fibre is 50 LB unit/33 $\mu$ m, this distance was chosen to allow for the droplet to diffuse and settle during the initialisation step. Table 6.8 shows the combinations of parameters considered.

In 2D LBM simulation, the fibre porosity was calculated using the useful domain area and number of fibres (Table 6.8 (B)) with their area (section 2.8.3). Then the capture efficiency of (E) was analysed using the number of upstream and downstream droplet:

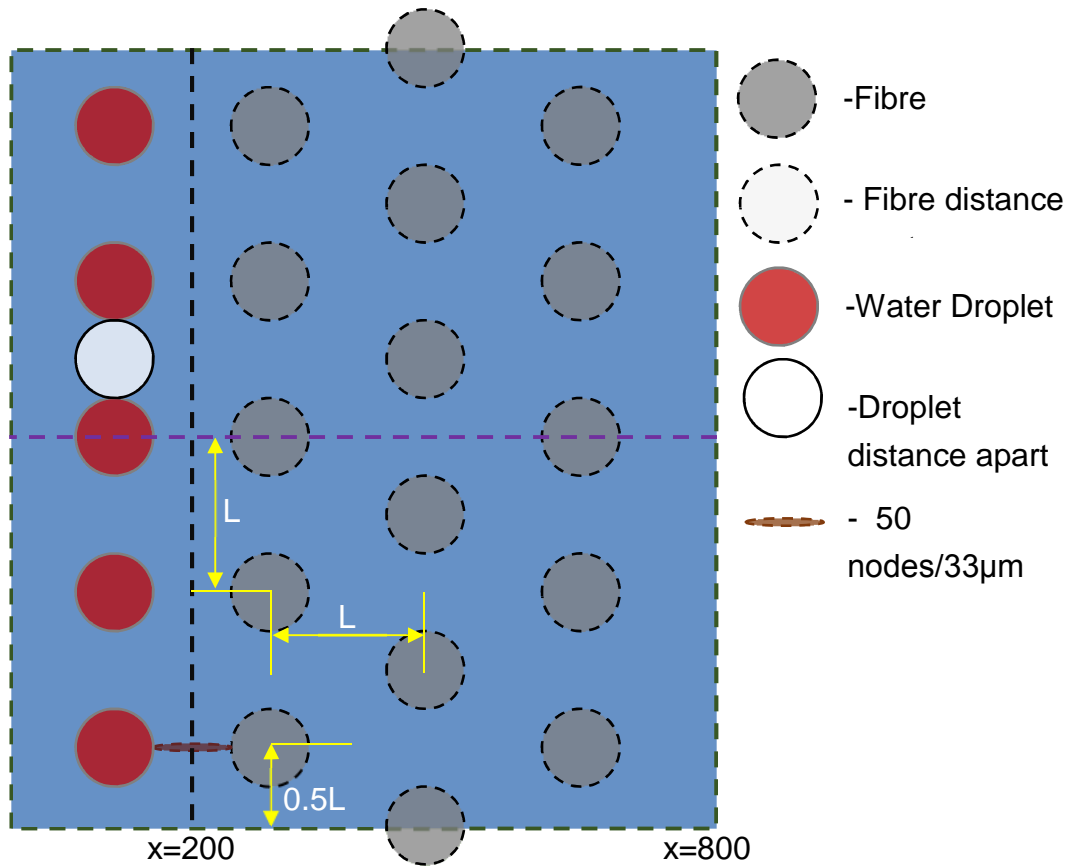
$$E = \left(1 - \frac{n_d}{n_u}\right) \times 100 \quad \text{Equation 6.1}$$

Where  $n_d$  is the number of downstream water droplets and  $n_u$  is the number of upstream water droplets. Downstream droplets were counted manually since there were fewer droplets. The downstream region was after  $x=800$  in Figure 6.13 (B). For example capture efficiency is 100%, the upstream droplets were coalesced in the domain.





Top & 2D view of staggered fibres with boundary condition (B)



Top & 2D view of staggered fibres with effective parameter  $L$  (C)

**Figure 6.13** (A) shows a sketch of 3D fibres top view, (B) is the boundary condition in 2D view and (C) is the effective parameter change for porosity.

**Table 6.8** Parameter studies for the effect of L value (A).

	Droplet radius	Fibre radius	Interfacial tension	L value	Dynamic viscosity ratio	Contact angle
Simulation 1	16 $\mu$ m	16 $\mu$ m	10mN/m	52,83 and,100 $\mu$ m	2	0°-180°
Simulation 2	16 $\mu$ m	16 $\mu$ m	20mN/m	52,83 and,100 $\mu$ m	2	0°-180°
Simulation 3	16 $\mu$ m	16 $\mu$ m	28.5mN/m	52,83 and,100 $\mu$ m	2	0°-180°
Simulation 4	16 $\mu$ m	16 $\mu$ m	28.5mN/m	52,83 and,100 $\mu$ m	3	0°-180°
Simulation 5	16 $\mu$ m	16 $\mu$ m	28.5mN/m	52,83 and,100 $\mu$ m	4	0°-180°
Simulation 6	16 $\mu$ m	16 $\mu$ m	28.5mN/m	52,83 and,100 $\mu$ m	5	0°-180°

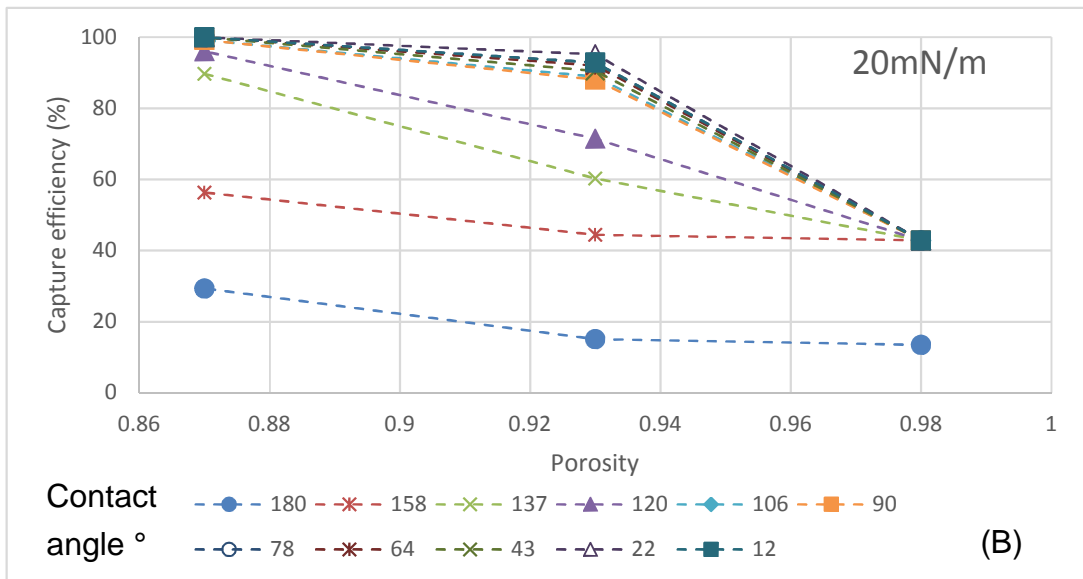
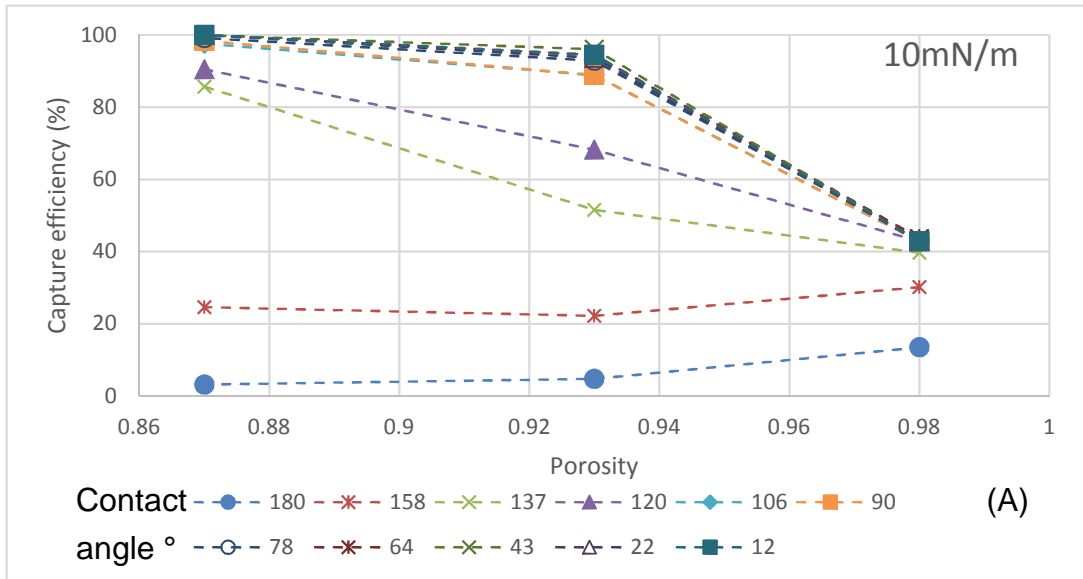
**Table 6.8** Equivalent porosity value for L (B).

L value	Porosity	Droplets in a layer	Number of layers	Number of fibres
52 $\mu$ m	0.87	7	5	35
83 $\mu$ m	0.93	5	4	20
100 $\mu$ m	0.98	3	2	6

#### 6.4.2 Effect of contact angle and interfacial tension

Simulations 1-3 in Table 6.8 (A) are simulated to explore the effect of interfacial tension for porosity values on Table 6.8 (B) . Figure 6.14 shows the capture efficiency versus porosity for different contact angle, (A),(B) and (C) are interfacial tension simulations of 10mN/m, 20mN/m and 28.5mN/m respectively. Higher contact angle tends to have a lower capture efficiency compared to lower contact angle. But increasing the interfacial tension will increase the capture efficiency of higher contact angle. Also  $\theta < 106^\circ$  tends to

have a small variation in capture efficiency and captures most of the droplets at porosity of 0.87.



The caption for the graphs above (A & B) are in Figure 6.14 on next page.

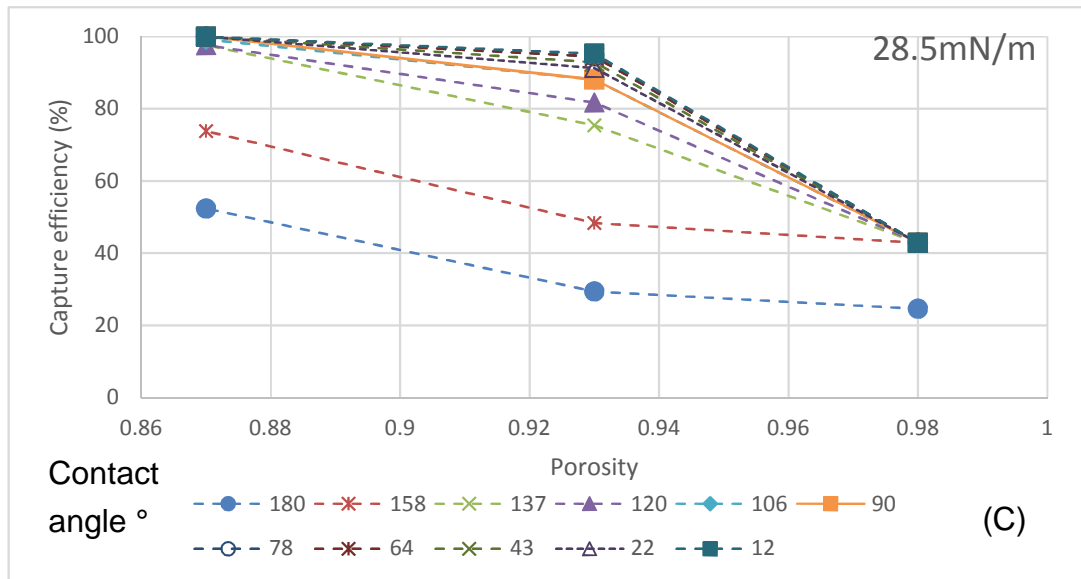
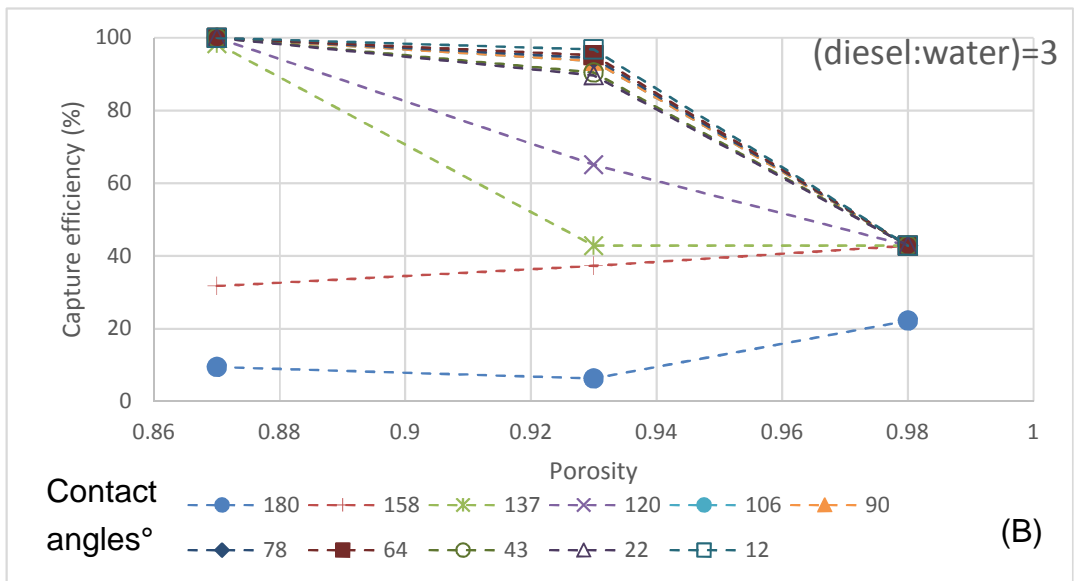
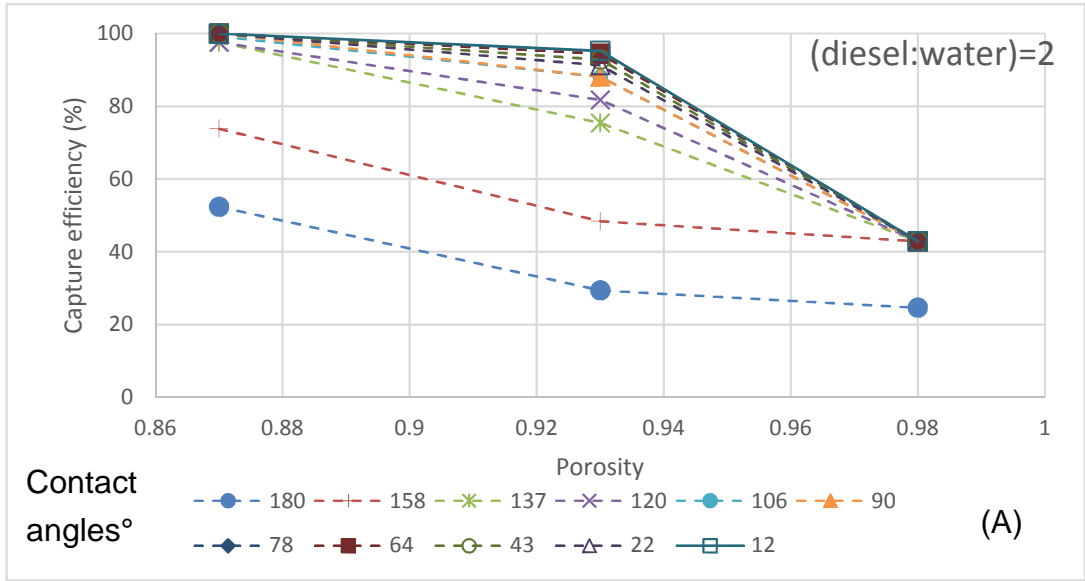


**Figure 6.14** show the capture efficiency versus porosity for different contact angles and (A), (B) and (C) represents the interfacial tension of 10mN/m, 20mN/m and 28.5mN/m respectively.

As shown in Figure 5.23, droplets with higher contact angle fibres are easily separated from the fibre. Hence droplets tend to pass through the fibre pack unchanged in size, Hence the capture efficiency is low. In contrast low contact angle leads to droplets spreading around fibres and being harder to detach (Figure 5.26). Hence they stay on fibres and coalesce. Therefore capture efficiency is higher.

### 6.4.3 Effect of dynamic viscosity ratio

The operating conditions are provided in Table 6.8 (A) for simulations 4-6 for the effect of dynamic viscosity ratio for porosity values on Table 6.8 (B). Figure 6.15 shows the capture efficiency versus porosity for different contact angle. Also (A),(B) (C) and (D) are dynamic viscosity ratio (diesel:water) of 2, 3, 4, and 5 respectively. Higher contact angle tends to result in lower capture efficiency compared to lower contact angle. But increasing the dynamic viscosity ratio will decrease the capture efficiency of higher contact angle. Also  $\theta > 106^\circ$  tends to have a higher variation in capture efficiency, and  $\theta < 106^\circ$  captures most of the droplets at porosity of 0.87.



The caption for the graphs above (A & B) are in Figure 6.15 on next page.

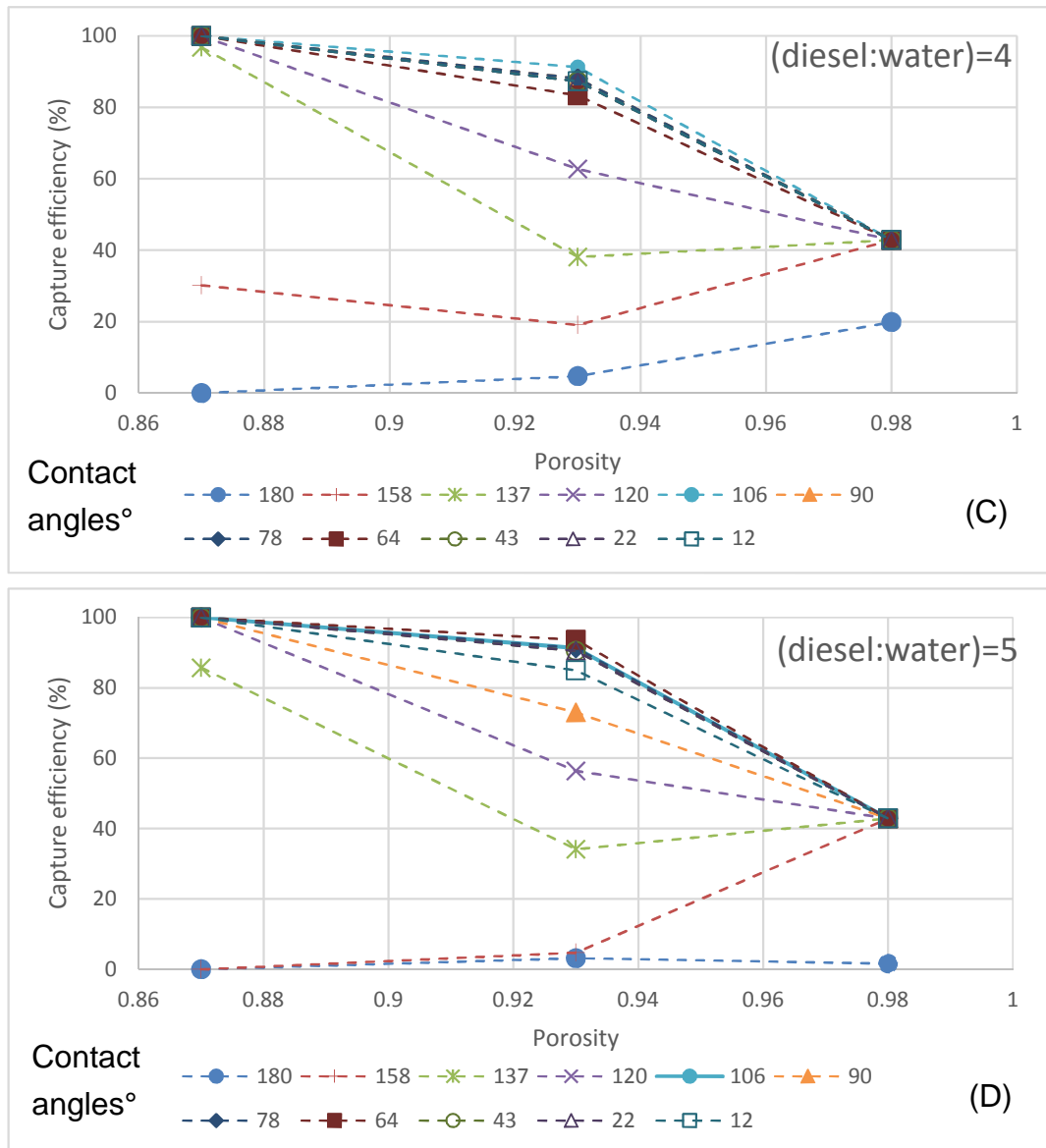
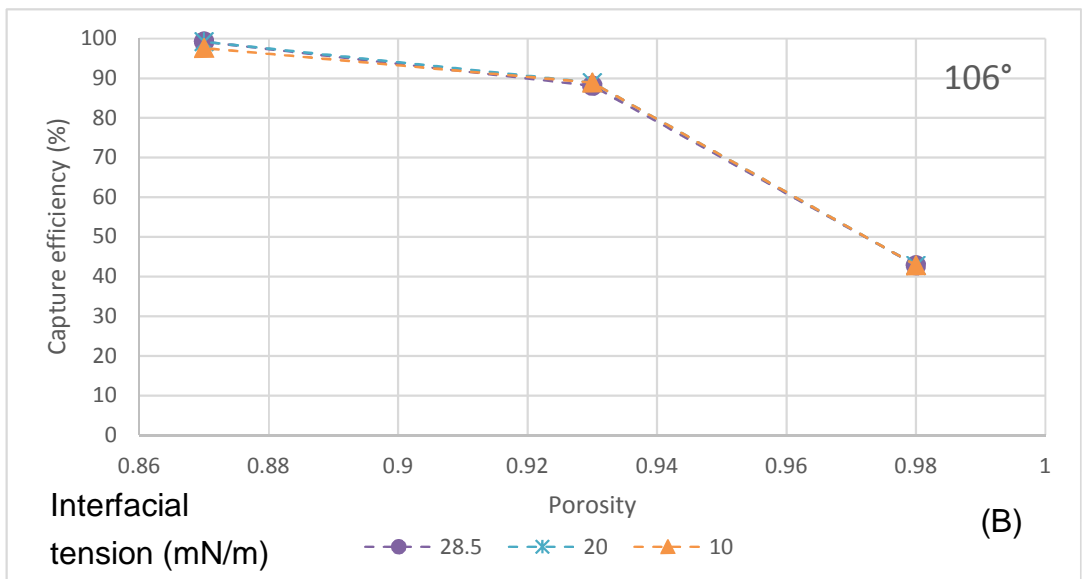
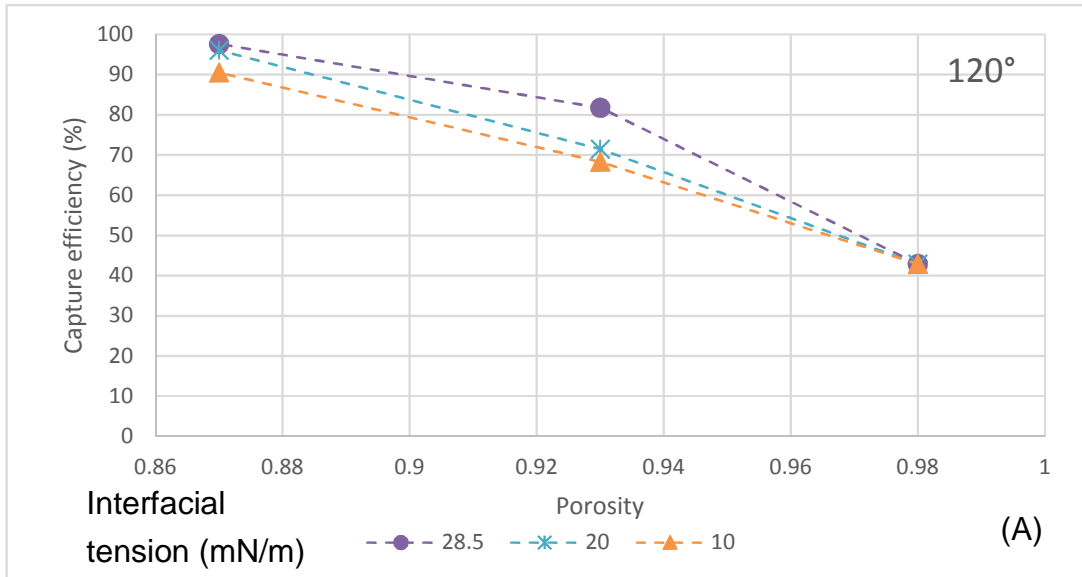


**Figure 6.15** show the capture efficiency versus porosity for different contact angles and dynamic viscosity ratio are 2, 3, 4 and 5 are respectively (A), (B) (C) and (D).

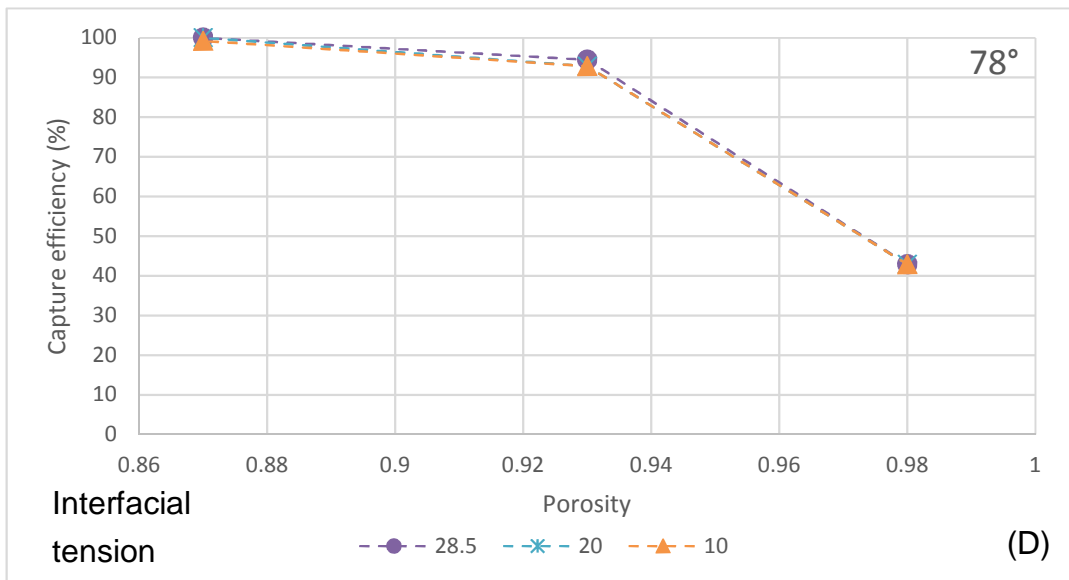
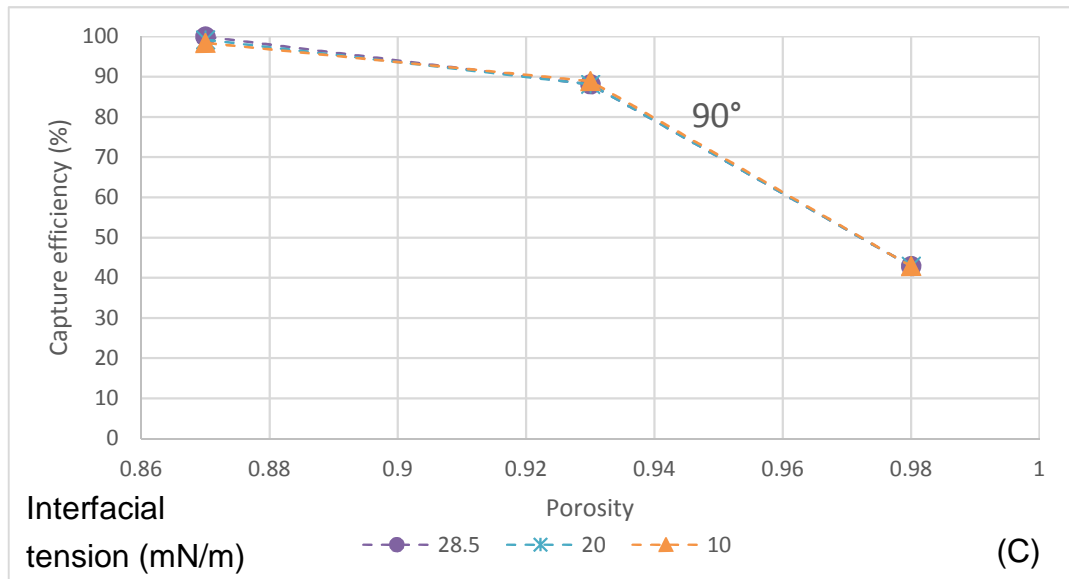
### 6.4.4 Discussion

Figure 6.14 shows the capture efficiency versus porosity for different contact angle. Also (A),(B) and (C) are interfacial tension simulations of 10mN/m, 20mN/m and 28.5mN/m respectively. Higher contact angle tends to have a lower capture efficiency compared to lower contact angle. But increasing the interfacial tension will increase the capture efficiency of higher contact angle. Also  $\theta < 106^\circ$  tends to have a small variation in capture efficiency and captures most of the droplets at porosity of 0.87. Figure 6.16 is analysed in terms of fixed contact angle for different surface tension in intermediate

wettability range.  $120^\circ$  contact angle has a less capture efficiency for interfacial tension value of 10 and 20 mN/m compared to contact angle of  $106^\circ$ ,  $90^\circ$  and  $78^\circ$ .



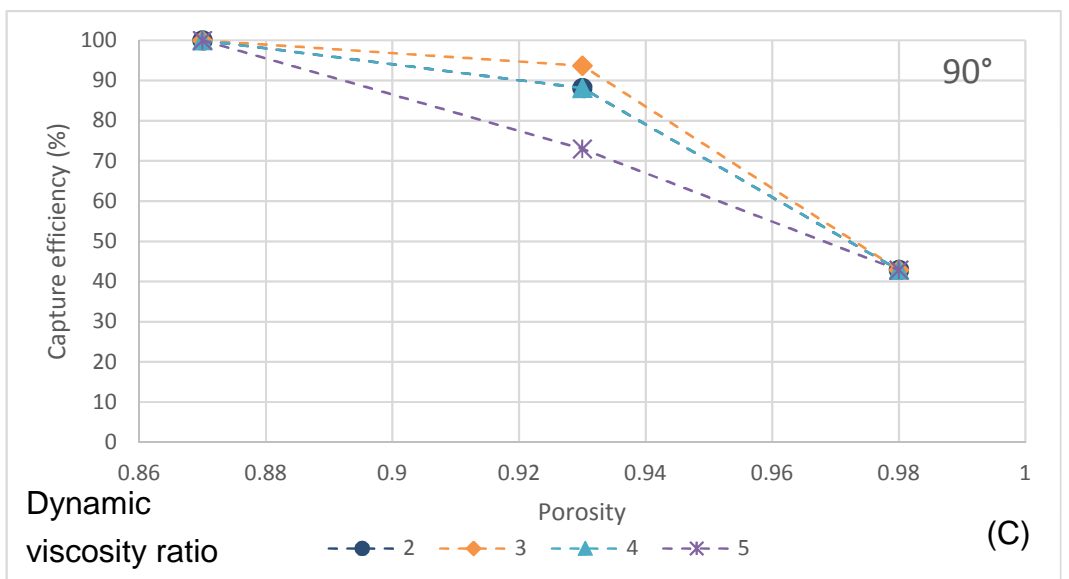
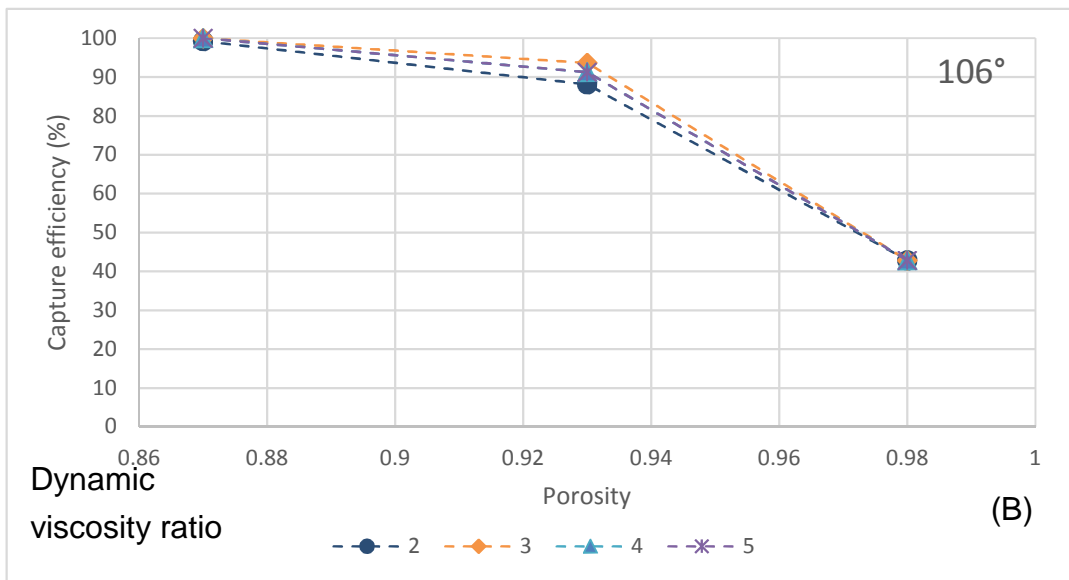
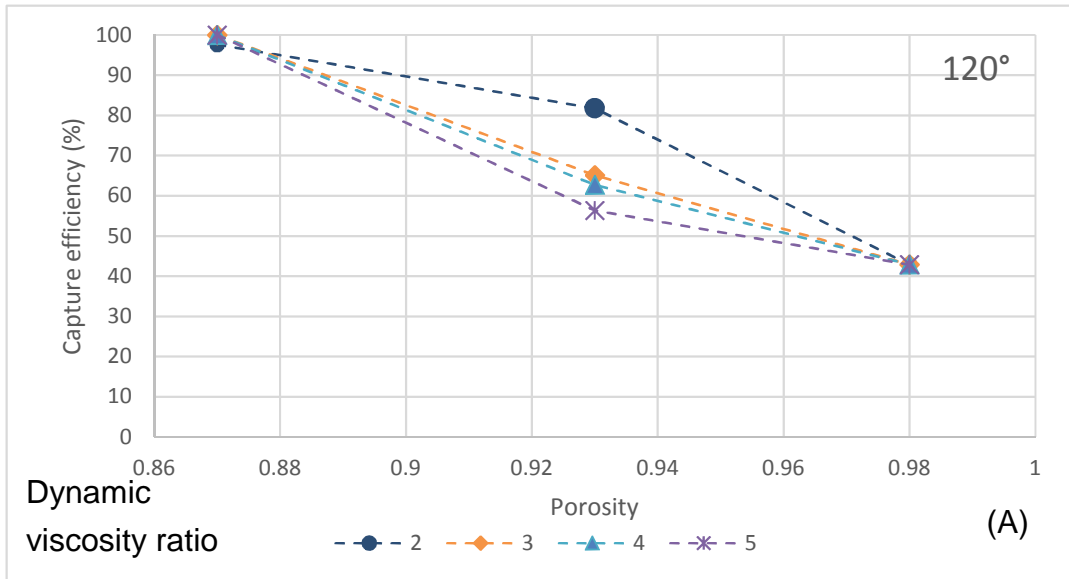
The caption for the graphs above (A & B) are in Figure 6.16 on next page.



**Figure 6.16** show the capture efficiency versus porosity for different contact angles.(A) is 120, (B) is 106, (C) is 90 and (D) is 78°.

Figure 6.15 shows the effect of dynamic viscosity ratio. Same as interfacial tension, higher the contact angle tends to have a lower capture efficiency compared to lower contact angle. But increasing the dynamic viscosity ratio will decrease the capture efficiency of higher contact angle. Figure 6.17 is analysed in terms of fixed contact angle for different dynamic viscosity ratio in intermediate wettability range. 120° tends to have a large variation in capture efficiency for different dynamic viscosity ratio of and 90° capture

efficiency at dynamic ratio of (diesel:water) 5 tends to have a low efficiency compared to 106° and 78°.



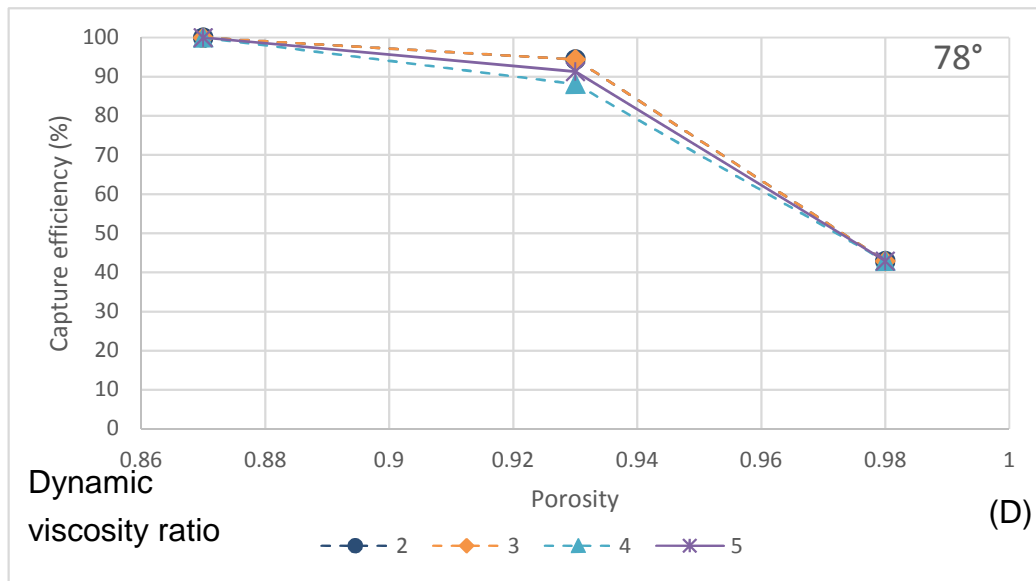


**Figure 6.17** show the capture efficiency versus porosity for different contact angles of 120°(A), 106°(B), 90°(C) and 78° (D).

## 6.5 Summary and conclusion

### ***Droplet attachment on a single fibre***

Increasing the velocity would decrease the effect of certain contact angles (mostly super hydrophobic). Also, at 0.15 m/s, as the contact angle increases ( $0^\circ < \theta < 180^\circ$ ),  $h^*$  decreases and all the contact angles have an effect on  $h^*$  at this velocity.

### ***Two droplets coalescing on a single fibre***

All the contact angles are useful below critical  $h^*$  of  $16\mu\text{m}$  for a droplet to adhere on a fibre. Also contact angle of  $78^\circ$  and  $106^\circ$  tends to have an advantage of higher critical  $h^*$  compared to other contact angles. A decrease in critical  $h^*$  for a higher a dynamic viscosity ratio of diesel:water. Larger droplets coalesce with a smaller droplet on a fibre and hangs on to the fibre. Therefore smaller fibres are essential in filtration process for droplet to adhere on a fibre.

### ***Continuous droplets on fibres***

Higher contact angle tends to have a lower capture efficiency compared to lower contact angle. But increasing the interfacial tension will increase the

capture efficiency of higher contact angle. Also  $\theta < 106^\circ$  tends to have a small variation in capture efficiency and captures most of the droplets at porosity of 0.87.  $120^\circ$  contact angle has a less capture efficiency for interfacial tension value of 10 and 20 mN/m compared to contact angle of  $106^\circ$ ,  $90^\circ$  and  $78^\circ$ . Then increasing the dynamic viscosity ratio will decrease the capture efficiency of higher contact angle. Also  $90^\circ$  capture efficiency at dynamic ratio of (diesel:water) 5 tends to have a low efficiency compared to  $106^\circ$  and  $78^\circ$ . Therefore inlet layer should have fibres of  $78^\circ$  contact angle and exit layer of  $106^\circ$ .

## **Chapter 7**

### **Conclusion and future work**

#### **7.1 Conclusions**

##### **7.1.1 Conclusions from changes to filter housing**

Droplet sizes below 1mm are commonly encountered within water in diesel mixtures [183]. The brief study in Comsol demonstrates that whilst small performance gains can be made through changing filter housing geometry, by far the most important part of the filter that can affect performance is the coalescence media. This gave credence to development of a modelling approach to allow a systematic study of the droplet coalescence process. For this the Shan-Chen multicomponent multiphase lattice Boltzmann method was used in subsequent chapters to build up a validation against other published work, followed by a systematic study of the coalescence of droplets onto fibres.

##### **7.1.2 Conclusions from validation of the model**

The Shan-Chen Lattice Boltzmann model was validated against published work of the finite volume numerical method (FVM) in conjunction with volume of fluid (VOF) approach (Mohammadi et al). In this work, a study was described of the simulation of free droplet coalescence. Results from both computational methods agreed closely. Key parameters of this study was the speed of approach of the droplets, the viscosity ratio of the two fluids and the interfacial tension. Whilst there was good overall agreement, there was one point of discrepancy between the two approaches – this was the time period for which for the LBM method showed a faster time to reach certain snapshots of the coalescence process than that found in Mohammadi et al with a maximum difference of 22%. The difference in time was observed because of two different computational methods, and the approach used to solve the Navier-Stokes equation (Figure 2.25). Therefore it is difficult to validate the time without experimental data. Key findings from a study of this work showed that a lower velocity of flow is much more beneficial to the

coalescence process. This is because the approaching droplet can push out the continuous phase of fluid before coalescence takes place. When the dynamic viscosity ratio of the diesel to water increases, a longer stage 1 coalescence time is required for the droplets to coalesce. Because a higher force is required to displace the thin film of diesel between water droplets. Finally for studies of a coalescing droplet, it was shown that for a higher interfacial tension between the two liquid phases, the coalescence process takes place much more easily. This can be attributed to the fact that the interface does not deform so easily, so during the approach of the droplet it remains more circular and this allows the fluid to flow from between the droplets more easily.

### **7.1.3 Conclusions of droplet coalescence studies**

Chapter 6 saw two key studies carried out in understanding the droplet coalescence process with regard to the use of a coalescing, non-woven filter. The first part of the study concerned droplet coalescence onto a single fibre. This was used to better understand how a droplet can be captured by a fibre, which is an essential part of the coalescing process.

#### Single Fibre Single Droplet Conclusions.

The conclusions here relate to the case where a droplet is located on the fibre at the start of the simulation, and the conditions are studied at which the droplet is released from the fibres. The first finding is that the nature of the droplet contact angle on fibre influences the critical detachment velocity. As the contact angle increases the critical detachment velocity decreases. This is because the contact line between the droplet and the fibre is decreased in size.

When a single droplet is located on the fibre, a larger interfacial tension between the two fluids means that the velocity required to detach the droplet is higher. Mainly because higher interfacial tension tends to have a high molecular interaction strength towards each other and a higher adhesion force towards the fibre. Likewise, a larger diameter of the droplet on the fibre reduces the critical detachment velocity. This is because the shear stress exerted on the droplet is increased with the larger size. In terms of fluid properties, when the viscosity ratio of the diesel to water is reduced, the

critical detachment velocity is increased. As with the previous point this is due to the influence of the shear stress on the water droplet.

The propensity for a water droplet carried by a diesel flow to be captured by a single solid fibre fixed in the flow was investigated by considering the maximum lateral offset between the approaching droplet and the fibre that leads to contact with and attachment to the fibre. The following key observations were made:

The critical offset  $h^*$  is greatly affected by the contact angle of the water droplet on the fibre. At very large contact angles, capture of the drop is only possible at low speeds and only if the droplet is on a close collision course with the fibre. For smaller contact angles,  $h^*$  increases substantially, and for hydrophilic fibres, capture is possible if the lateral separation between the droplet and fibre is up to 80% of the combined radii of the droplet and fibre. Increasing the flow velocity decreases  $h^*$  slightly at small contact angle, and more so at intermediate angles.

Larger fibres are not effective for small droplets. Small droplets (relative to the fibre) create much less local disturbance to the streamlined flow around the fibre, and are hence more easily 'steered' around the fibre without making contact. Larger droplets, on the other hand, influence the local flow field sufficiently to allow contact and with the fibre.

#### Single Fibre double droplets conclusions.

This part of the study considers the process of two droplets coalescing on a single fibre. The effective capture distance of the fibre is considered here, through the use of a parameter termed  $h^*$ , which describes the distance away from the centreline of the fibre where a droplet is no longer captured. From this a number of conclusions were drawn.

A contact angle of between  $78^\circ$  to  $106^\circ$  tends to have an advantage of higher critical  $h^*$  compared to other contact angles. This suggests that a fibre that is neither too hydrophobic or too hydrophilic is beneficial for the coalescence process. The location of the droplet hanging on a fibre with the respective contact line is important for the coalescence process.

A decrease in critical  $h^*$  is observed for a higher a viscosity ratio of diesel to water. This is because at higher ratios, the film between the droplet and the fibre is harder to squeeze from between the two, which is an essential component of the coalescence process.

Small fibre can hang on to a larger droplet. Therefore smaller fibres are essential in filtration process for droplet to adhere on a fibre.

### Continuous Droplets – Double Fibres

The final study in chapter 6 examined a continuous stream of droplets entering a fibre pack. Here it was found that fibres with higher contact angles ( $\theta > 120^\circ$ ) tends to have a lower capture efficiency compared to those with a lower contact angle.

Increasing the interfacial tension will increase the capture efficiency. This ties in with the work of a pair of droplets coalescing, where the film between the two has to be squeezed out of the contact before coalescence can take place.

Increasing dynamic viscosity ratio of diesel:water will reduce the capture efficiency. Also suggest that contact angles of  $78^\circ$  and  $106^\circ$  have less variation in all dynamic viscosity ratios. Inlet layer should have fibres of  $78^\circ$  contact angle and exit layer of  $106^\circ$ . Mostly hydrophilic fibres tends to coalesce and create a large droplet compared to hydrophobic fibres. Also there no complete droplet detachment for lower contact angle (Figure 5.22). Finally hydrophilic fibres could create capillary bridges between fibres and increase the pressure drop.

## **7.2 Future work**

1. There are a set of extensions to the studies carried out for the existing model that would add to the understanding.

- The extension of the work of the packs of fibres. This could be extended in a number of ways including a random distribution of fibres, and a deeper study into the mechanism of capture and release in a pack with a varying contact angle.

- the development of a Carnahan-starling in Shan-Chen model to control the density and surface tension values would be advantageous. In pseudo potential Shan-Chen model, the interaction potential  $G$  controls the interfacial tension and density. Spurious current decreases with the Carnahan-starling model.
- One limitation of the LB method is the relatively small (compared to real filters) number of fibres modelled. It may be possible to derive a statistical approach where small regions are statistically integrated together to give a better picture. For instance the regions could be described in terms of capture and release parameters which are then linked together analytically.

2. An extension of the modelling work to a three dimensional geometry. A key feature that is currently lacking in 2D is the existence of intersections between fibres and the interaction of a droplet with a fibre that runs in the same direction as the nominal direction of flow through the filter. This could be an essential part of the coalescence process that has not been captured with the current model, and may allow refinement of the non-woven mesh manufacturing process.

3. A key element that is currently missing from this work is validation of the computational results against experimental data. A partner project has been running ([184]), although this has generally focussed on bulk performance of the filter pack, rather than interaction at a small scale. There is an opportunity to study the interaction of fluids with fibres. This could be done by 3D printing fine structures, although the structures are bigger than typical fibres (a typical diameter on a printer is approximately 100 microns), and studying these.

## List of References

1. Cullen, J.M. and J.M. Allwood, *The efficient use of energy: Tracing the global flow of energy from fuel to service*. Energy Policy, 2010. **38**(1): p. 75-81.
2. Singh, N.K., *Experimental Investigations of Diesel Emulsions as Fuel in Small Direct Injection Compression Ignition Engines*. MIT Publications, 2012. **2**: p. 39-44.
3. DeltaExpo. *Diesel Engine: its advantages and disadvantages*. 2013 [cited 2013 17-05-]; Available from: <http://www.deltaexpo.com/content/view/118/>.
4. Sutherland, K., *Filters and Filtration Handbook*. Chemical, Petrochemical & Process. 2008: Butterworth-Heinemann. 1-524.
5. Filtration, C. *Fuel Filters and Fuel/Water Separators*. 2011 [cited 2013 17-05-]; Available from: [http://www.cumminsfiltration.com/pdfs/product\\_lit/americas\\_brochures/LT32599\\_01.pdf](http://www.cumminsfiltration.com/pdfs/product_lit/americas_brochures/LT32599_01.pdf).
6. Li, F., X. Wu, J. Wu, X. Xu, and S. Ma. *Kinetic study of adsorption of oil from oilfield produced water using modified porous ceramics filtration media in column mode*. in *2nd International Conference on Bioinformatics and Biomedical Engineering, iCBBE 2008, May 16, 2006 - May 18, 2006*. 2008. Shanghai, China: Inst. of Elec. and Elec. Eng. Computer Society.
7. Cort, A., Z. Jiang, and D.S. Suiter, *Fuel filter and water separator apparatus with integrated fuel pump*. 1999, Google Patents.
8. Council, F.M. *Diesel Fuel Contamination and Fuel Filter Plugging* 2007 [cited 2013 21-01-]; Available from: <http://www.aftermarketsuppliers.org/Councils/Filter-Manufacturers-Council/TSBs-2/English/95-1R2.pdf>.
9. Pecuniary, I. *The Water Eliminator*. 2004 [cited 2013 21-01-]; Available from: <http://www.diesel-fuels.com/water-contamination/water-eliminator.php>.
10. MAHLE. *Function of MAHLE diesel fuel filters*. 2013 [cited 2013 21-01-]; Available from: [http://www.mahle-aftermarket.com/MAHLE\\_Aftermarket\\_NA/en/Products-&-Services/Filters/Fuel-filters](http://www.mahle-aftermarket.com/MAHLE_Aftermarket_NA/en/Products-&-Services/Filters/Fuel-filters).
11. Vilcnik, A., I. Jerman, A.u. Vuk, M. Kozelj, B. Orel, B. Tomic, B. Simoncic, and J. Kovac, *Structural properties and antibacterial effects of hydrophobic and oleophobic sol-gel coatings for cotton fabrics*. Langmuir, 2009. **25**(10): p. 5869-5880.
12. ARTHURS, D. *Superhydrophobic spray means anything submerged in water comes out bone dry*. 2011 [cited 2013 21-01-]; Available from: <http://www.dailymail.co.uk/femail/article-2061484/Incredible-superhydrophobic-fabric-REPELS-water-revolutionise-ski-gear.html>.
13. Chambliss, S., J. Miller, C. Façanha, R. Minjares, and K. Blumberg, *The impact of stringent fuel and vehicle standards on premature mortality and emissions*. 2013.

14. Wilfong, D., A. Dallas, C. Yang, P. Johnson, K. Viswanathan, M. Madsen, B. Tucker, and J. Hacker, *Emerging Challenges of Fuel Filtration*, . American Filtration and Separation Society, Spring Conference, 2009: p. 105-115.
15. Erdemir, A., *Method to improve lubricity of low-sulfur diesel and gasoline fuels*. 2004, Google Patents.
16. Stanfel, C., *Fuel filtration: Protecting the diesel engine*. Filtration & Separation, 2009. **46**(3): p. 22-25.
17. Murugesan, A., C. Umarani, R. Subramanian, and N. Nedunchezian, *Bio-diesel as an alternative fuel for diesel engines—A review*. Renewable and Sustainable Energy Reviews, 2009. **13**(3): p. 653-662.
18. Wright, G., *Fundamentals of Medium/Heavy Duty Diesel Engines*. 2015: Jones & Bartlett Learning.
19. Cummins. *Fuel Filtration FACT SHEET*. 2010 [cited 2016 28/12]; Available from: [https://www.cumminsfiltration.com/pdfs/product\\_lit/americas\\_brochures/LT36179-GB.pdf](https://www.cumminsfiltration.com/pdfs/product_lit/americas_brochures/LT36179-GB.pdf).
20. Dickenson, T.C., *Filters and filtration handbook*. Vol. 4th. 1997, Oxford: Elsevier Advanced Technology.
21. Block, J., P. Klick, B. Grove, D. Zastera, J. Doyle, P. Johnson, Y. Elsayed, and A.J. Dallas. *CONTAMINANTS FOUND ON DIESEL FUEL STORAGE TANK FILTERS*. 2011. Florida USA: IASH.
22. Hardison, S. *Clogged Filter: Filter or Fuel Problem?* 2015 [cited 2015 07/12]; Available from: <http://www.racornews.com/#!Clogged-Filter-Filter-or-Fuel-Problem/c1m98/564bb5330cf292344da1b694>.
23. IPU, I.P.U.L. *Solid particulate contamination in diesel*. 2014 [cited 2015 14/12]; Available from: <http://www.ipu.co.uk/particulate-contamination/>.
24. Repetti, R.V. and M.H.S. Tseng, *Predict filter performance with beta ratios*. 2005, H.W. Wilson - Applied Science & Technology Abstracts. p. 44.
25. Brown, R. and T. Wines, *Improve suspended water removal from fuels*. Hydrocarbon Processing, 1993. **72**: p. 95-95.
26. Batts, B.D. and A.Z. Fathoni, *A literature review on fuel stability studies with particular emphasis on diesel oil*. Energy & Fuels, 1991. **5**(1): p. 2-21.
27. Chen, R., *Preliminary Studies of New Water Removal Element in Purification Applications of Diesel Fuels*. Journal of Fuels, 2014. **2014**.
28. International, A. *Standard Specification for Fuel Oils*. 2016; ASTM D396-16e1, :[Available from: [www.astm.org](http://www.astm.org)].
29. Tsanaktsidis, C.G., E.P. Favvas, G.T. Tzilantonis, S.G. Christidis, E.C. Katsidi, and A.V. Scaltsoyiannes, *Water removal from biodiesel/diesel blends and jet fuel using natural resin as dehydration agent*. The Canadian Journal of Chemical Engineering, 2015. **93**(10): p. 1812-1818.
30. Stone, W., G. Bessee, and C. Stanfel, *Diesel Fuel/Water Separation Test Methods—Where We Are and Where We Are Going*. SAE International Journal of Fuels and Lubricants, 2009. **2**(2009-01-0875): p. 317-323.

31. Shin, C. and G.G. Chase, *Water-in-oil coalescence in micro-nanofiber composite filters*. AIChE Journal, 2004. **50**(2): p. 343-350.
32. Stanfel, C. and F. Cousart, *Coalescence media for separation of water-hydrocarbon emulsions*. 2014, Google Patents.
33. Debra, W., D. Andrew, Y. Chuanfang, J. Philip, V. Karthik, M. Mike, and T. Brian. *Emerging Challenges of Fuel Filtration*. in *22th American Filtration and Separations Society Annual Meeting*. 2009.
34. Chesneau, H.L. *MICROBIAL GROWTH IN DIESEL FUEL*. 2014 [cited 2015 20/12]; Available from: <http://www.mycleandiesel.com/pages/SolutionMicrobialGrowth.aspx>.
35. Knothe, G., *Biodiesel and renewable diesel: a comparison*. Progress in Energy and Combustion Science, 2010. **36**(3): p. 364-373.
36. Bezergianni, S. and A. Dimitriadis, *Comparison between different types of renewable diesel*. Renewable and Sustainable Energy Reviews, 2013. **21**: p. 110-116.
37. Bolszo, C.D., A.A. Narvaez, V.G. McDonell, D. Dunn-Rankin, and W.A. Sirignano, *Pressure—Swirl Atomization of Water-in-Oil Emulsions*. Atomization and Sprays, 2010. **20**(12): p. 1077.
38. Yang, C., L. Senne, S. Larsen, and M. Madsen. *ULSD/biodiesel blend and its effect on fuel/water separation*. in *American Filtration and Separation Society Annual Conference*. 2008.
39. Wood, B.M., K. Kirwan, S. Maggs, J. Meredith, and S.R. Coles, *Study of combustion performance of biodiesel for potential application in motorsport*. Journal of Cleaner Production, 2015. **93**: p. 167-173.
40. Ally, J., E. Vittorias, A. Amirfazli, M. Kappl, E. Bonaccorso, C.E. McNamee, and H.-J. Butt, *Interaction of a Microsphere with a Solid-Supported Liquid Film*. Langmuir, 2010. **26**(14): p. 11797-11803.
41. Yang, W., H. An, S. Chou, K. Chua, B. Mohan, V. Sivasankaralingam, V. Raman, A. Maghbouli, and J. Li, *Impact of emulsion fuel with nano-organic additives on the performance of diesel engine*. Applied Energy, 2013. **112**: p. 1206-1212.
42. Nadeem, M., C. Rangkuti, K. Anuar, M. Haq, I. Tan, and S. Shah, *Diesel engine performance and emission evaluation using emulsified fuels stabilized by conventional and gemini surfactants*. Fuel, 2006. **85**(14): p. 2111-2119.
43. Fingas, M. and B. Fieldhouse, *Formation of water-in-oil emulsions and application to oil spill modelling*. Journal of Hazardous Materials, 2004. **107**(1–2): p. 37-50.
44. Alvarado, V., X. Wang, and M. Moradi, *Stability proxies for water-in-oil emulsions and implications in aqueous-based enhanced oil recovery*. Energies, 2011. **4**(7): p. 1058-1086.
45. Ithnin, A.M., H. Noge, H. Abdul Kadir, and W. Jazair, *An overview of utilizing water-in-diesel emulsion fuel in diesel engine and its potential research study*. Journal of the Energy Institute, 2014. **87**(4): p. 273-288.
46. Schramm, J., R.S. Sigvardsen, and M. Forman, *Bitumen/Water Emulsions as Fuels for High-Speed Ci Engines Preliminary Investigations*. 2003, SAE Technical Paper.
47. Jiao, J. and D.J. Burgess, *Rheology and stability of water-in-oil-in-water multiple emulsions containing Span 83 and Tween 80*. Aaps Pharmsci, 2003. **5**(1): p. 62-73.

48. Alahmer, A., J. Yamin, A. Sakhrieh, and M. Hamdan, *Engine performance using emulsified diesel fuel*. Energy Conversion and Management, 2010. **51**(8): p. 1708-1713.
49. Hagos, F.Y. and I.M. Tan. *Water-in-diesel emulsion and its micro-explosion phenomenon-review*. in *Communication Software and Networks (ICCSN), 2011 IEEE 3rd International Conference on*. 2011. IEEE.
50. Lif, A. and K. Holmberg, *Water-in-diesel emulsions and related systems*. Advances in Colloid and Interface Science, 2006. **123–126**: p. 231-239.
51. Yahaya Khan, M., Z. Abdul Karim, F.Y. Hagos, A.R.A. Aziz, and I.M. Tan, *Current trends in water-in-diesel emulsion as a fuel*. The Scientific World Journal, 2014. **2014**.
52. Lin, C.-Y. and K.-H. Wang, *The fuel properties of three-phase emulsions as an alternative fuel for diesel engines*☆. Fuel, 2003. **82**(11): p. 1367-1375.
53. Chen, G. and D. Tao, *An experimental study of stability of oil–water emulsion*. Fuel Processing Technology, 2005. **86**(5): p. 499-508.
54. Richardson, J.F., *Chemical Engineering, Volume 2*. Chemical, Petrochemical & Process. 2002: Elsevier Butterworth-Heinemann. 1-1232.
55. Yang, W.-C., *Handbook of fluidization and fluid-particle systems*. Vol. 91. 2003: CRC Press.
56. Svarovsky, L., *Solid-Liquid Separation*. Chemical, Petrochemical & Process. 2001: Elsevier Butterworth-Heinemann. 1-554.
57. GlobalSpec. *Scrubbers Information*. 2013 [cited 2013 02-05]; Available from: [http://www.globalspec.com/learnmore/manufacturing\\_process\\_equipment/air\\_quality/scrubbers](http://www.globalspec.com/learnmore/manufacturing_process_equipment/air_quality/scrubbers).
58. Pude, J.R.G., J.F. Hughes, and P.F. Coventry, *A study of electrostatic precipitation processes — calculation of electric fields due to a single unipolar source*. Journal of Electrostatics, 1983. **14**(3): p. 241-254.
59. Speth, H., A. Pfennig, M. Chatterjee, and H. Franken, *Coalescence of secondary dispersions in fiber beds*. Separation and Purification Technology, 2002. **29**(2): p. 113-119.
60. Ann, L.B.a.R.B. *Evolution of Respiratory Protection against Particulate Exposures*. 2009 [cited 2013 21-05-]; Available from: <http://blogs.cdc.gov/niosh-science-blog/2009/10/n95/#comments>.
61. Incorporated, T. *Mechanisms of filtration for high efficiency fibrous filters* 2012 [cited 2013 21-05-]; Available from: [http://www.tsi.com/uploadedFiles/Site\\_Root/Products/Literature/Application\\_Notes/ITI-041.pdf](http://www.tsi.com/uploadedFiles/Site_Root/Products/Literature/Application_Notes/ITI-041.pdf).
62. Camfil. *Diffusion and Electrostatic attraction*. 2011 [cited 2013 21-05-]; Available from: <http://www.camfil.co.uk/Filter-technology/Principles-of-Filtration/Electrostatic-attraction/>.
63. Xu, T., Q. Zhu, X. Chen, and W. Li, *Equivalent Cake Filtration Model*. Chinese Journal of Chemical Engineering, 2008. **16**(2): p. 214-217.
64. Rhodes, M. *Particle technology education 2006*. in *2006 AIChE Spring National Meeting - 5th World Congress on Particle Technology, April 23, 2006 - April 27, 2006*. 2006. Orlando, FL, United states: American Institute of Chemical Engineers.

65. Tien, C. and R. Bai, *An assessment of the conventional cake filtration theory*. Chemical Engineering Science, 2003. **58**(7): p. 1323-1336.
66. Tien, C., R. Bai, and B.V. Ramarao, *Analysis of cake growth in cake filtration: Effect of fine particle retention*. AIChE Journal, 1997. **43**(1): p. 33-44.
67. Jung, C.H. and K.W. Lee, *Analytic solution on critical suspended particle size and minimum collection efficiency in deep bed filtration*. Journal of Environmental Engineering, 2006. **132**(10): p. 1381-1386.
68. Osmak, S., D. Gosak, and A. Glasnovic. *Dynamic mathematical model of deep bed filtration process*. in *Joint 6th International Symposium on Process Systems Engineering and 30th European Symposium on Computer Aided Process Engineering. PSE '97-ESCAPE-7, 25-29 May 1997*. 1997. UK: Elsevier.
69. Gitis, V., I. Rubinstein, M. Livshits, and G. Ziskind, *Deep-bed filtration model with multistage deposition kinetics*. Chemical Engineering Journal, 2010. **163**(1-2): p. 78-85.
70. Ghidaglia, C., L. de Arcangelis, J. Hinch, and E. Guazzelli, *Hydrodynamic interactions in deep bed filtration*. Physics of Fluids, 1996. **8**(1): p. 6-14.
71. Jysoo, L. and J. Koplik, *Network model for deep bed filtration*. Physics of Fluids, 2001. **13**(5): p. 1076-86.
72. Holdich, R.G., I.W. Cumming, and I.D. Smith, *Crossflow microfiltration of oil in water dispersions using surface filtration with imposed fluid rotation*. Journal of Membrane Science, 1998. **143**(1-2): p. 263-274.
73. MEMOS. *Membrane filtration, Cross flow-system and Dead end-system 2013* [cited 2013 22-01-]; Available from: <http://www.memos-filtration.de/cms/en/index.php?section=12>.
74. Polyakov, Y.S., *Phenomenological theory of depth membrane filtration*. Chemical Engineering Science, 2007. **62**(7): p. 1851-1860.
75. Broeckmann, A., J. Busch, T. Wintgens, and W. Marquardt, *Modeling of pore blocking and cake layer formation in membrane filtration for wastewater treatment*. Desalination, 2006. **189**(1-3): p. 97-109.
76. Aimar, P., M. Meireles, P. Bacchin, and V. Sanchez, *Fouling and concentration polarisation in ultrafiltration and microfiltration*. NATO ASI Series E Applied Sciences-Advanced Study Institute, 1994. **272**: p. 27-58.
77. Li, L., L. Ding, Z. Tu, Y. Wan, D. Clause, and J.-L. Lanoisellé, *Recovery of linseed oil dispersed within an oil-in-water emulsion using hydrophilic membrane by rotating disk filtration system*. Journal of Membrane Science, 2009. **342**(1-2): p. 70-79.
78. Koris, A. and G. Vatai, *Dry degumming of vegetable oils by membrane filtration*. Desalination, 2002. **148**(1-3): p. 149-153.
79. Merdaw, A.A., A.O. Sharif, and G.A.W. Derwish, *Water permeability in polymeric membranes, Part I*. Desalination, 2010. **260**(1-3): p. 180-192.
80. Lin, C.L. and J.D. Miller, *Network analysis of filter cake pore structure by high resolution X-ray microtomography*. Chemical Engineering Journal, 2000. **77**(1-2): p. 79-86.
81. Hartmann, J., *Absorbent polymer technology*. Edited by L. BRANNON-PEPPAS and R. S. HARLAND. ISBN 0-444-88654-0. Amsterdam/Oxford/New York/Tokio: Elsevier 1990. 278 p., cloth

- bound, us \$107.75/df. 210.00. (Available in the USA/Canada from Elsevier Science Publishing Co., Inc., P.O. Box 882, Madison Square Station, New York, NY 10159, U.S.A.). *Acta Polymerica*, 1991. **42**(11): p. 612-613.
82. Lin, C.L. and J.D. Miller, *Pore structure analysis of particle beds for fluid transport simulation during filtration*. *International Journal of Mineral Processing*, 2004. **73**(2-4): p. 281-294.
  83. Lin, C.L. and J.D. Miller, *Pore structure and network analysis of filter cake*. *Chemical Engineering Journal*, 2000. **80**(1-3): p. 221-231.
  84. Garcia, X., L.T. Akanji, M.J. Blunt, S.K. Matthai, and J.P. Latham, *Numerical study of the effects of particle shape and polydispersity on permeability*. *Physical Review E*, 2009. **80**(2): p. 021304.
  85. Jönsson, K.A.-S. and B.T.L. Jönsson, *Fluid flow in compressible porous media: I: Steady-state conditions*. *AIChE Journal*, 1992. **38**(9): p. 1340-1348.
  86. Nemeč, D. and J. Levec, *Flow through packed bed reactors: 1. Single-phase flow*. *Chemical Engineering Science*, 2005. **60**(24): p. 6947-6957.
  87. Wadell, H., *Sphericity and roundness of rock particles*. *The Journal of Geology*, 1933. **41**(3): p. 310-331.
  88. Heywood, H., *Particle shape coefficients*. *J. Imp. Coll. Chem. Eng. Soc*, 1954. **8**(3): p. 25-33.
  89. Barreiros, F.M., P.J. Ferreira, and M.M. Figueiredo, *Calculating shape factors from particle sizing data*. *Particle & particle systems characterization*, 1996. **13**(6): p. 368-373.
  90. Vaughn, E.A. *Principles of Woven, Knitted, and Nonwoven Fabric Formation*. 2013 [cited 2013 07-05-]; Available from: <http://www.inda.org/events/training/reading/SuggestedReadings/Principles%20of%20Woven%20Knitted%20and%20Nonwoven.pdf>.
  91. Rushton, A. and A.S. Ward, *Solid-Liquid Filtration and Separation Technology: Book Review*. *Journal of the American Chemical Society*, 1997. **119**(27): p. 6454-6454.
  92. Inc, P.G. *Web Formation*. 2013 [cited 2013 12-10-]; Available from: <http://www.pgi-industrial-europe.com/en/web-formation>.
  93. Sakpal, P. and S. Landage, *Application of nonwovens for water filtration*.
  94. Schmieschek, S. and J. Harting, *Contact angle determination in multicomponent lattice Boltzmann simulations*. arXiv preprint arXiv:0910.3915, 2009.
  95. Johnson, K., K. Kendall, and A. Roberts. *Surface energy and the contact of elastic solids*. in *Proceedings of the Royal Society of London A: Mathematical, Physical and Engineering Sciences*. 1971. The Royal Society.
  96. Wolf, F., L.O. dos Santos, and P. Philippi. *Fluid interfaces in phase transition problems: Lattice Boltzmann method*. in *18th International Congress of Mechanical Engineering*. 2005.
  97. Jain, P.K., *Simulation of two-phase dynamics using lattice boltzmann method (LBM)*. 2010, University of Illinois.
  98. Young, T., *An essay on the cohesion of fluids*. *Philosophical Transactions of the Royal Society of London*, 1805. **95**: p. 65-87.

99. Yuan, Y. and T.R. Lee, *Contact Angle and Wetting Properties*, in *Surface Science Techniques*, G. Bracco and B. Holst, Editors. 2013, Springer Berlin Heidelberg: Berlin, Heidelberg. p. 3-34.
100. Magiera, R. and E. Blass, *Separation of liquid-liquid dispersion by flow through fibre beds*. *Filtration & Separation*, 1997. **34**(4): p. 369-376.
101. Patel, S.U. and G.G. Chase, *Separation of water droplets from water-in-diesel dispersion using superhydrophobic polypropylene fibrous membranes*. *Separation and Purification Technology*, 2014. **126**: p. 62-68.
102. Steerenberg, P.A., J.A.J. Zonnenberg, J.A.M.A. Dormans, P.N.T. Joon, I.M. Wouters, L.v. Bree, P.T.J. Scheepers, and H.V. Loveren, *Diesel Exhaust Particles Induced Release of Interleukin 6 and 8 by (Primed) Human Bronchial Epithelial Cells (Beas 2b) In Vitro*. *Experimental Lung Research*, 1998. **24**(1): p. 85-100.
103. Shin, C. and G. Chase, *The effect of wettability on drop attachment to glass rods*. *Journal of colloid and interface science*, 2004. **272**(1): p. 186-190.
104. Rajgarhia, S.S., S.C. Jana, and G.G. Chase, *Separation of Water from Ultralow Sulfur Diesel Using Novel Polymer Nanofiber-Coated Glass Fiber Media*. *ACS Applied Materials & Interfaces*, 2016. **8**(33): p. 21683-21690.
105. Contal, P., J. Simao, D. Thomas, T. Frising, S. Callé, J. Appert-Collin, and D. Bémer, *Clogging of fibre filters by submicron droplets. Phenomena and influence of operating conditions*. *Journal of Aerosol Science*, 2004. **35**(2): p. 263-278.
106. Cambiella, A., E. Ortea, G. Rios, J.M. Benito, C. Pazos, and J. Coca, *Treatment of oil-in-water emulsions: Performance of a sawdust bed filter*. *Journal of hazardous materials*, 2006. **131**(1): p. 195-199.
107. Chen, R., *Preliminary Studies of New Water Removal Element in Purification Applications of Diesel Fuels*. *Journal of Fuels*, 2014. **2014**: p. 6.
108. Hazlett, R.N., *Fibrous Bed Coalescence of Water. Steps in the Coalescence Process*. *Industrial & Engineering Chemistry Fundamentals*, 1969. **8**(4): p. 625-632.
109. Sokolović, R.M.Š., T.J. Vulić, and S.M. Sokolović, *Effect of bed length on steady-state coalescence of oil-in-water emulsion*. *Separation and purification technology*, 2007. **56**(1): p. 79-84.
110. Wang, J., S.C. Kim, and D.Y. Pui, *Figure of merit of composite filters with micrometer and nanometer fibers*. *Aerosol Science and Technology*, 2008. **42**(9): p. 722-728.
111. Miller, J.D., E.E. Koslow, and K.M. Williamson, *Coalescing filter for removal of liquid aerosols from gaseous streams*. 1988, Google Patents.
112. Šecerov Sokolovic, R.M., S.M. Sokolovic, and B.D. Đokovic, *Effect of working conditions on bed coalescence of an oil-in-water emulsion using a polyurethane foam bed*. *Industrial & engineering chemistry research*, 1997. **36**(11): p. 4949-4953.
113. Sherony, D.F. and R.C. Kintner, *Coalescence of an emulsion in a fibrous bed: Part I. Theory*. *The Canadian Journal of Chemical Engineering*, 1971. **49**(3): p. 314-320.

114. Sherony, D.F. and R.C. Kintner, *Coalescence of an emulsion in a fibrous bed: Part II. Experimental*. The Canadian Journal of Chemical Engineering, 1971. **49**(3): p. 321-325.
115. Sareen, S., P. Rose, R. Gudesen, and R. Kintner, *Coalescence in fibrous beds*. AIChE Journal, 1966. **12**(6): p. 1045-1050.
116. Rebelein, F. and E. Blass, *Separation of micro-dispersions in fibre-beds*. Filtration & Separation, 1990. **27**(5): p. 360-363.
117. Fahim, M. and F. Othman, *Coalescence of secondary dispersions in composite packed beds*. Journal of dispersion science and technology, 1987. **8**(5-6): p. 507-523.
118. Bitten, J.F., *Coalescence of water droplets on single fibers*. Journal of colloid and interface science, 1970. **33**(2): p. 265-271.
119. Rose, P.M., *Mechanisms of operation of a fibrous bed coalescer*. 1963, Illinois Institute of Technology: Chicago.
120. Vinson, C.G., *The coalescence of micron-sized drops in liquid-liquid dispersions in flow past fine-mesh screen*. 1965, University of Michigan: Michigan.
121. Viswanadam, G. and G.G. Chase, *Water–diesel secondary dispersion separation using superhydrophobic tubes of nanofibers*. Separation and Purification Technology, 2013. **104**: p. 81-88.
122. Kulkarni, P.S., S.U. Patel, S.U. Patel, and G.G. Chase, *Coalescence filtration performance of blended microglass and electrospun polypropylene fiber filter media*. Separation and Purification Technology, 2014. **124**: p. 1-8.
123. Voyutskii, S., K. Akl'yanova, R. Panich, and N. Fodiman. *Mechanism of separation of the disperse phase of emulsions during filtration*. in *Dokl. Akad. Nauk SSSR*. 1953.
124. Akagi, Y., K. Okada, T. Dote, and N. Yoshioka, *Effect of wettability of glass fiber beds on separation of oil droplets dispersed in water*. Journal of chemical engineering of Japan, 1990. **23**(1): p. 105-108.
125. Angelov, G., L. Boyadzhiev, and G. Kyutchoukov, *Separator for liquid-liquid dispersions*. Chemical Engineering Communications, 1984. **25**(1-6): p. 311-320.
126. Spielman, L.A. and S.L. Goren, *Experiments in coalescence by flow through fibrous mats*. Industrial & Engineering Chemistry Fundamentals, 1972. **11**(1): p. 73-83.
127. Moses, S. and K. Ng, *A visual study of the breakdown of emulsions in porous coalescers*. Chemical engineering science, 1985. **40**(12): p. 2339-2350.
128. Kocherginsky, N.M., C.L. Tan, and W.F. Lu, *Demulsification of water-in-oil emulsions via filtration through a hydrophilic polymer membrane*. Journal of Membrane Science, 2003. **220**(1–2): p. 117-128.
129. Lorenceau, É., C. Clanet, and D. Quéré, *Capturing drops with a thin fiber*. Journal of colloid and interface science, 2004. **279**(1): p. 192-197.
130. Zin, M. and M. Rody, *The simulation of droplet motion by using lattice boltzmann method*. 2009, Universiti Teknologi Malaysia, Faculty of Mechanical Engineering.
131. Yuan, P., *Thermal lattice Boltzmann two-phase flow model for fluid dynamics*. 2006, University of Pittsburgh.

132. Kutay, M.E., A.H. Aydilek, and E. Masad, *Laboratory validation of lattice Boltzmann method for modeling pore-scale flow in granular materials*. Computers and Geotechnics, 2006. **33**(8): p. 381-395.
133. Wolf-Gladrow, D.A., *Lattice Boltzmann Models*. Lattice Gas Cellular Automata and Lattice Boltzmann Models, 2004: p. 159-246.
134. Adhvaryu, C., *The Lattice Boltzmann Method For Computational Fluid Dynamics Applications*. 2008.
135. Ashgriz, N. and J. Mostaghimi, *An introduction to computational fluid dynamics*. Fluid flow handbook. McGraw-Hill Professional, 2002.
136. Paton, J.B., *Energy utilisation in commercial bread baking*. 2013: University of Leeds.
137. Lycett-Brown, D., I. Karlin, and K.H. Luo, *Droplet collision simulation by multi-speed lattice Boltzmann method*. Communications in Computational Physics, 2011. **9**(5): p. 1219-1234.
138. He, X. and L.-S. Luo, *Theory of the lattice Boltzmann method: From the Boltzmann equation to the lattice Boltzmann equation*. Physical Review E, 1997. **56**(6): p. 6811-6817.
139. Barber, R. and D. Emerson, *The influence of Knudsen number on the hydrodynamic development length within parallel plate microchannels*. Advances in fluid mechanics, 2002. **32**: p. 207-216.
140. Raabe, D., *Overview of the lattice Boltzmann method for nano-and microscale fluid dynamics in materials science and engineering*. Modelling and Simulation in Materials Science and Engineering, 2004. **12**(6): p. R13.
141. Comsol. *Comsol Multiphysics*. 2008 10-08-2015 [cited 1st; Available from: <https://www.comsol.com/multiphysics/navier-stokes-equations>].
142. Discacciati, M., P. Gervasio, and A. Quarteroni, *Interface control domain decomposition methods for heterogeneous problems*. International Journal for Numerical Methods in Fluids, 2014. **76**(8): p. 471-496.
143. Bundschuh, J., *Introduction to the numerical modeling of groundwater and geothermal systems: fundamentals of mass, energy and solute transport in poroelastic rocks*. 2010: CRC Press.
144. Kuzmin, A., *Multiphase simulations with lattice boltzmann scheme*. 2010, Canada: University of Calgary. 145.
145. Yu, Z., O. Hemminger, and L.-S. Fan, *Experiment and lattice Boltzmann simulation of two-phase gas-liquid flows in microchannels*. Chemical Engineering Science, 2007. **62**(24): p. 7172-7183.
146. Huang, H., D.T. Thorne, M.G. Schaap, and M.C. Sukop, *Proposed approximation for contact angles in Shan-and-Chen-type multicomponent multiphase lattice Boltzmann models*. Physical Review E - Statistical, Nonlinear, and Soft Matter Physics, 2007. **76**(6).
147. He, X. and L.-S. Luo, *Lattice Boltzmann Model for the Incompressible Navier-Stokes Equation*. Journal of Statistical Physics, 1997. **88**(3-4): p. 927-944.
148. Zou, Q., S. Hou, and G. Doolen, *Analytical solutions of the lattice Boltzmann BGK model*. Journal of Statistical Physics, 1995. **81**(1-2): p. 319-334.

149. Guo, Z., C. Zheng, and B. Shi, *Discrete lattice effects on the forcing term in the lattice Boltzmann method*. Physical Review E, 2002. **65**(4): p. 046308.
150. Koosukuntla, N.R., *Towards Development of a Multiphase Simulation Model Using Lattice Boltzmann Method (LBM)*. 2011, The University of Toledo.
151. Stensholt, S.K., *Lattice-Boltzmann modelling of spatial variation in surface tension and wetting effects*. 2010, The University of Bergen.
152. Thurey, D.I.N., *Physically based Animation of Free Surface Flows with the Lattice Boltzmann Method Physikalische Animation von Strömungen mit freien Oberflächen mit der Lattice-Boltzmann-Methode*. 2007.
153. Sukop, M.C. and D.T. Thorne Jr, *Lattice Boltzmann modeling: an introduction for geoscientists and engineers*. 2007: Springer Publishing Company, Incorporated.
154. Bao, J., *High Density Ratio Multi-Component Lattice Boltzmann Flow Model for Fluid Dynamics and CUDA Parallel Computation*. 2010, University of Pittsburgh.
155. Cheng, H., Y. Qiao, C. Liu, Y. Li, B. Zhu, Y. Shi, D. Sun, K. Zhang, and W. Lin, *Extended hybrid pressure and velocity boundary conditions for D3Q27 lattice Boltzmann model*. Applied Mathematical Modelling, 2012. **36**(5): p. 2031-2055.
156. Lou, Q., Z. Guo, and B. Shi, *Evaluation of outflow boundary conditions for two-phase lattice Boltzmann equation*. Physical review E, 2013. **87**(6): p. 063301.
157. Liu, H., Q. Kang, C.R. Leonardi, S. Schmieschek, A. Narváez, B.D. Jones, J.R. Williams, A.J. Valocchi, and J. Harting, *Multiphase lattice Boltzmann simulations for porous media applications*. Computational Geosciences: p. 1-29.
158. Rothman, D.H. and J.M. Keller, *Immiscible cellular-automaton fluids*. Journal of Statistical Physics, 1988. **52**(3-4): p. 1119-1127.
159. Gunstensen, A.K., D.H. Rothman, S. Zaleski, and G. Zanetti, *Lattice Boltzmann model of immiscible fluids*. Physical Review A, 1991. **43**(8): p. 4320.
160. Kehrwald, D., *Numerical analysis of immiscible lattice BGK*. PhD. diss, UNI Kaiserslautern, Germany, 2002.
161. Ba, Y., H. Liu, Q. Li, Q. Kang, and J. Sun, *Multiple-relaxation-time color-gradient lattice Boltzmann model for simulating two-phase flows with high density ratio*. Physical Review E, 2016. **94**(2): p. 023310.
162. Connington, K. and T. Lee, *A review of spurious currents in the lattice Boltzmann method for multiphase flows*. Journal of mechanical science and technology, 2012. **26**(12): p. 3857-3863.
163. Liu, H., Q. Kang, C.R. Leonardi, S. Schmieschek, A. Narváez, B.D. Jones, J.R. Williams, A.J. Valocchi, and J. Harting, *Multiphase lattice Boltzmann simulations for porous media applications*. Computational Geosciences, 2016. **20**(4): p. 777-805.
164. Wei, W., *Development of lattice Boltzmann CO2 dissolution model*. 2014, Heriot-Watt University.
165. Nourgaliev, R.R., T.N. Dinh, T.G. Theofanous, and D. Joseph, *The lattice Boltzmann equation method: theoretical interpretation,*

- numerics and implications*. International Journal of Multiphase Flow, 2003. **29**(1): p. 117-169.
166. Swift, M.R., W. Osborn, and J. Yeomans, *Lattice Boltzmann simulation of nonideal fluids*. Physical Review Letters, 1995. **75**(5): p. 830.
167. Nourgaliev, R., T.-N. Dinh, and B. Sehgal, *On lattice Boltzmann modeling of phase transition in an isothermal non-ideal fluid*. Nuclear Engineering and Design, 2002. **211**(2): p. 153-171.
168. Swift, M.R., E. Orlandini, W. Osborn, and J. Yeomans, *Lattice Boltzmann simulations of liquid-gas and binary fluid systems*. Physical Review E, 1996. **54**(5): p. 5041.
169. Takada, N., M. Misawa, A. Tomiyama, and S. Hosokawa, *Simulation of bubble motion under gravity by lattice Boltzmann method*. Journal of nuclear science and technology, 2001. **38**(5): p. 330-341.
170. Kamali, M.R., J.J.J. Gillissen, S. Sundaresan, and H.E.A. Van den Akker, *Contact line motion without slip in lattice Boltzmann simulations*. Chemical Engineering Science, 2011. **66**(14): p. 3452-3458.
171. Castrejón-Pita, J.R., E.S. Betton, K.J. Kubiak, M.C. Wilson, and I.M. Hutchings, *The dynamics of the impact and coalescence of droplets on a solid surface*. Biomicrofluidics, 2011. **5**(1): p. 14112.
172. Chan, T., S. Srivastava, A. Marchand, B. Andreotti, L. Biferale, F. Toschi, and J. Snoeijer, *Hydrodynamics of air entrainment by moving contact lines*. arXiv preprint arXiv:1303.1321, 2013.
173. Huang, H., Z. Li, S. Liu, and X.-y. Lu, *Shan-and-Chen-type multiphase lattice Boltzmann study of viscous coupling effects for two-phase flow in porous media*. International Journal for Numerical Methods in Fluids, 2009. **61**(3): p. 341-354.
174. Basit, R. and M.A. Basit, *Simulation of phase separation process using lattice Boltzmann method*. Can. J. Comput. Math. Nat. Sci. Eng. Med, 2010. **1**(3): p. 71Y76.
175. Delbosc, N., J.L. Summers, A.I. Khan, N. Kapur, and C.J. Noakes, *Optimized implementation of the Lattice Boltzmann Method on a graphics processing unit towards real-time fluid simulation*. Computers & Mathematics with Applications, 2014. **67**(2): p. 462-475.
176. Gross, M., F. Varnik, D. Raabe, and I. Steinbach, *Small droplets on superhydrophobic substrates*. Physical Review E, 2010. **81**(5): p. 051606.
177. Chen, Y., Q. Kang, Q. Cai, M. Wang, and D. Zhang, *Lattice Boltzmann Simulation of Particle Motion in Binary Immiscible Fluids*. Communications in Computational Physics, 2015. **18**(3): p. 757-786.
178. Schmieschek, S. and J. Harting, *Contact Angle Determination in Multicomponent Lattice Boltzmann Simulations*. Communications in Computational Physics, 2015. **9**(5): p. 1165-1178.
179. Mohammadi, M., S. Shahhosseini, and M. Bayat, *Direct numerical simulation of water droplet coalescence in the oil*. International Journal of Heat and Fluid Flow, 2012. **36**: p. 58-71.
180. Hotz, C., R. Mead-Hunter, T. Becker, A. King, S. Wurster, G. Kasper, and B. Mullins, *Detachment of droplets from cylinders in flow using an experimental analogue*. Journal of Fluid Mechanics, 2015. **771**: p. 327-340.

181. Li, X., X. Fan, A. Askounis, K. Wu, K. Sefiane, and V. Koutsos, *An experimental study on dynamic pore wettability*. Chemical Engineering Science, 2013. **104**: p. 988-997.
182. Fan, J., M.C.T. Wilson, and N. Kapur, *Displacement of liquid droplets on a surface by a shearing air flow*. Journal of Colloid and Interface Science, 2011. **356**(1): p. 286-292.
183. Pangestu, F. and C. Stanfel, *Separation media and methods especially useful for separating water-hydrocarbon emulsions having low interfacial tensions*. 2011, Google Patents.
184. Arouni, H., *Enhanced water/fuel coalescing filter media for diesel engines: overview and future directions*. forthcoming.